Fluorescence Excitation Emission Matrix Spectral Imaging Microscopy

by

Emma X. Abbey

A Dissertation Submitted in Partial Fulfillment of the Requirements for the Degree of

— DOCTOR OF PHILOSOPHY —

in the Department of Chemistry

University of Victoria

We acknowledge and respect the Lək̓ʷəŋən (Songhees and Xʷsepsəm/Esquimalt) Peoples on whose territory the university stands, and the Lək̓ʷəŋən and W̱SÁNEĆ Peoples whose historical relationships with the land continue to this day.

Fluorescence Excitation Emission Matrix Spectral Imaging Microscopy

by

Emma X. Abbey

Supervisory Committee

Dr. Hans-Peter Loock, Supervisor
Department of Chemistry

Dr. Alexandre Brolo, Departmental Member
Department of Chemistry

Dr. Julian Smazynski, Outside Member
Department of Biochemistry and Microbiology

Abstract

With this dissertation the capabilities of fluorescence microscopic imaging are greatly extended to allow for fast chemical fingerprinting in each pixel of an image. Spatial fluorescence imaging microscopy using multispectral and hyperspectral cameras with multiplexed excitation sources has been thus far not described in the literature. Three systems to acquire fluorescence excitation-emission matrix (F-EEM) spectra are demonstrated in this work, using Hadamard-multiplexed programmable excitation light sources. Computational approaches to bypass the limitations of multi- and hyperspectral camera hardware are implemented to increase the time resolution and emission spectral resolution.

The first chapter contains background and instrumentation used in F-EEM spectroscopy and multispectral imaging. Microscopy illumination methods are described as they relate to the methods used in this work, and a brief overview of parameters used for creating spatially distinct dye samples under a microscope are described. Raman spectroscopy and how it relates to multiplexed fluorescence spectroscopy is described and is followed by an overview of multivariate analysis methods used in F-EEM analysis.

F-EEM imaging requires a fully programmable excitation light source and an imaging detector. The work shown here develops and uses Hadamard-multiplexed excitation sources based on instruments built by our group in the past. The basis for multiplexed spectroscopy and the theory of the Hadamard transform are described in Chapter 2. The optical design and software integration of two programmable light sources—one white-light source based on a digital micromirror array and one using an array of discrete-wavelength laser diodes—are described in Chapter 3.

Acquisition of F-EEM images is done through one of two cameras—a snapshot multispectral camera using an eight-channel colour filter array, or an interferogram-based hyperspectral camera providing up to 141 spectral channels over a wide wavelength range. These commercial cameras and their integration into our systems are described in Chapter 4.

The processing and analysis for F-EEM images acquired using Hadamard-modulated light sources and some unique challenges to these datasets are detailed in Chapter 5.

Four fluorescent components are spatially and spectrally separated in a macroscopic application of the multispectral camera and Hadamard-modulated white-light excitation source, described in Chapter 6. Here, an image of capillaries containing fluorophores and mixtures thereof is analyzed using multivariate analysis to demonstrate the spatial and spectral separation of four fluorescent components in an F-EEM image.

The excitation light source is then modified for use in numerous microscopy illumination methods. F-EEM microscopic imaging using three distinct combinations of excitation source and imaging detectors is demonstrated in Chapter 7 using combinations of dye emulsions. Multivariate analysis of F-EEM images taken with an 8-channel multispectral camera and using seven laser diodes can find ten fluorophores in a microscopy image when those spectral signatures are known. Without prior knowledge of the fluorophores, at least four fluorescent dyes in a microscope image are separated using multivariate analysis of an F-EEM photomicrograph taken using the same multispectral camera and a white-light programmable light source.

The emission spectra of F-EEM images acquired with the eight-channel multispectral camera are spectrally upscaled in Chapter 8 to increase the spectral resolution without hardware modifications. The upscaled spectra are demonstrated to provide a superior method of fluorophore identification and separation in an F-EEM image—more fluorophores can be identified in F-EEM images using upscaled spectra than raw spectra. A new computational method for increasing the time resolution of F-EEM images acquired using a Hadamard-modulated excitation light source is also demonstrated. These two computational techniques allow us to obtain chemical identifiers and intensities for each of the 65,536 pixels per frame, when these frames are obtained at a rate between 3-10 per second.

Numerous avenues for experiments using the programmable light sources with the multispectral and hyperspectral cameras are described in Chapter 9, along with future work on a multi-wavelength multiplexed Raman and fluorescence spectroscopy experiment.

Acknowledgements

More than anything, this PhD has been a continuous process of learning more new skills than I could have imagined at the start. I am very grateful to have spent this time learning in a great environment. Thank you to my supervisor, Dr. Hans-Peter Loock, for your endless enthusiasm for research and unwavering confidence in my projects and work. Thank you for all the opportunities and support you provided through these years.

To all the staff at UVic who have made my project, and so many others, successful. To Nick Braam in the Physics and Astronomy electronics shop for all your work, troubleshooting, and for answering my many electronics questions, this project would not have been possible without your support. Thank you to Chris Secord in the UVic Science machine shop for your knowledge and insight, and all the work on designing and machining parts for many projects for our group. To Dr. Jack Barnes—thank you for being a fountain of knowledge and to Dr. Stanislov Konorov for all the optics advice. Thanks to Dr. Mehraveh Seyedalikhani for all your support while I was a teaching assistant and to Dr. Irina Paci for the same. Thank you to the funding agencies that made this and so much other amazing research possible—the National Sciences and Engineering Research Council of Canada—and to the donors and organizations who support students, especially to Optica for the opportunities and funding. Thanks to Dr. Jean-Pierre van Helden and Dr. Sarah-Johanna Klose for the generous donation of the light source and installation.

To my lab mates—thank you for the many discussions, troubleshooting sessions, and problem-solving that shaped this work. A special thanks to Dr. Swapnil Daxini who has been an invaluable sounding board and the best desk mate you could ask for to stick this journey out with, and to Oren Katz, Monique-Anne Bueno, Sara Joulai, Deniz Aydin, Arthur Santos, Yasaman Shaharestani, Mackenzie McNiven, and Paul Reid. Thank you to Dr. Sarah Klose for your constant enthusiasm for science and solving problems, to Dr. Chris Prüfert for all you taught me about research and communication, and to Dr. Travis Ferguson for the many discussions and your analysis wizardry.

To my family—thank you for your constant and unwavering support and for explaining my work as “lasers”. Thank you for the phone calls, visits, food, and inspiration. To my partner Cole Philipp—thank you for maintaining my sanity and motivation, and for always being able to put a smile on my face—and to my Sammie for the same.

Table of Contents

List of Figures

List of Tables

List of Appendices

List of Acronyms

AOTF	Acousto-Optic Tunable Filter
APD	Avalanche Photodiode
AR	Acid Red
BFB	Bifurcated Fiber Bundle
BFM	Brightfield Microscopy
CAMTEC	Center for Advanced Materials and Technology
CANDECOMP	Canonical Decomposition
CBB	Carbazole Bromobenzothiodiazole
CC	Core Consistency
CCD	Charge-Coupled Device
CE	Capillary Electrophoresis
CFA	Colour Filter Array
CLSM	Confocal Laser Scanning Microscope
CMOS	Complementary Metal Oxide Semiconductor
CNN	Convolutional Neural Network
CP	Continuous Phase
CT	Charge Transfer
DAQ	Data Acquisition Card
DFM	Darkfield Microscopy
DIC	Differential Interference Contrast
DMA	Digital Micromirror Array
DMA-PLS	Digital Micromirror Array Programmable Light Source
DOM	Dissolved Organic Matter
DP	Dispersed Phase
EEL	Excitation Emission Lifetime
EEM	Excitation-Emission Matrix
EFL	Effective Focal Length
EM	Electron Multiplying
EMCCD	Electron Multiplying Charge Coupled Device
E/O	Ethanol-in-Oil (Emulsion)
ESD	Electrostatic Discharge
FEP	Fluorinated Ethylene Propylene
FFT	Fast Fourier Transform
FLEEMSI	Fluorescence Excitation Emission Matrix Spectral Imaging
FLIM	Fluorescence Lifetime Imaging Microscopy
FOV	Field of View
FrTIR	Frustrated Total Internal Reflection
FT	Fourier-Transform
FTIR	Fourier Transform Infrared (Spectroscopy)

FT-PI	Fourier Transform Polarization Interferometer
FWHM	Full Width at Half Maximum
GE/O	Glycerol Ethanol in Oil (Emulsion)
GOI	Gated Optical Intensifier
GUI	Graphical User Interface
HLB	Hydrophilic Lipophilic Balance
HOSVD	Higher Order Singular Value Decomposition
HPLC	High-Performance Liquid Chromatography
HSC	Hyperspectral Camera
HT	Hadamard Transform
HT-PLS	Hadamard Transform Programmable Light Source
ICCD	Intensified Charge Coupled Device
IR	Infrared
LC	Liquid Crystal
LCD	Liquid Crystal Device
LCW	Liquid Core Waveguide
LD	Laser Diode
LDA	Laser Diode Array
LDA-PLS	Laser Diode Array Programmable Light Source
LDPS	Laser Driven Plasma Source
LED	Light Emitting Diode
LLG	Liquid Light Guide
LVF	Linear Variable Filter
MLA	Machine Learning Algorithm
MSC	Multispectral Camera
NA	Numerical Aperture
Nd:YAG	Neodymium-Doped Yttrium Aluminum Garnet
NDF	Neutral Density Filter
NEP	Noise Equivalent Power
NMR	Nuclear Magnetic Resonance
NN	Neural Network
NS	Nanostar
NSOM	Nearfield Scanning Optical Microscopy
PARAFAC	Parallel Factor Analysis
PCA	Principal Component Analysis
PCR	Principal Component Regression
PD	Photodiode
PDMS	Polydimethylsiloxane
PE	Percentage of Explained Variance
PEG	Polyethylene Glycol
PLS	Programmable Light Source

PMT	Photomultiplier Tube
RB	Rhodamine B
RGB	Red-Green-Blue
RGGB	Red-Green-Green-Blue
ROI	Region of Interest
SCA	Supercycle Algorithm
SDK	Software Development Kit
SEM	Scanning Electron Microscope
SERS	Surface-Enhanced Raman Spectroscopy / Scattering
SiPM	Silicon Photomultiplier
SNE	Signal-to-Noise Enhancement
SNR	Signal-to-Noise Ratio
SR	Sulforhodamine
SRB	Sulforhodamine B
SVD	Singular Value Decomposition
TCSPC	Time-Correlated Single Photon Counting
TERS	Tip Enhanced Raman Scattering
TFTF	Thin Film Tunable Filter
TIR	Total Internal Reflection
TIRF	Total Internal Reflection Fluorescence
TIRFM	Total Internal Reflection Fluorescence Microscopy
TWINS	Translating-Wedge-based Identical pulses eNcoding System
UV	Ultraviolet
W/O	Water-in-Oil (Emulsion)
2D	Two-dimensional
3D	Three-dimensional

Chapter 1 Introduction

Analytical chemistry is largely motivated by the detection and quantification of chemicals.

The perfect instrument to analyse all chemicals in any environment does not exist. All existing instruments trade of between detection limit (how little can be detected), specificity (how well can the chemical be identified) and cost, complexity, and/or size. For example, mass spectrometry and NMR spectroscopy provide high chemical specificity and often extraordinary sensitivity, at an enormous cost of the instrumentation, sample preparation, and acquisition time. By contrast, optical techniques such as infrared spectroscopy, Raman spectroscopy and fluorescence spectroscopy can be comparably inexpensive, often at the cost of lower specificity. To improve the detection limits to single molecules, the instrumental cost and complexity increases.

Spectroscopic imaging is a subfield of analytical spectroscopy in which chemical information is obtained with spatial resolution in addition to spectroscopic resolution. Fluorescence imaging—the subject of this dissertation—is one of the most widely used techniques especially on medical or microbiological samples, but it is not the only one.

Confocal Raman imaging uses the Raman effect to identify and quantify molecules by their Raman signatures in-a pixel-by-pixel scan over the sample surface. Photoacoustic imaging exploits the photoacoustic effect to map the absorption cross section of a sample following excitation with a focused laser pulse.

In this work we focus on fluorescence imaging since it is conceptually simple, already wide-spread, and many inexpensive instruments exist. We show that we can dramatically increase the information content of fluorescence micrographs using new multiplexed light sources, a commercial multispectral camera and new algorithms for data analysis. Our contributions to this field are therefore more likely to have a large impact and face the lowest barriers to adoption.

This chapter contains an introduction and background for the main topics covered in this dissertation—fluorescence excitation-emission matrix spectroscopy, imaging, microscopy, multivariate analysis, and Raman spectroscopy. The chapter begins with a discussion of the applications and instrumentation used for fluorescence excitation-emission matrix (F-EEM) spectroscopy. Chemical analysis by fluorescence imaging is discussed, including recent

developments of imaging using consumer and high-performance devices. Microscopy techniques will be briefly discussed in the following section to provide a background for some of the instrumentation used in this work. A background on emulsion formation is given for use as proof-of-concept for my experiments. Section 1.4 contains a brief overview of Raman spectroscopy and various enhancement methods and a focus on surface enhancement. A tutorial on multivariate analysis and decomposition methods used in F-EEM analysis are presented in Section 1.5.

Our instruments use programmable light sources for the fluorescence excitation of samples. Specifically, we use the Hadamard transform technique—essentially a binary version of the Fourier transform—to increase the data acquisition rate. Chapter 2 contains an overview of the Hadamard Transform technique when applied to fluorescence microscopy, along with its advantages and shortcomings. Chapter 3 discusses the two different programmable light sources used for the fluorescence excitation in F-EEM spectroscopy and imaging, as well as the associated optical elements. Chapter 4 focusses on the detection of the fluorescence emission using two different types of multispectral or hyperspectral cameras. The datasets acquired by our new technique are very large and preprocessing is required to reduce the size of the data to be analysed by multivariate techniques. Chapter 5 describes these computational methods conceptionally and with examples, and the details and algorithms are found in the appendices. Chapter 6 demonstrates the capabilities of the F-EEM imaging method for detection of spatially overlapping fluorophores, and Chapter 7 demonstrates the power of these techniques for microscopic applications. The spectral and temporal resolution of the acquired F-EEM spectra are improved through computational approaches in Chapter 8.

We show that we can provide a chemical fingerprint in the form of an F-EEM for each pixel in an image—for example, 65,536 F-EEM spectra in 11 seconds, far faster than the few minutes to acquire a single similar spectrum using a conventional spectrometer. The strengths and limitations of our approach, as well as possible extensions for interesting applications and further development of the light sources and cameras, and some steps and preliminary data for multiplexed Raman spectroscopy.

Much of the content in Chapters 1 (Sections 1.1, 1.2, and 1.4) and 2 will be included in a review article on EEM spectroscopy, with co-authors Dr. Sarah-Johanna Klose (first), Dr. Travis Ferguson, and Dr. Hans-Peter Loock. Before I begin the chapter, I would like to acknowledge the huge

amount of work that went into this review article from all contributors, and make it known that not all the writing contained in the specified chapters is my own.

1.1 Fluorescence Excitation-Emission Matrix Spectroscopy

Excitation-Emission Matrix (EEM) spectroscopy is a powerful tool to identify and quantify molecules, particularly in liquid solutions. Today, the two most common uses of EEM spectroscopy are the classification of samples by their composition of fluorophores, and measurements of the transformation kinetics of a sample by determining the relative contribution of fluorophores as a function of time.

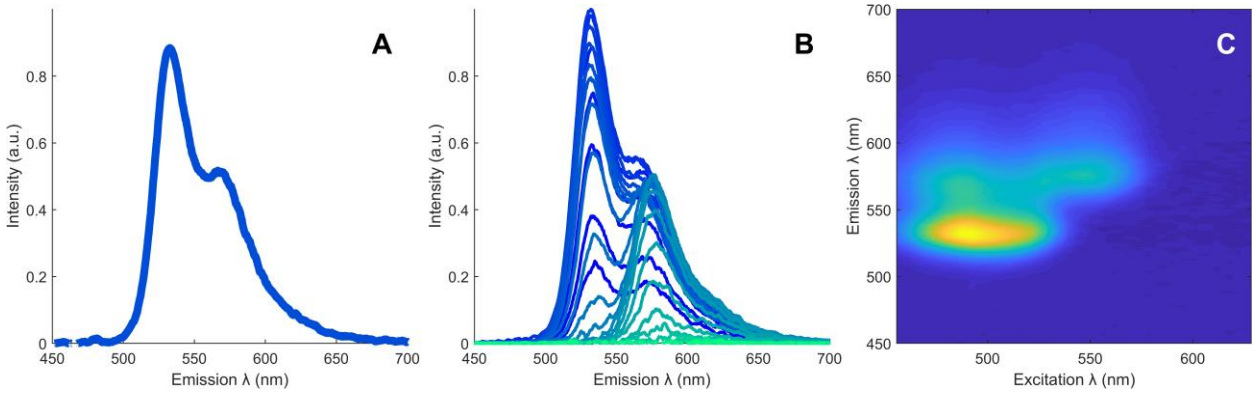

Figure 1.1. Comparison of two- and three-dimensional fluorescence emission spectra. Fluorescence emission of a mixture of rhodamine 110 (300 μM in ethanol) and rhodamine B (15 μM in ethanol), excited using one wavelength band (480 nm) (A), and 31 wavelength bands (460–580) nm (B, C), plotted as individual lines (B) and a contour plot (C).

A fluorescence EEM (F-EEM) is typically obtained by recording the fluorescence emission spectra for many different excitation wavelengths. The F-EEM therefore consists of a three-dimensional data cube with two spectral dimensions (excitation and emission wavelengths), and the intensity as a function of both wavelengths. Compared to one-dimensional techniques such as single-wavelength absorption or fluorescence intensity measurements, or two-dimensional spectroscopic techniques such as absorption or single-wavelength-excitation fluorescence (Figure 1.1 left), F-EEM frequently permits unambiguous identification and quantification of a variety of fluorophores that coexist in a sample and that may have similar excitation or emission features. Figure 1.3 highlights the unique capabilities of F-EEM spectroscopy—a fluorescence emission spectrum obtained by excitation of a solution of rhodamine and fluorescein dyes with 440 nm light would result in a broad spectrum with two overlapping features. By contrast, the corresponding F-EEM spectrum shows the contributions from these dyes well-separated and readily quantifiable.

1.1.1 Information Content of F-EEM Spectroscopy

According to Kasha's rule [1], the light emission of an excited atom or molecule originates from the vibronically excited level having the lowest energy within the same multiplicity as the ground state, since vibrational relaxation processes within an electronic state are typically fast. Accordingly, the simplest EEM spectra show a single maximum at the [λ_{ex}, λ_{em}] wavelength pair, where λ_{exc}^{max} corresponds to the maximum in the absorption spectrum and is given by the maximum of the Franck-Condon absorption integral, and λ_{em}^{max} corresponds to the maximum of the emission spectrum at this excitation wavelength. The emission maximum (λ_{exc}^{max}) is red shifted by an energy difference that corresponds to the non-radiative vibrational relaxation of the fluorophore in the excited states and the ground state, called the "Stokes shift".

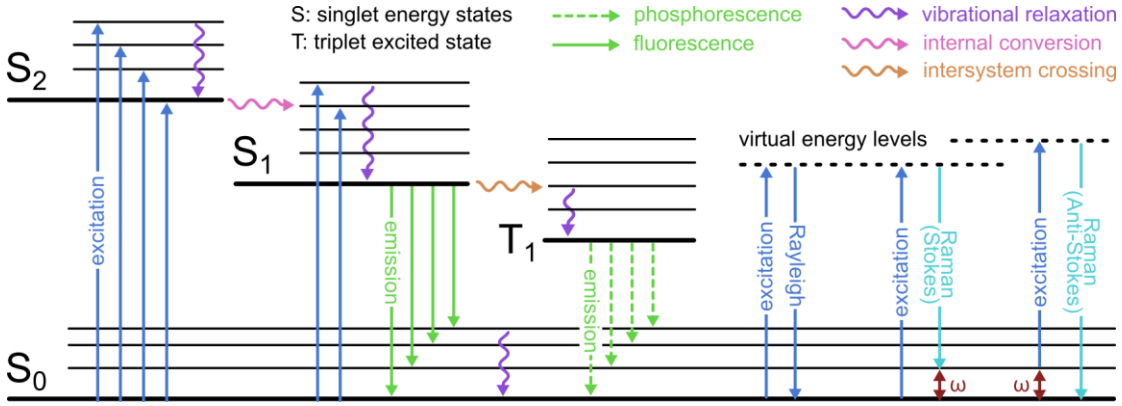

Figure 1.2. Energy diagram of various spectroscopic processes.

Both excitation and emission spectra are frequently dependent on the polarity and/or viscosity of the solvent and may be governed by both kinetic and thermodynamic solvent effects. F-EEM spectra can therefore provide a sensitive probe for the local chemical environment of the fluorophore [2]. Generally, the environmental modification of the ground state potential energy surface, by *e.g.*, a solvent, is reflected by a change of the excitation spectrum, whereas the fluorescence emission spectra primarily report on the relaxed or partially quenched environment of the photoexcited molecules.

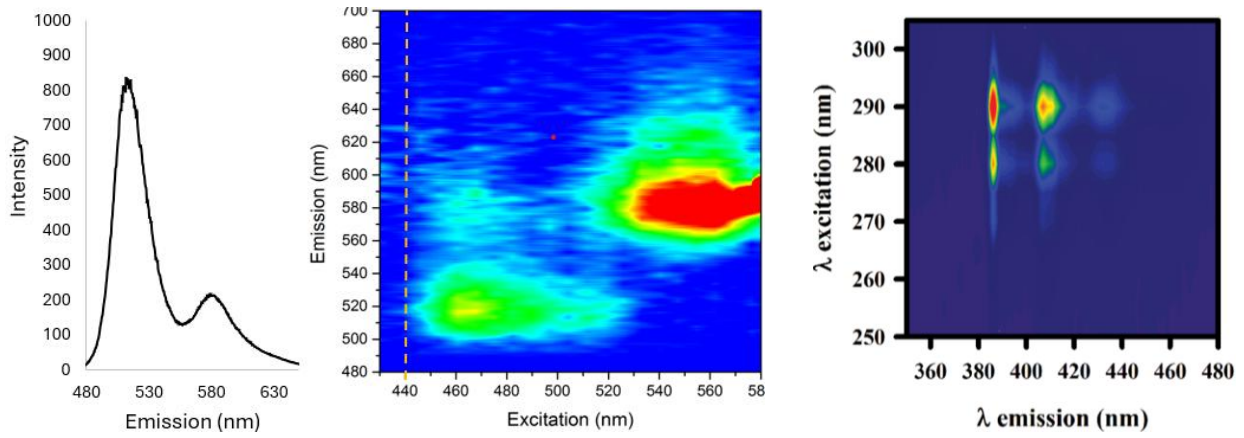

Figure 1.3. Representation of fluorescence excitation-emission matrix spectra. Fluorescence emission spectrum (**left**) and associated EEM spectrum (**middle**) of a solution of rhodamine B and fluorescein dyes. The red dashed line indicates the excitation wavelength for the left spectrum λ_{exc} = 440 nm. (**right**) EEM spectrum of chrysene at 77 K [3].

In practice, EEM spectra frequently contain far more information about the vibronic structures of the ground state and lowest lying excited state(s). The EEM spectrum of a pure diluted sample of chrysene exhibits multiple peaks in both the excitation and emission spectra due to the vibrational structure of the excited and ground states [3]. As seen in Figure 1.3, even the EEM spectrum of chrysene, a pure, diluted fluorophore, may exhibit multiple peaks in the excitation spectrum and in the emission spectrum due to the vibrational structure of the excited state and ground state.

Historic Developments of EEM Techniques

In 1954 Donaldson published on an instrument that allowed for the determination of fluorescence spectra as functions of the wavelength of a tunable excitation light source [4]. The resulting two-dimensional spectrum was given in tabular form and may be the first reported excitation-emission matrix. EEMs are therefore sometimes referred to as "(bispectral) Donaldson matrices" although this term is most frequently used in the colour mapping field. At about the same time, Bowman, Caulfield, and Udenfriend also developed an instrument that could record a fluorescence emission spectrum at an adjustable excitation wavelength [5]. The first commercial instrument developed by this group was the 1955 AMINCO-Bowman spectrophotofluorometer, which was, in 1957, further developed into the Farrand Spectrofluorometer and became a commercial success. A 1995 article by Udenfriend provides a fascinating personal account of the early days of commercial spectrofluorometer developments [6]. EEM spectroscopy gained more popularity with the development of commercial rapid-scanning fluorescence spectrometers [7-9] and subsequent commercial developments in the 1990s. The simultaneous introduction of ready-to-use algorithms for parallel factor analysis (PARAFAC) and principal component analysis (PCA) and regression

(PCR) facilitated the classification and decomposition of fluorescence excitation-emission data into individual fluorescent components [10]. The characterization of dissolved organic matter (DOM) and of water samples [11-19] are good examples of a useful and well-used application of this.

The field now appears to undergo another rapid transformation—new computational approaches, alongside cheaper, faster, and better optical components, and new developments in imaging and multiplexing technology generate renewed interest in EEM spectroscopy. Portable spectrometers, some based on smartphones, have made the technology for acquiring EEM spectra widely accessible—albeit with a somewhat reduced spectral resolution [20-31]. In analytical laboratories, EEM spectroscopy has also been combined with separation techniques like high-performance liquid chromatography (HPLC) [32] or capillary electrophoresis (CE) [33], or with other spectroscopic techniques such as absorbance spectroscopy [34] or Fluorescence Lifetime Imaging Microscopy (FLIM) [35, 36].

1.1.1 Applications of Fluorescence Spectroscopy

Since the initial developments by Johnson, Callis and Christian in 1977 [8] EEM spectroscopy has evolved to a workhorse technology to characterize a variety of environmental samples such as dissolved organic matter in surface water [13-18], and to monitor the quality of water in rivers, lakes, oceans [15, 18, 37-39]. It has also been applied to monitor microalgae [40, 41], pollutants [42], and the quality of food during processing and storage [43-48]. EEM spectroscopy has proven especially useful in the classification of foodstuff such as wine [49-56], cheese [57], brandy [58, 59], olive oil [60-64] and other edible oils [65]. The use of fluorescence techniques in food quality assessments has been recently reviewed by Gu *et al.* [29].

EEM spectroscopy has also been employed to characterize manufactured materials including bioactive glass [66], engine lubricants [67-70], colloidal quantum dots for light emitting diodes and solar cells [71], atomically precise gold nanoclusters [72], carbon nanotubes [73], and materials with twisted charge transfer states [2]. Finally, EEM spectroscopy is used to characterize pathological samples [9, 74-79], *in-vitro* and *in-vivo* [23]. Figure 1.4 gives examples on the use of EEM spectroscopy to understand the photochemical degradation of scintillator liquids for neutrino detection [80]. This incomplete list is meant to illustrate the vast variety of samples and applications in which EEM spectroscopy has found uses.

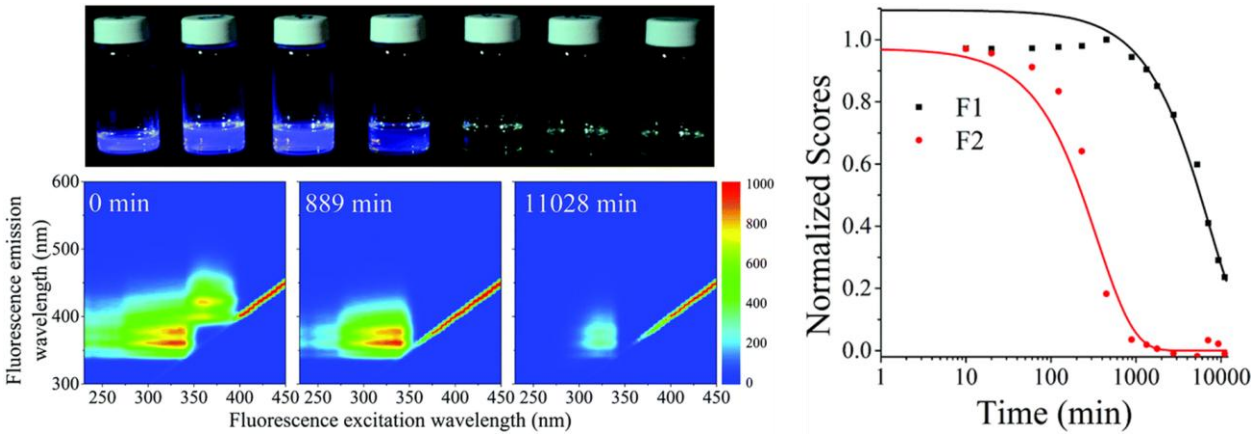

Figure 1.4. F-EEM monitoring and analysis of scintillator solution photodegradation. (**left**, top) Photo series of scintillation solution for neutrino detection after irradiation by 365 nm ultraviolet light, taken at 0, 20, 123, 449, 1329, 2759, 7049 min (left to right). (bottom) Three selected EEM spectra of the same samples. The fluorescence intensity decreases as the sample is exposed to ultraviolet light. (**right**) Normalized scores of two scintillator dyes from a multivariate analysis, where the lines represent single exponential decay processes. Samples were (F1) photo-degraded 2,5-diphenyloxazole and (F2) 1,4-bis(2-methylstyryl)benzene [80].

In all these cases the two-dimensional EEM spectra (three-dimensional data cubes) can be used to distinguish contributions from related chemical constituents that might have similar absorption spectra or fluorescence emission spectra following single-wavelength excitation. For example, EEM spectroscopy can readily distinguish between chlorophyll A, chlorophyll B, pheophytin A, and pheophytin B, despite their very similar emission spectra [81, 82]. EEM spectroscopy is therefore useful in distinction and classification of components in complex mixtures.

In almost all classification studies, the collection of EEM spectra from different samples is subjected to multivariate analysis. Principal Component Analysis (PCA) techniques are common methods used to generate cluster maps for classification of unknown samples [83]. Several software packages exist that facilitate the analysis [18, 84-86].

Using EEM spectroscopy for dynamic/kinetic measurements is somewhat less common and is typically hampered by the long acquisition time for an EEM spectrum. It may take tens of seconds and up to many minutes to acquire a single spectrum, depending on the instrument and the required spectral resolution and range. Several kinetic studies using EEM have been reported, however. Using a fast EEM spectrometer Bernicky *et al.* continuously monitored the transformation of chlorophyll into pheophytin and from pheophytin into copper-pheophytin in the reaction vessel [34, 87]. Stamplecoskie and coworkers monitored the conversion of Au-nanoclusters by measuring the fluorescence EEM spectra of aliquots of the solution taken at set time intervals [88]. There are several studies that describe the photodegradation of environmental samples [89-92], the stability of

scintillator liquids [80], and the oxidative degradation of engine lubricants [67, 68]. Because of the low data acquisition rate, the processes must be either very slow (hours) or the sample reaction must be quenched before analysis. Much faster EEM spectrometers would be useful in that regard.

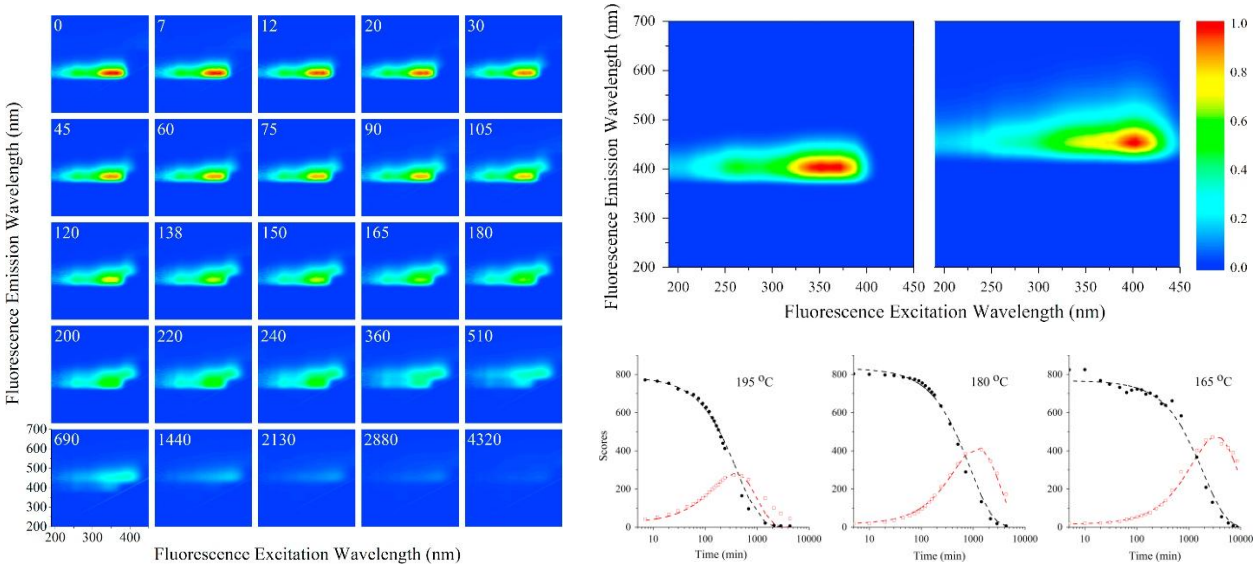

Figure 1.5. F-EEM jet engine oil monitoring and analysis. (**left**) Raw EEM spectra of jet turbine oil samples aged at 195°C. The white numbers refer to the number of minutes at this temperature. (**right, top**) Component EEMs of jet turbine oil samples. Two signatures (normalized to 1) produced by a PARAFAC analysis of all 157 EEM spectra obtained by the fiber probe. (**right, bottom**) Time evolution of components from jet turbine oil produced by a PARAFAC analysis. The black solid circles and red empty squares represent component 1 (PAN, Phenyl-α-Naphtylamine) and component 2 (PAN_2), respectively. The dashed lines are obtained by fitting the data to a kinetic model [68].

The analysis of a time series of EEM spectra is usually undertaken using Parallel Factor (PARAFAC) analysis [18, 93]. In many cases PARAFAC analysis can correlate the component spectra to the EEM spectra of the neat chemical species. It is then possible to obtain EEM spectra of intermediates that would otherwise be difficult to access (Figure 1.5). Recently, machine learning approaches based on Convolutional Neural Networks, CNNs, have also shown promise [94] in the analysis of a series of EEM spectra. Several common 3-way multivariate analysis techniques are discussed in Section 1.4.

Fluorescence imaging with multiple excitation sources (or excitation filters) and a conventional colour camera may be considered a coarse variant of spatially resolved EEM spectroscopy as it uses 3-10 excitation wavelengths and just three emission bands corresponding to the red, green and blue—RGB—colour channels. Multi-wavelength fluorescence imaging has enabled imaging and classification of biological samples and is nowadays a standard method for microscopy of, for example, cell or tissue samples [95-101]. The polarization response or fluorescence lifetime measurements of a given sample, add additional information to a fluorescence spectroscopy

experiment. In Section 1.2 we discuss EEM imaging methods that provide more spectroscopic detail—a fluorescence EEM for each pixel in an image.

Any variant of fluorescence spectroscopy is based on the radiative emission of energy following electronic excitation (light absorption) by the sample. Fluorescence spectroscopy is therefore complementary to spectroscopic methods that probe only the non-radiative dissipation of energy following absorption [102]. For example, photoacoustic and photothermal spectroscopy probe the local change of the density resulting in the propagation of acoustic waves, or the local change of the refractive index, respectively. A combination of radiative and non-radiative detection methods can then be used to recover the atomic and molecular absorption spectra [103, 104]. In trace absorption spectroscopy a small reduction of the large optical transmission signal must be accurately quantified, whereas the measurement of the radiative and non-radiative response of the sample to electronic excitation is largely background-free. Fluorescence, photothermal and photoacoustic spectroscopy are therefore the methods of choice for weakly responding, small, or dilute samples.

1.1.2 Fluorescence Detection

Fluorescence in the visible region can be detected by human eyes—highly capable photon detectors with a wide dynamic range and a roughly logarithmic sensitivity response. However, human light perception is limited in its ability both to resolve small spectral shifts and to quantify precise concentrations and cannot reliably distinguish complex colour mixtures. Additionally, because modern analysis methods rely on computer processing, an optical signal must be first converted into a digital form. A transducer is therefore required to convert photon information into a machine-readable signal.

Spectral Separation and Detection of Light

To take advantage of all the information available from the fluorescence emission by a molecule, a spectrometer can detect the emission intensity at a range of wavelengths. In the simplest setup, light is spectrally dispersed by a diffraction grating or prism and the intensity at different wavelengths is observed by a detector. An example of a spectroscope which uses your own eye or a cellphone camera as a detector and can be made at home is shown in Figure 1.6 [105].

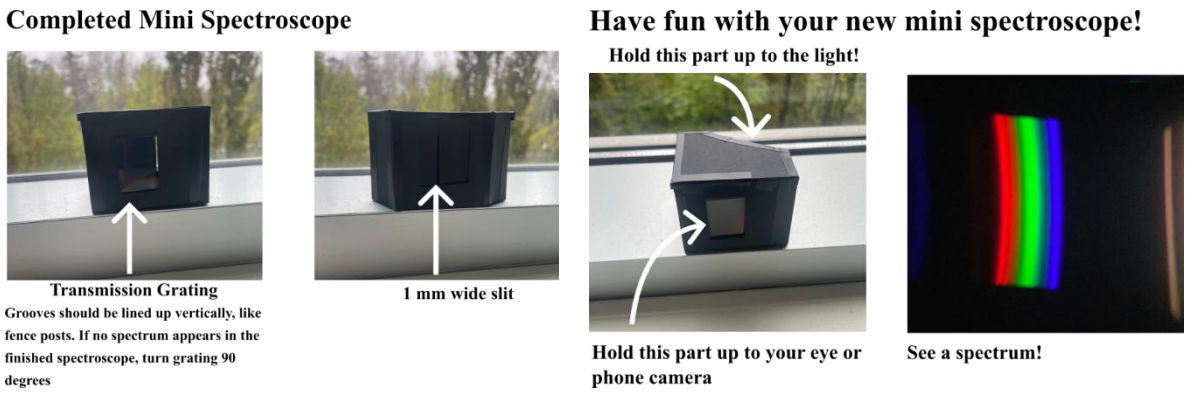

Figure 1.6. Images of a simple spectroscope which can be built at home [105].

Spectroscopic detectors for fluorescence emission may be classified into single pixel detectors detecting fluorescence intensity, I, linear array detectors for recording dispersed fluorescence emission spectra, $I(\lambda_{em})$, imaging array detectors, $I(x,y)$, and hyperspectral imaging arrays $I(x,y,\lambda_{em})$. Devices used to detect fluorescence signals range between simple photodiodes (PDs) for detecting strong signals to two-dimensional arrays of amplified detection elements for weaker signals. Photodiodes—semiconductor devices often made from silicon (Si) for visible-wavelength detection—are simple photon detectors that can be modified to include internal gain mechanisms to permit detection down to the single photon level. Such devices include avalanche photodiodes (APDs) or silicon photomultipliers (SiPMs), which act as alternatives to photomultiplier tubes (PMTs) which are still the most common single-photon detector. These devices provide a spectrally indiscriminate response and can be used to detect single-pixel intensity.

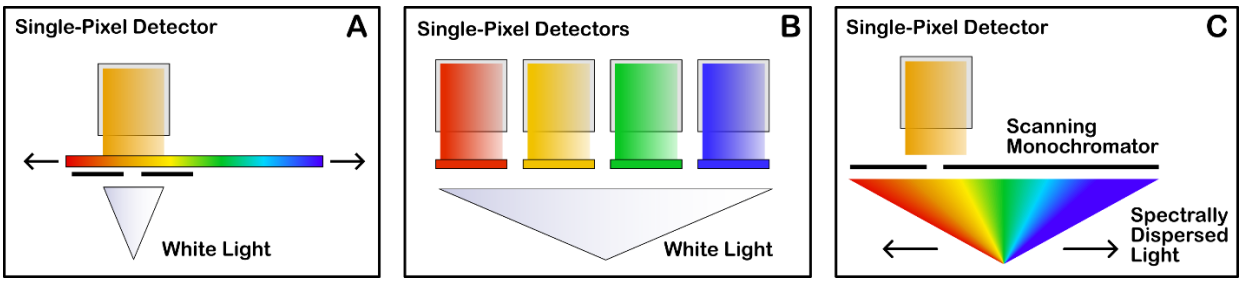

Figure 1.7. Single-pixel detectors with different spectral discrimination methods. White light from a light source or emitted light from a sample (A) passes through a linear variable filter for detection of a single wavelength band, (B) is detected through four detectors each with a different colour filter for different wavelength bands. (C) A scanning monochromator selects a single wavelength band for detection from spectrally-dispersed white or emitted light using a slit exit.

Single-pixel detectors can be combined with a spectral discrimination technique such as colour filters or a linear variable filter, an interferometer, or a dispersion element such as a diffraction grating in a scanning monochromator, to gather spectral information about the fluorescence emission (Figure 1.7). Alternatively, a single-pixel detector can be used for spectral detection with

lower loss than a scanning monochromator by multiplexing the spectrally dispersed light, for example using a digital micromirror device [106]. By combining several single-pixel detectors with colour filters, spectral bands can be distinguished, e.g., for flow cytometry measurements [107, 108].

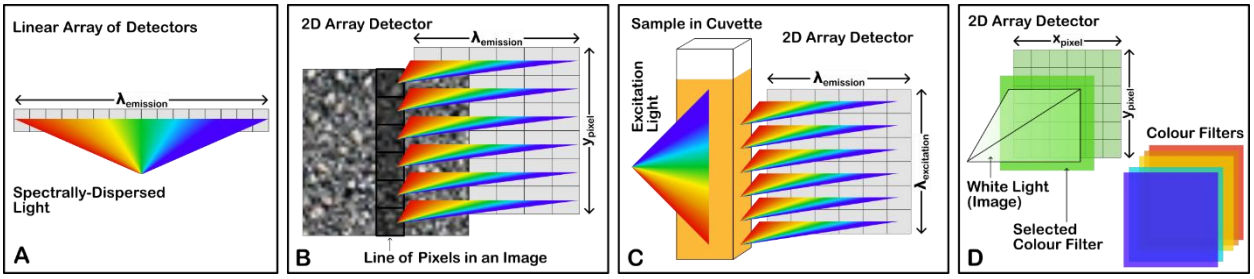

Figure 1.8. Linear and two-dimensional detector arrays. (A) Linear array of detectors used in an array spectrometer, (B) a series of linear arrays to form a two-dimensional array used for a line-scanning hyperspectral camera in which the light from each pixel in a line of the image is spectrally dispersed onto a linear pixel array, (C) single-shot excitation-emission matrix acquisition, as described by Booksh and Muroski [41, 109] in which each horizontal linear array of pixels detects the spectrally-dispersed emission from a wavelength band of the excitation light, for a spatially homogeneous sample, (D) a two-dimensional array used for imaging, with spectral distinction using a single interchangeable colour filter.

Single-pixel detectors can be combined in arrays to form linear or imaging charge-coupled device (CCD) or complementary metal oxide semiconductor (CMOS)-type sensors. Linear detector arrays can be combined with a dispersion element such as a diffraction grating to detect a spectrum without scanning (Figure 1.8A), as in miniaturized array spectrometers, which are found in many teaching laboratories and research labs. Fluorescence emission spectra can be obtained using two-dimensional (2D) detector arrays—for example to collect single-pixel one-shot excitation-emission matrices (λ_{ex}, λ_{em}) [41, 109] (Figure 1.8C). 2D detectors can also be used to collect emission spectra for each pixel in a line (λ_{em}, y) (Figure 1.8B) or as imaging chips (x, y) to collect spatially resolved fluorescence when combined with an external spectral discrimination technique such as filters linear variable filter, colour filters, or an interferometer.

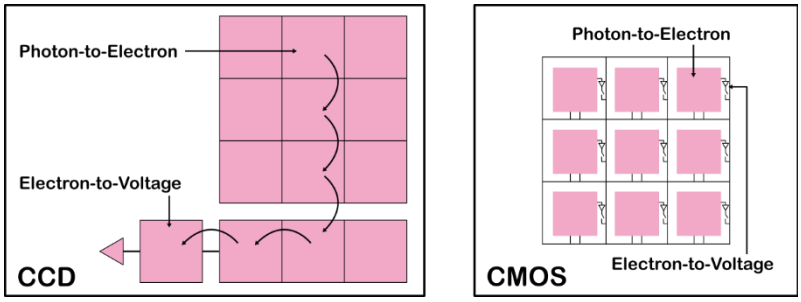

Figure 1.9. Charge-coupled device (CCD) and complementary metal oxide semiconductor (CMOS) photodetector arrays. Readout of a CCD occurs via a register—charges from each pixel are read out sequentially by the register shown in the bottom. The speed at which pixels are read out is accompanied by a read noise—increase the speed and the noise increases—limiting the overall readout speed and time between image acquisitions. Readout of a CMOS sensor occurs on each pixel individually, allowing for faster readout, however leading to some inter-pixel variation due to slight differences in each pixel electronics due to manufacturing. The photoactive area of a CCD and CMOS photodetector array is shown in pink, and each pixel is shown by black borders.

Previously, image sensors using cooled and/or back-thinned CCDs have been preferred for high-performance applications due to their superior sensitivity and overall performance. However, CMOS sensors have a few inherent advantages over CCD sensors, primarily due to their lower manufacturing cost and higher frame rate. Figure 1.9 shows the difference between CCD and CMOS sensors in their readout architecture and active photosensitive areas. Reducing the limitations of CMOS sensors, such as the lower inactive areas between photosensitive regions, is an ongoing area of research. CCD and CMOS image sensors are each found in consumer-grade electronics such as cellphones and digital cameras, as well as more demanding applications which require a better-performing sensor. Signals can be improved using a gain mechanism, such as the electron multiplying (EM) register in an EMCCD camera, or a microchannel plate in an intensified CCD (ICCD) camera. Parameters that may determine which detection device is chosen for a particular application might include the required wavelength range, noise level, dynamic range, signal linearity, detection efficiency, and cost.

The recent development of inexpensive and sensitive photodetector arrays accelerated the development of compact fluorescence spectrometers and hyperspectral imaging systems. EEM spectrometer designs responded to these new tools and, in turn, facilitated field-based applications in forestry, agriculture, wastewater analysis, medicine, microbiology and fluorescence microscopy.

In the following paragraphs we discuss some applications of these one-, two-, and three-dimensional spectroscopy methods. We highlight the role of consumer devices and their integration into innovative EEM spectrometer designs.

Single Pixel Detection Systems

Single-pixel detectors, such as PMTs and APDs, can detect a signal from a very weakly-emitting sample, allowing for single-molecule detection and spectroscopy. In the context of EEM detection, we describe devices that record the fluorescence emission spectrum using a scanning monochromator or an interferometer, before briefly highlighting their application in time-resolved fluorescence measurements.

Scanning Monochromators

Many commercial fluorometers use a monochromator based on a diffraction grating on a rotation stage combined with an adjustable-width slit and detection by a PMT. This setup can record highly

resolved fluorescence emission spectra over a large spectral range (*e.g.,* 200–900 nm) with high sensitivity and low background [110-114]. The low background (noise floor) allows for long integration times, which is important when the fluorescence signal is weak. Unfortunately, due to their inherent optical path requirements these instruments tend to be large, and since they reject a large fraction of photons at the detection slit, they are often slow.

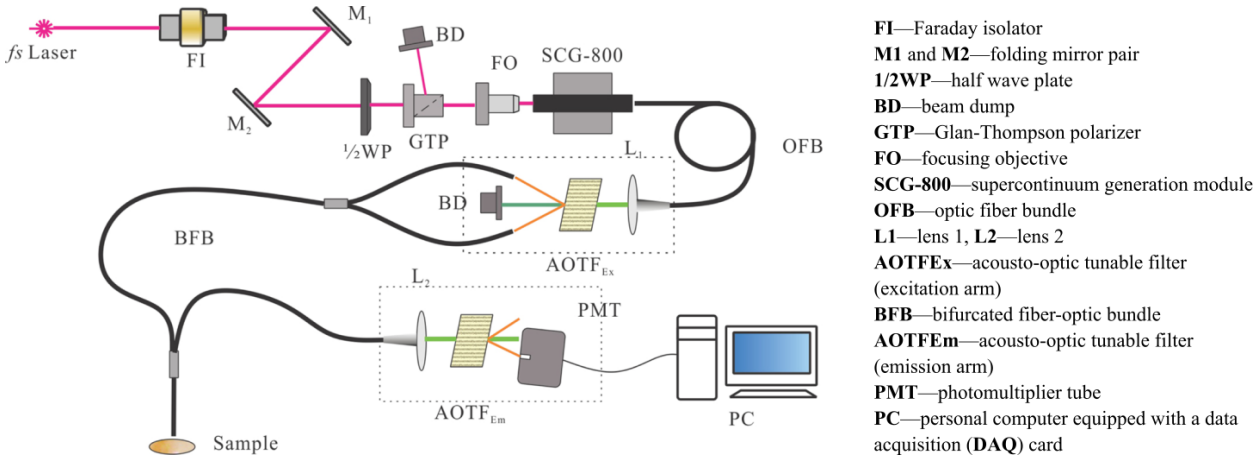

Figure 1.10. Schematic layout of EEM system having two acousto-optical tunable filters [115] (reprinted with permission).

Several other wavelength discrimination designs have been implemented in place of the "grating and slit" monochromators for detection. For example, Senga *et al.* [116] created an EEM spectrofluorometer which employed a circular variable interference filter to capture emission spectra at 31 wavelengths with 17 nm resolution between 300 nm and 550 nm. The excitation light was provided by a monochromator, which selected 26 excitation wavelengths within the same range, with a resolution of 2 nm [116]. A similar and simplified setup with a higher detection limit and faster acquisition time (51 excitation wavelengths, 93 emission wavelengths in 3.2 minutes) has been presented by Destrampe *et al.* [117].

Tunable bandpass filters based on Acousto-Optic Tunable Filters (AOTFs) have also been used for wavelength selection, both for emission and excitation light. Li *et al.* reported on an EEM spectrometer based on two sets of two cascading AOTFs. One set was used to select 41 excitation wavelengths from the spectrum of a xenon arc lamp with a resolution of approximately 5 nm in the range from 550 nm to 950 nm, and another set was used to select 44 emission wavelengths in 10 nm increments in the range of 570 nm to 1000 nm. With this setup, a full EEM spectrum could be acquired within 10 seconds [118]. Using a bright supercontinuum laser instead of the xenon arc lamp, Wang *et al.* developed an EEM spectrometer which used an AOTF for the selection of both

the excitation wavelengths and the emission wavelengths. Their EEM spectrometer provided a full EEM spectrum with 20 excitation and 40 emission wavelengths in less than 5 seconds [115] (Figure 1.10). The emission was scanned from 550 nm to 830 nm, and the excitation wavelengths ranged from 550 nm to 790 nm with full width half maxima between 3.2 nm and 14.5 nm.

Unfortunately, in any fluorometer based on bandpass filters or slits, a large fraction of photons will be rejected—approximately $1/N$, where N is the number of pass bands. A monochromator with a 2 nm resolution over a spectral region from 400–600 nm would have $N = 100$ pass bands and a collection efficiency of no more than 1%. By contrast, interferometric detection directs a much larger fraction of the light emission to the detector.

Interferometric Detection

Fourier-Transform (FT) spectrometers take advantage of wavelength multiplexing, allowing up to 50% of the light to reach the single broadband detector. Peng *et al.* [119] modulated the excitation light source with a Michelson-interferometer, and detected the emission with a second, synchronized Michelson-interferometer. Yuan *et al.* [120] demonstrated a setup to measure excitation, emission, and cross-correlated excitation-emission spectra of samples with a strong Förster resonance energy transfer, simultaneously. Different from the design in [119], their system is based on a double-pass interferometer—the same Michelson interferometer was used to transform both the excitation and emission spectra (Figure 1.11).

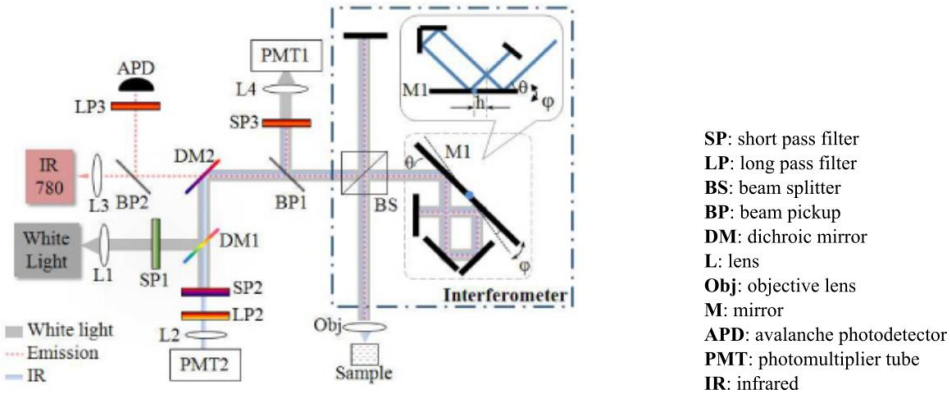

Figure 1.11. Double pass Michelson interferometer-based EEM spectrometer, by Yuan *et al.* [120] (reprinted with permission).

Note that the multiplex advantage afforded by FT spectroscopy does not necessarily translate to lower detection limits. As Griffith and de Haseth pointed out [121], the noise floor in single pixel detectors in both scanning monochromators and in ultraviolet-visible FT-spectrometers is ultimately determined by shot noise. When the detector is photon shot-noise limited, as is generally

the case for a PMT and often for other sensitive detectors such as APDs and other junction devices [122], the noise level is proportional to the square root of the incident power of the fluorescence emission. This means that shot noise is proportional to the square root of the number of resolution elements in the spectrum, $m^{½}$. This disadvantage therefore precisely offsets Fellgett's (multiplex) advantage. According to Griffith and de Haseth [121] the effect of shot noise is the main reason that Fourier spectrometry never became popular for measurements of ultraviolet and visible spectra. This statement was revisited recently in the context of FT-Raman spectroscopy, where Dzsaber *et al.* experimentally confirmed that the multiplex advantage depends on the type of spectrum that is measured with the FT-Raman/visible technique [124]. The multiplex enhancement is 1 (*i.e.,* no advantage) when the spectrum is broadband [121, 123] and has a maximum multiplex advantage of $m^{½}$ for a hypothetical Raman spectrum consisting of a single line whose line-width matches that of the instrument resolution [124].

Notwithstanding the ultimate Signal-to-Noise Ratio (SNR) that can be achieved by averaging, it is important to realize that much less *time* is required to approach the same SNR in FT-spectroscopy. For spectra measured in the same time and at the same resolution, optical throughput and efficiency, the SNR of a spectrum measured on an FT-IR spectrometer exceeds the SNR of an identical spectrum measured on a grating spectrometer by the square root of the number of resolution elements in the spectrum, $m^{½}$, or conversely, to measure spectra with the same SNR, a scanning instrument would require m-times more time [121]. The main advantage when using multiplexed methods such as Hadamard and FT-spectroscopy therefore lies in the data acquisition rate and not in the ultimate (shot-noise limited) detection limit.

Time-Resolved Detection with Single-Pixel Detectors

Fluorescence lifetime measurements can be done using detectors such as PMTS, APDs, or SiPMs due to their fast response times (nanoseconds or less). These measurements can further characterize fluorophores and applications are relevant in many fields, primarily in biosciences, where these very fast detectors can be combined with conventional imaging and microscopy to add an additional dimension to the data cube. We refer to recent review articles on fluorescence lifetime imaging microscopy (FLIM) for more information [35, 125-135].

Information obtained from fluorescence lifetimes has also been combined with EEM spectroscopy. For instance, Yuan *et al.* used a gated microchannel plate PMT combined with an AOTF to measure

the time integrated fluorescence signal and its temporal evolution for a mixture of two dyes, fluorescein and 9-cyanoanthracene [136]. Their spectrometer determined emission spectra within four seconds in the range of 370 nm to 570 nm with a spectral resolution varying from 1.6 nm to 4.2 nm. Manning *et al.* employed a 16-channel PMT connected to a matched polychromator to measure wavelength-specific lifetimes of a phase-sensitive membrane probe and to characterize protein-protein interactions via Förster resonance energy transfer [137]. Their lifetime measurements were conducted synchronously with fluorescence EEM measurements.

Photodetector Array Instruments

Compared to single pixel detection using a monochromator or interferometer, instruments using gratings and photodetector arrays for emission detection ("polychromators") can substantially increase the spectral acquisition rate while reducing the complexity and footprint of an EEM spectrometer [20, 138]. The photodetector array typically consists of a "single line" of photodetector elements—typically a semiconductor photodiode array—but may also involve other photodetector arrays such as a multichannel PMT assembly [139] or CMOS photodetectors elements such as those found in consumer cameras and smartphones (Figure 1.8).

Commercial Photodetector Array Instruments

Though most commercial fluorescence EEM instruments are based on a double monochromator design, at least one commercial fluorescence EEM instrument using a photodetector array has been available for several years (Horiba, Duetta [140]). Stamplecoskie and co-workers use this spectrometer for the identification and characterization of complex mixtures of fluorescent silver clusters [72]. Many more in-house instruments use tunable excitation sources and commercial miniaturized spectrometers. These instruments are inexpensive, simple and portable and may be taken into the field to determine, for example, the freshness of apples [141]. Miniaturized spectrometers have also been employed in vacuum ultraviolet spectrofluorometry [142], and to investigate microfluidic systems [143]. Many commercial compact fluorescence spectrometers are configured for collecting light using multimode optical fibers. It is then straightforward to also fiber-couple the excitation light source, interleave the excitation and emission fiber bundles and thereby obtain an all-fiber-coupled EEM spectrometer [144, 145]. These bifurcated fiber bundles can then be designed to be submersible into liquid samples such as lubricants [67, 146], or configured for

in-vivo analysis of tumors during surgery [23]. Puiu *et al.* reported on a fully submersible portable fluorimeter for water analyses in the ocean at depths of up to 20 meters [147].

Portable, Simplified Instruments

In portable fluorometers, it is often advantageous to pre-select the excitation and emission wavelength bands based on the maxima in the EEM spectrum of the target compound. For example, chlorophyll *a* absorbs in the 360–440 nm region and fluoresces between 660–680 nm while phycocyanin absorbs light at 570–600 nm and fluoresces at 630–650 nm. A simple device using just two light-emitting diodes (LEDs) to generate excitation in these two wavelength bands and a photodetector behind two bandpass filters then suffices to discriminate between these two compounds in an environmental sample [148]. A third light source provides additional information on the spectroscopic background. Many of these simple, compact, and inexpensive devices have been built around unique applications and often use LEDs as light sources and optical bandpass filters combined with photodiode detectors to select the emission wavelength bands [27, 31, 148-151].

Imaging Spectrometers for EEM Acquisition

A fundamentally different design produces the EEM spectrum directly onto an imaging detector—a 2D array of photodetector CCD or CMOS elements.

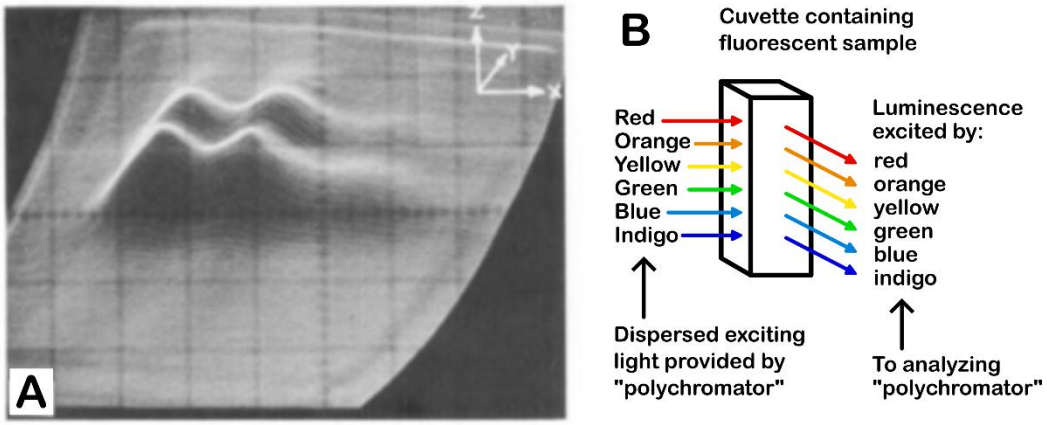

Figure 1.12. First published three-dimensional view of an EEM. (A) The fluorescence intensity of perylene as a function of the excitation and emission wavelengths [152] is shown taken using the (B) "Video Fluorimeter" developed by Warner *et al.* [152], diagram reproduced by Emma Abbey.

This was first demonstrated by Warner *et al.* with the "Video Fluorimeter" capable of producing a single-shot EEM in 16.7 ms with 241 excitation and emission wavelengths [152]. Muroski *et al.* demonstrated and fully characterized a spectrometer using similar principles and used multivariate analysis to examine ocean water samples [41, 109]. With these methods, excitation light is dispersed

onto a homogenous sample solution, and the fluorescence emission is collected after dispersion in the orthogonal direction.

In the setup by Johnson, Callis, and Christian [8], a mercury lamp was vertically dispersed onto a cuvette containing the sample and an imaging spectrometer was then used to disperse the fluorescence horizontally, producing an EEM spectrum on a two-dimensional video detector. They note that many averages—up to 4096—had to be acquired to improve the signal-to-noise ratio. In the system developed by Muroski *et al.*, the vertical dispersion of the excitation spectrum on the sample was about 25 nm/mm for a spectral range of 115 nm in the excitation dimension. The emission was sampled over 105 nm using a CCD imaging chip with 750 × 242 pixels.

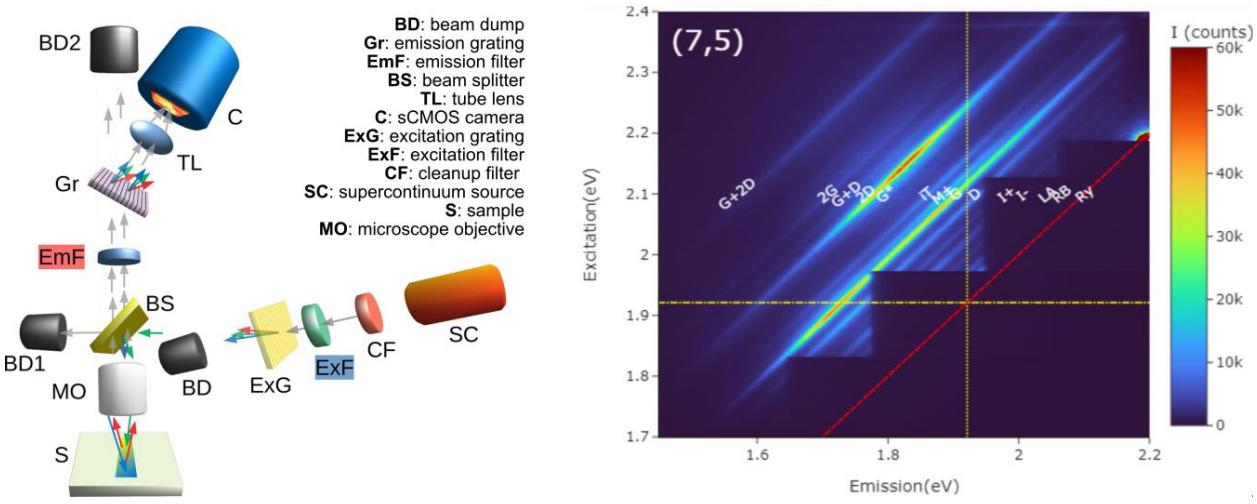

Figure 1.13. Full spectrum Raman excitation mapping using epi-illumination. (**left**) Instrument schematic, (**right**) Raman excitation maps for carbon nanotubes with indices (7,5). Bands are labeled according to Finnie *et al.* The excitonic resonance (E_{22}) is marked on the excitation axis by a horizontal yellow line, and the emission axis (x axis) by a vertical yellow line. The red diagonal line marks the position of Rayleigh scattering, *i.e.,* zero Raman shift. Adapted from Finnie *et al.* [73].

Fluorescence EEM acquisition using an imaging spectrometer presents advantages both because no scanning is required and it has near-optimal photon efficiency. When the detector is sensitive enough, acquisition is single-shot and acquisition speed then depends only on the integration time. Of course, this system will work best on samples that have a high degree of spatial homogeneity. A similar technique has also been used by Finnie *et al.* to determine Raman excitation spectra of single-walled carbon nanotubes [73, 153] (Figure 1.13).

1.1.3 Fluorescence Excitation

Several recent developments facilitated new possibilities for excitation sources. Among these developments are blue, violet, and ultra-violet LEDs [154-156], organic LEDs (OLEDs) and liquid

crystal device (LCD) screens [157], commercially available supercontinuum fiber lasers [158, 159], laser-pumped plasma light sources [160, 161], and AOTFs. Fiber-coupled lasers and LEDs provide experimental flexibility due to their compact form, while AOTFs accelerate the scanning speed of tunable devices for wavelength selection, as the tuning forgoes mechanically moving parts. Xenon arc lamps remain the standard excitation source for benchtop spectrofluorometers. These point light sources provide a high and approximately constant spectral radiance over the spectral range between approximately 300 nm and 750 nm. Xenon arc lamps can easily be combined with a monochromator to provide tunability over the full range of the spectrum of the light source. Here, the spectral resolution is limited by the resolution of the dispersive element within the monochromator and the slit width.

Filter wheels or filter cubes are commonly used for fluorescence imaging and microscopy [162-166]. Here, bandpass filters or dichroic filters select excitation bands from the broadband spectrum of a light source such as a xenon arc lamp [166]. Recently, Johnson *et al.* reported on a prototype for an excitation light source based on an array of thin-film tunable filters mounted on a rotational stage [167]. In this system, narrowband light was coupled to a fluorescence microscope via a liquid core waveguide and provided a wavelength range of 380 nm to 550 nm with a step size of 5 nm. While the authors demonstrated a very rapidly scanning light source, they did not use it for fluorescence EEM spectroscopy.

Gouzman *et al.* presented an EEM spectrometer based on linear interference filters, that were adjusted by a motorized stage [168]. With this instrument, a wavelength range of 300 nm to 720 nm was covered at a full width half maximum for the excitation between 12 nm (at 410 nm) and 16 nm (at 720 nm).

Other light sources are based on either fixed wavelength or tunable laser light sources. Zangaro *et al.*, reported on a dye laser system based on a pulsed N_2-laser, which was pumping one of nine different dye cells mounted on a wheel, thereby delivering an excitation between the pump wavelength of 337 nm and the longest dye laser wavelength of 500 nm [76], for a total of 10 excitation wavelengths that were accessible within 600 ms. Kieleck *et al.* presented a setup based on an Nd:YAG laser-driven optical parametric oscillator, which was used to illuminate macroalgae and classify them according to their fluorescence [169]. Their source produced five-nanosecond pulses in 10 nm intervals from 400 nm to 640 nm. The resulting fluorescence was filtered at

680 nm. Similarly Taylor *et al.* demonstrated the generation of 14 distinct wavelength between 247 nm and 355 nm from a Raman shifter that was driven with the third or fourth harmonic of an Nd:YAG laser [170]. The excitation wavelength was selected using a Pellin-Broca prism on a rotation mount and a fixed iris. In these experiments, laser light is generated at several fixed wavelengths. By contrast, tunable lasers are more often employed in laser-induced fluorescence of gases and molecular beams than in EEM spectroscopy due to their relatively small tuning range [171, 172].

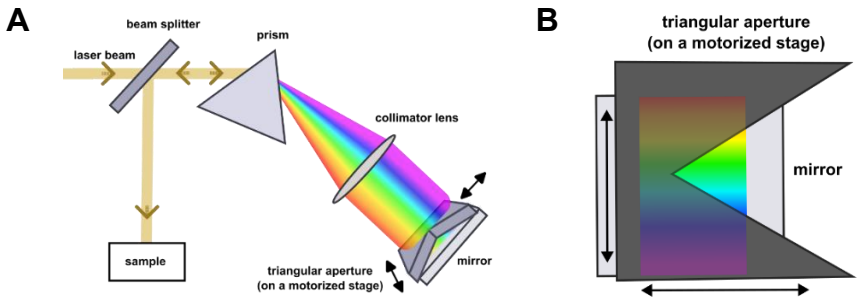

Figure 1.14. Schematic of a setup for a selection of excitation bands with adjustable centre wavelength and full width half maximum. Adapted from [137, 173, 174].

Larger excitation wavelength ranges have been reported using pico- or femtosecond pulsed supercontinuum lasers [51, 73, 115, 137, 173, 175-180]. The short pulses also allow for a measurement of the time between the excitation pulse and the fluorescence emission, thereby adding an additional dimension to the excitation emission matrix [115, 137, 174-177]. Furthermore, the inherent fiber coupling of supercontinuum lasers allows for a larger flexibility and compactness than that of benchtop systems. Dunsby *et al.* reported on a home-built spectrograph to select a band for the excitation with a center wavelength and an adjustable peak width. The setup is presented schematically in Figure 1.14 [174]. Light from a supercontinuum laser was dispersed by a prism onto a mirror, which had a triangular aperture on a motorized x-y stage in front of it. The center wavelength could be chosen by translating along the x-direction, and translation along the y-direction controlled the full-width half-maximum of the peak (Figure 1.14). This selection method has also been used by others to select wavelength bands for fluorescence lifetime imaging [137, 173]. Other selection methods for the excitation by using supercontinuum lasers include gratings [73, 178] and filters [115, 175, 176, 180].

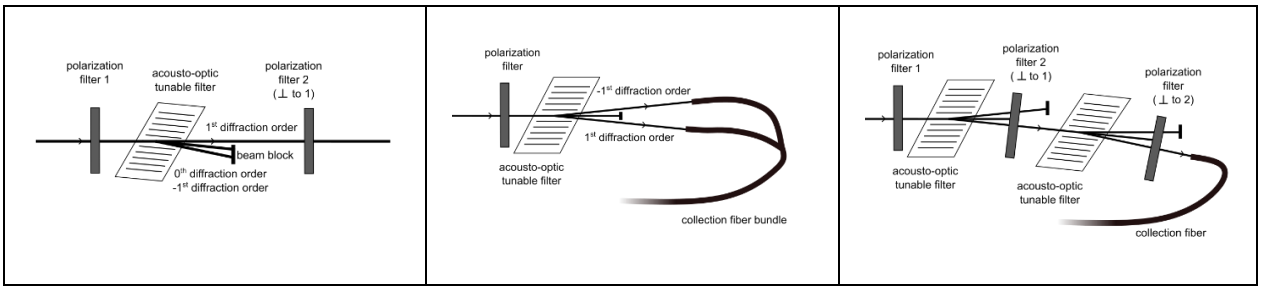

Figure 1.15. Configurations for a wavelength selection by acousto-optic tunable filters. (left) Free space coupling with two polarizers as reported, for instance, in reference [181], (middle) fiber coupled approach, where both diffraction orders are used as reported in reference [115], (right) cascade of two AOTFs combined with polarizers, coupled to a fiber as reported in reference [118, 182].

For EEM spectroscopy, the acquisition time for an EEM spectrum strongly depends on the scanning mode of the excitation and the emission bands. When investigating kinetic processes, the acquisition time of an EEM spectrum is a limiting factor. Mechanically moving parts, such as gratings in monochromators and dye lasers, motorized wheels and motorized stages restrict the scanning speed. Consequently, alternate wavelength selection optics have been explored, such as AOTFs as reported by Li *et al.* [118] and others [115, 136, 176, 181, 183-185]. Here, the scanning speed is fundamentally only limited by the speed of the acoustic waves in the AOTF [181].

In the configuration reported by Kurtz *et al.* (Figure 1.15a) two polarizers, one in front of the AOTF to optimize the polarization for an efficient diffraction, and one behind the AOTF to select the first diffraction order, are used to obtain an approximate 3 nm wavelength band of the excitation beam, with resolution and width dependent on the AOTF material and the excitation range [181]. A fiber-coupled variant has been presented by Wang *et al.,* where only one polarizer is employed, and both diffraction orders (1 and -1) are coupled to an optical fiber which is guided towards the sample [115] (Figure 1.15b). Li *et al.* reported on a setup consisting of tandem AOTFs separated by a polarizer [118] (Figure 1.15c). With this cascade of AOTFs, side ripple effects could be reduced by approximately two orders of magnitude compared to single AOTF.

Methods to acquire a multiplexed EEM spectrum, particularly to multiplex the excitation light, are discussed further in Section 2.1.

1.2 Four-Dimensional Fluorescence Imaging

In applications such as fluorescence microscopy or environmental imaging it is important to resolve the fluorescence emission additionally *spatially*. To image a sample emitting fluorescence, any monochrome camera chip with sufficient sensitivity for the respective colour range can be used. To determine the spectral properties of the fluorophores, a spectral discrimination method

must be added to the system. When the fluorescence emission is spatially and spectrally resolved, a four-dimensional dataset (x, y, λ_{em}, I) containing the spectral intensities over the field of view is created. When numerous excitation wavelengths are used, the dataset then is five-dimensional with (x, y, λ_{em}, λ_{ex}, I). An example is shown in Figure 1.16.

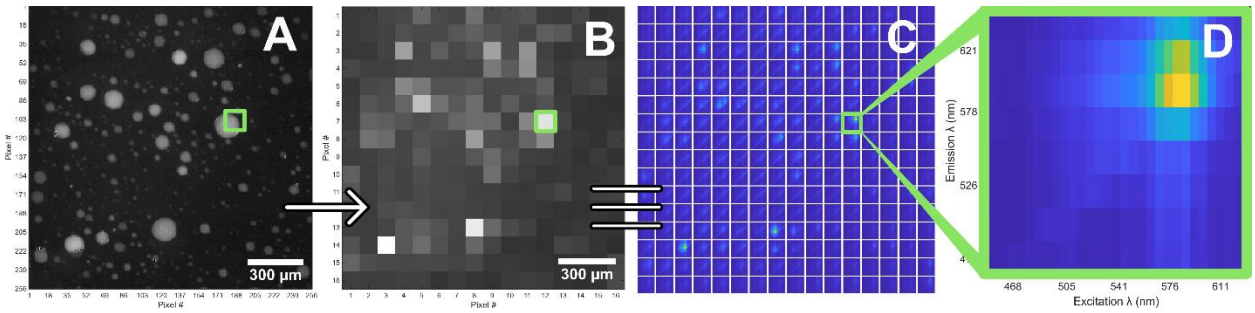

Figure 1.16. Four-dimensional fluorescence EEM image. The image was taken using an 8-channel multispectral camera through an Olympus CK2 microscope with a 10x objective lens, shown as the mean of all excitation and emission channels for the (A) full 256 × 256-pixel image, (B) pixelated image created by summing groups of n pixels together, to create a 16 × 16-pixel image. (C) EEM for each summed pixel in the pixelated image, (D) EEM from a single pixel (green box, same area of each panel), enlarged.

The simplest approach to spectrally resolve the intensity associated with each pixel in an image uses fluorescence images recorded sequentially through different colour filters. We can then obtain an F-EEM for each pixel when the excitation bands are additionally varied, using either different light sources or a white light source and a second set of colour filters. Fluorescence microscopy uses this type of imaging already, for example in multiplexed immunofluorescence [186, 187]. Here, fluorescence images are taken using combinations of excitation and emission filters to match the excitation and emission maxima of fluorophores in a sample. Applications of these instruments in food inspection were recently reviewed by Huang *et al.* [188]. Of course, a conventional RGB camera would provide an emission "spectrum" for each pixel, even though the resolution of that spectral dimension is very low, with just three colour bands. In Section 1.2.1, EEM instruments based on consumer RGB image sensors are discussed, with a particular focus on smartphone cameras.

For very high-resolution emission spectra, an F-EEM image can be built by collecting the emissions sequentially at each point in a sample grid using an array spectrometer, akin to confocal (Raman or fluorescence) spectroscopy. However, the instrumentation requirements are quite complex and expensive (stage control and alignments), spectra are acquired at different points in time throughout the image, and acquiring an image with a reasonable spatial resolution is time consuming. Using an image sensor is more straightforward in some ways, however limitations include reduced sensitivity to photons and increased complexity of spectral discrimination

methods. We provide examples in Section 1.2.2 of instruments that have a considerably higher spectral resolution and are based on hyperspectral imaging systems.

1.2.1 Consumer Colour Cameras

Consumer RGB Camera Devices

The availability of inexpensive and sensitive CMOS detectors as cameras in smartphones and other consumer electronic devices opened new design options for portable fluorometers [25, 30, 189] including imaging fluorometers. The many different uses of consumer imaging devices were recently as reviewed for their use in analytical instruments [190], for microfluidics [191] and for educational use [192-194]. Consumer cameras are limited to just three—red, green, and blue (RGB)—wavelength bands but can also be configured to record a fluorescence emission spectrum when coupled to a dispersive device such as a grating or prism, or to (tunable) filters.

To give a few examples related to fluorescence emission sensing, Hossain *et al.* reported on smartphone-based instrument to determine the pH-value of water samples [26]. In their work, the sample was excited by a smartphone flashlight and the emission was detected by the integrated camera. Here, the fluorescence emission captured by all pixels was integrated over the entire image and binned into the three emission channels corresponding to the RGB colour filters that are included in the camera sensor. Similar uses of the three-colour (RGB) filter of smartphone cameras include the detection of Mn^{2+} in cosmetics [195] and simultaneous absorption and ratiometric fluorescence measurements of rhodamine B dye [196].

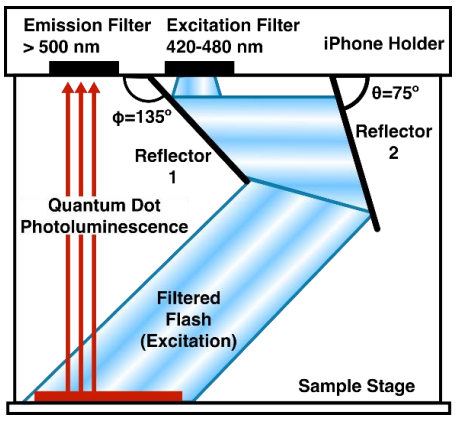

Figure 1.17. Schematic for a smartphone accessory for excitation and imaging of photoluminescence demonstrating the excitation light path. Adapted from [25].

Following calibration with a fluorescence spectrometer, the green and red wavelength bands in an RGB camera can be used to record two-channel fluorescence emission images, as reported by

Zheng *et al.* when exciting a sample using an ultraviolet (UV) laser light sheet [197]. Koenig *et al.* reported on a setup used for teaching purposes, where a set of cuvettes was excited by the light of a tablet screen, while the emission was captured by a digital RGB camera [198]. Malik *et al.* used the light from an LCD screen to sequentially illuminate a sample with 50 colors in the visible spectrum, and collected the RGB values of the fluorescence emission via the web camera of a portable computer [157]. Algar and coworkers further integrated a compact fluorimeter based on the flashlight of a smartphone combined with excitation filters. The emission from quantum dots and fluorescent dyes was imaged using the camera of the same smartphone (Figure 1.17) [25].

While one may assume that a fluorescence emission spectrum can be constructed from the RGB values obtained using a colour camera, the problem is inherently ill-defined for all but the simplest cases. For example, it is possible to estimate the wavelength of a single wavelength emitter, such as a laser, from its RGB values, if the spectra of the camera's bandpass filters are well-known. It is, however, ***not*** possible to construct an emission spectrum from just three values, since that conversion is inherently under-determined. Spectral upscaling using machine learning algorithms—especially neural networks—is an active area of research [199-202]. However, any spectral upscaling algorithm requires additional information about the emission in addition to the RGB values, such as the number of the emitters and each of their spectral bandwidths.

In addition, when extracting quantitative colour information from a digital RGB image, care must be taken to use the raw, unprocessed images which have not yet been demosaiced by the device. Since most consumer cameras use a broadband image sensor with an overlain by a colour filter array, pixels contain only the intensity information about one of the three colour bands. Demosaicing is a process that interpolates colour information between neighbouring pixels so that each pixel can be assigned three colour values without losing spatial resolution.

Similarly, an RGB *light source*, such as a smartphone screen cannot by itself generate an excitation spectrum with more than three wavelength bands, even though it may appear that any colour in the spectrum can be represented by a combination of the three RGB channels. Without additional spectroscopic selection, *e.g.*, using filters, or additional information (from an external spectrometer), EEM spectroscopy using smartphones and other RGB devices is therefore inherently limited to 3 × 3 channels. That said, a high spectral resolution is not always required in

both dimensions, and for many purposes, RGB-type devices are a readily accessible and very useful tool.

1.2.2 Multispectral and Hyperspectral Cameras

The development of multispectral (typically 4–10 colour bands) and hyperspectral (>10 colour bands) imaging systems remains a very active field of optical engineering and is propelled by a myriad of applications from agriculture to health technology and industrial quality control. A detailed discussion of multispectral and hyperspectral camera designs is beyond the scope of this contribution, and the reader is directed to a recent review [203]. It is intriguing, that after decades of development there is still no single optical design that is clearly superior to all others and that the sheer number of design options available today is astonishing. Here, we will provide a brief overview of some of the imaging detection systems used for fluorescence EEM detection.

To improve the spectral resolution of a colour camera, it would be, of course, straightforward in principle (not always in practice) to increase the number of emission bands that can be sampled using a broadband imaging sensor by overlaying a colour filter array that has more than three different pass bands. Indeed, commercial multispectral "snapshot" cameras exist that have 8 or 16 pass bands, such as those by Spectral Devices [204]. Unfortunately, there exists an inherent trade-off resulting in lower spatial resolution, as the sensor must be divided by a greater number of bands.

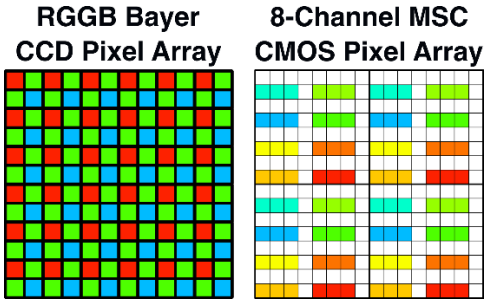

Figure 1.18. Colour filter arrays for a Bayer-style colour camera and multispectral camera.

A simple multispectral imaging system can also be designed in-house using external filters in front of monochromatic CMOS or CCD cameras, using filter wheels [95, 165, 205-207], liquid-crystal tunable filters [208, 209], AOTFs [210-214], or any other spectral selection filter. For example, Suo *et al.* demonstrated a system using two liquid crystal tunable filters, one in front of the excitation source and one in front of a monochromatic digital camera to create an image in which each pixels contains an EEM with six excitation and 10 emission wavelength channels [215].

Hyperspectral cameras can have a much higher spectral resolution than snapshot cameras, often resolving more than 20 wavelength bands. Many are based on push broom spectral acquisition, line scan imaging, interferometry, light field imaging [203], or liquid-crystal tunable filters [216]. Some of these cameras resolve 140 or more wavelength bands [216].

In this work, different multiplexed light sources are used to generate the excitation light, and a multispectral or hyperspectral camera records the fluorescence. The resulting data "cube" has five dimensions—for each pixel [*x, y*] one obtains the fluorescence intensity, *I*, as a function of both excitation and emission wavelength [λ_{ex}, λ_{em}]. The F-EEM "image" contains therefore an EEM spectrum for each pixel. To the best of our knowledge only few examples of such multiplexed systems have been reported [217] [218-220] [221-223].

For the system developed in our group using a 31-channel programmable light source for excitation and an 8-channel snapshot multispectral camera with a 256 × 256-pixel resolution for detection, over 65,000 EEM spectra with 8 × 31 wavelength pairs are generated every few seconds—refer to Chapter 4, Chapter 6, and Chapter 7.

We note that hyperspectral imaging cameras are usually not designed for low light applications and that the method requires bright light sources or comparably long integration times (up to a second). Using a multiplexed light source alleviates some of the problems, at the cost of increased complexity, of course.

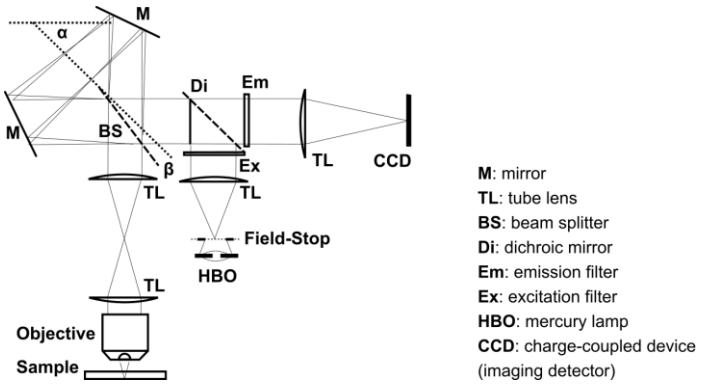

Figure 1.19. Diagram of the Fourier transform EEM imaging spectrometer. The excitation wavelength of a Hg-arc lamp (HBO) is multiplexed using a Sagnac interferometer (adapted from [217]).

Using a very different approach, Heintzmann *et al.* reported on an imaging EEM-spectrometer built on a double-pass Sagnac-type interferometer, which can be used for fluorescence imaging with a high spectral resolution [217]. The system was tested on two types of polystyrene beads. A schematic drawing of the experimental setup is depicted in Figure 1.19. The interferometer

consisted of two mirrors facing each other with a tilt angle, α, and of a beam splitter with a variable tilt, positioned close to the symmetry axis between the mirrors. The excitation light passes the dichroic mirror and the Sagnac interferometer with two alternate paths before interfering on the sample. Similarly, the fluorescence emission passes in two different paths through the same Sagnac interferometer before forming an image on the CCD detector. These two fluorescence paths interfere at the CCD, such that the detected intensity in every pixel is dependent on the wavelength and the optical path difference between A and B, which can be adjusted by tilting the Sagnac interferometer (mirrors and beamsplitter) by angle α. An interferogram is acquired by taking CCD images through a series of angular positions of the interferometer with equal increments in α. This setup could not independently record the emission spectrum at each excitation wavelength, since the optical path difference of respective excitation and emission are forced to be identical. The resultant spectra therefore consist of two (linear) excitation and emission spectra, which may be multiplied to obtain an estimate of the two-dimensional EEM spectrum.

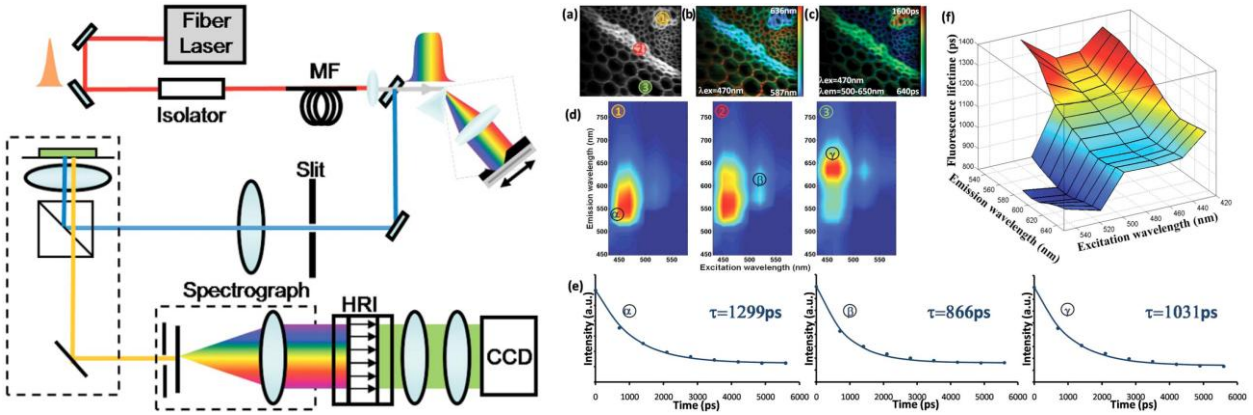

Figure 1.20. Schematic of an F-EEM and FLIM (EEL) setup. (left) The illumination source is a supercontinuum laser (5 ps pulse width, 350-650 nm, 8 W power). The fluorescence collected from the epi-microscope is dispersed and gated using a gated optical intensifier, GOI, (200 ps – 2 ns gate) and imaged by a cooled electron-multiplying CCD. (right) Excitation-emission-lifetime (EEL) resolved fluorescence imaging of stained Convallaria. (a) Integrated fluorescence intensity image. (b) Mean emission wavelength image. (c) FLIM image for excitation at 470 nm. (d) EEM corresponding to regions indicated in (a). (e) Selected fluorescence decay profiles corresponding to regions α, β, and γ, respectively, indicated in (d). (f) Mean fluorescence lifetime as a function of emission and excitation wavelength [173].

An even more sophisticated system based on a tunable supercontinuum light source and gated "push broom" detection system was demonstrated in 2007 by Manning *et al.* [218]. The same group also developed an integrated hyperspectral FLIM setup [218] (Figure 1.20), where the output from a broad band pulsed supercontinuum source was directed to a microscope slide. The fluorescence spectrum of a line was then obtained through a Gated Optical Intensifier (GOI) by dispersion into the dimension orthogonal to the line. The time gate was adjusted with respect to the laser pulse to

obtain the fluorescence lifetime, τ. An alternative source provided a tunable pulsed output (not shown) and, using the same scheme a six-dimensional data cube (x, y, λ_{ex}, λ_{em}, τ, I) was obtained. Figure 1.20 (right) shows images of a triple-stained *Convallaria* rhizome test sample.

Even the best colour filter array (CFA)-based cameras will not be able to resolve more than say 16 colour channels—inherently limiting the possible spectral resolution. In Section 8.2 we will discuss an algorithmic approach that provides a higher spectral resolution using these cameras. Briefly, we will show that one can train a neural network on a combined input of the spatially resolved multispectral images and highly spectrally resolved spectrometer data to "upscale" the spectral resolution attainable with a colour filter array-based camera.

1.3 Fluorescence Excitation Emission Matrix Spectral Imaging Microscopy

This dissertation focuses primarily on the building of instruments for fluorescence EEM microscopy using multi- and hyperspectral cameras and programmable multiplexed light sources. Coarse F-EEM imaging using RGB cameras is common in life sciences, as discussed in the previous section. For example, imaging of multiplexed immunofluorescence samples frequently involves several different fluorescent tags, the respective number of excitation wavelengths and an RGB camera for detection. This allows for the quantification of multiple fluorophores in a single image. This work attempts to produce a more information-rich method for this type of imaging, with a shorter acquisition time, to allow for a greater number of fluorophores to be distinguished within an F-EEM microscopy image.

This section describes techniques used in fluorescence microscopy with an emphasis on the illumination methods used in this work. The last part of this section discusses emulsions and provides an overview of the parameters that were adjusted in creating emulsions to act as a stand-in for tagged fluorescent samples.

1.3.1 Microscopy Techniques

Brightfield Microscopy

Light microscopes are used to examine structures resolvable by approximately the wavelength of light being used (400–650 nm). Sample features with variations that are much smaller than about one-half of the wavelength of light cannot be resolved as described by the Abbe diffraction limit

[224]. Total magnifications for light microscopes are typically between 40x to 1000x using objective lenses from 4x to 100x and an eyepiece magnification of 10x.

Historically, microscopes use a light source under a sample placed on a transparent slide, and the transmitted light is collected using an objective lens above the sample, chosen from a rotating lens turret often containing 4x, 10x, 20x, and 40x magnifications. Inverted microscopes flip the position of the light source and objective lenses and can accommodate taller samples such as an agar plate in a petri dish [224]. As light passes through a scattering or absorbing sample, light is attenuated and the sample features are seen as dark shadows on a bright background—hence the name "brightfield". This is somewhat analogous to an absorption spectrum, where the absorbed light is removed from a bright broadband background illumination. It can be difficult to identify features which do not absorb strongly, in both the microscopy and absorption spectroscopy techniques. Importantly, brightfield microscopy is not well suited for fluorescence microscopy since the fluorescence signal competes with the brightfield background. This is not a great problem if long-pass filters or notch filters can be used to remove the excitation light. For fluorescence EEM microscopy one would require as many of these filters as there are excitation wavelengths, thereby greatly increasing the complexity of the setup. Multiplexed EEM imaging would be all but impossible with such a configuration.

Consequently, "background-free" methods have been developed which provide a higher contrast for samples that fluoresce, weakly absorb, or scatter light.

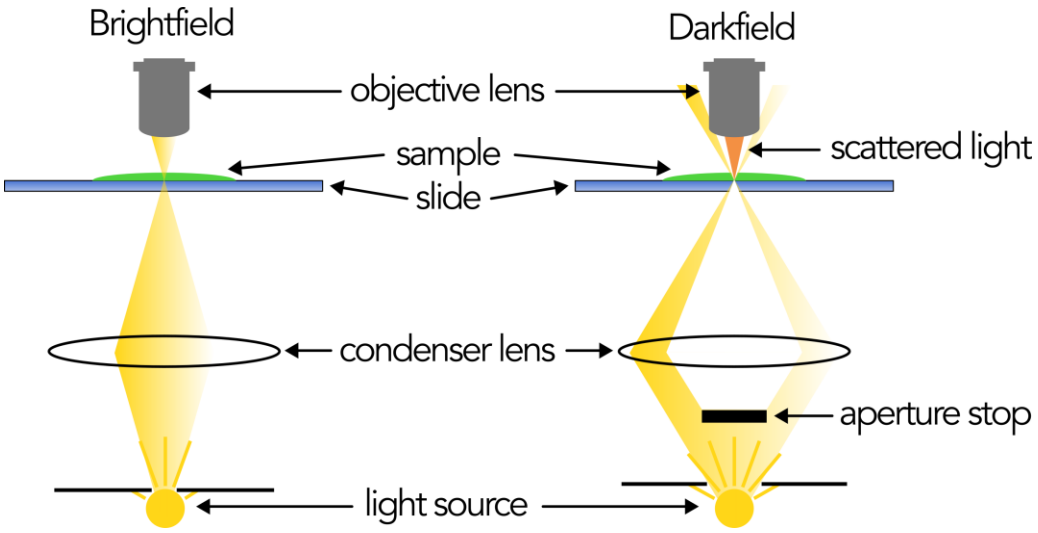

Figure 1.21. Brightfield and darkfield microscopy setups. Additional optics for collimating and focusing the light from the light source are not shown, and only the objective lens without any of the following lenses used in a microscope are shown.

Darkfield Microscopy

Darkfield microscopy (DFM) is an alternative for samples which are difficult to characterize using brightfield microscopy (BFM) and for samples which fluoresce, as DFM is only sensitive to sample features that scatter light or that fluoresce. In this method, the sample is illuminated by oblique rays of light which are not collected by the objective lens. Because a scattered photon will have a random orientation and an emitted photon (for example by fluorescence photoluminescence) has a nearly random orientation, the light which is scattered or emitted by the sample enters the objective lens with a near-zero background. Highly scattering (or refractive) structures and fluorescing features can be visualized well with DFM. Importantly, the technique cannot observe simple absorption, since the light rays are not redirected into the objective lens.

Typically, DFM can be performed on a microscope already equipped for BFM when an aperture can be placed into the light path and blocks the center cone of light, allowing only the outside rays to illuminate the sample.

There are other methods for improving contrast of specimen to background. We mention them briefly below but consider them largely to be beyond the scope of this work.

Phase Contrast Microscopy (Zernike) uses the differing path lengths created by the varying refractive indices throughout the sample and its thickness to find intensity differences when passed through a ¼ waveplate, introducing a $\pi/2$ phase shift. The background light will be unchanged, however the phase shifted light interferes with light diffracted by the specimen, creating an image. This is often used for transparent and unstained cells [224].

Differential Interference Contrast (DIC) uses the recombination and interference of two beams of polarized light which are split and travel through adjacent points in a sample. The resulting image represents gradients in optical path length and shows high edge definition and minimal haloing. Unlike phase contrast microscopy, DIC microscopy emphasizes boundaries over absolute phase.

Polarization Microscopy uses two perpendicular linear polarizers to visualize only the linearly polarized light which has been optically rotated altered by the sample. Structures which alter light are birefringent materials such as some crystals or collagen, and this is a useful technique to selectively image those structures.

Fluorescence Microscopy will be discussed in much more depth in the next section. Fluorescence is observed typically using dichroic filters to select excitation and emission wavelengths to view fluorophores of interest. Fluorescence microscopy allows for a nearly background-free image, as only fluorophores should emit light, and excitation light is removed before reaching the detector, either by filters or physical methods [225].

1.3.2 Fluorescence Microscopy Techniques

Fluorescence microscopy uses the autofluorescence or fluorescent tags or stains to improve the visibility of target structures in a sample. This could include parts of a cell such as nuclei or cell walls, specific proteins, or microorganisms, all of which can be difficult to visualize with brightfield microscopy.

Epifluorescence Microscopy

The simplest instrument for fluorescence microscopy is an epifluorescence microscope, in which both the excitation beam and emitted light from the sample use the same objective lens and the beams are separated by a dichroic mirror (Figure 1.22). Excitation bands are selected using filters to choose regions from broadband sources or using multiple discrete sources such as light-emitting diodes (LEDs) or lasers [166]. The dichroic mirror directs the excitation light to the objective lens to be focused onto the sample and acts as a filter to select the required excitation band from a broadband source. The light emitted from the sample is directed back through the objective lens to the dichroic mirror which selects only light emitted from sample by wavelength to reach the detector [225]. This is a widefield method in which the entire area of the sample is illuminated at once and does not require scanning as confocal microscopy does. When using excitation filters, the bandwidth is usually limited to approximately 10 nm (full width at half-maximum, FWHM) for a high-quality filter.

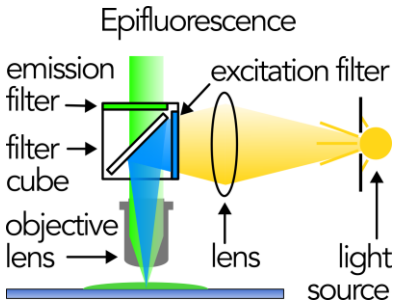

Figure 1.22. Epifluorescence microscope optics and light paths. Excitation light is shown in blue, and emission is shown in green.

Confocal Microscopy

For an application which requires high-resolution spatial data in any of the *xy*- or *z*-planes, confocal microscopy (CM) or confocal laser scanning microscopy (CLSM) can be used. In this method [225], light is focused precisely on a sample plane and out-of-focus light is effectively blocked. Pinholes are used for both the excitation source and the emitted light. Due to the precise focus, this is a scanning method, so the sequential images are taken point-by-point to build a two-dimensional or three-dimensional image. The resulting images are not blurred by out-of-focus fluorophores, scattering, or background (Figure 1.22).

Confocal microscopy works well for single-wavelength excitation and emission. When multiple excitation bands are required, different filter cubes or sources are used to create sequential images. To create an F-EEM image, this would require many sets of filters or many narrow band light sources with matched emission filters. This is costly both for equipment but also for the time required to scan the many combinations at each point in the sample space.

In fluorescence microscopy, it is important to block any bright excitation light from the detector. Beside filters, one can physically prevent the excitation light from reaching the detector, such as in darkfield microscopy, described above. An alternative technique is based on total internal reflection fluorescence microscopy (TIRFM), described in the following section.

1.3.3 Frustrated Total Internal Reflection Fluorescence Microscopy

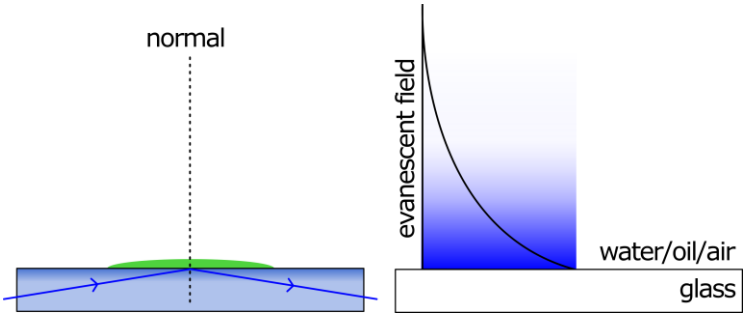

Figure 1.23. Evanescent field generation at an interface. (**Left**) angles important in evanescent field generation, (**right**) generated evanescent field with exponential decay, shown as an exponential curve and a decreasing gradient.

Total internal reflection fluorescence microscopy (TIRFM) uses the evanescent field created upon total internal reflection (TIR) of light at an interface. This near-field phenomenon creates an evanescent field with a frequency which matches that of the incident light and with an exponential decay in intensity with distance from the interface (Figure 1.23).

The depth an evanescent field will penetrate into a medium is dependent on the refractive indices n of the two media, the incidence angle θ_i from the surface normal, and the wavelength [226]. Light undergoes TIR and creates an evanescent field when θ_i is above the critical angle θ_c:

$$\theta_c = \sin^{-1}(n_1 / n_2) \qquad [1.1]$$

The field penetration d into a medium with refractive index n_2:

$$d = \frac{\lambda_0}{4\pi}\sqrt{n_2 \sin^2\theta - n_1 \sin^2\theta} \qquad [1.2]$$

With an intensity $I(z) = I_0 e^{-z/d}$ where I_0 is the initial intensity and z is the depth. I direct a reader to the interactive tutorial created by Evident Scientific [227] to visualize factors affecting evanescent field penetration depths.

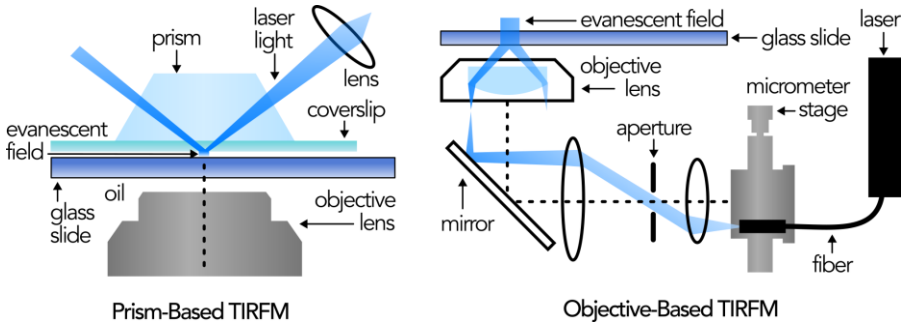

Figure 1.24. Total internal reflection fluorescence microscopy (TIRFM) general concepts. (**Left**) TIRFM using a prism, (**right**) TIRFM using an objective lens. The black dotted line shows the image path.

Total internal reflectance fluorescence (TIRF) microscopy (TIRFM) typically uses lasers incident at an angle above θ_c to excite fluorescence in a sample within a few hundred nanometers of the glass surface, with very low background and little out-of-focus fluorophores [226]. The first implementation of TIRFM used a prism to direct the light to the sample surface [228], and later versions used an objective lens [229] (Figure 1.24).

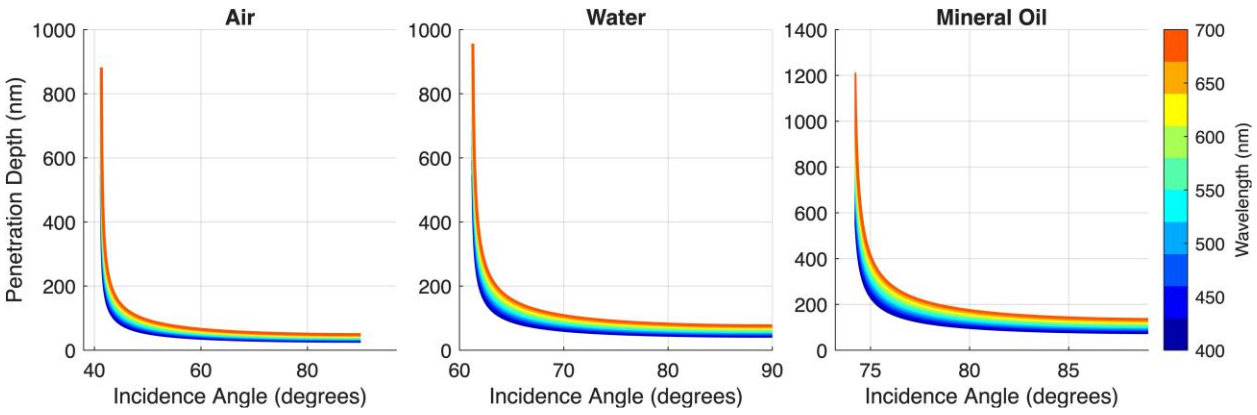

Figure 1.25. Penetration depth of an evanescent field from glass to air, water, and mineral oil, as a function of incidence angle and wavelength. For this demonstration, refractive indices 1.00, 1.33, 1.47, and 1.52 were used for air, water, mineral oil, and glass, respectively.

Figure 1.25 demonstrates that the sample medium must be selected carefully when using TIRFM, as the higher the refractive index of the sample (closer to that of glass), the narrower the angle range at which TIR can occur. For a sample composed of water (n_1=1.33) or mineral oil (n_1=1.47) and a glass slide (n_2=1.52), these angles are 61° and 75°, respectively. Any light below these angles will be refracted into the sample, reaching fluorophores spatially above those which would be excited by an evanescent field.

Frustrated Total Internal Reflection (FrTIR—though it is often referred to as FTIR in literature) [230, 231] is closely related to TIRFM, but here the refractive indices of the glass slide—the waveguide—and the sample are so similar that the light is refracted into the bulk sample at nearly all incidence angles allowed by the waveguide. The slide then acts as a light source which can irradiate nearly the entire sample. While FrTIR appears to be more effective in irradiating the sample, one of the primary advantages of TIRFM—the spatial resolution in the z-direction—is lost. When only a very thin section of the sample is exposed to an evanescent wave, sharp images can be generated in which all features are in focus and the very shallow depth of field is defined by the excitation light and not by the objective lens. By contrast, in FrTIR the entire sample fluoresces and out-of-focus regions appear as a blurry background.

1.3.4 Emulsions

To demonstrate and characterize F-EEM microscopy methods using various cameras and light sources, we required a fluorescent sample that varied spatially and spectrally, and one that would

ideally change over time. We decided to use droplets of fluorescent dyes—emulsions—since they can be readily prepared and modified to test different compounds of the system.

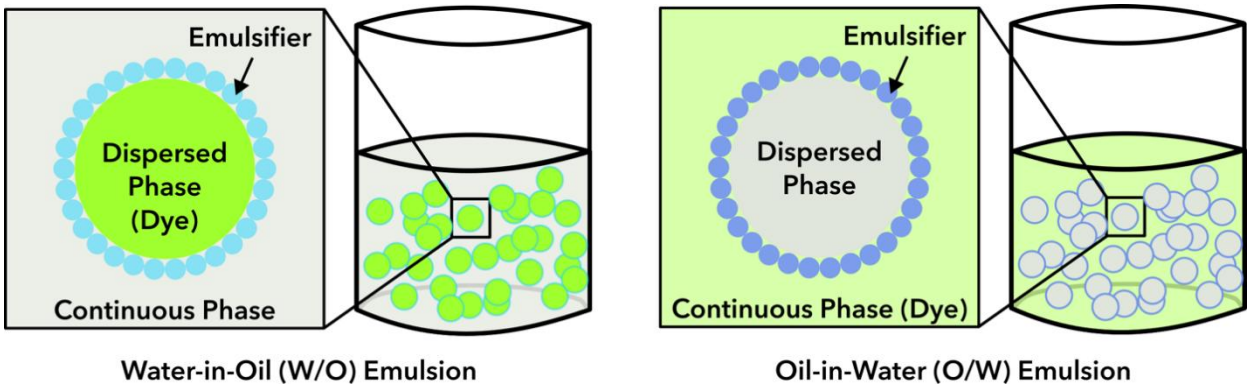

Figure 1.26. Components of two types of emulsions. The water-in-oil emulsion contains a fluorescent dye in the dispersed phase, and the oil-in-water shows the fluorescent dye in the continuous phase.

Emulsions are mixtures of immiscible liquids belonging to the general class of colloids. Aside from microemulsions which are thermodynamically stable, macroemulsions and nanoemulsions are kinetically stable but thermodynamically unstable, and will eventually break or revert to separated continuous and dispersed phases. Generally, emulsions are formed from two liquids using an emulsifier/surfactant and energy. The surfactant reduces the interfacial tension and allows for smaller droplets to be created, as well as prevents coalescence during emulsion formation. Energy is provided by shaking, stirring, shearing, or ultrasonic agitation. The result is kinetic stability from an energy barrier between droplets. The books authored by Tadros [232] and Sharma and Shah [233] are useful references for emulsion properties.

Within an emulsion, droplets experience Van der Waals attractive forces as well as steric and electrostatic repulsion. These forces must be balanced for an emulsion to remain stable, in addition to intact interfacial barriers. Instability in an emulsion can be classified as flocculation, creaming or sedimentation, coalescence, and Ostwald ripening. Each of these effects were observed in the attempts to create emulsions, and steps were taken to prevent each from occurring.

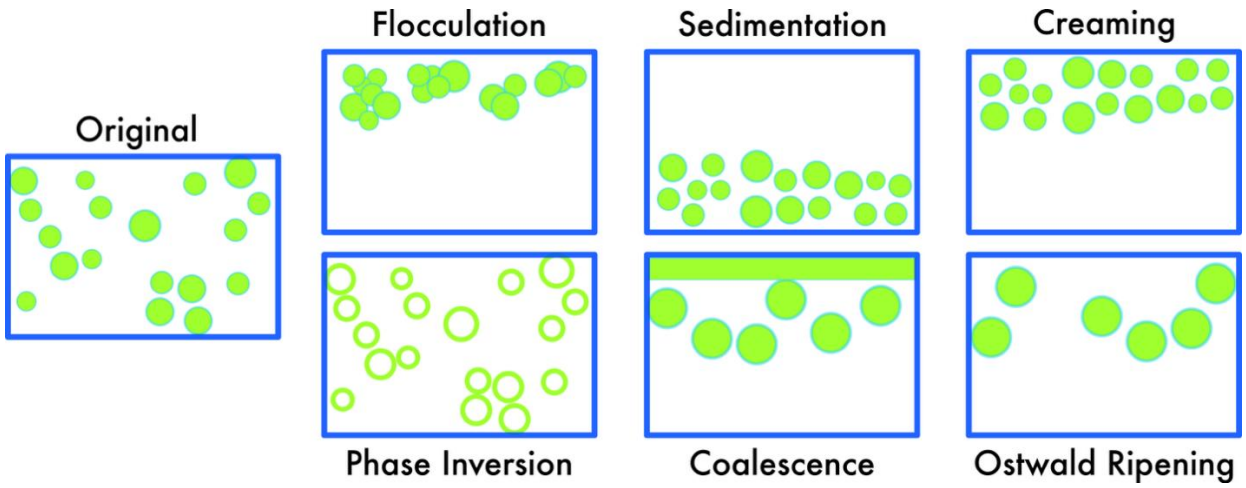

Figure 1.27. Types of instability in emulsions.

Flocculation results from attractive forces (van der Waals interactions) between droplets which are greater than any electrostatic or steric repulsive energies introduced by the system. Visually, this appears as droplets which cluster together but have not merged or broken. Flocculation is more common with smaller and polydisperse droplets, whereas creaming or sedimentation result from similar effects but often refer to larger droplets. An illustration of this can be seen in Figure 1.27 and an image of an emulsion with some flocculation is shown in Figure 7.14. To prevent flocculation, either electrostatic or steric repulsion may be introduced. Ionic surfactants introduce electrostatic repulsion, and some polymers introduce steric repulsion. Flocculation is a reversible effect and does not indicate that the emulsion has broken.

Creaming and Sedimentation occur when the density of the dispersed phase is greater or less than the continuous phase, respectively. As in flocculation, droplets retain their shape, but cluster near the surface or bottom of the container. This effect is also reversible. Sedimentation and creaming are governed by the competing effects of gravity and thermal motion. This is shown in Equation [1.4] when the thermal motion (Brownian diffusion, kT, where k is the Boltzmann constant and T is the absolute temperature) of the droplets is superseded by gravity—specifically, when densities of the dispersed and continuous phases are sufficiently different and the droplets are large enough. The force of gravity experienced by the emulsion in a container of height L is $m_{drop}gL$ where m_{drop} is the mass of the droplet and g is acceleration due to gravity [1.3] [232]

$$m_{drop} = (4/3)\pi R^3 \Delta\rho \qquad [1.3]$$

All emulsions except those in which $kT >> m_{drop}gL$ (nanoemulsions) should undergo creaming or sedimentation eventually [232]. The rate at which this occurs is impacted by both the viscosity of the continuous phase and the concentration of the emulsion—a higher viscosity and/or a higher emulsion concentration should result in a slower rate of creaming or sedimentation. Note that sedimentation or creaming rates depend on the different droplet sizes within an emulsion. A representation of the droplet dispersity of an emulsion is shown in [1.4] where the concentration of droplets at a particular height *h* in the container (C_h) depends on the concentration of droplets at the bottom or top (for sedimentation or creaming, respectively) of the container before sedimentation or creaming occur.

$$C_h = C_o \exp\left(-\frac{m_{drop}gh}{kT}\right) \qquad [1.4]$$

An expected rate of sedimentation or creaming can be calculated for a dilute emulsion with a volume fraction less than approximately 0.2, by taking into consideration hydrodynamic and gravity forces, using the viscosity of the continuous phase, the Stokes' velocity, and the droplet masses m_{drop} [232].

$$H = 6\pi\eta_o R v_o \qquad [1.5]$$

$$v_o = \frac{2}{9}\frac{\Delta\rho g R^2}{\eta_o} \qquad [1.6]$$

To reduce sedimentation or creaming, we attempt to decrease the force of gravity acting on the droplets. This can be done using similar densities for the continuous and dispersed phases, smaller droplets, or higher viscosity in the continuous phase. Properties of the dispersed and continuous phases can be modified by changing the solvent or by adding additional components to either of the phases [232]. Thickeners are commonly used to increase viscosity of the continuous phase [234].

Ostwald Ripening is a process in which smaller droplets are solubilized into the continuous phase and others are absorbed into larger droplets. Taylor [235] describes this as a reduction in the interfacial area to reduce the free energy of the system. Ostwald ripening reduces the polydispersity of the size distribution irreversibly, eventually leading to evenly sized large droplets.

The large interfacial area exposed in an emulsion of two insoluble phases causes the emulsion to be thermodynamically unstable [235, 236]. The droplets (dispersed phase) will then tend toward

increasingly large size to decrease the interfacial area due to the radius-dependent solubility [235, 236] described by [1.7] (the Kelvin effect or Gibbs-Tomson relation).

$$c(r) = c(\infty)\exp\left(\frac{2\sigma V_m}{rRT}\right) \approx c(\infty)\exp\left(1 + \frac{2\sigma V_m}{rRT}\right) \qquad [1.7]$$

Where c is the solubility, r is the radius of the particle, σ is the interfacial tensions, V_m is the molar volume of the substance of the disperse phase, R is the gas constant and T is the absolute temperature. The Kelvin effect results from the size dependence of the dispersed phase chemical potential [1.9] which occurs due to the increased Laplace pressure within a smaller-radius droplet. The Laplace pressure, describing the difference in pressure inside and outside a droplet, as determined by the radii of curvature of the droplets, for a spherical droplet:

$$\Delta p = \frac{2\gamma}{r} \qquad [1.8]$$

The Kelvin effect shows that for the simplest case in which the interfacial tension and molar volume are constant (the system is not changing for other reasons), the excess chemical potential $\delta\mu = \mu - \mu(\infty)$ is inversely proportional to the radius r.

$$\Delta\mu(r) = \mu(r) - \mu(\infty) = \int_0^{2\sigma/r} V_m(p)dp \approx \frac{2\sigma V_m}{r} \qquad [1.9]$$

Kabalnov [237] explains that the first derivative of the chemical potential versus size is negative unless the surface tension is negative [1.10] which demonstrates that for a polydisperse emulsion, the equilibrium becomes unstable and is lost, because with increasing polydispersity, the system moves further from a stable equilibrium.

$$\frac{d(\Delta\mu)}{dr} = -\frac{2\sigma V_m}{r^2} < 0 \qquad [1.10]$$

The effect of droplet radius r on chemical potential $\Delta\mu$ depends on the Laplace pressure as derived by Kabalnov [237]

$$\Delta\mu = \frac{4\kappa V_m}{r}\left(\frac{1}{r - H_0}\right)^2 \qquad [1.11]$$

using κ as the bending modulus and H_0 as the spontaneous curvature for a flat macroscopic interface, and r as the radius of the particle. An energy minimum is found when the system droplets are near the size preferred by the surfactant $r^* = 3/H_0$; the system here is metastable as a large kinetic barrier exists, however the system can decompose by Ostwald ripening if a large droplet

exists in the system. When the initial droplet size is large ($r_0 > r*$) then the system is not stable and decomposes via Ostwald ripening, while when the droplet size is too small ($r_0 < 1/H_0$) the system is also unstable and droplet radii tend toward $r = 1/H_0$ [237]. Ostwald ripening does not practically occur for droplets over 100 μm, as estimated by Kabalnov [237].

As described by Taylor [235], Ostwald ripening should not occur if droplets satisfy $2\varepsilon > \gamma$ where γ is the interfacial tension between the dispersed and continuous phases and $\varepsilon = d\gamma / d\ln A$ (dilational elasticity of the interface) where A is the area of the interface.

Ostwald ripening in a water-in-oil (W/O) emulsion can be effectively prevented by adding electrolytes to the aqueous phase, such as sodium chloride [238] or magnesium sulfate [239]. For an oil-in-water (O/W) emulsion, however, this is more difficult and cannot be slowed or stopped as for W/O emulsions. I refer to the review by Koroleva and Yurtov [240] for a discussion of these methods.

Coalescence occurs when interfacial barriers between droplets thin to the point of merging. Coalescence results from fluctuations of the film thickness between nearby droplets—when the film thickness becomes below the critical thinness for coalescence or when the apices of surface waves resulting from Van der Waals interactions between droplets join. Coalescence can be reduced by strengthening the interfacial barrier [232] to increase the stability of the films to resist merging when nearby. This strength can be described as a "disjoining pressure" π_h [241] calculated as the counter to additional pressure on a film when in contact with another droplet P_h. The disjoining pressure is affected by the electrostatic repulsion π_E, steric repulsion π_S, and van der Waals attraction π_A and can be calculated as

$$\pi_h = P_h - P_o = -\frac{\Delta G_T}{\Delta h} = \pi_E + \pi_S + \pi_A \qquad [1.12]$$

The film pressure P_h with a net interaction free energy $\Delta G_T = 0$ is P_o. Here, h represents the thickness of the barrier.

To prevent coalescence, a stable barrier π_A is required, such that $\pi_A > \pi_E + \pi_s$. Although smaller droplets can reduce coalescence due to their reduced surface fluctuations [241], we require larger droplets for these experiments, so must attempt other stability-enhancing techniques. This can be done by increasing repulsion and Gibbs elasticity, for example by using mixed surfactant systems or by using wraps of bilayers around droplets [242].

Viscosity of the continuous and dispersed phases and the similarity between the two values are important considerations for both emulsion formation and for rate of sedimentation or creaming. Increased viscosity in the continuous phase causes higher external (outer) stresses and droplet breakup is more likely [241]. As described by Tadros [241], the droplet size is dependent on the ratio of stresses to the Laplace pressure given by the capillary number Ca:

$$\mathrm{Ca} = \frac{\eta_0 \dot{\gamma}}{\sigma r} \qquad [1.13]$$

Where η_o is the viscosity of the medium, $\dot{\gamma}$ is the shear rate, σ is the interfacial tension, and *r* is the droplet radius. The capillary number Ca* which describes the possibility the drop will break up depends on the ratio of viscosities of the continuous and dispersed phases $\mathrm{Ca}^* = 0.054\lambda^{-2/3}$ for $\lambda < 1$ and droplets should break when Ca>Ca* [241].

Then, for an increasing shear rate and/or a continuous phase viscosity, Ca increases and causes an increase in the breakup likelihood for a given system. When the dispersed phase viscosity increases, Ca* increases and droplet breakup becomes less likely for a given system. To create larger droplets (10-100 μm), a smaller shear rate, lower continuous phase viscosity, and higher dispersed phase viscosity should be used.

Emulsifiers. For a two-phase system such as water and oil, a surfactant can be selected to produce water-in-oil or oil-in-water emulsions. The type of emulsion is determined by the hydrophobic-lipophilic balance (HLB) value of the surfactant, and the requirements of the two solvents—in this case, water and oil. The HLB value is roughly calculated as the weight fraction x_n of hydrophilic chemical moieties in the emulsifier divided by 5 [232, 243]. If some emulsifier was 50% hydrophilic the HLB would be 50/5 = 10. HLB values for different surfactants can be added by weight fraction:

$$HLB = x_1 HLB_1 + x_2 HLB_2 \qquad [1.14]$$

Tween 20 (HLB = 16.7) and Span 80 (HLB = 4.3) are both molecular or non-ionic surfactants and can be combined to create stronger interfacial barriers [244, 245].

Emulsion stability and size are based on many physical interactions and chemical components, and many possibilities exist to optimize or adjust an emulsion. This creates both lots of opportunity and a great deal of difficulty in determining which factors should be changed. Descriptions of changes or optimizations made to the emulsions created here are described in Section 7.3.1 along with the specific emulsions that we used for the experiments contained in this work.

1.4 Raman Spectroscopy

1.4.1 Background

Raman spectroscopy measures the vibrational spectrum of molecules following inelastic scattering of photons (Raman effect). It offers several advantages over fluorescence spectroscopy, notably due to the distinctiveness of their spectra and the larger number of molecules that can be identified; there are far more Raman-active molecules than strong fluorophores. In Raman scattering, an incident photon interacts with a molecule in an inelastic scattering event, as shown in Figure 1.2. The photon scattered after the interaction with a molecule at a virtual energy level has lost or gained a small amount of energy with respect to the incident photon, creating a Stokes or Anti-Stokes shift (ω) in the photon frequency, respectively. Raman spectra provide a unique vibrational "fingerprint" allowing for a comparably straightforward identification of molecules.

Raman scattering events are rare with approximately one Raman scattering event occurring per 10^6–10^8 incident photons [246], whereas fluorescence is a common process where each incident photon can produce a fluorescence photon, when the quantum yield is at unity and the molecule is excited at its maximum absorption peak. The fluorescence background can therefore be a significant challenge. In our instrument, we instead hope to use the information contained in both processes for greater analysis abilities, but to do so, the Raman signal must be enhanced.

Typically, a Raman spectrum is obtained by irradiating a sample with one wavelength of light and recording the Raman emission with a sensitive, high-resolution spectrometer. The difference of the energies between incident and Raman scattered photons are given in wavenumbers and represent the energy of the vibrational states of the molecule in its electronic ground state (ω, in Figure 1.2). Because a molecule is excited to a virtual state, the excitation wavelengths are not limited to those which have enough energy to excite a molecule to one of its electronic excited states, as is the case with fluorescence. Although the same spectrum should be obtained using any excitation wavelength, red and near-IR wavelengths are preferably used for biological samples to reduce autofluorescence and sample damage. Blue-green wavelengths are often used in place of red/near-IR when possible because of the $1/\lambda^4$ dependence of Raman (and unfortunately Rayleigh) scatter on wavelength. Although ultraviolet wavelengths result in even higher Raman signals over blue-green excitation, the risk of sample damage and autofluorescence are much greater.

Many techniques have been developed to enhance Raman scattering including surface enhanced Raman scattering (SERS), tip enhanced Raman scattering (TERS), and resonance Raman scattering (RRS), among others. We have chosen to use SERS for this project, as the technique has demonstrated both enhancement in Raman scattering and quenching of fluorescence [247, 248] in a sampling setup that can be easily integrated into our system. Ideally, this will allow us to detect both a relatively weak fluorescence signal and the enhanced Raman signals on a similar scale.

1.4.2 Surface-Enhanced Raman Spectroscopy

First discovered in the 1970s [249-251], SERS has undergone great advancements and is a powerful technique used for many applications, such as biological [252-255], food contaminant [256-258], and single-molecule sensing [259-261], among many more [262, 263]. When molecules closely interacting with an appropriate metallic substrate are irradiated with a light beam, their Raman signal increases through a number of mechanisms, both electromagnetic (EM) and chemical [246, 247, 262, 263].

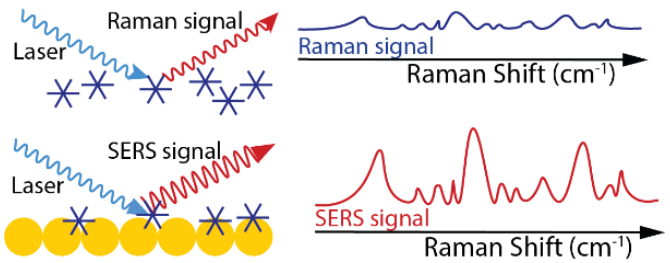

Figure 1.28. Surface-enhanced Raman spectroscopy diagram. Blue stars depict analyte molecules, and yellow circles indicate a SERS substrate, in this case spherical gold nanoparticles. The enhanced signal is shown depicted on the right for the regular and enhanced versions.

EM enhancement arises from the surface plasmons caused by the collective oscillation of electrons on a roughened metal surface and results in increased local electric fields in particular locations on the surface. The Raman signal is increased when a molecule is adsorbed at one of these locations ('hot spots'). Roughened surfaces can include aggregate colloidal nanoparticle solutions, deposited nanoparticles, and electrochemically roughened surfaces. Surface plasmons have a characteristic resonance frequency, corresponding to a wavelength of light, at which they create the largest Raman enhancement for an analyte. This resonance frequency can be measured using absorption spectroscopy and depends on the roughness, pattern, shape of nanoparticle, and the metal.

Similar properties define the strength of both chemical and electronic enhancements on SERS. Though there are several different mechanisms by which chemical enhancement occurs, charge transfer (CT) between the analyte and metal seems to be the largest contributor [264].

In this work, silver nanoparticles were chosen as SERS substrates because silver's resonant frequencies are at visible wavelengths, matching the wavelengths of the laser diodes in the setup. We chose to use nanostars instead of one of the many other nanoparticle shapes for the best potential enhancement and reproducibility using a colloidal nanoparticle suspension. In nanospheres and some other shapes, the distance between particles is essential in creating hot spots, and solutions rely on aggregation [262, 263]. In nanostars, hot spots are created both on the tips of the arms and between the arms [248, 265], and consequently do not require aggregation, which could improve reproducibility of SERS measurements.

1.4.3 Multiplexed Raman Spectroscopy

Using multiplexed excitation light, it should be possible to collect both Raman and fluorescence spectra from a sample using a SERS substrate. Because the fluorescence of a sample is often suppressed in SERS experiments due to the nature of the nanoparticles, we think that it would be possible to use the numerous excitation wavelengths to model a fluorescence signal out of a dataset in which both Raman and fluorescence are acquired. Additionally, multiplexed Raman spectroscopy using numerous wavelengths can successfully separate analytes [73, 153].

1.5 Multivariate Analysis for EEMs

Excitation-Emission Matrices (EEMs) must be mathematically interpreted to retrieve chemical information. There is no single technique that is superior for all applications, and researchers need to identify the algorithm that best suits their needs. The development of algorithms is an active area of research that is best described in separate reviews. Here, we will focus on multivariate analysis techniques and highlight some commonly used algorithms, their differences, capabilities and shortcomings. Other approaches based on *e.g.,* neural network analysis have shown great potential but are still less common [266-268] and will not be reviewed here.

EEMs may be acquired either randomly or as a function of time [67, 69], location [219], or other correlated variable. Both cases give rise to a 3-way data cube—a data cube having three "modes". In the first case of random EEM acquisition, the "sample number" just serves as an index, and no information would be lost if the stack of EEMs was shuffled. In the second case, the order of the EEM stack is important and contains information on *e.g.*, the kinetics of a chemical process, or the spatial distribution of chemical compounds, illustrated in Figure 1.29.

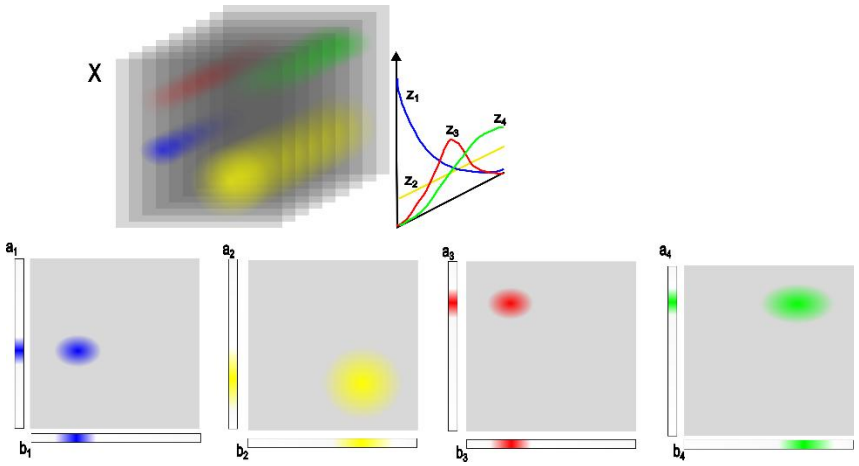

Figure 1.29. Sketch of the PARAFAC decomposition of a three-way dataset **X** consisting of a stack of time-varying EEMs, $\mathbf{Y}_1$. Each of the four component EEMs is constructed by a product of the perspective excitation and emission spectra, a_1 and b_1, and is weighted by the score vectors z_1.

EEMs may also depend on more than one variable such as time *and* location. Alternatively, more than one type of spectrum can be associated with (a) variable(s). For example, in the latter case, EEM spectra may be obtained synchronously with Raman spectra or absorption spectra. Both cases result in higher-dimensional, multi-way datasets that will not be discussed here.

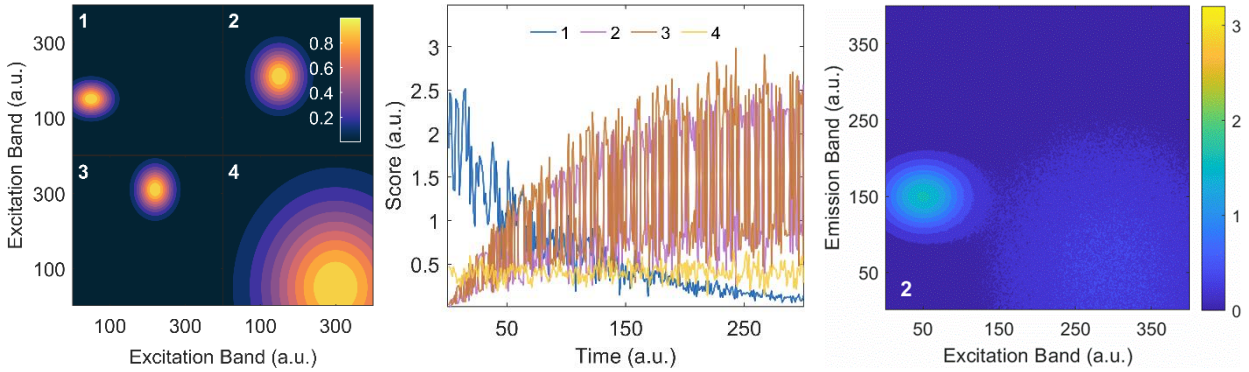

Figure 1.30. Input data representations. (**left**) Average EEM spectra of the four components, (**middle**) their weight as a function of sample number, and (**right**) representation of one of a sequence of EEM images in the 3-way data cube (spectrum 2 of 300).

The **parallel factor, PARAFAC, analysis** technique (also called "canonical decomposition": CANDECOMP) is conceptually the simplest multivariate analysis method. It decomposes a three-way stack of EEMs into several "components". The product of the excitation and emission spectrum vectors makes up the EEM spectrum of each component. These "component EEMs" are then weighted by a third vector that describes the weight of each component along the third (*e.g.,* time or location) variable, *z*. In an ideal case, each component corresponds to a single fluorophore, and the weight or "score" is related to its concentration.

The vectors each approximate a single dimension of the data cube—excitation, emission, and time—thus reducing the size of the data stored in this example from 400 × 400 × 300 (48 million data points) to (in this case) four component vectors with sizes 400 × 4 (1600 data points) for emission, 400 × 4 (1600 data points) for excitation, and 300 × 4 (1200 data points) for the time evolution.

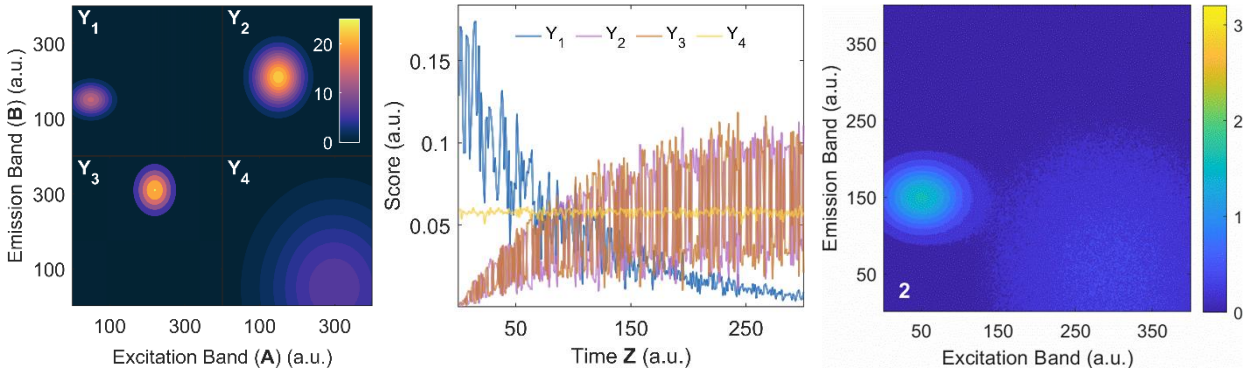

Figure 1.31. PARAFAC analysis of input data representations. PARAFAC analysis provides a decomposition that largely recovers the four components and their scores. The relative values of the scores and, conversely, of the EEM component spectra is not uniquely recovered. (**left**) the four component EEM spectra obtained from the analysis, (**middle**) the scores of those components through time (Z), and (**right**) the reconstructed data cube (spectrum 2 of 300).

More specifically, PARAFAC expresses the three-way data, **X**, as a trilinear outer product of vectors (really: rank-1 tensors) that are aligned along the respective three modes corresponding, here, to λ_{ex}, λ_{em}, and z.

$$\mathbf{X} = \mathbf{a} \circ \mathbf{b} \circ \mathbf{z} + \mathbf{E} \qquad [1.15]$$

This can be expressed differently for each component.

$$\mathbf{X} = \sum_{f=1}^{F} \mathbf{X}_f = \sum_{f=1}^{F} \mathbf{a}_f \circ \mathbf{b}_f \circ \mathbf{z}_f + \mathbf{E} \qquad [1.16]$$

Each tensor element of **X** is therefore defined as[93]

$$x_{ijk} = \sum_{f=1}^{F} a_{if}^{exc} b_{jf}^{em} z_{kf} + e_{ijk} \qquad [1.17]$$

where x_{ijk} is the data point corresponding to the fluorescence intensity of the k^{th} sample at the j^{th} excitation wavelength, λ_{ex} and at the j^{th} emission wavelength, λ_{em}. The indices $i = 1...I$ indicate the I excitation wavelengths, $j = 1...J$ indicates the emission wavelengths, and $k = 1...K$ give the K sample numbers, or time stamps, or location values. The 3-way tensor **E** with elements $[e_{ijk}]$ contains the residuals, *i.e.,* the fluorescence variability that has not been accounted for by the

model. Each f corresponds to one of the F PARAFAC components, which are modelled with respective EEM spectra:

$$\mathbf{Y}_f = \mathbf{a}_f \circ \mathbf{b}_f$$
$$y_{ij,f} = a_{i,f}^{exc} b_{j,f}^{em} \qquad [1.18]$$

Each such component has K values (scores) for z. The z-mode therefore contains the relative contributions of each component and may be used to derive kinetic information, spatial concentration distributions and the like. The rank-1 tensors, $\mathbf{A}_f$ and $\mathbf{B}_f$, are described by the elements (loadings), a_{if} and b_{jf}, and are uniquely identifiable as the result of the best fit of the experimental data to the model, $\mathbf{X}$, i.e., the fit that minimizes $\mathbf{E}$.[269]

To illustrate the different multivariate approaches, we synthesized an EEM dataset with 400 × 400 wavelength pairs, and four distinct components, $f_{1,2,3,4}$, that each produce a two-dimensional Gaussian EEM spectrum, $\mathbf{Y}_f$. Three of the components have low spectral noise and a fixed $\{\lambda_{ex}, \lambda_{em}\}$ maximum, whereas the fourth component is broader, has a varying maximum wavelength pair, and some spectral noise. Components 2 and 3 are anticorrelated and their sum increases as component 1 decays. The noise component 4 remains constant. Figure 1.30 shows each of these four raw component spectra, their deliberately "noisy" time evolution, and the weighted sum of the spectra resulting in a stack of EEM images.

As expected, the PARAFAC decomposition recovers the four component spectra, $\mathbf{Y}_f$, and gives accurate scores, $\mathbf{z}_f$, for each of the four components. The relative contribution of the spectra (and conversely of the scores) is not uniquely defined since each increase in a component's EEM brightness can be offset by reducing its score.

Equations [1.17] and [1.18] highlight the advantages and limits of the PARAFAC model. Equation [1.18] and Figure 1.31 show that an ideal PARAFAC model may generate the EEM spectra of all components in a mixture even if that component was not chemically isolated. Previously, this has been used to obtain EEM spectra, $\mathbf{Y}$, and concentrations, $\mathbf{z}$, of intermediates in chemical reactions [67, 68]. The PARAFAC model requires that the fluorescence EEMs are distinct—when two chemical components have perfectly covarying fluorescence intensities or identical spectra they will not be distinguished. Equation [1.17] also implies that the components are linearly additive and, in particular, that fluorescence increases linearly with concentration—a condition that is not always fulfilled due to quenching, self-absorption, inner filter effects, etc.

Another, less obvious, limitation arises from the type of EEM spectra that can be expressed by [1.18]: the equation does not permit modelling of spectral features arising from reflections of the excitation light or from Rayleigh scattering, *i.e.,* when $\mathbf{Y}_f$ is expressed as

$$y_{ij}^{scat} = \delta_{ij}\, s(\lambda_i) \qquad [1.19]$$

where δ_{ij} is the Kronecker-delta function and $s(\lambda)$ is proportional to the wavelength-dependent scattering cross section. Contributions from reflections or scattering, y_{ij}^{scat} are apparent in many EEM spectra as diagonal lines and must then be removed prior to PARAFAC analysis.

In many experiments the third mode is simply a sample number and does not contain valuable information, *i.e.,* no information is lost by shuffling the EEMs. Principal Component Analysis (PCA) and Singular Value Decomposition (SVD) methods can then be expanded to multidimensional arrays, such as the three-mode data cube $[\lambda_{ex}, \lambda_{em}, z]$ shown in Figure 1.30C. Tucker decomposition algorithms factorize that large experimental data cube into a smaller core tensor, **G**, and a set of three factor matrices, that is, one for each mode $[\lambda_{ex}, \lambda_{em}, z]$. In the most general case, a 3-way Tucker analysis produces the model tensor **X** with size $I \times J \times K$ according to

$$\mathbf{X}^{I,J,K} = \mathbf{G} \times_1 \mathbf{U}^{(1)} \times_2 \mathbf{U}^{(2)} \times_3 \mathbf{U}^{(3)} + \mathbf{E} \qquad [1.20]$$

Here, the *n*-mode product (*n* = 1, 2, 3) of **G** with $\mathbf{U}^{(n)}$ is denoted as $\mathbf{G} \times_n \mathbf{U}^{(n)}$.[270] The tensor elements of the model tensor **X** are therefore given by multiplication of the elements $g_{p,q,r}$ of the small core tensor **G** with elements of the two-dimensional factor matrices $\mathbf{U}^{(n)}$.

$$x_{i,j,k} = \sum_{p}^{P} \sum_{q}^{Q} \sum_{r}^{R} g_{p,q,r}\, u_{p,i}^{(1)}\, u_{q,j}^{(2)}\, u_{r,k}^{(3)} + e_{i,j,k} \qquad [1.21]$$

The size $P \times Q \times R$ of the core $\mathbf{G} = g_{p,q,r}$ specifies the number of components included in the fit. It can, of course, be as large as $I \times J \times K$, but is frequently much smaller, since experimental data tends to contain most of its variability in only a few components. Here, we show three different Tucker variants of the decomposition of the 3-way hypercube of Figure 1.30 into the **G** matrix and three factor matrices, $\mathbf{U}^{(n)}$ as shown in Figure 1.33. Representations of the tucker1, tucker2, and tucker3 models are shown in Figure 1.32.

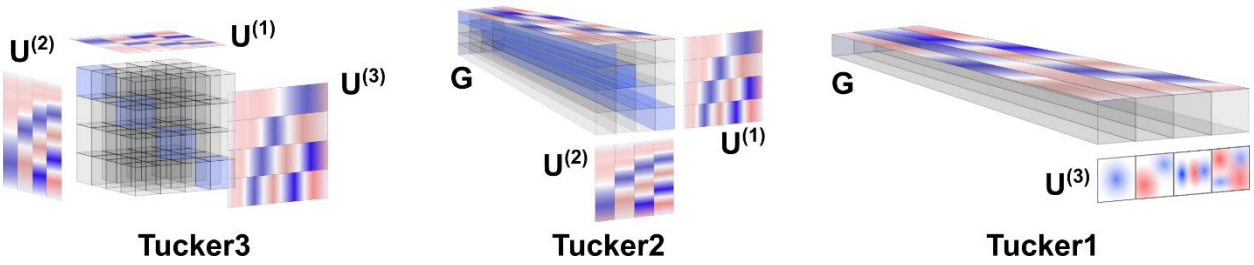

Figure 1.32. Tucker decomposition of the tensor **X** with four components. (**left**) **Tucker3:** the center cube illustrates the 4 × 4 × 4 elements of the core tensor **G**. The [4 × 400] elements of the $\mathbf{U}^{(1)}$ and $\mathbf{U}^{(2)}$ matrices and the [4 × 300] elements of $\mathbf{U}^{(3)}$ are multiplied and weighted by each of the 64 entries of **G**. (**middle**) **Tucker2**: the center illustrates the 4 × 4 × 300 elements of the core tensor **G**. The [4 × 400] elements of the $\mathbf{U}^{(1)}$ and $\mathbf{U}^{(2)}$ matrices are multiplied and weighted by each of the 4 × 4 × 300 entries of **G**. In Figure 1.34 and Figure 1.33 only the four component spectra corresponding to the diagonal elements shaded in blue are shown. (**right**) **Tucker1 / PCA**: the center illustrates the 4 × 300 elements of the core matrix **G**. The [400 × 400] elements of the four $\mathbf{U}^{(3)}$ matrices are multiplied and weighted by each of the 4 × 300 entries of **G**. The decomposition corresponds to higher-order principal component analysis.

Tucker3. The **Tucker3 model** does not impose restraints on the vectors $\mathbf{u}_p^{(1)}, \mathbf{u}_q^{(2)}, \mathbf{u}_r^{(3)}$ that form the respective $\mathbf{U}^{(1,2,3)}$, allowing for maximum flexibility of the fit. For a 4-component fit the core tensor **G** has then 4 × 4 × 4 elements, where the first two modes represent the four spectral components and the last represents their scores.

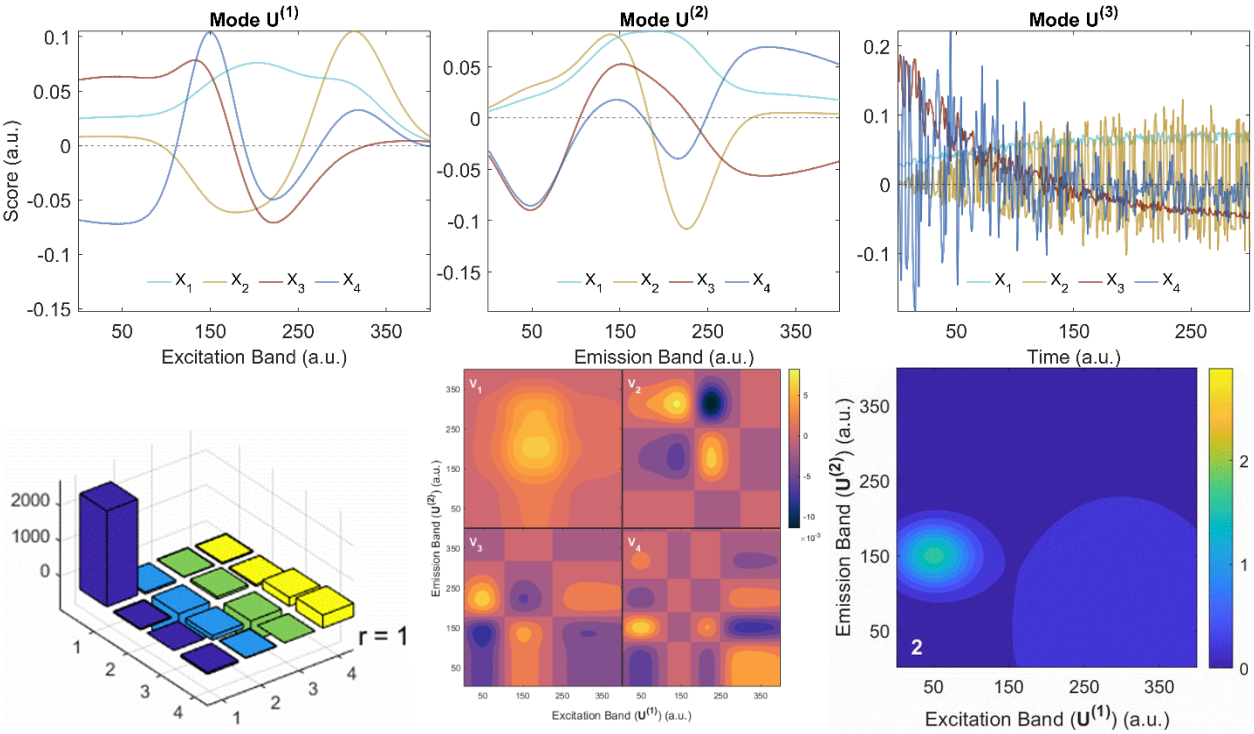

Figure 1.33. **Tucker3** analysis of the data cube in Figure 1.30, using four components. The top row shows the [4 × 300] elements of the **U**(1), and **U**(2) matrices and the [4 × 300] elements of **U**(3). The bottom row shows (**left**) the 4 × 4 × 4 elements of the core tensor G (the first in the series of four), (**middle**) four of the possible 16 EEM-type spectra corresponding to the diagonal elements in the G-tensor according to [1.21] and (**right**) the resulting model according to [1.20] and [1.21] (spectrum 2 of 300).

When $\mathbf{u}_p^{(1)}, \mathbf{u}_q^{(2)}$ and $\mathbf{u}_r^{(3)}$ are columns from *orthogonal* matrices $\mathbf{U}^{(1)}$, $\mathbf{U}^{(2)}$ and $\mathbf{U}^{(3)}$, the model is referred to as higher-order, singular value decomposition, HOSVD. [271] In Figure 1.33, we constrained the fit to give three mutually orthogonal factor matrices, $\mathbf{U}^{(k)}$. Additionally, when considering only the diagonal $f = (p = q)$ elements in $\mathbf{U}^{(1)}$ and $\mathbf{U}^{(2)}$ (shaded blue in Figure 1.32), we can display each of the 4 components $\mathbf{V}_f$ in an "EEM-type" matrix using

$$v_{ij,f} = u_{i,f}^{(1)} u_{j,f}^{(2)} \qquad [1.22]$$

in analogy to [1.18]. These four (out of 64 possible) matrices are given in Figure 1.33.

We note that if, in addition, the core tensor $\mathbf{G}$ is restricted to be diagonal $g_{p,q,r} = \delta_{p,q,r}$ and if $P = Q = R$, the HOSVD decomposition is identical to the PARAFAC model ([1.17] [270, 272]).

The Tucker3 model has considerable advantages, arising from the flexibility that is inherent in the model, but that also means that it has no unique solution. It has been proposed to preferentially identify mathematical solutions that either use prior knowledge about the chemical system, or that orient the core matrix to be close to diagonal [270, 273].

Tucker2. Alternatively, one can impose additional constraints, such as requiring that one of the modes is described by a component matrix $\mathbf{U}^{(3)}$, that is identical to the identity matrix. [273] This **Tucker2-model** then gives:

$$x_{i,j,k} = \sum_{p}^{P} \sum_{q}^{Q} g_{p,q,k} \, u_{p,i}^{(1)} \, u_{q,j}^{(2)} + e_{i,j,k} \qquad [1.23]$$

or, equivalently:

$$\mathbf{X}_k = \mathbf{G}_k \times_1 \mathbf{U}^{(1)} \times_2 \mathbf{U}^{(2)} + \mathbf{E}_k \qquad [1.24]$$

In this case, the matrix $\mathbf{X}_k(\mathrm{I} \times \mathrm{J})$ is the k^{th} frontal plane of the modelled data cube, and $\mathbf{G}_k(P \times Q)$ is the k^{th} plane of the "extended core" tensor, where P and Q give the number of components. The core is "extended", because the number of elements in the third mode, K, is no longer given by the number of components as in the Tucker3 model above, but rather by the size of the original data cube. Our Tucker2 modeling of the data cube in Figure 1.30, produces a core matrix $\mathbf{G}$ that has dimensions of $4 \times 4 \times K$, where K is the number of EEM spectra, and two component matrices $\mathbf{U}^{(1)}$ and $\mathbf{U}^{(2)}$ with dimensions [400 × 400 × 4] that are given by the size of the EEMs and the number of components. The component "EEM-type" spectra can be obtained as in [1.22] and are shown for our particular case in Figure 1.34.

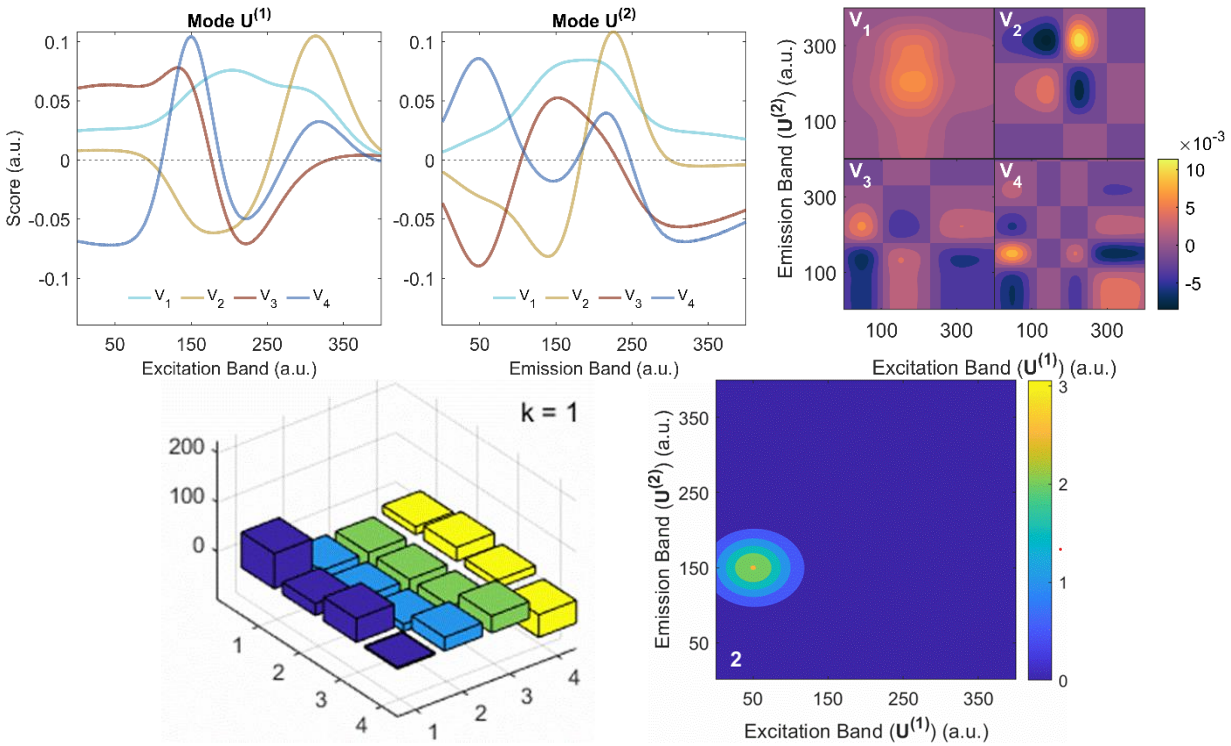

Figure 1.34. **Tucker2** analysis of the data cube in Figure 1.30, using four components. Top row shows (**right**) the EEM-type spectra obtained by multiplication of the four rank-1 tensors obtained from $\mathbf{U}^{(1)}$ (**left**) with those obtained from $\mathbf{U}^{(2)}$ (**middle**) as in [1.22]. Bottom row (**left**) shows the 4 × 4 × 300 elements of the core tensor **G** (k=1 of 300), and (**right**) provides the resulting model according to [1.24] (spectrum 2 of 300).

The Tucker2 model gives the principal components for each of the EEM spectra but does not include principal components along the third mode, *z*, *i.e.,* for the mode containing the sample number (or time, or location). The time evolution of the decomposition is instead contained in **G**. Figure 1.34 (bottom, left) shows how each of the 4 × 4 elements varies as a function of *k*. Since the Tucker2 model is more constrained than Tucker3, unique solutions can be found using, for example, a least-squares algorithm.

Tucker1. In the Tucker1 model an additional restriction is imposed by leaving *two* modes uncompressed, *i.e.,* by writing:

$$\mathbf{x}_{i,j} = \mathbf{G}_{i,j} \times_3 \mathbf{U}^{(3)} + \mathbf{e}_{i,j} \qquad [1.25]$$

or, equivalently for all *k*

$$x_{i,j,k} = \sum_{r}^{R} g_{i,j,r}\, u_{r,k}^{(3)} + e_{i,j,k} \qquad [1.26]$$

where we chose to compress just the *z*-axis and leave the EEM spectra uncompressed. Here, $\mathbf{x}_{i,j}(K)$ with elements $[x_{ij,k}]$ is the vector of length *K* that describes the EEM intensity for each wavelength

pair $\{i, j\}$. The core tensor elements $\mathbf{G}_{i,j}(R)$ are the $\{i, j\}^{th}$ "tube" or "fiber" of the tensor, where R gives the number of components as before. In our example $\mathbf{G}$ has size 400 × 400 × 4 and contains the four EEM-type spectra shown in Figure 1.35 (middle). The factors in $\mathbf{U}^{(3)}$ with size [4 × 300] contain the scores of these four components shown in Figure 1.35 (left).

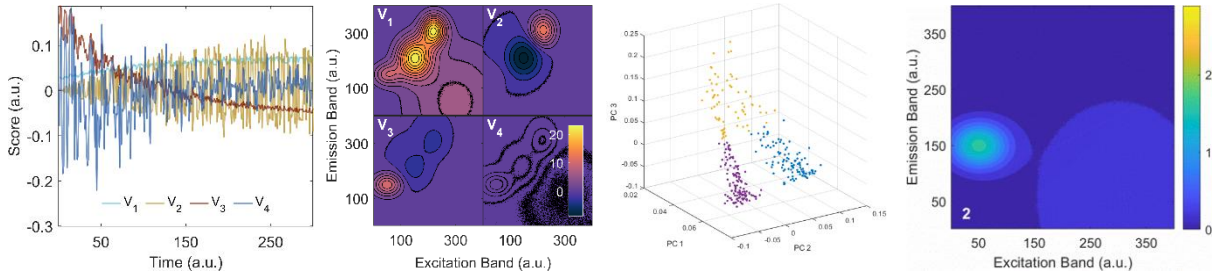

Figure 1.35. **Tucker1** analysis of the data cube in Figure 1.30, using four components. (**left**) The respective scores as obtained from $\mathbf{u}_r$, (**middle left**) the four EEM-type spectra obtained $\mathbf{G}_{ij}$, (**middle right**) principal component correlation plot of the first three principal components from $\mathbf{G}$ in three dimensions, (**right**) the result of the Tucker1 model (spectrum 2 of 300).

It was pointed out that the **Tucker1 model** is equivalent to performing a conventional N-way **principal component analysis (PCA)** on the stack of EEM spectra. PCA uses the variability of the EEM spectra between different samples to identify the principal components which can then help classifying samples according to their similarities and differences. The relation between Tucker1 analysis and PCA may be illustrated as follows.

In two-dimensional (two-way) PCA the data is modelled as [274]

$$\mathbf{X} = \sum_{r=1}^{R} \mathbf{t}_r \mathbf{p}_r^T = \mathbf{T}\,\mathbf{P}^T + \mathbf{E} \qquad [1.27]$$

Where the vectors $\mathbf{t}_r$ are the scores and the $\mathbf{p}_r$ vectors are the loadings and are given by the eigenvectors of the covariance matrix. [274] Similarly, three-way data cubes, $\mathbf{X}$ can be analysed by multiway-PCA as the sum of the product of R score vectors ($\mathbf{t}_r$) and R loading matrices ($\mathbf{P}_r$) so that a residual array tensor $\mathbf{E}$ is minimized.

$$\mathbf{X} = \sum_{r=1}^{R} \mathbf{u}_r \otimes \mathbf{G}_r + \mathbf{E} \qquad [1.28]$$

In general, the n-mode product (n=1,2,3) of $\mathbf{G}$ with $\mathbf{U}^{(3)}$ is denoted as $\mathbf{G} \times \mathbf{U}^{(3)}$ [270] as in [1.26],but since $\mathbf{U}^{(3)}$ consists of just the R score vectors $\mathbf{u}_r$, and $\mathbf{G}$ describes the R loading matrices we write

$$\mathbf{X} = \sum_{r=1}^{R} \mathbf{G}_r \times_3 \mathbf{u}_r + \mathbf{E} \qquad [1.29]$$

It is now apparent that [1.28] and [1.25] are equivalent.

As was pointed out previously,[274] multiway-PCA can also be performed using two-way PCA on a large two-dimensional matrix which is obtained by unfolding the three-way array **X** in one of six possible ways, only three of which are mathematically unique. For example, one might unfold **X** in such a way that its $I \times J$ vertical slices are aligned side-by-side to the right, starting with the slice corresponding to the first *z* interval. The resulting two-dimensional matrix has the size $I \times JK$ and this unfolding allows one to analyze variability among the EEMs in **X**.

Chapter 2 Hadamard-Transform Spectroscopy

2.1 Multiplexed Spectroscopy

In our work we use the Hadamard Transform to multiplex the excitation light for fluorescence spectroscopy analogous use of the Fourier Transform in absorption spectroscopy. Multiplexing the light and demultiplexing the resulting signal has distinct advantages for some spectroscopic methods, which can be mathematically illustrated.

In their book on Infrared Fourier Transform Spectroscopy Griffiths and De Haseth explain the spectroscopic "trading rules" that govern the relationships between the Signal-to-Noise Ratio, (*SNR*), the spectral resolution $(\Delta\tilde{\nu})$, and the data acquisition time (T_{aq}) [121]. This relation is:

$$\begin{aligned} SNR &= C'\frac{I_{source}\Delta\tilde{\nu}\sqrt{T_{aq}}}{NEP} \\ &= \frac{C'\left(\tilde{\nu}_{\max}-\tilde{\nu}_{\min}\right)}{NEP}\frac{I_{source}\sqrt{n\,t_{aq}}}{n} \\ &= \frac{C'\left(\tilde{\nu}_{\max}-\tilde{\nu}_{\min}\right)}{NEP}I_{source}\sqrt{\frac{t_{aq}}{n}} \end{aligned} \qquad [2.1]$$

where I_{source}, is the brightness of the light source, and *NEP* is the noise equivalent power of the detector. The *NEP* can be understood as the optical power that gives an electric signal equivalent to the noise level. It can be determined as the ratio of the standard deviation of the noise voltage to the sensitivity (responsivity) of the detector. The constant C' collects other instrument-specific parameters such as the etendue of the system, the detection area, and - in case of fluorescence detection—the quantum yield. All terms in equation [2.1] have a different dependence on wavelength, λ, or wavenumber $\tilde{\nu} = hc_0 / \lambda$.

If the excitation light over a range $(\tilde{\nu}_{\max}-\tilde{\nu}_{\min})$ is multiplexed using Michelson interferometry (in Fourier-transform (FT) multiplexing) or using a programmable binary light source (Hadamard-transform (HT)), the source brightness (I_{source}) is increased by a factor of $n/2$, in an ideal case, where $n = (\tilde{\nu}_{\max}-\tilde{\nu}_{\min})/\Delta\tilde{\nu}$ is the number of wavelength bands, or spectral elements, that one wishes to acquire. The total acquisition time for a spectrum $T_{aq} = nt_{aq}$ depends on the number of

channels, n, where t_{aq} is the integration time for each wavelength band, or FT-interferogram, or HT-Walsh function.

Compared to scanning sources, wavelength multiplexing has the potential to substantially increase the acquisition rate or the SNR. Katz *et al.* determined the Signal to Noise Enhancement (SNE) due to multiplexing the HT source as [219]

$$SNE_{HT} = \frac{SNR_{HT}}{SNR_{seq}} = \frac{n+1}{2\sqrt{n}}. \qquad [2.2]$$

In the limit of large n, the SNE approaches the SNE obtained for Fourier-transformation based multiplexing of the fluorescence EEM signal is:

$$SNE_{FT} = \frac{SNR_{FT}}{SNR_{seq}} = \frac{\sqrt{n}}{2} \qquad [2.3]$$

These relations were experimentally tested and found to hold true within the margin of error [219].

For EEM spectrometers, multiplexing techniques, such as Fourier transformation [119, 177, 275] and Hadamard-sequencing [32, 34, 87, 219, 276] show therefore particular promise and are described in more detail in the next sections.

Besides the multiplex-advantage (Fellgett's advantage), Fourier transform spectrometers have a higher light throughput than conventional monochromator-based EEM instruments due to an increased etendue of the system (Jacquinot's advantage). Recently, several designs for EEM-spectrometers with an excitation light source based on Fourier transformation have been published.

2.1.1 Fourier-Multiplexed Fluorescence Excitation

Peng *et al.* reported on an EEM spectrometer, which was based on two synchronized and high-speed differential-delay scanning Michelson interferometers [119]. For the excitation, collimated light of a fiber-coupled Xe arc lamp was multiplexed in a Michelson interferometer and guided towards the sample. The emission was captured by a PMT after transmission through a second, slower scanning Michelson interferometer, which was synchronised to the excitation interferometer by sharing a (double-sided) mirror. To monitor the mirror positions of the interferometers, a helium-neon laser and a green laser diode have been implemented, *i.e.* the differential delays could be determined by monitoring the interference fringes. In total, one measurement signal and four monitoring signals were recorded. EEM spectra were obtained after

two-dimensional Fourier transformation. With this setup, spectra over a wavelength range from 425 nm to 550 nm for the excitation and from 580 nm to 750 nm for the emission were obtained at a spectral resolution of 81 cm^{-1} (equivalent to 2 nm at 500 nm, or 3.4 nm at 650 nm), with an acquisition time of just 40 s. The performance of the spectrometer was tested with two dye solutions. The limitations of the spectrometer were related to the incoherence of the arc lamp.

A similar setup was developed by Yuan *et al.* who combined the excitation and emission components into a double-pass interferometer. The interferograms of the excitation light (from 450 to 540 nm) and of the fluorescence emission (from 550–700 nm), provided cross-correlation spectra within just 1.5 ms. By design, a full EEM spectrum cannot be obtained with this setup [120].

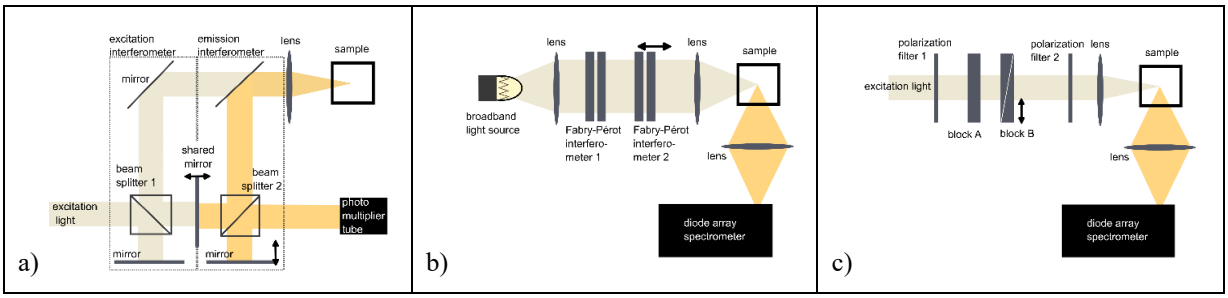

Figure 2.1. Schematics of three EEM spectrometers based on interferometry. **a)** simplified setup based on two Michelson-Morley interferometers, adapted from Peng *et al.* [119]. **b)** EEM spectrometer based in two Fabry-Pérot interferometers as reported by Anzai *et al.* [275], **c)** setup based on translating wedges as reported by Perri *et al.* [177].

A more compact solution has been presented by Anzai *et al.* [275]. They demonstrated an excitation source based on a xenon arc lamp in front of a tandem Fabry-Pérot interferometer with a mirror reflectivity of 50% and a spacing at around 20 µm for each stage. The mirror spacing of the second stage Fabry-Pérot interferometer could be varied by a piezoelectric actuator from 18.5 µm to 22.5 µm in steps of 20 nm or more, thereby enabling a tuning range from 380 nm to 800 nm with a resolution of approximately 1 nm. A diode array spectrometer was used to detect the fluorescence emission in the range from 200 nm to 1100 nm with a resolution of approximately 1.5 nm. With this setup, a full EEM spectrum with approximately 130 data points could be obtained after a Fourier transformation in less than 3 minutes. The experimental setup is shown in Figure 2.1b.

Perri *et al.* reported on an EEM spectrometer based on a pair of birefringent wedges named Translating-Wedge-based Identical pulses eNcoding System (TWINS) [177]. This setup provided a higher light throughput, a larger spectral resolution for the excitation light, and fewer parasitic spectral fringes compared to a Fabry-Pérot spectrometer. Depending on the employed light source, either a range from 400 nm to 700 nm in the case of a white LED, or from 500 nm to 2300 nm in the case of a supercontinuum laser was covered in the excitation. After passing through a

polarisation filter set to 45 degrees relative to the optical axis, light from the light sources was transmitted through a birefringent block towards a second birefringent block, which was divided into two wedges. The second wedge was positioned on a translation stage to change its position relative to the first wedge. A fixed delay between the two orthogonal polarization components was introduced by the first birefringent block, whereas a variable, and partially compensating delay with the opposite sign was added by the two wedges. Both polarization components were then combined by a second polarizer to build the interferogram that was directed towards the sample. Again, an array spectrometer (CCD detector) was used to detect the emission (Figure 2.1c). With this spectrometer, the fluorescence EEM and the absorption was obtained simultaneously. This is of interest when identifying fluorescing and non-fluorescing species in a sample side by side, or when quantifying the quantum yield of a compound. Here, an acquisition time of 40 s at a sub-nanometer resolution was obtained for the supercontinuum laser, and 16 minutes for the less intense LED lamp.

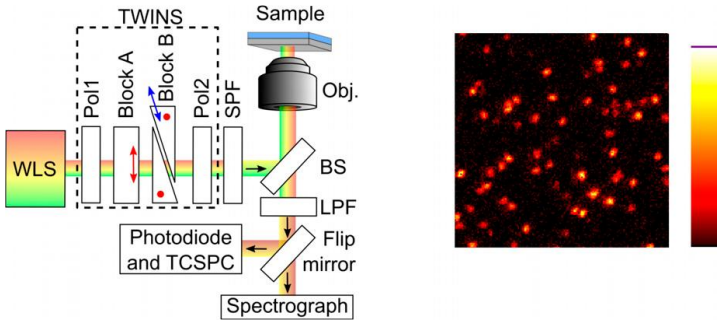

Figure 2.2. Schematic of the interferometry-based confocal microscope(**left**). The birefringent interferometer (TWINS) creates two time-delayed, copropagating beam replicas from the output of the white-light source (WLS). Image of a 15 × 15 µm region of the sample; each "spot" corresponds to a single molecule (**right**). Adapted from [277].

Finally, in an impressive demonstration of high spatial, temporal and spectral resolution, Thyrhaug *et al.* performed single-molecule EEM spectroscopy using a confocal microscope for diffraction-limited imaging on dye molecules derived from terylene diimide. They used a common-path birefringent interferometer (Translating-Wedge-based Identical pulses eNcoding System (TWINS) to multiplex white light from a supercontinuum laser light source. The detection was performed either by time-correlated single photon counting (TCSPC) to obtain fluorescence lifetimes of the sample within the same setup or using a very sensitive spectrometer to obtain the EEM map [277] (Figure 2.2).

2.1.2 Hadamard-Multiplexed Fluorescence Excitation

Hadamard-transform (HT) multiplexing can be seen as a binary equivalent of the Fourier transformation. The light source spectrum is divided into *n* distinct spectral bands, using filters or dispersive elements (gratings, prisms) combined with masks, or simply using an array of LEDs. These *n* wavelength bands are then combined into *n* distinct barcode patterns that each form one instance of the excitation light cycle. The HT-multiplexing technique has been used since the late 1960s [278-280] [281, 282], but remained less common compared to Fourier transform multiplexing, likely due to the technical difficulties in creating a "programmable" light source in which many wavelength bands can be rapidly turned on and off at will. A detailed description of Hadamard multiplexing can be found in reference [87], and only a brief description is provided here.

These binary barcodes ("masks") are usually derived from the rows (or columns) of a Paley I-type Hadamard matrix. In general, a Hadamard matrix is composed of rows and columns of mutually orthogonal Walsh functions. Hadamard matrices are square and symmetric (rows and columns are identical) matrices in which the elements are either +1 or -1. If only one detector is used, a simplified version derived from the Hadamard matrix is used to describe the multiplexing patterns. These S-matrices are obtained from Paley I type Hadamard-matrix, by removing the first row and the first column which contain only 1's and exchanging all entries of -1 with 0. Here, 1 means that the respective wavelength band is turned on, while 0 means that it is turned off. For a light source that has 7 distinct wavelength bands, an S-matrix would look like:

$$\mathbf{H}_8^* = \begin{pmatrix} 1 & 1 & 1 & 1 & 1 & 1 & 1 & 1 \\ 1 & 1 & -1 & -1 & 1 & -1 & 1 & 1 \\ 1 & 1 & 1 & -1 & -1 & 1 & -1 & 1 \\ 1 & 1 & 1 & 1 & -1 & -1 & 1 & -1 \\ 1 & -1 & 1 & 1 & 1 & -1 & -1 & 1 \\ 1 & 1 & -1 & 1 & 1 & 1 & -1 & -1 \\ 1 & -1 & 1 & -1 & 1 & 1 & 1 & -1 \\ 1 & -1 & 1 & 1 & -1 & 1 & 1 & 1 \end{pmatrix} \rightarrow \mathbf{H}_7 = \begin{pmatrix} 1 & 0 & 0 & 1 & 0 & 1 & 1 \\ 1 & 1 & 0 & 0 & 1 & 0 & 1 \\ 1 & 1 & 1 & 0 & 0 & 1 & 0 \\ 0 & 1 & 1 & 1 & 0 & 0 & 1 \\ 1 & 0 & 1 & 1 & 1 & 0 & 0 \\ 0 & 1 & 0 & 1 & 1 & 1 & 0 \\ 0 & 0 & 1 & 0 & 1 & 1 & 1 \end{pmatrix} \quad [2.4]$$

The multiplexed excitation spectrum **HS** is then given by the Hadamard product (element-by-element product) of the S-Hadamard matrix **H** and the source matrix **S**, which is composed of *N* identical rows each containing the emission light source spectrum S_i:

$$\mathbf{H}\circ\mathbf{S}=\mathbf{H}\circ\begin{pmatrix} S_1 & S_2 & S_3 & \cdots & S_n \\ S_1 & S_2 & S_3 & \cdots & S_n \\ S_1 & S_2 & S_3 & \cdots & S_n \\ \vdots & \vdots & \vdots & \ddots & \vdots \\ S_1 & S_2 & S_3 & \cdots & S_n \end{pmatrix}=\begin{pmatrix} H_{11}S_1 & H_{21}S_2 & H_{31}S_3 & \cdots & H_{n1}S_n \\ H_{12}S_1 & H_{22}S_2 & H_{32}S_3 & \cdots & H_{n2}S_n \\ H_{13}S_1 & H_{23}S_2 & H_{33}S_3 & \cdots & H_{n3}S_n \\ \vdots & \vdots & \vdots & \ddots & \vdots \\ H_{1n}S_1 & H_{2n}S_2 & H_{3n}S_3 & \cdots & H_{nn}S_n \end{pmatrix} \quad [2.5]$$

For each mask, an emission spectrum F_j is recorded, such that the total measured signal $\mathbf{F}=\left[F_1\ldots F_n\right]^T$ can be written as a matrix:

$$\mathbf{F}=\left(\mathbf{H}\circ\mathbf{S}\right)\times\mathbf{M} \quad [2.6]$$

Here, $\mathbf{M}$ is the desired EEM spectrum, which can then be obtained after demultiplexing—multiplication with the inverse of the multiplexed excitation spectrum (Figure 2.3):

$$\mathbf{M}=\left(\mathbf{H}\circ\mathbf{S}\right)^{-1}\times\mathbf{F} \quad [2.7]$$

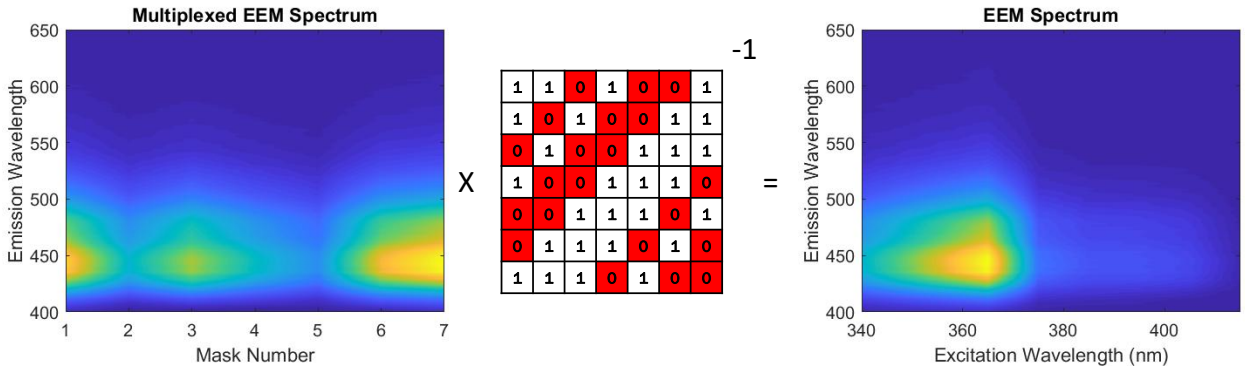

Figure 2.3. Visual illustration of the inverse Hadamard transform. A series of fluorescence emission spectra obtained using a 7 × 7 S-matrix shown in the center (Equation [2.7]) yields an EEM spectrum [276].

There exist several designs for programmable light sources. Arguably, the simplest consists of an array of distinct narrow-band light sources, such LEDs or lasers, which are turned on in accordance with the above Hadamard masks. For example, we recently presented a programmable excitation light source composed of seven fiber-coupled UV-LEDs with wavelengths between 340 nm to 415 nm. The LEDs were programmed to switch on and off according to the Hadamard pattern [32]. The light of the LEDs was collected by emission fibers, which were part of a fiber probe that was guided towards the sample in a high-performance liquid-chromatography setup (Figure 2.4). Using a photodetector array spectrometer to collect the fluorescence emission, an acquisition rate of 146 ms per EEM spectrum was realized. This acquisition rate is several times faster than that obtained when using excitation light sources combined with a monochromator. The setup was

tested with a mixture of five different dyes (coumarins 307, 440, 450, 460, 540A) in acetonitrile during chromatographic separation.

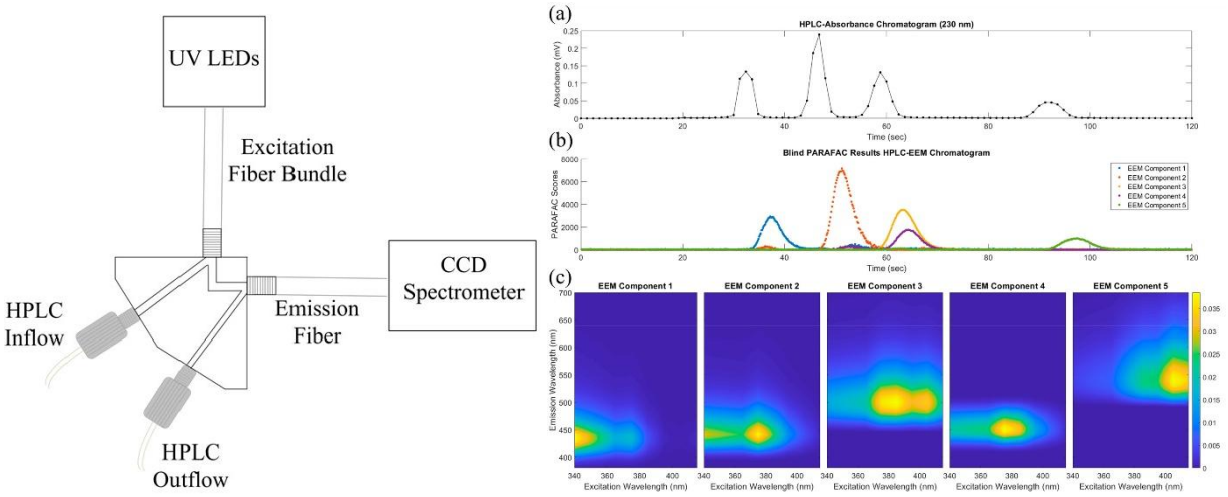

Figure 2.4. Programmable light source and application to HPLC detection. (**left**) Schematic of a programmable excitation light source based on Hadamard-transformation, which was composed of 7 separate light-emitting diodes (LEDs). (**right**) (a) Chromatogram recorded with an absorption detector operating at 230 nm, (b) "blind" PARAFAC analysis on a chromatogram recorded with an in-line fluorescence detector, (c) spectra of each of the five components from the PARAFAC model [32].

A more sophisticated and far more adaptable light source was developed by MacKinnon *et al.* and later by *OneLight Corp.* in 2005-2010. In this fully programmable light source, each combination of wavelength bands can be selected at will. Light from a bright white LED was dispersed by a grating onto a commercial Digital Micromirror Array (DMA) and the colour bands were selected by tilting the respective mirror columns such that reflected light can be collected using a waveguide [283, 284]. In the first prototype the spectral resolution was 10 nm over a wavelength range of 400–700 nm. To the best of our knowledge this programmable light source was not used for spectroscopy.

Our group developed independently a similar light source with up to 127 excitation bands with a spectral resolution determined by the column width, and limited at ~5 nm over a 450–650 nm excitation wavelength range [80, 219]. Here, light of a white light source was dispersed by a diffraction grating in a Czerny-Turner-style array spectrometer. The dispersion spectrum was captured by a digital micromirror array (DMA) consisting of 768 × 1024 micromirrors, which could be programmed and flipped individually, and columns of the DMA each comprised a small portion of the spectrum in narrow wavelength bands.

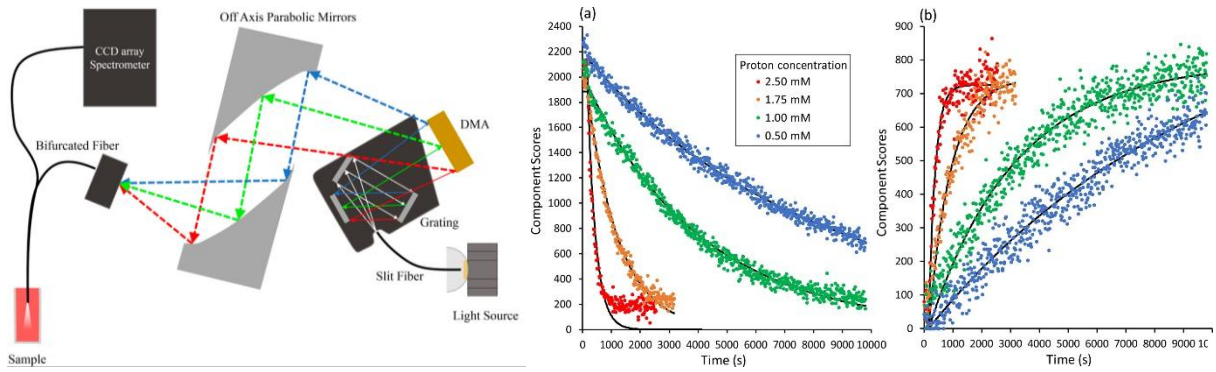

Figure 2.5. Programmable light source using a digital micromirror array and its application in monitoring chlorophyll demetallation. (**left**) Schematic of instrument, (**right**) PARAFAC scores of demetallation of chlorophyll-a with different concentrations of sulfuric acid, showing (a) increased rate of decay of chlorophyll-a and (b) increased rate of growth of pheophytin-a with the increase in acid concentration [87].

The mirrors of the DMA were programmed to switch columns on and off according to a Hadamard pattern, thereby creating a programmable and multiplexed excitation light source. The light reflected by the DMA was captured by a second fiber bundle and then guided towards the sample (Figure 2.5). With this light source, a full EEM-spectrum with 31–127 excitation bands was obtained. For bright fluorophores the exposure time could be reduced to 15 ms per mask and an EEM-spectrum could be obtained in just 500 ms. The system was used to determine the chlorophyll-a concentration in a solution generated from spinach extract and follow its conversion to pheophytin-a upon addition of acid (Figure 2.5) [87].

2.1.3 Hadamard-Multiplexed *versus* Sequential Illumination

To demonstrate the advantages of Hadamard-multiplexed illumination in comparison to a sequential scan of the wavelengths, Oren Katz acquired images using a multispectral camera (Section 4.1) and the DMA-based programmable light source. The results show that the sequential scan has a lower SNR than the multiplexed source as described in Section 2.1.3 and [285,286].

Part of the multiplex advantage is due to the greater amount of light illuminating the sample, with 16 of the 31 channels in the multiplexed source, compared to only one in the sequential scan. One may then assume that using all-but-one excitation wavelengths, here 30 out of 31 wavelengths, would further increase the SNR. To demonstrate that the multiplex advantage is not solely due to the increased brightness of the signal, but also the multiplexed pattern, I used the same DMA-PLS to illuminate the sample with all wavelength channels except one at a time, and in a Hadamard-multiplexed illumination pattern (Figure 2.6).

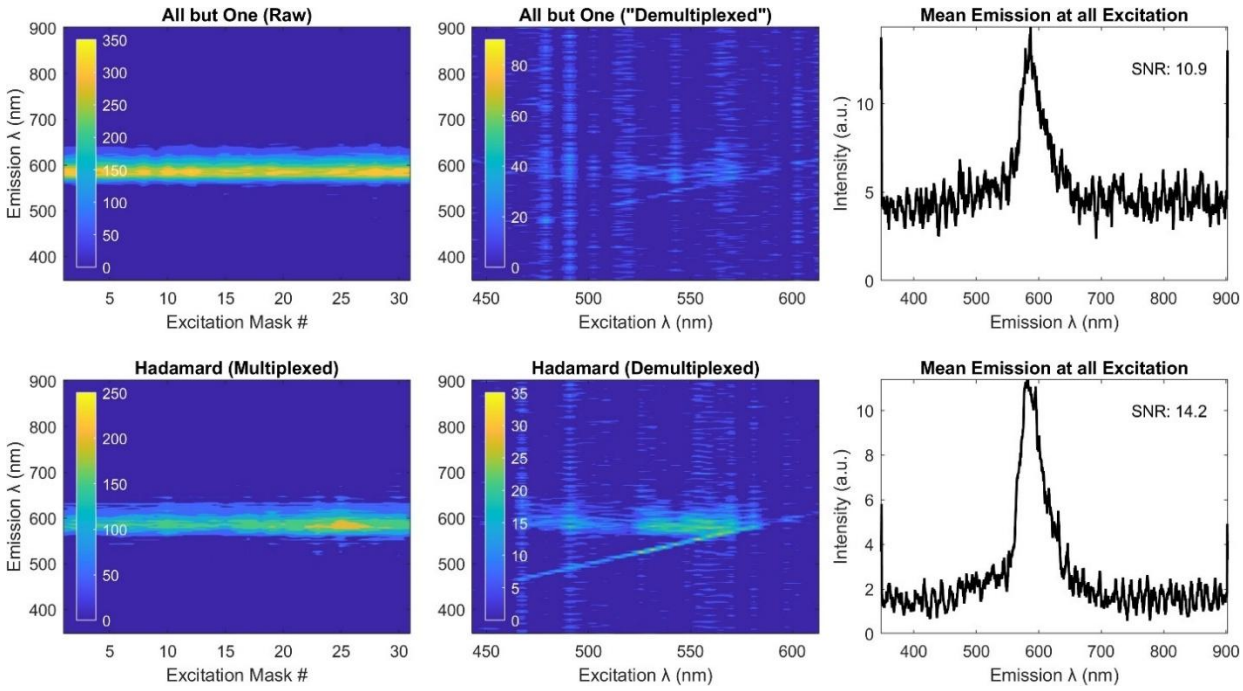

Figure 2.6. Effect on SNR of a Hadamard-multiplexed and sequential illumination. Spectra were acquired using the DMA-based programmable light source which illuminated the sample using either (**top**) all wavelength channels but one, in a sequential pattern or (**bottom**) multiplexed wavelength channels according to a size-31 Paley S-matrix.

Analogous to the lower SNR due to the strong background of an absorbance spectrum in comparison to a fluorescence spectrum, the illumination by all wavelengths but one are expected to return a brighter signal but with worse excitation resolution.

We can see this in Figure 2.6, where the illumination using all the wavelengths except one at a time returned a brighter signal (maximum of 300) compared with the multiplexed illumination (maximum 250). Once the EEMs were demultiplexed, the overall signal-to-noise ratio was calculated as shown in Appendix A.1. We find that the overall SNR is lower for the all-but-one compared with the Hadamard-multiplexed illumination, with SNR values of 10.9 and 14.2, respectively.

Chapter 3 Programmable Light Sources

Two multiplexed programmable light sources (PLS) will be discussed and used in this dissertation; a system based on a digital micromirror array (DMA) and an array of laser diodes. The two sources are useful in different circumstances which are explained in Section 7.1.4. The DMA-based white programmable light source has been previously demonstrated for fluorescence spectroscopy in a variety of modalities [34, 67, 87, 285, 287, 288] and its fundamental functionality has not been changed in this work. I have made improvements to the light throughput of the system by switching from an LED-based white light source [286] to a laser-driven plasma light source by modifying the coupling modalities. I have then integrated the source into several new applications. I developed the second system, the laser diode array, initially to be used in a multiplexed Raman spectroscopy setup, briefly described in Section 9.4, but then applied it to fluorescence microscopy as a bright, fiber-coupled light source. Although the wavelength range is perhaps more suited to Raman spectroscopy, the brightness and spectral coverage of the lasers were found to be useful in fluorescence imaging, especially when using detectors with lower sensitivity, dilute solutions, or weak fluorophores.

This chapter will describe the optical setups and characterization of two programmable Hadamard-multiplexed excitation light sources—the DMA-PLS and the LDA-PLS. The general fundamental concepts used to select optics for these light two systems are discussed in Section 3.1. Improvements to the light throughput of the DMA-PLS as well as characterization of that source and methods for coupling the light various waveguides are discussed Section 3.2. Section 3.3 describes the optics involved with fiber-coupling the laser diodes, a brief characterization of them, and the electronics and software involved in laser control via a laser driver board and Arduino.

3.1 General Optical Considerations

In this section, I discuss the optical considerations for optimizing and developing the two light sources and the coupling of that light to deliver it to a sample. The lenses and optics are first discussed, and tables are provided for quicker reference to specific optic components used in our setups. Next, a discussion of fiber-coupling both individual laser and white-light sources along with a demonstration of fiber bundling methods used for the sources in this work is shown. Finally, liquid-core waveguides are briefly discussed.

3.1.1 Lens Selection

It is beyond the scope of this work to provide an in-depth tutorial on optical element properties however this section will provide a brief overview of some elements that were considered in the design for the optical setups developed in this work. I hope this will serve as a useful basic reminder why particular options were chosen, and what changes might be useful to make for future iterations.

Optical elements should be chosen for the specific optical considerations of the system. Mirrors work very well over a wide wavelength range without causing chromatic or spherical aberrations [289], though they can take up more space in an optical setup than lenses. Spherical aberrations, caused by the differing interactions of the outer and inner parts of a spherical lens, can be corrected for using aspheric lenses or combinations of spherical lenses, or apertures can be used to restrict the outer regions from interacting with the lens and preventing the aberrations from occurring [230]. Chromatic aberrations are a result of the differing focal points for each wavelength, caused by the differing angles of refraction due to the wavelength dependence of the refractive index [230], and are present in optical systems covering a range of wavelengths such as the programmable light sources used in these experiments. These can be corrected or mitigated using achromatic lenses composed of a combination of low-index and high-index glasses and can be created with an aspheric surface to improve spherical aberration correction. When light is highly multichromatic, such as the DMA system with a wavelength range of ~180 nm in the visible region, an achromatic lens is useful for reducing both chromatic and spherical aberrations.

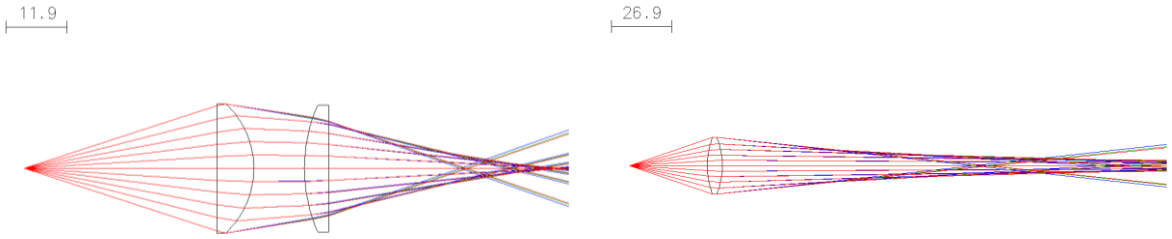

Figure 3.1. Optical simulations of two focal lengths and their effect on spot size. This is a demonstration using the laser driven plasma source with two different focal lengths (**left**) short focal length creating small spot size and (**right**) long focal length creating a larger spot size.

Longer focal length lenses will converge to a larger spot size [230] as shown in Figure 3.1. For the DMA system in which light must not be in focused on the fiber front faces for optimal coupling (Section 3.2.4), a longer focal length lens reduces the impact of the differing focal length from the

wide wavelength range, so long as the numerical aperture (NA) is still well-matched to the fibers. The fibers used in this work are multimodal and have NA = 0.22 or NA = 0.39. To calculate the focal length of a lens, the curvature radii R of the two surfaces, the index of refraction n, and lens diameter d are used in the following equation:

$$\frac{1}{f} = (n-1)\left(\frac{1}{R_1} + \frac{1}{R_2}\right) - \frac{(n-1)^2 d}{nR_1R_2} \qquad [3.1]$$

For thin lenses, only the first term of the sum need be considered. The second term is applicable for a thick lens with a large curvature R. This formula uses the paraxial approximation which assumes light does not diverge significantly from an axis through the system. When the NA of a lens is known, the focal length f of a lens is given by [3.2].

$$f = \frac{r}{\tan(\theta/2)} \qquad [3.2]$$

Where r is the radius of the beam waist and θ is the full-cone angle of the light from a lens with a known numerical aperture, where:

$$NA = n\sin\theta \qquad [3.3]$$

These equations are used to calculate the NA or focal lengths required by the system for collimating and/or focusing light at points throughout the systems.

3.1.2 Fiber Coupling Light Sources

Fiber-coupled illumination offers some experimental flexibility—for example, moving the output to different locations, immersing the probe in solution, operating in harsh environments, conserving bench space, and running different experiments without repeated optical realignment. However, factors such as the size and geometry of both the source and the output, the system etendue, and the wavelength range and intensities of the light source must be considered.

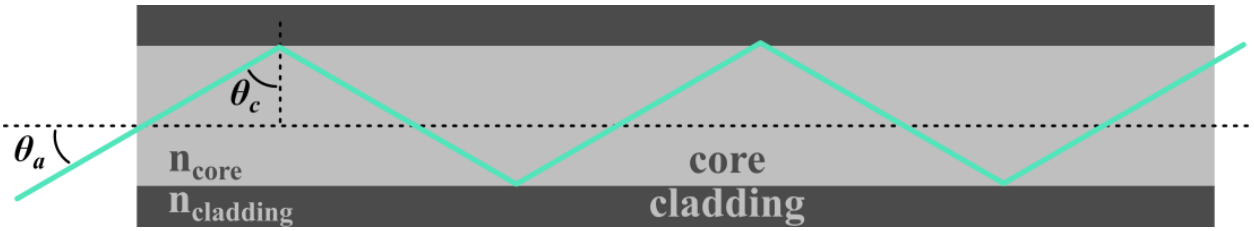

Figure 3.2. Ray propagation in a fiber optic cable.

Coupling Light into a Fiber.

Light which is incident at an angle within the acceptance cone of a fiber-optic cable will be propagated via TIR. The maximum acceptance angle θ_a (the half-angle of the acceptance cone) can be calculated using the NA of the fiber NA_{fiber} as determined by the refractive indices of the core and cladding:

$$NA_{fiber} = \sqrt{n_{core}^2 - n_{cladding}^2} \quad [3.4]$$

The NA_{fiber} is used to calculate the maximum acceptance angle θ_a of that fiber:

$$\theta_a = \sin^{-1}\left(NA_{fiber} / n_0\right) \quad [3.5]$$

This is related to the critical angle θ_c below which TIR will occur, based on Snell's laws, where:

$$\theta_c = \sin^{-1}\left(n_{cladding} / n_{core}\right) \quad [3.6]$$

Larger acceptance angles—a larger ratio of the refractive indices of core and cladding—allow both for more angles of light to propagate through a fiber and cause a larger divergence of that light at the exit of the fiber. Note that although θ_a can be calculated for a given fiber, when a fiber is "underfilled" or light does not populate the entire acceptance cone, the divergence of light exiting the fiber will also be less than the θ_a value [289] which will impact *e.g.,* collimation optics for the fiber output, and should be taken into account when designing a system.

If an emitter is a point source—or can be approximated as one—coupling the emitter's light into a single fiber can be accomplished simply using lenses, as is done for fiber-coupling the laser diode system in Section 3.3.2. When the emitter is not a point source, as in the DMA-PLS, coupling into a single fiber is not possible. Although a large-core fiber, such as a 1 mm diameter core, has a large area into which light can be focused, fibers of this size are rigid—lacking both the literal and metaphorical flexibility of fiber-coupling. Instead, we arrange an array of fibers into a bundle, as has been previously shown [87].

Fiber Bundles

The design of a fiber bundle receiving light from an emitter (or even from a sample) should first consider the ratio of the cross-sectional area attributed to the fiber cores to the cross section of the entire fiber bundle. In an ideal case of fibers having an infinitely small cladding cross section ("no-core fibers"), that ratio is given by the total area of hexagonally packed circles $A = \left(3\pi / 4\right)d^2$ and

the area of the total fiber bundle and is approximately 91%. Using the more realistic case of a step-index fiber with 440 μm cladding and 400 μm core diameters, this acceptance ratio is lowered by another factor corresponding to the ratio of these two areas $A_{core} / A_{total} = (400\mu m / 440\mu m)^2 = 82\%$. Multiplying these ratios yields 75% for the maximum coupling efficiency achievable in this case of an infinitely extended fiber bundle.

Compared to single, large-core waveguides, fiber bundles have greater coupling losses due to the geometries of circle-packing, cladding and/or buffer area, and differences in filling of the fibers depending on the radial position within the bundle. The primary disadvantage to using fiber bundles—aside from any experimental difficulty in coupling—is in the light loss inherent in the space between the fibers as described above.

In one of our fiber bundles, a 12 × 2 arrangement of 400/440 μm fibers (core/cladding), the area occupied by the fibers is $A = L \times W$ or 5.28 mm, while the area occupied by the fiber cores is 3.02 mm^2 as defined by the area of a circle $A_{circle} = \pi r^2$, or just 65% of the total area. Then, at best, we lose 35% of the light with an otherwise ideal optical setup. We note that one can purchase fused-end bundles which minimize the distance between fibers to minimize loss, however making these requires industry know-how and likely quite a bit of process optimization. These do represent a good commercial option for a lower-loss fiber-coupling solution.

3.2 Programmable White Light Source

To multiplex our excitation light source, our group required a method of selecting numerous wavelength bands of light at once, unlike a traditional scanning monochromator. This led to the invention of a technique to simultaneously select multiple wavelength bands from a white light source spectrally dispersed on a digital micromirror array (DMA)[87]. Applications of this system and the work done by previous group members has included chemometric monitoring of chlorophyll demetallation [34] and to separate co-eluting fluorophores in a modified high-performance liquid chromatography system [32], and spatial monitoring of two fluorophores through a heat degradation [219]. These experiments have shown a 500-fold decrease in acquisition time over commercial instruments, from over 30 minutes to collect an F-EEM on a Varian Eclipse to a few seconds on a system built by the group using this DMA-based light source [34].

This section will describe how the DMA programmable light source (DMA-PLS) selects wavelength bands from a white light source and the optimizations and modifications made to the system for increased light throughput and integration for microscopy illumination. The optics used to deliver light to the DMA for wavelength selection and for guiding that light to a sample to be used for excitation are described. Lastly, I will discuss the software controlling the DMA-PLS.

3.2.1 Digital Micromirror Array

The DMA-based system for wavelength band selection and multiplexing selects wavelengths spatially from a spectrally dispersed white light source. A reflective diffraction grating separates a white light source which is then projected onto a DMA consisting of 1024 × 768 micromirrors (10 × 10) μm of which columns are selectively tilted to a position of ±12°. Positive (+12°) and negative (–12°) tilts correspond to "on" and "off", respectively. The positively tilted mirrors direct light to be focused into a light guide.

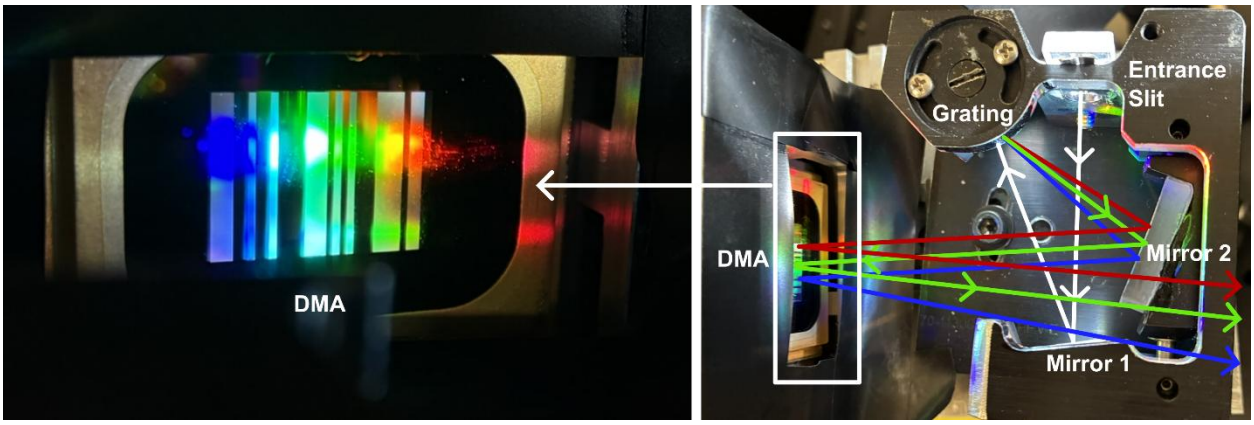

Figure 3.3. Photo of digital micromirror array (DMA)-based light source. (**left**) DMA with a dispersed white light spectrum, mirrors are directed to ±12° based on the first mask in an n = 31 S-matrix, (**right**) setup for dispersion of white light onto DMA.

Figure 3.3 (left) shows a single multiplexed mask on the DMA and a graphic depicting the ones and zeros sent to the DMA to flip each mirror to on or off positions. We use this method to multiplex our excitation light for fluorescence spectroscopy in a technique we describe as Hadamard-Transform Excitation Emission Matrix (HT-EEM) Spectroscopy.

The system (Figure 3.3)—built from a repurposed miniature Czerny-Turner-style array spectrometer—provides a useable wavelength range of ~180 nm. This range can be shifted by manually translating the DMA, however the DMA coating prevents the practical use of wavelengths below ~430 nm, where the coating rejects a large portion of the light. If a portion of the spectrum has a much lower intensity than others, excitation correction can distort the observed

EEM in that region. This occurs when a weak signal, such as that from a faint fluorophore, is overcorrected when divided by a very small intensity value relative to other spectral regions.

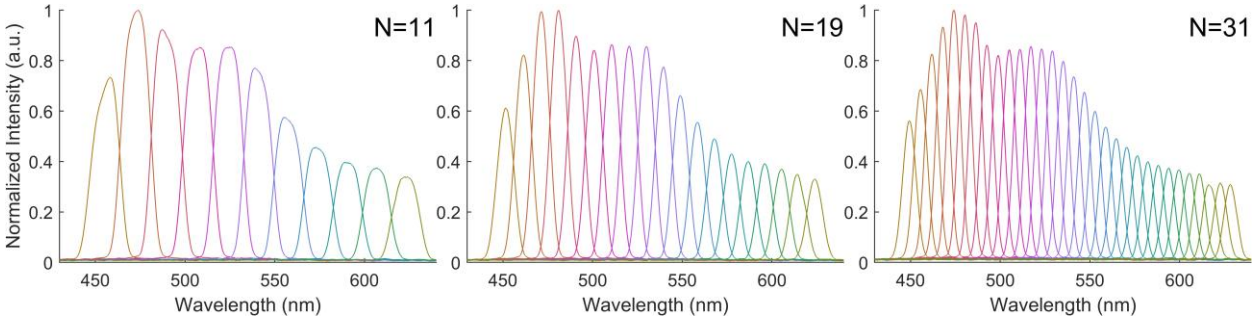

Figure 3.4. Wavelength bands using different size Hadamard matrices. The digital micromirror array uses different sized Hadamard masks (N = 11,19,31) to select wavelength bands for illuminating a sample.

Masks are created by dividing the DMA into a specific number of columns, which is set by the size of the Hadamard matrix. Because the wavelength bands are represented by mirror columns on the DMA, the FWHM of the wavelength band depends on the number of mirror columns. With narrower sections (fewer mirror columns), the FWHM is smaller (Figure 3.4). For a mask size of 31, the FWHM is between 4–5 nm, depending on the alignment. We find that 31 is a reasonable size for excitation spectral resolution without requiring too many image acquisitions.

The DMA-PLS is a useful source for F-EEM spectroscopy and imaging; however, the system suffers from many losses which diminish the output of even a very bright white light source. These include coupling losses from the white light source into the spectrometer—numerical aperture mismatches, alignment faults, fiber-coupling of the white light input source when applicable, diffraction grating order selection, reflections at optics interfaces—and those of coupling the multiplexed light into a waveguide to use at a sample as described above. Many of these losses are inherent, such as those arising from the spectral dispersion using a diffraction grating, however others can be reduced. Although the light source was used previously for imaging applications [219], for rapid imaging using the multi- and much less sensitive hyperspectral cameras as detectors through a microscope, we required a brighter light source that is spatially and spectrally more homogenous. We therefore replaced the LEDs with a laser-driven plasma light source.

3.2.2 White Light Laser-Driven Plasma Source

Both the brightness and spectral uniformity are important for F-EEM images, as discussed in Section 3.2.1. To address these requirements, the previous white-light source was replaced with a laser-driven plasma source (LDPS) (Energetiq, EQ-99X), a broadband source which emits

between 170–2500 nm. Dr. Sarah-Johanna Klose, a former post-doctoral researcher in our group, and I integrated the LDPS, which was donated by the group of Dr. Jean-Pierre van Helden at the Leibniz Institute for Plasma Science and Technology, into our system. Earlier DMA system configurations used visible white LEDs as the source, supplemented with a blue LED in the previous iteration, to address the dip in the white phosphor-coated LED [286]. The LEDs were fiber-coupled into a bundle of 100/125 µm multimode fibers which was linear at one end to create an entrance slit for the Czerny-Turner-style spectral dispersion and DMA setup.

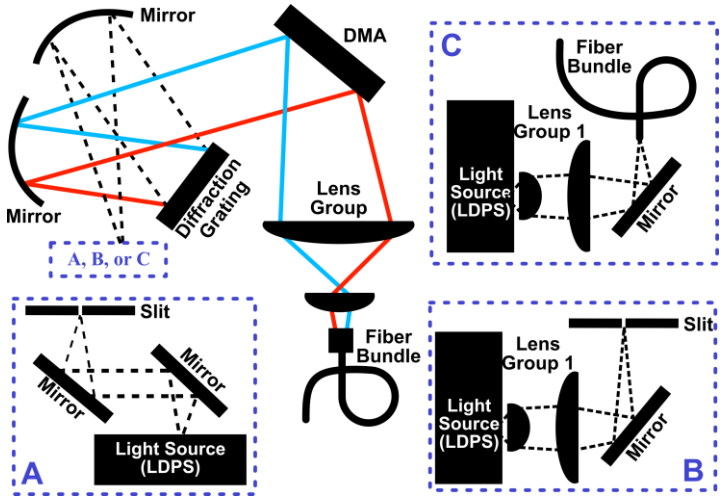

Figure 3.5. Schematic for coupling a white-light source to the DMA system. Configurations shown for free-space coupling into the DMA using a slit using (A) two mirrors, and (B) lenses and a single mirror, and fiber-coupling into the spectrometer using a slit created by a linear fiber bundle using (C) lenses and a mirror. In each setup, a 400 nm long-pass filter is placed at the exit of the quartz window to the LDPS.

For a free-space alignment of the LDPS into the DMA spectral dispersion system (Figure 3.5a), the intensity values were calculated and shown in Appendix A.12. Center wavelengths and FWHM values were measured with a calibrated spectrometer and power in µW/nm was calculated using the FWHM values and the intensities as measured using a photodetector.

Figure 3.6 shows a comparison of a Hadamard-modulated excitation spectrum containing 31 bands for the previous LEDs and newly integrated LDPS as the white-light source in the DMA-PLS.

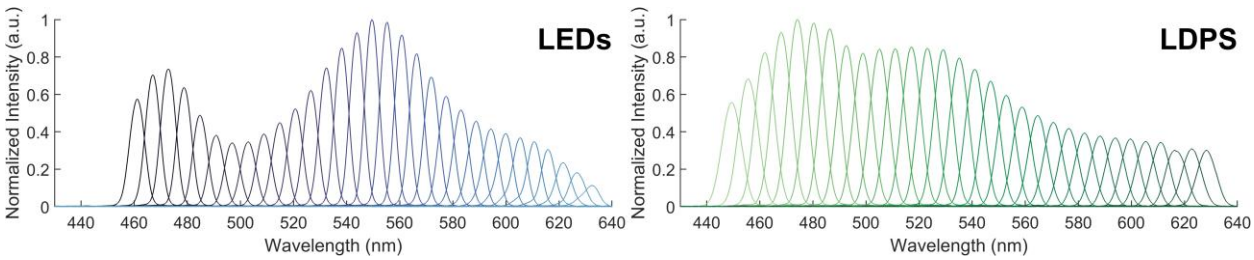

Figure 3.6. Wavelength band spectrum using different white-light input sources. Shown are the 31 wavelength channels from an N=31 Hadamard S-matrix, using white and blue LEDs (**left**) and a laser-driven plasma source (**right**) as the white-light source.

FWHM, Corrector, and Peak Positions

For the most accurate characterization of the FWHM and peak positions of the wavelength bands from the DMA for a given alignment, a 105 μm core SMA patch cord to the fiber-coupled AvaSpec-ULS2048XL-EVO equipped with a 200 μm × 1 mm entrance slit. The light from the DMA is diffused using a diffuser plate or white paper and the fiber is positioned at such a distance to obtain an even sampling of the illuminated area, and this setup is used to collect spectra for an alignment file which is used for excitation intensity corrections.

An alignment file is created for each mask size from 7–127 using a Gaussian fit of each individually-illuminated peak for each mask. Peaks are found using *findpeaks* (MATLAB) with parameters chosen to match the alignment file, such as a minimum peak height above the noise level. The FWHM value is calculated from a Gaussian fit ("GaussFit1" in the *gaussfit* function in MATLAB) of data ±50 spectrometer bands from the peak center. The output of this function is three variables—a, b, c—corresponding to height, peak position, and standard deviation, for the Gaussian fit equation:

$$f(x) = a_1 \exp\left(-\left(\frac{(x - b_1)}{c_1} \right)^2 \right) \quad [3.7]$$

Which differs from a typical gaussian equation where μ is the mean (wavelength, here) and σ is the standard deviation:

$$f(x) = \frac{1}{\sigma\sqrt{2\pi}} \exp\left(-\frac{(x - \mu)^2}{2\sigma^2} \right) \quad [3.8]$$

These two equations then find that the MATLAB fit multiplies a typical σ by $\sqrt{2}$ to give a c_1 value. So, the FWHM of our peaks then is calculated using:

$$FWHM = 2\sqrt{\log(2)} \times c_1 \quad [3.9]$$

Where c_1 is output from the Gaussian fit. This correction was found by Dr. Chris Prüfert, a former post-doctoral researcher in our group. The peak position (wavelength) is then found using the closest spectrometer value to the Gaussian mean, μ or b_1. The relative intensities of each peak are given by the a_1 coefficients normalized for the mask to 1. These are used to correct for excitation intensity differences in EEM spectra.

Coupling the LDPS to the DMA

The LDPS has been coupled to the DMA system both in free space and through fibers. In all versions, a long-pass ultraviolet (UV) filter (FGL400M, Thorlabs) has been placed in front of the source window. This filter attenuates wavelengths below 400 nm to minimize UV exposure to users and to avoid photodamage to the fibers and DMA. The plasma emission is approximately 100 μm with a 56° full angle, and the nearest a lens can be physically placed to that emission is 28.58 mm for a 25.4 mm diameter lens. Consequently, a lens to collimate the highly divergent plasma was difficult to find. Because we could not find a lens with the exact requirements for diameter and focal length, we chose one which would have a focal length and working distance slightly shorter than ideal, so the beams would begin to slightly focus and not defocus, as would be the case with a focal length a bit longer than we could place the lens. Figure 3.7 shows the effect of a lens with a shorter and longer focal length.

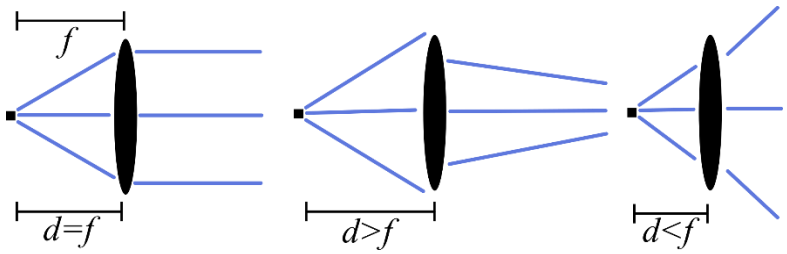

Figure 3.7. Effect of lens distance on a lens with a given focal length.

The LDPS was initially fiber-coupled to the same bundle that had been used for the white and blue LEDs (Figure 3.5b). Although this configuration provided brighter illumination than the previous LED source, the improvement was less substantial than anticipated or required, likely due in large part to the losses from the fiber coupling. Fiber-coupling losses may result from chromatic dispersion, due to the wavelength dependence of focal length causing unequal coupling efficiency across the wavelength spectrum. This was observed during alignment—as the distance between the fiber bundle input face and light source was adjusted, there was an inverse intensity change of the red and blue spectral regions—when one increased, the other decreased.

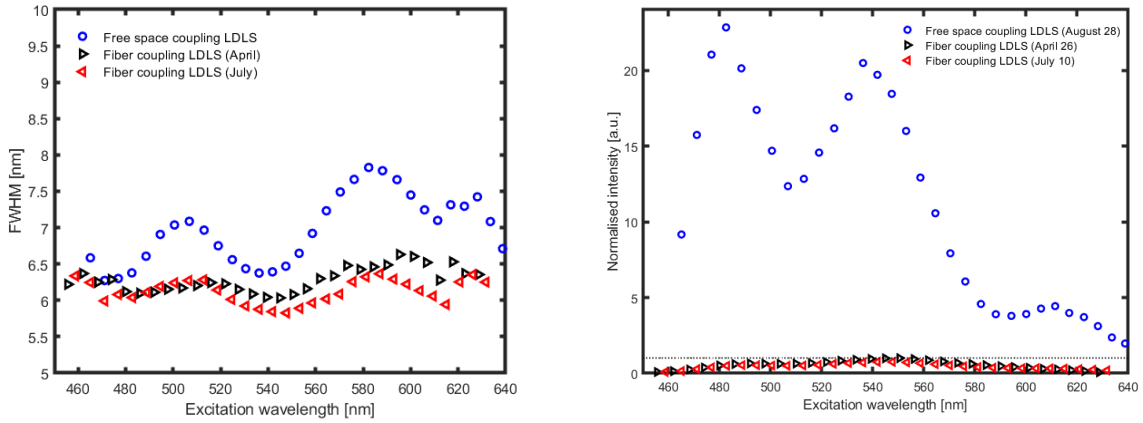

Figure 3.8. Full width at half-maximum (FWHM) and intensities using free-space or fiber-coupled plasma source in the DMA-PLS. The LDPS was coupled to the DMA dispersion setup using a fiber bundle with a linear array of fibers as the slit or coupled in free space using a 100 µm slit, as shown in Figure 3.5 (A and C) The FWHM (**left**) and intensities (**right**) are shown for the different versions. Plot made by Sarah Klose.

To avoid the losses associated with fiber-coupling to improve light throughput, Dr. Klose designed an optical setup to couple the LDPS to the DMA in free space (Figure 3.5a). The difference in FWHM and intensities between this free-space version (Figure 3.5a) and the previous fiber-coupled versions using the LDPS are shown in Figure 3.8.

The same achromatic lens and 400 nm long pass filter were used as described in the previous setup, followed by a 25.4 mm diameter achromatic lens with a focal length of 250 mm (AC254-250-A-ML, Thorlabs) to focus the light toward the entrance of the DMA dispersion setup. At the entrance of the DMA system, a cylindrical lens was used to couple a line of light into the system instead of a single spot, through the 105 µm slit. This design improved the light throughput greatly, as seen in Figure 3.8, however at the cost of a larger FWHM, resulting from the NA mismatch of the cylindrical lens to the collimating (first) lens of the dispersion setup. The increased FWHM caused some strange effects in demultiplexing the Hadamard-acquired EEM spectra, so it was ultimately fiber-coupled once again, using optics which were more optimized than those shown in Figure 3.8.

Current Setup

The current version uses the achromatic lens (f=100 mm) and 400 nm long pass filter described previously, with a 105 µm slit for entrance into the DMA system. Premade slits for this repurposed spectrometer were not commercially available, so I made slits shown in Figure 3.9. The slit is made using the edges of two trimmed surgical blades placed on an open gap drilled into a piece of acrylic

and spaced using a stripped 105 μm fiber. There is an additional through-hole drilled below the gaps which attaches the slit to a threaded hole in the spectrometer housing.

Figure 3.9. Image of slits used for free-space coupling into spectrometer. (left) Dimensions for the acrylic pieces shown on the right, units in millimeters, (right, top) 105 μm slit, (right, bottom) 200 μm slit.

Improvements to Setup

Although this alignment is working for our current purposes, light throughput could be improved in several ways, including free-space coupling (Figure 3.5a) without a cylindrical lens but using an additional lens with an NA matching that of the system (NA = 0.22) before the entrance slit.

3.2.3 Diffraction from a Digital Micromirror Array

We observed a diffraction-like pattern from the DMA while using the LDPS as a white-light source. The apparent diffraction pattern is shown in Figure 3.10 when the DMA is illuminated with a red laser pointer (left) and the spectrally dispersed white-light source (LDPS) (right).

The observation is consistent with previous reports in the literature describing DMAs acting as diffraction gratings [290-292]. Presumably the effect had not been observed by us previously because the LED light sources had much lower intensity than the LDPS. In practice, this effect limits the light that can be collected after specular reflection from the DMA, different diffraction orders are dispersed away from the principal axis and consequently not captured by the system optics. We expect the diffraction to appear more pronounced in the infrared region than the visible region. The main complication for our purposes is the extended spatial pattern of the reflected light which makes coupling the light output from the DMA into a fiber bundle even more difficult.

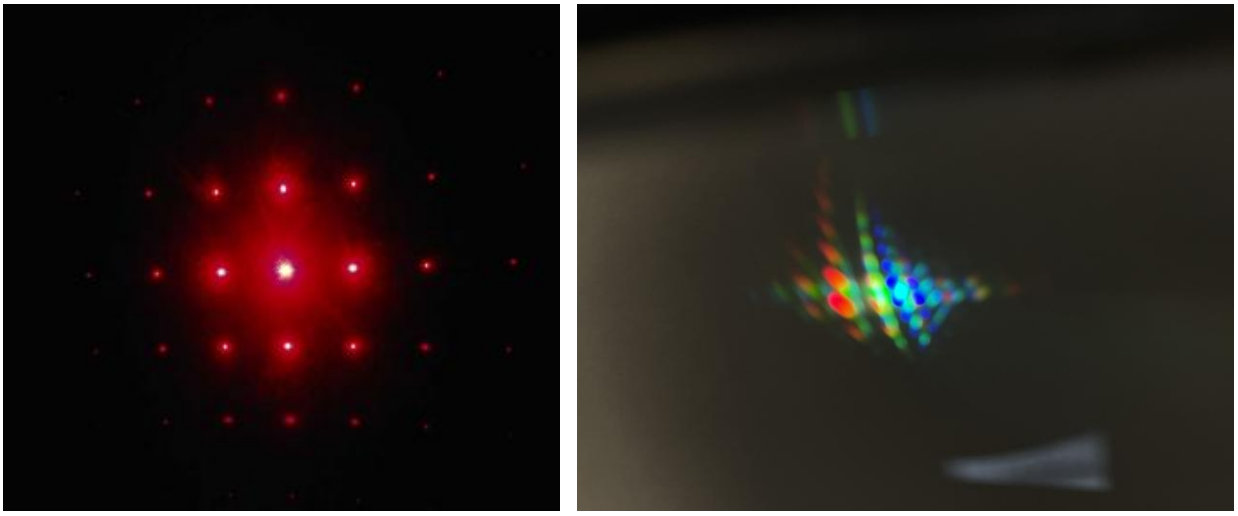

Figure 3.10. Diffraction pattern of digital micromirror array from (**left**) red laser pointer and (**right**) spectrally dispersed white light.

3.2.4 Fiber-Coupling the Programmable White Light Source

To collect the Hadamard-modulated light from the DMA-PLS and guide it to the sample, we have primarily used fiber bundles. Because the shape of the light output from the DMA is rectangular, we make the fiber bundles into a matching shape. It would be more difficult, for example, to force the rectangular-shaped image from the DMA onto a circular array of fibers, as many would not collect light. The off-axis parabolic mirrors and cylindrical lens which have been used by students in the past were replaced with achromatic lenses to reduce the bench space taken up by the coupling optics, with no reduction in coupling efficiency.

The bifurcated fiber bundle probe was made by a previous student [293] and contains 22 fibers to bring light from the DMA to the sample and 15 fibers to collect fluorescence from the sample and guide the light to the spectrometer. The bundle end used for collecting the light from the DMA uses 22 fibers arranged as 2 × 11. The spectrometer side has fibers arranged linearly in front of a spectrometer with a three-dimensional(3D)-printed slit [293]. The fibers are aligned using *xyz*-stages in front of the spectrometer entrance.

It is important when designing new fiber bundles to consider the size of the array detector of the spectrometer. If the CCD array is a linear array of one or a few pixels, then replacing a single fiber with a linear array of the same core size will not necessarily increase the detected light intensity without modifications to the array detector such as a cylindrical lens in front of the CCD array.

Other bundles made for the FrTIR and darkfield microscopy (Sections 7.1.1 and 7.1.2setups , respectively) use 22 fibers in a hexagonal packed 6,5,6,5 arrangement (Figure 3.11) to more closely match the shape of the light from the DMA without requiring an additional cylindrical lens.

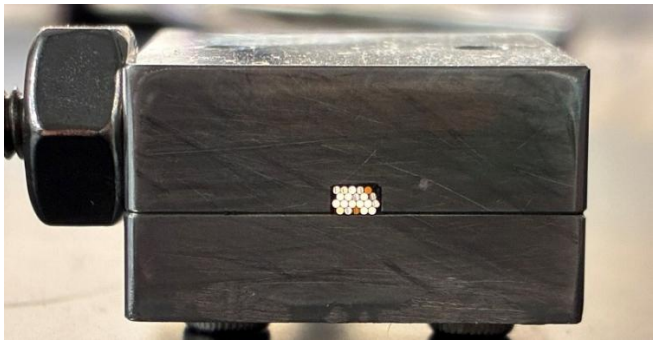

Figure 3.11. Image of front face of a fiber bundle used for microscopy. This is a bundle which was used for FrTIR microscopy with the DMA-PLS and was used for testing a darkfield microscopy set. The other end of each fiber is cleaved.

Note that for coupling the light reflected by the DMA into a fiber bundle, the beam must be slightly defocused at the fiber end face. When the beam is focused at the face of the fibers, some of the wavelengths couple into the fibers very well while others couple in very poorly, leading to a very inconsistent spectrum for Hadamard-modulated light. This is likely explained by the consistent planes from the reflection off the DMA which fill only a few modes in the fibers. Although these select modes are filled and propagate as expected, other modes are not filled, and no light is propagated through them. When defocused, the fibers can instead be overfilled, and more modes populated, however this results in lower intensity across the spectrum. To do this in a way that is intentionally designed, instead of "misaligning" the system, adding an element that scrambles the structured light should help in coupling the light more effectively into the fibers.

This was attempted using a hexagonal light rod, which should homogenize a non-uniform beam. Lenses were used to focus the beam onto the face of the light rod and to collimate then focus the light into the fiber bundle. Unfortunately, this resulted in only small differences in the light output and FWHM compared to the same system without the light rod. I suspect the reason for this is that a longer rod would be required, as the one used to test this was 25 mm long and 4 mm in diameter (HMR425-A, Thorlabs). Using a longer hexagonal light rod could be attempted for improvement to the system. Additionally, it would be interesting to use this light rod to homogenize the output light from the liquid-core waveguide described next.

Other methods to scramble the light before it reaches the fibers could also improve the coupling and could be a good place for future students to increase the light throughput. These components

could include a microlens array, a holographic diffuser engineered to scatter at 20°, a longer light pipe (hexagonal or glass rod), or an array of small polymer fibers, especially with fused ends.

The simplest method to increase light available light to the DMA would be to "butt-couple" [294] bright LEDs each to their own fiber and use a linear arrangement of those fibers as the entrance to the DMA system. Although this method would likely result in greater total light in the system and less variability between the spectral output of different fibers—as for the fiber-coupled LDPS version—it would be very inefficient for usage of space and power. Additionally, the spectral intensity distribution would not be as uniform as for the LDPS that we are currently using. Other possible methods include using a larger slit at the entrance of the DMA dispersion setup at the cost of an increased FWHM of the wavelength bands.

3.2.5 Liquid-Core Waveguides

In place of a fiber bundle or a stiff large-core glass fiber, other waveguide options exist. Any material which has a refractive index higher than that of the surrounding medium and is transparent to the light frequencies of interest can guide light. The incidence angles which satisfy this condition will differ depending on the materials, as will the effectiveness of the light guiding. Material properties such as transparency, inclusions, refractive indices, and imperfections such as air bubbles or scratches, will all greatly affect the ability of the material to guide light. Although hydrogels are useful in demonstrating light guiding, they have significant absorption of the light, resulting in low transmission.

Light is guided within a liquid-core waveguide (LCW) or liquid light guide (LLG) in the same way it is guided within a fiber optic cable—a material with a higher refractive index is surrounded by a material with a lower refractive index and any light rays with an angle below the critical angle undergo total internal reflection in the inner material. LCWs use a liquid material as the "core", surrounded by a transparent tube with an appropriate refractive index, and often a light-tight coating such as a metal tube.

Dr. Klose attempted to create an LCW for coupling the rectangular output of the light from the DMA-PLS to the rectangular input required for FrTIR illumination with a microscope slide (Section 7.1.1). Initially, Dr. Klose and I investigated a polymeric material such as PDMS—a hydrogel which could provide a flexible cable created in the shape of a mold—a rectangular "tube".

Polydimethylsiloxane (PDMS) is used for waveguiding in chips for electronics, especially in applications where the distance required is short (a few centimeters) [295]. It is quite effective for these purposes, as it is flexible and easy to both fabricate and to couple light into. Additionally, the refractive index can be changed by altering the ratios of base and curing agents, as well as curing temperatures [296] which is interesting for an all-PDMS waveguide with more tunable properties than using PDMS or another similar material in air. Analogous to glass fiber manufacturing, dopants can also be added to PDMS to alter the refractive index [295, 297]. Methods have been created to fabricate such waveguide such as [296-299]. Unfortunately, the transmission is not high enough that it is feasible to use over a meter or longer, as for our purposes. Amouzou *et al.* suggested a 0.37 dB/cm transmission for their PDMS/PDMS waveguide [297], corresponding to a loss of about 99.98% over the distance of one meter.

Because the transmission losses were also too great for any of the hydrogels we found, the construction of a true liquid-core waveguide was attempted. An added difficulty for a version which uses a tube was forcing that tube into an ellipsoidal shape, as required for a system without a loss of etendue. In a typical glass fiber, the refractive index of the core is close to that of the cladding to minimize losses at the exit interface. An attempt to find materials with similar refractive indices resulted in a glycerol core and Teflon tubing "cladding", with refractive indices 1.38 and 1.47, respectively.

Critical angles $\theta_c = \sin^{-1}(n_2 / n_1)$ and acceptance angles $\theta_{\max} = \sin^{-1}\sqrt{n_2^2 - n_1^2}$ are shown in Table 3.1 for different combinations of core and cladding materials.

Table 3.1. Effect of core and cladding materials with varying refractive indices (n) on critical angles (θ_c) and acceptance angles (θ_{max}). FEP = Fluorinated Ethylene Propylene.

Core		**Cladding**			
Material	n	Material	n	$\boldsymbol{\theta_c}$	$\boldsymbol{\theta_{max}}$
Glycerol	1.47	Teflon	1.38	69.8	30.4
Glycerol	1.47	FEP	1.34	65.7	37.2
Glass	1.52	Air	1	41.1	All

The tube (cladding) was filled using a vacuum pump and a section of glass microscope slide was inserted in each end of the tube. An ideal system would have used a rectangular bundle all the way through, however it was difficult to find a tube with a sufficiently thin wall which could be molded into a desired ellipse which also had the required refractive index.

The project was ultimately terminated due to practical construction difficulties including an inability to rid the system of air bubbles, solvent leakage, and other transmission losses. Instead, I created a fiber bundle to send light from the DMA-PLS through the side of the microscope slide, described in Section 3.2.4. In addition, a 5 mm diameter LCW was purchased from Thorlabs (LLG05-4H) and used for the DMA-PLS excitation source and was successfully integrated into a microscopy system (Section 7.1.3).

3.2.6 Alternatives to the Digital Micromirror Array

Because the DMA system has many inherent losses, another way to obtain high-intensity multiplexed light could use an alternative to this setup. Replacing the diffraction grating-based spectral dispersion system with a prism-based one could provide better light throughput, described by Hagen [300], and an alternative to the DMA setup could use a physical Hadamard mask [279, 301-303].

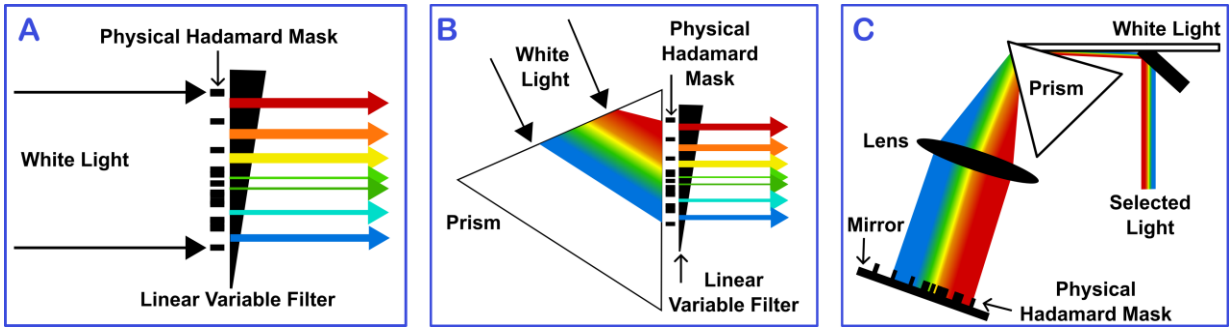

Figure 3.12. Methods for wavelength selection using a physical Hadamard mask. Colours are chosen from a collimated white light by spatial location on a linear variable filter after passing through a Hadamard mask (A) or a prism to first disperse the light, then a Hadamard mask (B). The Hadamard mask allows through only selected wavelength bands depending on a Hadamard matrix described previously. (C) A physical Hadamard mask over a mirror selects wavelength bands from a dispersed white source, the chosen light is directed through a slightly mis-aligned prism to the sample.

Prism, Linear Variable Filter & Physical Hadamard Mask

One example of a prism and physical mask could use a linear variable filter (LVF), which has a range of coating thicknesses, allowing wavelength band to be selected depending on the spatial incidence of the input beam on the filter. Though using an LVF would typically select only one wavelength at a time, using a physical Hadamard mask in front of the filter in place of a single slit, would allow for numerous wavelengths to be chosen at once (Figure 3.12a). This would still lead to poor light throughput as only a fraction of the light at each point on the filter would pass through.

To improve this, a prism could be used to first disperse the light into a spectrum matching that of the linear variable filter, and the mask placed after the prism, instead (Figure 3.12b). This would allow much more of the red light to pass through the part of the filter allowing that part of the light

through. The spatial aspects of this could be difficult as the spatial dispersion of the prism would have to closely match that of the LVF, but it represents an interesting possibility.

Prism & Physical Hadamard Mask

In this setup (Figure 3.12c), wavelengths of light would be chosen from a white light source spectrally dispersed by a prism, using a physical Hadamard pattern above a mirror to either block the light or reflect it back through the system, and then separate the reflected light from the white light using a knife-edge mirror or a slight misalignment. This setup was attempted for just one wavelength, as a proof-of-concept, shown in Figure 3.13. Because the dispersion element is a prism instead of a diffraction grating (as is used in the DMA setup), the light throughput should be higher, and the diffractive effects of the DMA itself will be removed. I am confident there would be problems with this arrangement as well, however I do think there would be possibility for much higher throughput. Additionally, and perhaps more importantly, this technique wouldn't be limited to light above ~430 nm, so it could be used to extend the range or even in the ultraviolet region.

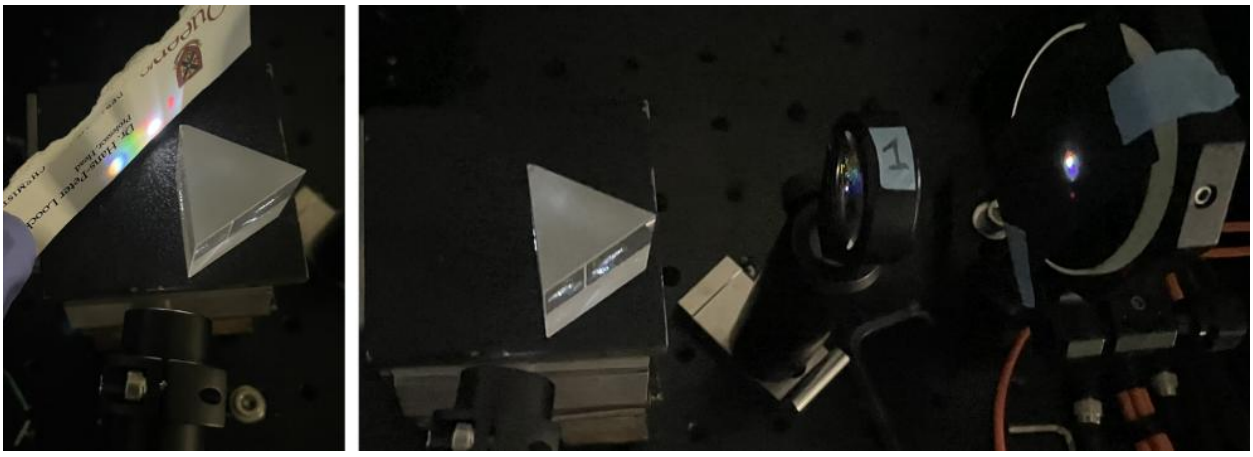

Figure 3.13. Photos of a preliminary test of a prism-based excitation separation. Setup based on Figure 3.12c on the work by [174].

3.3 Programmable Laser Diode Array

The array of laser diodes was created with the initial intent of using them in a Raman setup using Hadamard-multiplexed illumination of the laser wavelengths. The goal was to use surface-enhanced Raman spectroscopy (SERS) at numerous excitation wavelengths to reduce the fluorescence of a sample and use the Raman signal from numerous wavelengths to help with compound identification. The project is interesting and has potential to work, but modifications are required to the setup and are described in Section 9.4.

This section will describe the laser diodes which make up the array and how they are controlled. I will begin briefly with specifics of the LDs, then discuss the optics used and calculations for their fiber-coupling. Next, the method for controlling the power output and current control into the LDs using a custom-built laser driver board and the integration of the LDs into MATLAB for control with our other instruments will be discussed, followed by a summary of their characterization.

3.3.1 Laser Choices

The laser diode array (LDA) is composed of seven laser diodes (LDs) with outputs in the visible wavelength spectrum (405, 450, 488, 505, 515, 620, 660) nm (Table 3.4). LDs are controlled via a custom-built laser driver board that supplies a controllable current and voltage to each LD. The LDs are turned on and off individually through a microcontroller (Arduino Uno R3) commanded through MATLAB. The selected LDs were spaced at least 10 nm apart and have output power between 30–100 mW, and were chosen primarily by availability, as there are a small number of different wavelengths for LDs in this package type (TO-can).

Table 3.2. Properties of laser diodes in array. Resistivity is for DET36A based on the resistivity curve provided by Thorlabs (Appendix A.16). Values are as listed in the specifications sheets provided by the manufacturer, not measured values.

Part Name	Stated Central λ (nm)	Power (mW)	Operating Voltage (V)	Threshold Current (mA)	Operating Current (mA)	Resistivity (A/W)	Pin Code
DL-514S-101S	405	45	5.2	35	70	0.065	B
PL450B	450	100	5.3	20	110	0.113	G
BLD-488-58	488	55	6.1	40	105	0.154	EURO
GLD-505-30	505	30	6.0	70	125	0.170	EURO
L520P50	515	50	7.0	150	160	0.188	A
L638P040	638	40	2.4	92	115	0.319	A
L658P040	658	40	2.2	35	75	0.344	A

The LDs have varying pin connections or pin codes, described in Section 3.3.3, and were purchased from Thorlabs and LaserTack GmBH.

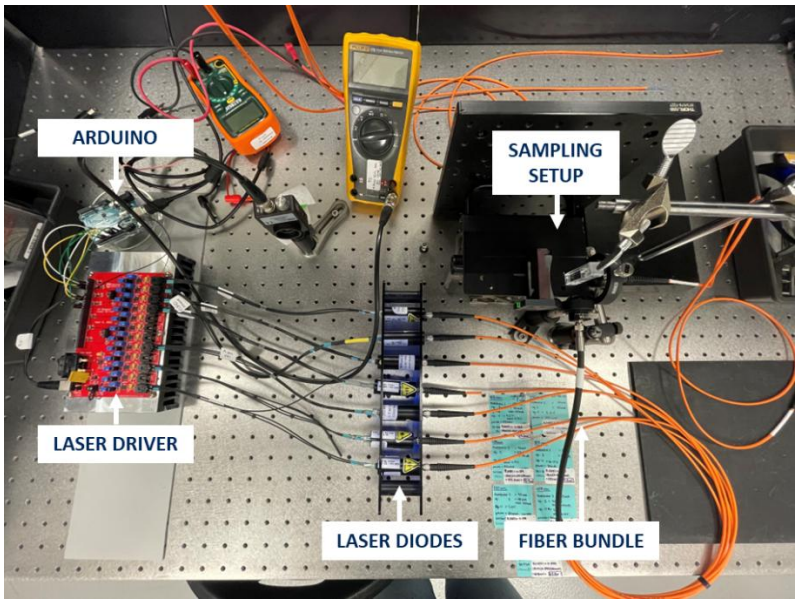

Figure 3.14. Laser diode array instrumentation setup photo.

3.3.2 Fiber-Coupling Laser Diodes

Optics for Fiber-Coupling

Fiber-coupling laser diodes can be done using a "butt-coupling" approach [304, 305], in which a fiber is placed directly in front of the laser diode window, or through optics to collimate and focus the light into a fiber [305-307]. The latter was selected for this work, as the former technique generally has more losses and does not allow for simple replacement of a laser diode. The chapter written by Sun [305] on manipulating laser diode beams was a useful resource in this work.

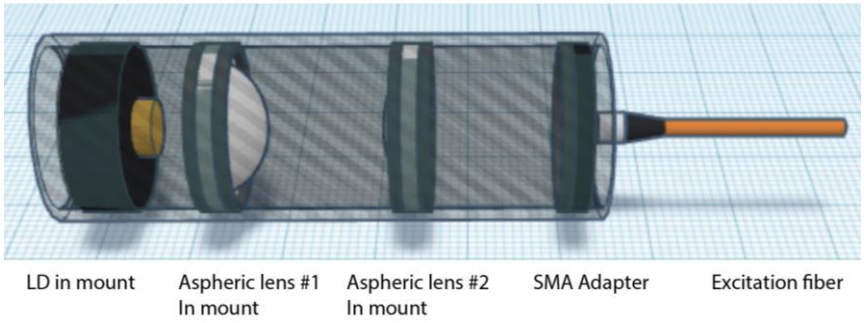

Figure 3.15. Optics used for fiber-coupling laser diodes.

Aspheric lenses were chosen to correct for the ellipsoidal beam shape of a laser diode for optimal coupling into the optical fiber [305]. These were used to collimate and focus the beam emitted from the laser diodes. The first lens was chosen to have a shorter focal length (larger NA) for collimation, while the second was chosen to have a longer focal length (smaller NA) to fall below

that of the fiber (Table 3.3). The LDs are treated as point sources with two divergence angles—$\theta_{\parallel}$ and $\theta_{\perp}$—for the parallel and perpendicular beam axes, also referred to as the slow and fast axes, respectively.

Table 3.3. Beam properties of laser diodes using aspheric lenses for fiber-coupling. Beam divergences (div.) and beam waists for the seven laser diodes are shown for calculations of aspheric lenses used in collimation and focusing the beams for fiber-coupling.

Laser Diode						Chosen Asphere #1			Fiber		Chosen Asphere #2		
Laser λ (nm)	Beam Div. (⊥)	Beam Div. (range)		NA (laser)	Minimum NA for Asphere 1	NA	f (mm)	Beam Diameter (mm)	NA	Cone angle	NA	f (mm)	Cone angle at fiber
405	19°	16°	23°	0.20	0.40			1.8					9.5°
450	23°	18°	25°	0.22	0.43			2.0					10.4°
488	23°	16°	26°	0.22	0.45			2.1					10.8°
488	23°	-	23°	0.20	0.40	0.55	4.51	1.8	0.39	23.0°	0.3	11.0	9.5°
505	23°	-	23°	0.20	0.40			1.8					9.5°
520	22°	16°	25°	0.22	0.43			2.0					10.4°
638	21°	16°	25°	0.22	0.43			2.0					10.4°
658	20°	16°	22°	0.19	0.38			1.8					9.1°

The minimum required NA of the first aspheric lens ("Chosen Asphere #1" in Table 3.3), used to collimate the laser diodes, is calculated as twice the NA of the laser diode output $NA_{1(\min)} = 2NA_{LD}$.

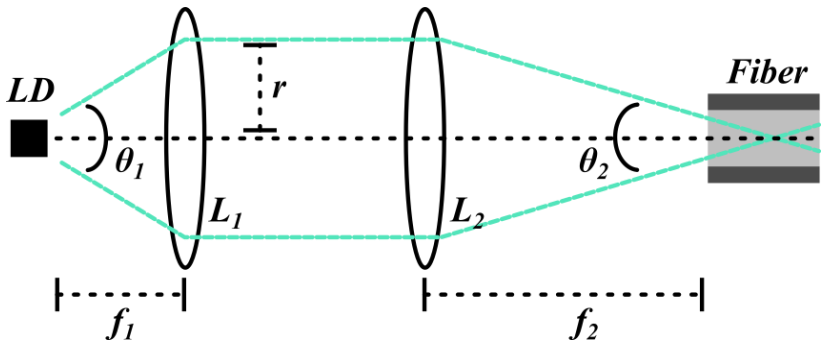

Figure 3.16. Diagram for calculations for fiber coupling a laser diode. Lenses chosen for laser diode array were C230TMD-A (NA 0.55, EFL 4.51 mm) (Thorlabs) for collimation and C220TMD-A (NA 0.25, EFL 11.00 mm) (Thorlabs) for focusing into the fiber.

A lens with a value above this is chosen with a clear aperture (CA) greater than that of the collimated beam diameter *d* where f_1 is the focal length of the first aspherical lens and $\theta_{\parallel}$ is the parallel beam divergence (θ_1)—the larger of the two beam divergences from the LD.

$$d = 2f_1 \tan\left(\theta_{\parallel} / 2\right) \qquad [3.10]$$

The calculated half-cone angle within which light will be accepted into the 400 μm core fiber uses $\theta_{halfcone} = \sin^{-1}(NA_{fiber})$. The second aspherical lens is chosen to have a cone angle less than that of the acceptance angle of the fiber, using twice the half cone angle:

$$\theta_{halfcone} = \tan^{-1}(r / f_2) \quad [3.11]$$

where r is the radius of the collimated beam found in [3.10].

Coupling Efficiency

The lenses listed in the previous section were used along with adapters for the laser diode and SMA connector in aluminum 12.7 mm diameter lens tubes to achieve coupling efficiencies between 80–95%. The coupling efficiency (CE) was determined using a photodetector as shown in Section 3.3.4, for the 520, 638, and 658 nm LDs. Voltage was read from a photodetector (DET36A, Thorlabs) using a multimeter and measurements were taken of the non-fiber-coupled LD and then the output after fiber-coupling with a one-meter long 0.39 NA 400 μm SMA-connectorized patch cable. The coupling efficiency was calculated by dividing the initial by the final intensity values and converting to a percentage.

$$CE = \frac{P_{LD(\text{fiber})}}{P_{LD(\text{fiber})}} \times 100\% \quad [3.12]$$

Fiber Bundles

The seven laser diodes were fiber coupled primarily because using fibers rather than aligning each in free space allows more flexibility in changes to the setup. To reduce the intensity reaching a fiber, a neutral density filter (NDF) could be placed in the beam path, though the SMA adapter would have to removed first, and the system would then require realignment.

The end of the fiber bundle to illuminate samples using the LDA-PLS contains seven fibers arranged hexagonally in a circle in a 1.275 mm SMA ferrule (11275A, Thorlabs). The fibers have 400 μm core diameters and a 0.39 NA and are SMA-connectorized on the LD side as well as the emission side. To use the light from the bundle in free space, optics are added after the exit of the fibers to collimate and focus the light to a spot, and an optional 10% and/or 50% transmission neutral density filter for application requirements or for user safety.

3.3.3 Laser Diode Control

Laser Driver Board

A custom-built laser driver board was built for controlling the current and voltage supply for the LDs and their associated output power. The board and connections to the LDs are described in detail in this section briefly, with reference to a more in-depth description in Appendix A.15.

When the current supplied to an LD is too large, irreparable damage can occur very quickly [308]. Consequently, care must be taken in their handling prevent electrostatic discharge (ESD) such as grounding via a grounded wristband, and the diodes must be supplied with a controlled power supply to avoid current spikes [309].

The UVic Physics & Astronomy Electronics Shop created a custom-made laser driver board (Appendix A.14, Figure 3.18) based on 6-channel laser switches (iC HG laser switches, iC Haus). The board uses two of the iC HG chips, each with six separate output channels with a maximum current supply rating based on the current heat control mechanisms of 400 mA per chip (800 mA total for the board). This could be increased if needed, but additional thermal dissipation would be required. The LDs are dispersed across the chips to ensure the maximum current supply is not exceeded. The chips have small heat sinks attached, and the board is mounted on a large aluminum block with fins cut out, made by the UVic Faculty of Science Machine Shop.

The lasers are triggered to turn on and off by an Arduino Uno R3 board through digital input/output pins. The supply voltage is set to a value approximately 1 V above the voltage required by the laser to allow sufficient voltage. The current that reaches the LD is controlled via a voltage potentiometer. The lasers are attached via click-in connectors (Figure 3.17, right) on the board and a three-pin connector at the laser—one pin for each the cathode, anode, and ground (Figure 3.17, left). Pins for ground or monitor photodiodes, when applicable, were left floating.

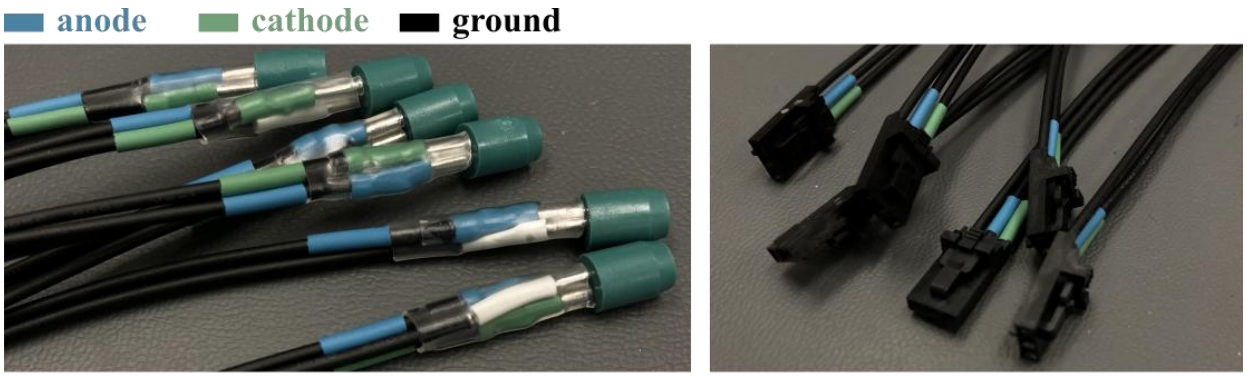

Figure 3.17. Images of cables for connection between laser diodes and driver board.

Note that ground loops can become quite problematic when operating LDs. The control board is placed on a rubber mat to isolate it from the benchtop or floating table. There were some difficulties with the communication with the Arduino as well, so it was placed in a glass petri dish which has isolated it from any ground loops being caused by the setup. Kapton tape could also likely be used in place of the glass dish to electrically isolate the Arduino.

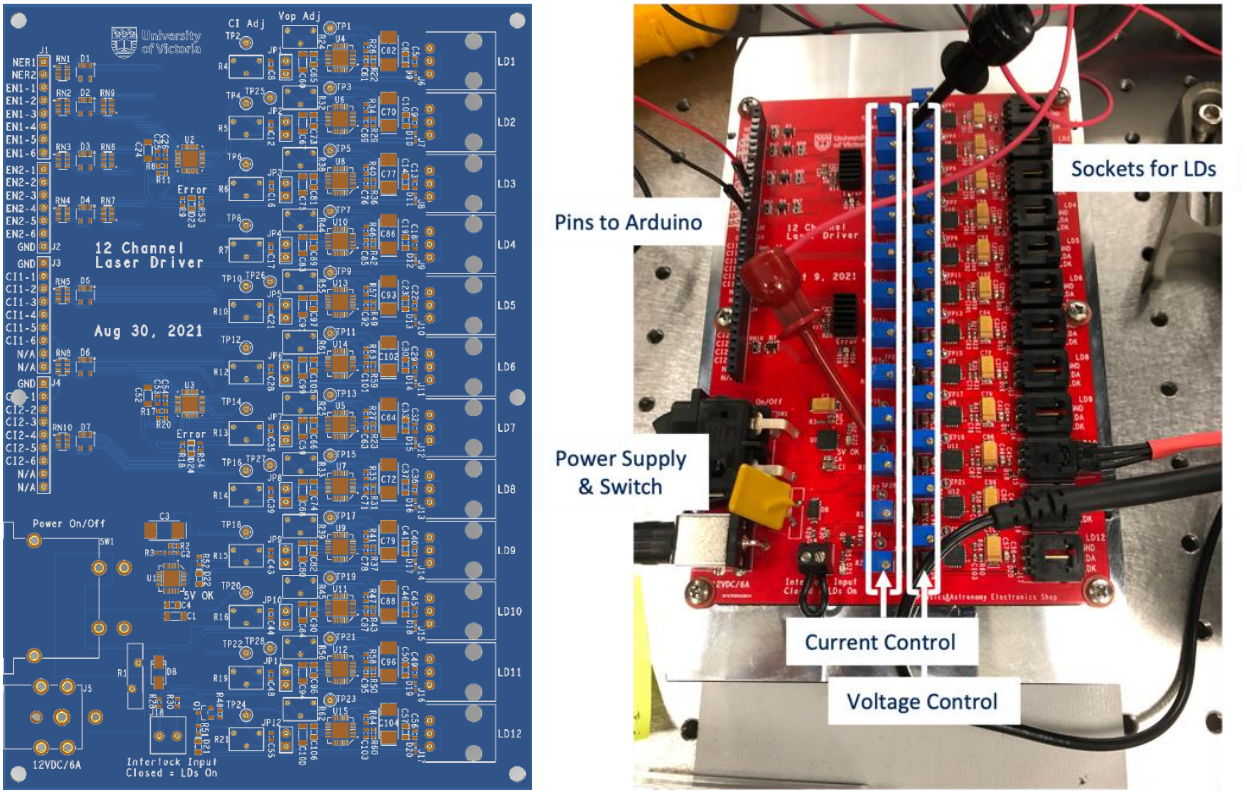

Figure 3.18. 12-channel laser driver board (**left**) and annotated with connections made for testing current and voltages shown (**right**).

Many different configurations of pins (pin codes) and housings (TO-cans: TO18, TO56, TO38) are used for LDs and will be specified by the manufacturer. Factors which determine the pin configuration by the manufacturer might include separation of the ground from the anode or cathode and inclusion of a monitor photodiode. Figure 3.19 shows the three pin arrangements of the LDs in the LDA. By convention, the anode is located on the flat side of the diode, while the diode points toward the cathode. The cable for attachment to the driver board was soldered to pins on a connector which would attach to the LD, to circumvent the need to directly solder the LD pins. The pin code used for each LD are labelled on each cable and it is important they are not interchanged in the setup.

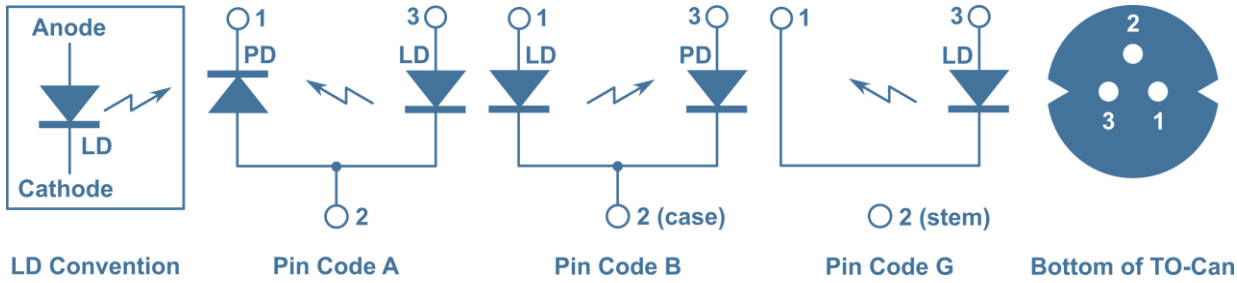

Figure 3.19. Laser diode pin codes used in this work and a bottom view of the pin locations on a TO-can as it might appear in a datasheet. Pins are labelled corresponding to the pin diagrams on the right, which vary for different LDs.

The attachment of these connectors (Figure 3.17) to the LD pins created some lateral space for movement of the connector, which caused the pins to bend when strain was applied from incidental movements. To prevent the pins from bending, a short piece (~5 mm) of plastic tubing was placed around the connector before inserting the LD pins into it. This prevented lateral movement of the connector in the lens tube.

The LDs in the connectors should be tested with a very low current and voltage applied through the driver board to ensure the pins are first correct to avoid "frying" the diode. The 488 nm LD specified a "EURO" pin code (pins 1 and 3 of G type are reversed), however when connected in this orientation, the diode did not work connected as suggested. When pins 1 and 3 were switched—G type pin out—it operated within expected current, voltage, and power output.

Setting Laser Current

Lasers are connected to the board at connectors J6–J17 using connectors which have an anode, cathode, and ground terminal. The connectors J6–J17 are connected as well to an Arduino Uno board which is used to send on and off triggers to the channels.

The amount of current supplied to each LD is set via an on-board potentiometer which can be adjusted using a flathead screwdriver. The values can be measured using a multimeter in parallel, as described in Appendix A.15, and the current reaching the laser diode can be measured using a multimeter in series as described in A.16 and the output power of the laser diode at a set voltage and current can be monitored using a photodetector as described in Section 3.3.4 and Appendix A.16. The output power was measured over a range of input voltages and currents to determine the correct voltage and current reading on the board for a given output power, an example is shown in Figure 3.21.

Software for Laser Control

To control the on/off state of the LDs via the Arduino board, 5 V / 0 V is sent through to the digital I/O pin for that LD. A program was created to do this in the C++ Arduino programming language (Appendix A.2), so that the lasers could be addressed through MATLAB as all our instrument control is through MATLAB. The MATLAB Support Package for Arduino Hardware is used to facilitate the connection between the Arduino and MATLAB. Commands were created to address individual lasers and combinations thereof, which can be called through MATLAB using the command *writeline*. Lasers are addressed individually with the phrases l1, l2, l3, l4, l5, l6, and l7 which correspond to the (405, 450, 488, 505, 515, 638, 658) nm LDs in specified channels on the driver board. For combinations of lasers, m1, …, m7 refer to the seven masks of an $N = 7$ size Hadamard Paley S-Matrix (Section 2.1.2), "all" turns all lasers on, and "off" turns all lasers off.

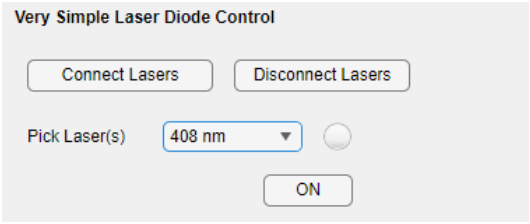

Figure 3.20. Simple MATLAB control to turn on individual or combinations of laser diodes.

A very simple control graphical user interface (GUI) was created in MATLAB to turns on lasers or combinations by selecting an option from a dropdown (Figure 3.20). To control the lasers in an app for the multispectral camera, a separate GUI was created, shown in Section 4.1.1.

3.3.4 Laser Diode Characterization

The laser power output as a function of current and voltage was obtained so that not all parameters needed to be measured each time the power needed to be adjusted. I measured the current being supplied to the LDs and their corresponding power, over a range of voltages (V_{op}).

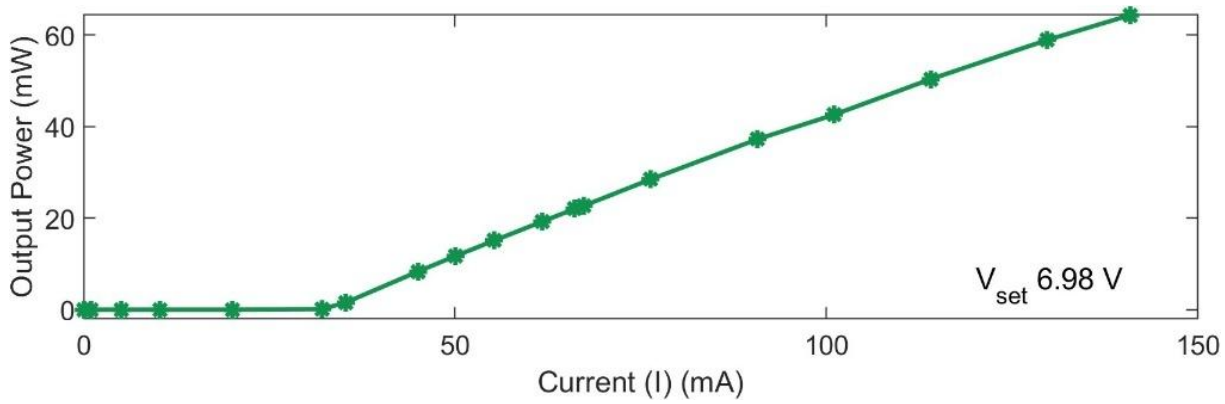

Figure 3.21. Current-power (IV) curve for a 488 nm laser diode. Power measured using a photodetector at various set currents on the driver board, as determined using a multimeter connected in series.

Power output was monitored for various current settings to characterize the LDs as shown in Figure 3.21, where a voltage setting corresponds to a current setting to give a power output. This is used to see the response of the driver board adjustment of current to laser power output. The LD power was measured using the voltage as read from a photodetector (DET36A, Thorlabs) by a multimeter with a 50 Ω terminating resistor and coaxial cable.

The measured voltage V_{out} is a product of the load resistance R_{load} of 50 Ω and the generated photocurrent, and is the output measured by the multimeter in volts.

$$V_{out} = I_{out} \times R_{load} \qquad [3.13]$$

The power can be calculated for a laser at a particular wavelength using the resistivity of the photodiode at that wavelength R_λ in A/W given by the resistivity curve (Appendix A.16), represented by:

$$R_\lambda = \frac{I_{PD}}{P} \qquad [3.14]$$

where I_{PD} is the ratio of generated photocurrent to incident light power at a given wavelength. The output power is calculated using the resistivity, output voltage, and the load resistance:

$$P_{LD} = \frac{V_{out}}{R_{load} \times R_\lambda} \qquad [3.15]$$

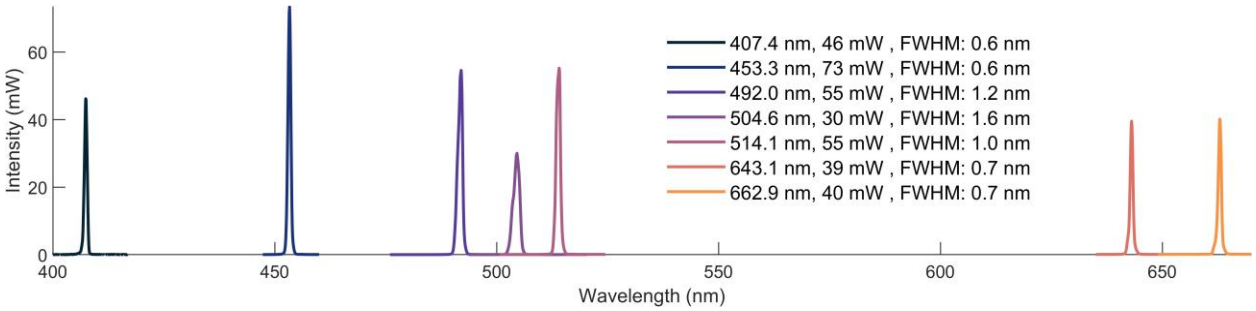

Figure 3.22. Peak characteristics of laser diodes. Spectra taken using a calibrated spectrometer. Full width at half maximum (FWHM) values were calculated using Equation [3.16].

Note that we included a 10% transmission NDF (NE510A, Thorlabs) threaded onto the PD (DET36A) to prevent oversaturation of the detector. The output powers have been adjusted to match as closely as possible to one another, while remaining above the lasing threshold and below the 80% recommended threshold to extend LD lifespan.

The peaks were measured using a calibrated spectrometer (Figure 3.22) and the FWHM of the laser diodes were calculated by the difference between the two wavelength values of half the maximum peak intensity, shown below:

$$FWHM = \lambda_2 - \lambda_1 \qquad [3.16]$$

The measured properties for each LD are shown in Table 3.4.

Table 3.4. Measured properties of the seven laser diodes. Central wavelengths were found using a calibrated spectrometer and full-width at half maximum (FWHM) is calculated as described in [3.16]. Power was found using a photodetector as in [3.15].

Part	Central λ (nm)	Power (mW)	FWHM (nm)
DL-514S-101S	407	46.2	0.61
BLD-450-100	453	73.3	0.6
BLD-488-58	492	54.5	1.2
GLD-505-30	505	30.0	1.62
L520P50	514	55.2	1.02
L638P040	643	39.5	0.67
L658P040	663	40.1	0.75

Using the high-resolution calibrated spectrometer, we were also able to discern the different modes of the laser diodes. The broadening of the peaks by the various modes illuminated at different times demonstrates the need for either cooling the laser diodes or for feedback control (mode locking) to achieve a smaller FWHM value, if the LDs are to be used for a Raman-type experiment.

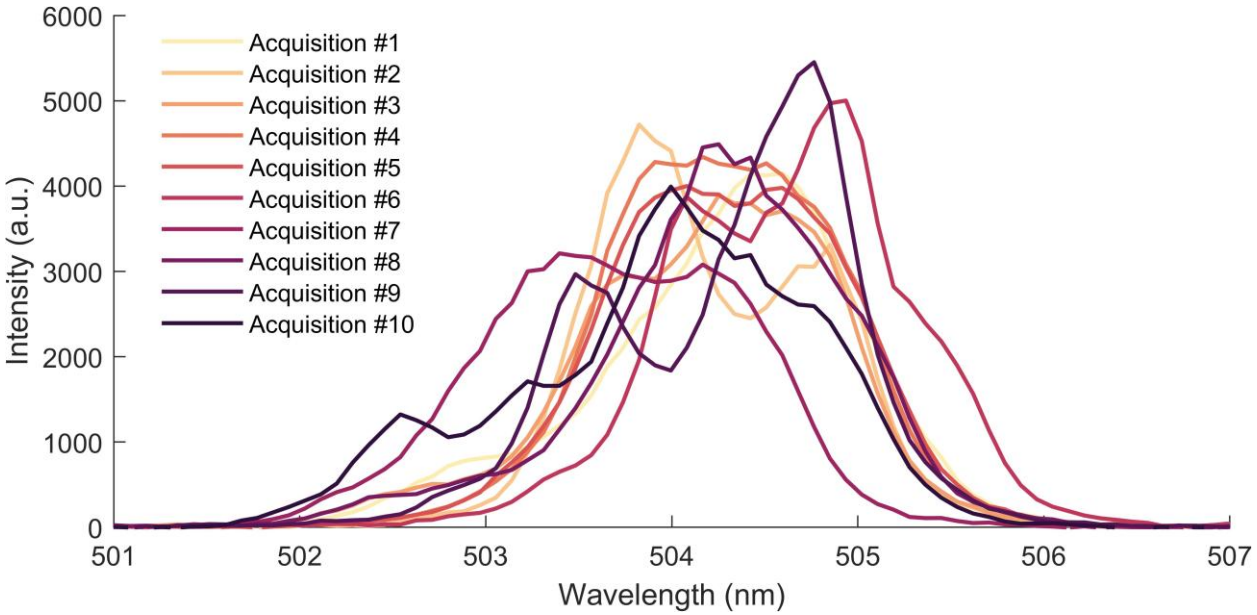

Figure 3.23. Mode hopping of a 505 nm laser diode. Lines represent sequential acquisitions using a calibrated spectrometer, with an integration time of 1 ms with 10 averages.

Figure 3.23 demonstrates that the isolation of a particular mode would be useful to achieve a reliable Raman signal. Muller [310] describes creating an external distributed feedback laser using an etalon and prism to isolate and amplify a single mode of the LD, thus decreasing the linewidth of the LD. The authors find that for an off-the-shelf blue laser diode with 3 W output power with selection along the fast axis, the feedback was stable until a temperature change of numerous degree Celsius was observed. This would suggest that for our uses, some temperature stabilization would be advantageous when running the LDs for numerous minutes, however complete temperature control or cooling wouldn't seem to be required. This is also briefly discussed in Section 9.4.3.

Chapter 4 Multispectral and Hyperspectral Cameras

To determine what colour a fluorescent sample emits, a common camera imaging chip could be used. Commercial colour cameras contain a Bayer RGGB colour filter array (CFA) on the imaging sensor, composed of four-pixel groups, each with one red, two green, and one blue colour filter (Figure 1.18). Colour imaging would allow us to distinguish a red fluorophore quite easily from a yellow fluorophore and from a green fluorophore. This distinction fails when multiple overlapping fluorophores are present, creating wavelength combinations that are indistinguishable for an RGB CFA, as discussed in the introduction (Section 1.2.1).

Alternatively, the number of spectral channels can be increased to more reliably increase the number of distinct dyes that can be reasonably quantified. The number of emission channels can be increased by using a multispectral or hyperspectral camera, and the number of excitation channels can be increased using a light source capable of providing distinct wavelength bands. This chapter will describe the two cameras used to capture F-EEM images for fluorescence microscopy. Each of the two cameras use a different method of determining the spectrum. In this chapter these two methods and their integration into our Fluorescence EEM Spectral Imaging (FLEEMSI) microscopy systems are described. Examples of MATLAB code for each of the two cameras are also provided.

4.1 Multispectral Camera

The multispectral camera, MSC, (Spectral Devices) uses an 8-channel CFA on an imaging sensor to create rather coarse emission spectra for each pixel in an image. This “snapshot” camera was first characterized for F-EEM imaging using a Hadamard-modulated light source by Katz [219, 286]. Building on this work, I have applied this camera to an F-EEM microscopy system.

In this section, I describe the basic hardware and settings of the camera available to a user, and the interface I built to integrate the camera with the programmable light sources for microscopy and for processing the raw images efficiently.

4.1.1 Hardware

The visible-wavelength CFA is composed of 256 × 256 “super-pixels”, each containing eight colour filters spanning three pixels each, surrounded by border pixels for a total area of 8 × 8 pixels

(Figure 1.18). The imaging sensor is a complementary metal-oxide semiconductor (CMOS) photodetector array containing 2048 × 2048 elements and the colour filters are centered at (474, 495, 526, 546, 578, 597, 621, 640) nm with FWHM values of ~20 nm [286]. Below we describe settings which we use frequently.

Acquisition Time. In contrast to most hyperspectral cameras, our snapshot camera acquires a multispectral image in a single exposure. This has the important advantage that all 65,536 pixels are acquired at the same point in time. In practice, the acquisition or integration times (shutter speed) are within a range of 15 ms to 500 ms. A lower integration time is technically not possible and higher integration times tend to accumulate dark noise which overwhelms a fluorescence signal. Since the camera heats up during operation, the dark current contribution to the dark noise and background then also increases.

Paul Reid, a current undergraduate researcher in our group has attached a heat sink and fan to the camera casing. These devices keep the camera casing at room temperature which nearly eliminates the increase of dark noise during operation. Since the camera is not actively cooled below room temperature, the base thermal noise of the camera remains constant. This was measured using the mean value of a histogram of pixel values in images were acquired sequentially over an hour. It was found that the mean value rose from 8 to 17 within the first 10 minutes then remained at 17 for the next 50 minutes. Without the heat sink and fan, the mean value continued to rise until it reached 28. Additionally, the camera remains cool to the touch with the addition of the heat sink and fan while it becomes noticeably warm without. Future work will use a small Peltier cooler to reduce electronic noise contributions.

Gain and Black Level. Both the gain and black level can be adjusted, however as both are software-level adjustments and not physical gain mechanisms, no new information is gained. None of the data acquired in these experiments adds gain or adjusts the black level, as these settings were not found to produce higher-quality images nor more information-rich F-EEM spectra.

Lenses. The camera is equipped with a standard c-mount lens connector, and commercial lenses can and have been used. Attachment to a microscope through a camera port requires an adapter for the correct sensor size and sometimes for the correct magnification. The adapters used for the Olympus CK2 inverted microscope are the U-PMTVC (Olympus) adapter paired with the NFK 2.5 Photo Relay Lens Set (Olympus) and the PM-ADF adapter (Olympus). The adapter used for

the Zeiss Axiovert 200—a research-grade fluorescence microscope generously donated by BC Cancer—was the DD63ZNC 0.63X (Diagnostic Instruments).

4.1.2 Software Control

To acquire F-EEM images using the MSC with both programmable light sources—the LDA and the DMA-PLS—a new graphical user interface (GUI) was created (Figure 4.1). Though a previous GUI existed, modifications were made for new system requirements. These included a change to the camera connectivity due to changed MATLAB compatibility, illumination using the LDA in addition to the DMA-PLS, and larger-format image display for focusing the camera image when using the microscope, which is positioned a larger distance from the computer monitor than previous setups allowed.

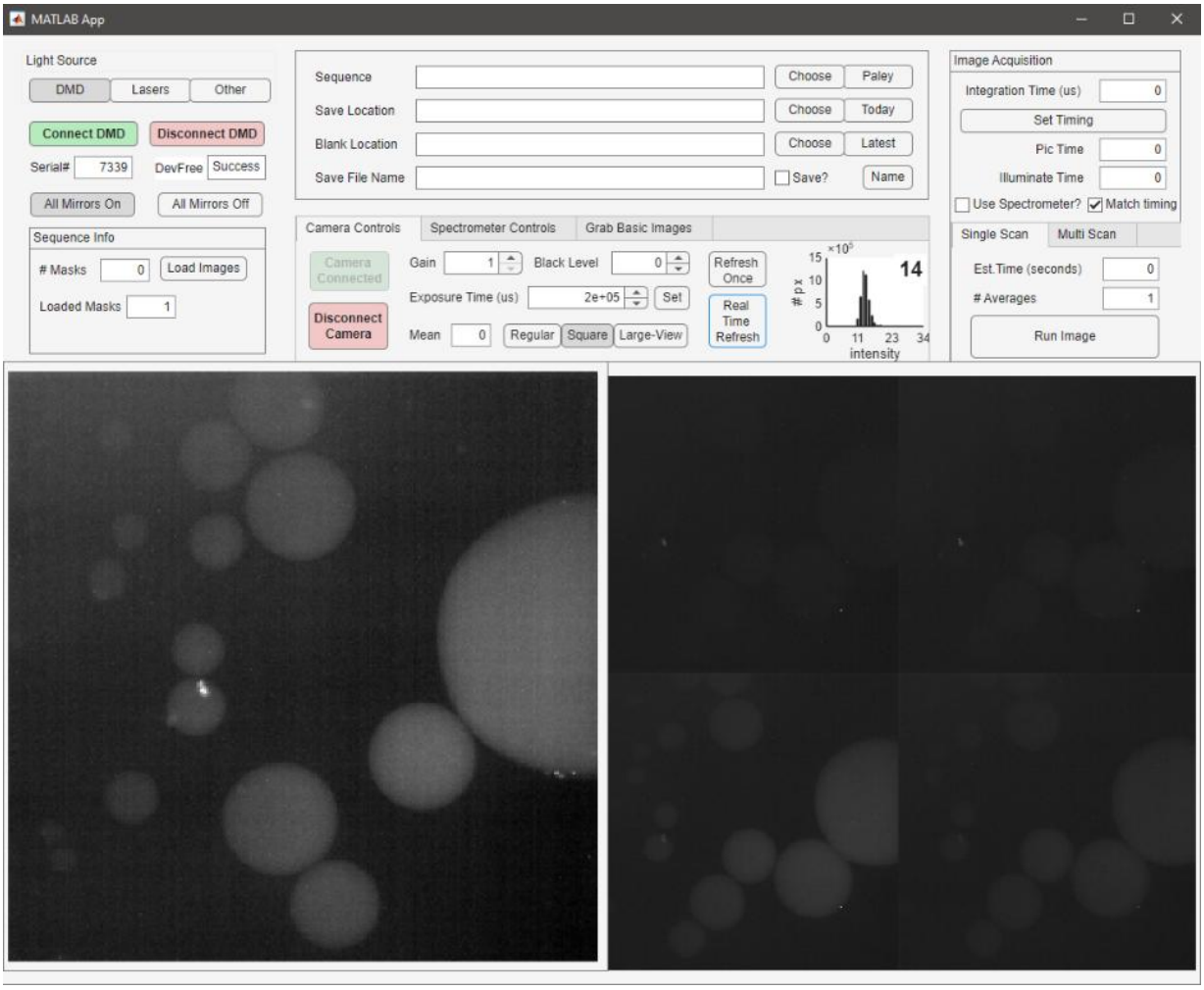

Figure 4.1. Interface for F-EEM image acquisition with the 8-channel multichannel camera. This view shows the larger image displayed on the left, used for focusing a sample under a microscope. The right shows the uncovered portion of the grid of eight images with one image representing each colour channel.

Communication with MATLAB. Spectral Devices uses an imaging chip from another company which provides a thorough software development kit (SDK) that we use to adjust settings and image readout parameters. Communication with the camera to set parameters, send triggers, and receive image data is done using ActiveX through MATLAB. Previously, this was set up using ActiveX control in *actxcontrol*, however this function can only be used in GUIDE (Graphical UI DEsigner) (unsupported as of MATLAB R2025a), not AppDesigner, the newer MATLAB GUI builder. As of version R2025a, MATLAB no longer supports *actxcontrol*, and to keep the camera working for future researchers without relying on previous versions of MATLAB, I switched communication to an ActiveX server, *actxserver*, which has nearly all the same functionalities. They are described in supporting notes in the code but not included here for brevity. Note additionally that the camera uses a USB3.0 port and it is essential that this is used for the computer connection. We found that streaking (described below) arises when a USB2.0 port is used.

Image Acquisition

A listener function is now used for image acquisition. The function sends a "ready" flag when an image has been acquired and is ready to be transferred from the buffer. Because the readout and the on-chip processing take a variable amount of time, a while loop waits for the "ready" flag before grabbing the image. This allows us to have a variable amount of time between images, which also allows acquisitions to be faster than setting an acquisition rate value which would rely on a conservative estimate of the slowest processing times. When the new image is not yet available from the camera buffer, often an error prevents the image from being grabbed, however on occasion, the recorded images contained only zeros (all-black) or the previous image. I added a check to ensure that the values are neither all zeroes nor identical to the previous image.

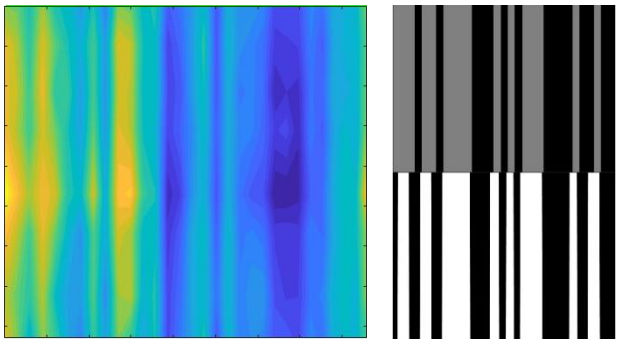

Figure 4.2. Demonstration of the "streaking" behaviour in F-EEMs. (**left**) An F-EEM exhibiting the "streaking" appearance, (**right, top**) the 31st mask in a 31-mask Hadamard-modulated excitation pattern, and (**right, bottom**) the "streaked" F-EEM converted to a binary image to compare with the mask.

Together both check procedures prevented a previously common issue where the EEMs would appear as streaks. Figure 4.2 demonstrates that the streaking behaviour seemed to be either associated with masks being displayed at incorrect intervals during image acquisition, or with images that were acquired as zeros causing issues in the demultiplexing process. In the example shown, the 31st mask in a size 31 Hadamard Paley S-matrix used for excitation matches almost perfectly with the streaks appearing in the EEM.

Additionally, the interface image displays are frozen during acquisition, as interaction of a cursor within those frames adds a task to MATLAB's task list during an image acquisition loop, which can interfere with the image timings. This is because pauses are required in the acquisition loop, and at a pause, MATLAB updates the list of tasks, and if there is a queue, MATLAB will execute those first, causing delays.

Integration with Programmable Light Sources

The software integration of the LDA and DMA-PLS are described in Section 4.1.2 and by previous students [286,293,285], respectively. Simplified image acquisition loops to acquire excitation-multiplexed images using the MSC with the DMA-PLS and LDA-PLS are shown in appendices A.4 and A.5, respectively.

Integration with a Spectrometer

An emission spectrum is acquired using a fiber-coupled Avantes spectrometer simultaneously with each image, and a display panel to connect the spectrometer, set its timing, and view the spectrum is also included in the GUI.

4.1.3 Image Processing

The raw images output by the MSC contain 2048 × 2048 pixels (256 × 256 groups of 8 × 8 pixels, each containing eight groups of three pixels for each colour channel) (Figure 4.3). F-EEM images with dimensions $x_{px} \times y_{px} \times \lambda_{emission} \times \lambda_{excitation}$ are assembled using n images, one for each excitation band and a background image taken with no illumination. The background image is subtracted from each raw F-EEM image, leaving the dimensions 2048 × 2048 × $n_{\text{excitation}}$. Each of the n images are acquired as unsigned 8-bit integers (uint8). Each 2048 × 2048 image is ~4 MB, and a set of n = 32 images (*i.e.,* one FLEEMSI hypercube) occupies 131 MB when saved. The images

are acquired using the GUI described in Section 4.1.1 and are saved in the 2048 × 2048 uint8 format, along with acquisition and camera parameters.

Band Separation & Demosaicing

For cameras with a 3-channel CFA (*e.g.*, an RGGB Bayer pattern), the term demosaicing refers to the interpolation of neighbouring pixel colour values. This leaves each pixel with an RGB value, even though only one colour is recorded physically by each pixel. This is done via algorithms; their improvement remains an active area of commercial and academic research [311]. In this 8-channel CFA, no interpolation is done. This is due both to the differences in CFA layout—a larger spatial grouping of pixels and the greater number of empty pixel locations compared with an RGGB CFA—and to preserve quantitative and spectral data.

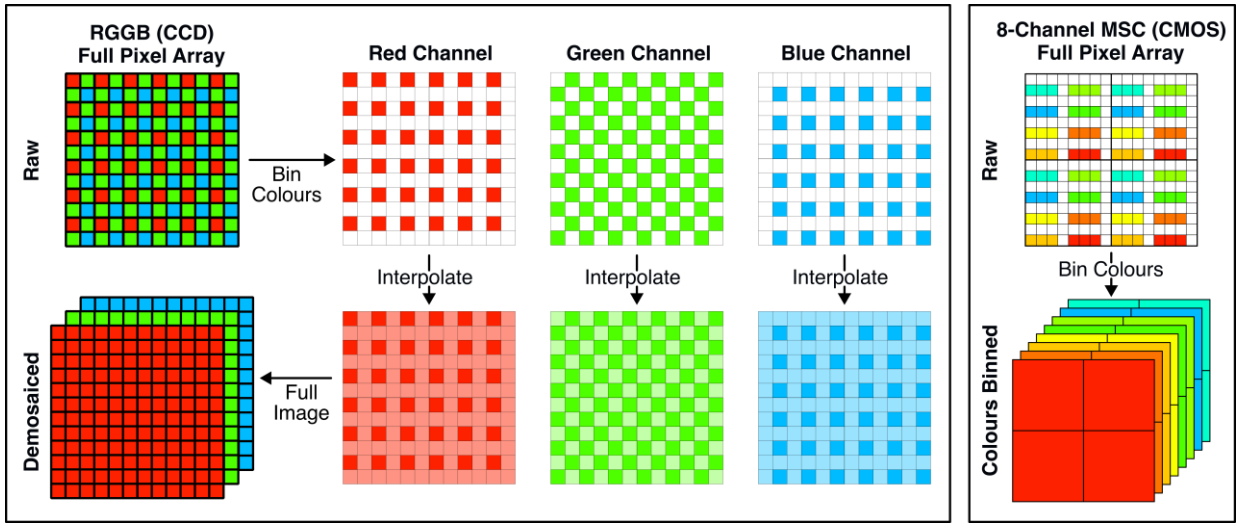

Figure 4.3. Colour filter arrays of a typical colour camera and a multispectral camera. Colour filter layout on arrays of pixels and processed results from (**left**) demosaiced RGGB Bayer-style array producing a 12 × 12-pixel image with three colour channels for each pixel (12 × 12 × 3), and (**right**) non-demosaiced 8-channel array of 16 × 16 pixels producing a 2 × 2 super-pixel image with eight colour channels for each pixel (2 × 2 × 8).

The 2048 × 2048 raw images are each reorganized by spectral band into 256 × 256 × 8 "hypercubes" (Figure 4.3), where each of the 65,536 super-pixels contain eight colour or emission channels. To create F-EEM images, we take n images—one for each excitation band and one blank image with no excitation light. This creates n hypercubes of size 256 × 256 × 8 × ($n_{\text{excitation}}$ + 1). Below is a short section of code used for band separation of a background-subtracted excitation-multiplexed image (2048 × 2048 × $n_{\text{excitation}}$).

```
% Reorganize 2048 x 2048 image into a 256 x 256 x 8 hypercube
nEx: number of multiplexed images (number of excitation bands)
Datatype: 'uint8','uint16','double' (depends on input)
```

```
img = zeros(256,256,8,slices,datatype);  % preallocate
rawimg = pagetranspose(rawimg);        % transpose for indexing
exslice = zeros(256,256,8,3,datatype);   % preallocate
for a = 1:nEx+1                 % 1 added for blank image
    I = rawimg(:,:,a);          % index over multiplexed img
    for b = 1:3                 % each channel has 3 pixels
        c1 = 1+b-1; c2 = 5+b-1; % pixel locations for indexing
        exslice(1:256,1:256,1,b)=I(3:8:2048,c1:8:2048);%474 nm channel
        exslice(1:256,1:256,2,b)=I(1:8:2048,c1:8:2048);%495 nm channel
        exslice(1:256,1:256,3,b)=I(3:8:2048,c2:8:2048);%526 nm channel
        exslice(1:256,1:256,4,b)=I(1:8:2048,c2:8:2048);%546 nm channel
        exslice(1:256,1:256,5,b)=I(5:8:2048,c1:8:2048);%578 nm channel
        exslice(1:256,1:256,6,b)=I(7:8:2048,c1:8:2048);%597 nm channel
        exslice(1:256,1:256,7,b)=I(5:8:2048,c2:8:2048);%621 nm channel
        exslice(1:256,1:256,8,b)=I(7:8:2048,c2:8:2048);%640 nm channel
    end
    img(:,:,:,a) = sum(exslice,4);       % sum of the three values
end
```

Optimizations. Some adjustments were made from previous methods to work more efficiently with larger images and to decrease the run time. These included:

1. Replaced the MATLAB-standard “double” value format (8-byte, 64-bit, double-precision floating point values) with a uint8 or uint16 (unsigned integer 8- or 16-bit) to reduce the memory capacity of the data, which has a uint8 format. The smaller data footprint allows for faster processing. Unsigned 16-bit integers can store values from 0 to 65535, far above the maximum possible value for the sum of the three uint8 pixels with values ranging from 0 to 255.

2. Replaced the mean of the three pixels per colour channel with a sum, which was necessary to allow for the integer data types to be used without the quantization loss that would come from converting a double (the mean) into an integer. This was done to support the use of unsigned integer values.

3. Restructured the variable *exslice* to have a fourth dimension of size 3 (for the three pixels of each colour channel per super-pixel) which could then be summed over. The sum over the fourth dimension (single line) a mean of three variables—one for each of the three pixels for each colour channel—which was calculated using a loop for all the pixels.

4. Used vectorized and compiled functions in MATLAB, specifically *pagetranspose* which is an array-optimized MATLAB built-in function and is faster than the equivalent looped

version. This step improved from ~0.367 seconds to ~0.087 seconds (≈4× faster). This reduced the run time from ~0.934 seconds to ~0.045 seconds (≈20× faster).

Replacing loop calculations with MATLAB-optimized array operations and the other modifications described reduced the total run time and memory requirements. Because our excitation sources are multiplexed, each pixel in each of the *n* multiplexed images is then demultiplexed using the inverse of the Hadamard matrix used for image acquisition (Figure 2.3, Equation [2.4]), as described in Section 5.1.2.

Experiments demonstrating F-EEM microscopy imaging using the MSC are shown in Chapter 7. The second camera we use for F-EEM microscopy is a hyperspectral camera (HSC) developed by BaySpec and is described next.

4.2 Hyperspectral Camera

The GoldenEye™ hyperspectral camera (HSC) from BaySpec [216] provides higher spectral resolution than the 8-channel MSC described above. Where the MSC used colour filters, the HSC acquires per-pixel wavelength spectra through a liquid crystal-based polarization interferometer. This Fourier-Transform Polarization Interferometer (FT-PI) uses the Fast Fourier Transform (FFT) of these interferograms to recover the wavelength spectra. Because there is no separation of pixels into blocks as with a CFA, all the pixels on the chip can be used for light detection. Consequently, the spatial resolution is larger than that of the MSC, in this case 1024 × 1280 pixels. In addition, interferograms reject less light per recording, so that the image brightness should be larger compared to an 8-channel MSC. Consider that even in an ideal MSC with 8 colour channels, no more than 12.5% of incident photons of a particular colour can be detected—*i.e.,* the chance of a photon striking the "correct" colour filter cannot be higher than 1-in-8. In practice, this number is much lower since only 37.5% (3 pixels per colour channel per super-pixel of 8 × 8 pixels) of the light reaches a photoactive area on the imaging array for a total *ideal* detection efficiency of 37.5/8 = 4.7%. This efficiency is further reduced by the quantum efficiency of detection and through light scattering and absorption losses at the different optical elements. If optical transmission losses were equal, a hyperspectral camera based on interferometry should have an increased photodetection efficiency, since ideally 50% of the light strikes the detector instead of

12.5% (or 4.7%) for a CFA-based detector. Unfortunately, in practice, we could not observe the expected increase in photodetection efficiency.

This section will describe the basic workings of the polarization interferometer, validation of camera hardware and software parameters, and the integration of the camera into MATLAB to use with the multiplexed excitation sources. Thank you to Dr. Klose for the work done on validation tests for the camera and SDK.

4.2.1 Hardware

Birefringent materials such as some liquid crystals (LCs) contain ordinary n_o and extraordinary n_e refractive indices. When linearly polarized light interacts with these two indices, two paths are created following n_o and n_e and different phases are accumulated as they travel through the material. Temperature, wavelength, and applied voltage all affect the birefringence of LCs. As described by Hegyi [312] this difference in phase φ is:

$$\varphi = k\Delta nT \qquad [4.1]$$

where λ is the wavelength and the magnitude of the wavenumber is $k = 2\pi/\lambda$. The thickness of the LC layer is represented by T and $\Delta n = |n_o - n_e|$ [312]. The intensity I at each pixel is the sum of all intensities:

$$I(\lambda) = \frac{I_0}{2}\left[1 + \cos\left(\frac{2\pi\Delta nT}{\lambda}\right)\right] \qquad [4.2]$$

where each value of $I(\lambda)$ corresponds to one wavelength in the transmitted spectrum. This spectrum can then be obtained by Fourier transformation using a fast-Fourier transform (FFT).

The wavelengths (λ) of the spectra are usually expressed in wavenumbers $\sigma = 1/\lambda$. A spectrum can be reconstructed if the Nyquist sampling criteria are met. For this system, this would equate to a specific number of frames where each $\sigma > 2\sigma_{max}$, and each frame is obtained by tuning Δn through the voltage applied to the layer of LCs between the polarizers. As in all interferometers, the spectral resolution scales with the inverse of the path length difference, *i.e.,* the small wavelength differences are only resolvable with large phase delays. Here, interferograms with phase delays much greater than 2π must be recorded to resolve wavelength differences significantly smaller than the center wavelength [313].

The spectral resolution of the system can be approximated, when neglecting dispersion at different wavelengths (assuming n=constant) and using a uniform grid across the wave-vector space, by $\Delta\lambda \approx \lambda^2 / \varphi$ where φ is the optical path delay calculated using $\varphi = T\Delta n$. Note that in application of this FT-PI to an imaging chip, T, referred to as β in the patent literature [313] incorporates the change in incidence angle for the chief ray for an imaging system. More precisely, the spectral resolution at each λ and pixel is $\Delta\lambda = 2\pi\lambda / \Delta\varphi$ where $\Delta\varphi$ is the range of optical phase delays in radians at which the interferogram is recorded [313].

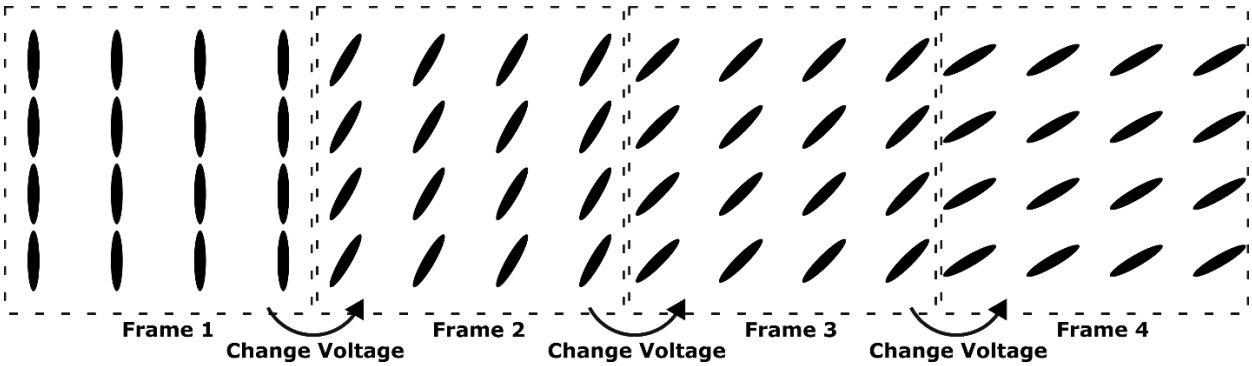

Figure 4.4. Orientation of liquid crystals changing depending on the bias voltage, for a Fourier-Transform Polarization Interferometer (FT-PI)-based spectral imaging chip.

Spectral Band Selection

The spectral range of the HSC is between 400–1100 nm with an adjustable number of wavelength bands up to a maximum of 141. Because the spectral range is fixed, reducing the number of bands equates to a larger FWHM and shorter acquisition time. The number of bands is determined by the number of frames used for acquisition, as described above, where an increased number of frames is proportional to an increased spectral resolution. For any Fourier-transform spectrometer, a longer optical path length will provide a higher spectral resolution. For an LC device such as this, a voltage applied to the LCs causes a phase change corresponding to an optical path length difference. LCs have a response time of tens to hundreds of milliseconds, dependent on, among other factors, the thickness and viscosity of the LC layer. A thicker and more viscous layer requires both a higher voltage to make the change and incurs a longer response time. Since that response time becomes quite large when acquiring 200 frames per full image, the company has divided a single thicker LC layer into four thinner layers, each requiring a smaller voltage and having shorter response times. Additionally, the manufacturers apply a constant voltage waveform to the LCs which has been calibrated to provide a constant retardance value change over time [313].

Lenses

The camera has a 47° field-of-view which requires that a higher f-stop lens be used. The lens provided with the camera has a focal length of just 8 mm and f-stop (apertures) between $f1.4$ and $f2.4$, though the f-stop must be set no lower than $f1.8$ or spectral artifacts appear in the images. This is the result of the differing distances travelled by a beam travelling nearly perpendicular to the sensor and one at an angle, causing different path lengths and phase delays through the LC layers and consequently artifact problems in the frequency response.

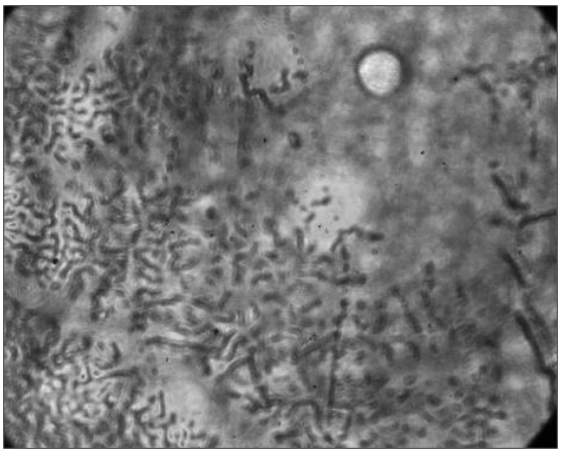

Figure 4.5. Image of "floaters" observed using a high-magnification objective lens. Image was taken with a hyperspectral camera (BaySpec, Section 4.2) through the camera port of a Zeiss Axiovert 200 inverted microscope with a 40x objective lens. The image was acquired by Mackenzie McNiven and used with permission.

Microscope Floaters

The camera, when used with very low numerical aperture systems, such as that of a microscope tube lens, can cause apparitions in the image. The cause of these artefacts is identical to apparitions observed by someone with vitreous floaters in their eyes looking through a microscope. Low numerical aperture optics create near-parallel rays reaching the detector—eyes or a camera—which allow for clear imaging of any imperfections in the path of that beam. In eyes, this arises due to altered vitreous structures in the eye [314], whereas in a camera, it is more likely a surface which has some level of contamination. The observed artifacts may also be caused by the LC layers and contaminants on the imaging chip for the BaySpec camera. Illumination methods that differ from the conventional top-down illumination for inverted microscopes reduce the presence of these spots, and we have not noticed them when the camera was used for fluorescence imaging.

Low-Light Performance

Although advertised as a low-light camera, we have had difficulty using the HSC for fluorescence microscopy due to the low sensitivity likely due to both the integration times required and light throughput of the imaging system. Many possibilities exist for light loss through the system, though they differ from those losses in a CFA-based MSC. First, the linear polarizers—preceding and following the LC layers—each reject approximately 50% of the incoming randomly-polarized light, leaving at most 25% of the incident light to be detected by the camera. Additionally, even with antireflection coatings on the separators between the layers of liquid crystals, with four layers, likely each with one or two surfaces at which reflection occurs, there is likely light loss. Assuming a 5% loss at each of the 8 interfaces due to Fresnel reflections this would account for an additional loss of 0.95^8=66%. The camera software also allows integration times of up to 50 ms per frame, which is frequently too short to record low-intensity fluorescence. Even when 200 frames are obtained per acquisition, if each frame has a poor SNR, the SNR advantage gained with a multiplexed detection system cannot be realized. This is discussed in the next section.

4.2.2 Validation

We noticed performance issues with the GoldenEye™ HSC, notably in the limited range of exposure times that could be set in the SDK and GoldenEye™ software, strange background behaviour, poorly normalized images, and lower image quality using the SDK compared with the GoldenEye™ software. Dr. Klose, a former post-doctoral researcher and I tested the camera extensively and reported our findings to BaySpec, to find a solution to some of these problems. Images analyzed in this section were taken with the GoldenEye™ HSC (BaySpec) equipped with an *f*/4 lens, using 200 frames, 20 millisecond exposure per frame and no added gain, using the Python SDK through MATLAB as described in Section 4.2.2. The object imaged is transmitted light from the DMA-PLS through a white matte business card.

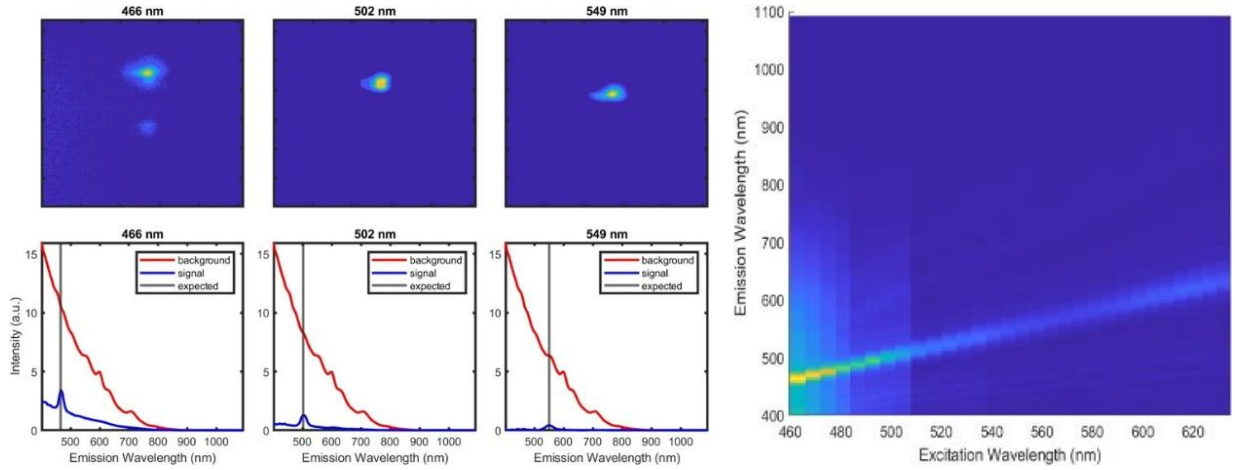

Figure 4.6. Peak center accuracy of BaySpec camera. (**left**) (Top row) illumination with a single colour (466, 501, 548) nm, image represents the sum of all (141) channels of the hyperspectral camera. (Bottom row) spectra containing the sum of all pixel values. Signal line from the transmission spectrum from illumination with one colour, illuminated by the DMA programmable light source. Background line shows the transmission spectrum with the light source turned off, demonstrating the electronic background (note the large background magnitude could be from rescaling of the Python SDK data. (**right**) Wavelength response of BaySpec camera. Camera parameters: f/4 lens, 200 frames, 20 ms exposure, gain 2. [Scene]: DMA PLS, scattered through ground glass diffuser plate. EEM is from the sum of all the pixels, acquired with the python SDK through the MATLAB GUI.

Peak Center Accuracy

The camera identifies wavelength centers accurately, when using a DMA with a single colour illuminated through a white business card. Figure 4.6 shows three wavelength bands of the 31 wavelength bands tested, all 31 are shown in Appendix A.11. For illumination using the DMA-PLS through a ground glass diffuser plate, Figure 4.6 (right) shows the Rayleigh scatter line at the expected wavelengths over the range covered by the source.

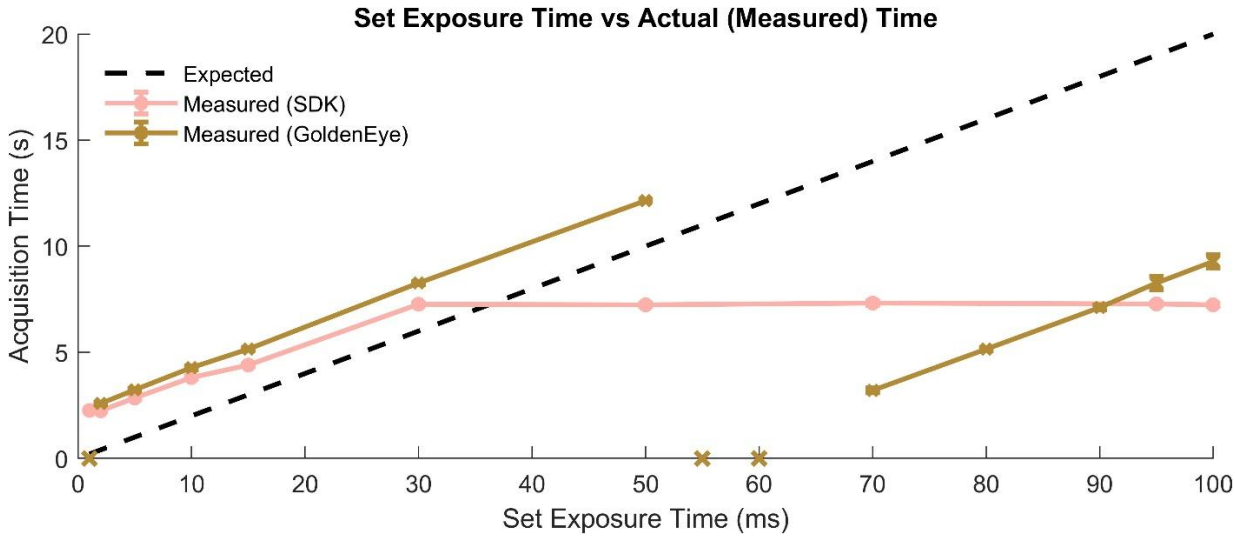

Figure 4.7. Actual and expected acquisition times using BaySpec camera. Acquisition times were measured for several images at a range of integration (exposure) times, using the Python SDK through the MATLAB GUI and the GoldenEye™ camera. "×" points represent the GoldenEye™ software crashing for all three replicates on that set exposure time. Error bars are the standard deviation of the three measured values shown in Appendix A.12.

Exposure Time

When exposure times were set above 30 milliseconds using the Python SDK via our MATLAB GUI, total acquisition time did not increase, suggesting an override on the exposure time limited at 30 ms. When the camera was instead controlled using the GoldenEye™ software, acquisition time increases linearly for exposure times up to 50 ms per frame with a data processing time of about 1.2 s.

$$T_{acquisition} = T_{exposure} \times n_{frames} + T_{process} \quad [4.3]$$

Above 50 ms exposure time the camera freezes when the times are set in the rage of 50–60 ms. With exposure times larger than 60 ms it appears that the effective exposure time is simple reduced by 50 ms. When exposure times were set at (1, 55, 60) ms, the software crashed for all three replicates at that time point. This test showed that the advertised integration times provided by the manufacturer are not possible likely due to software limitations. Timing for image acquisition by the SDK was determined by a software clock and measured with a stopwatch for the GoldenEye™ software. Three replicate images were timed for each time point.

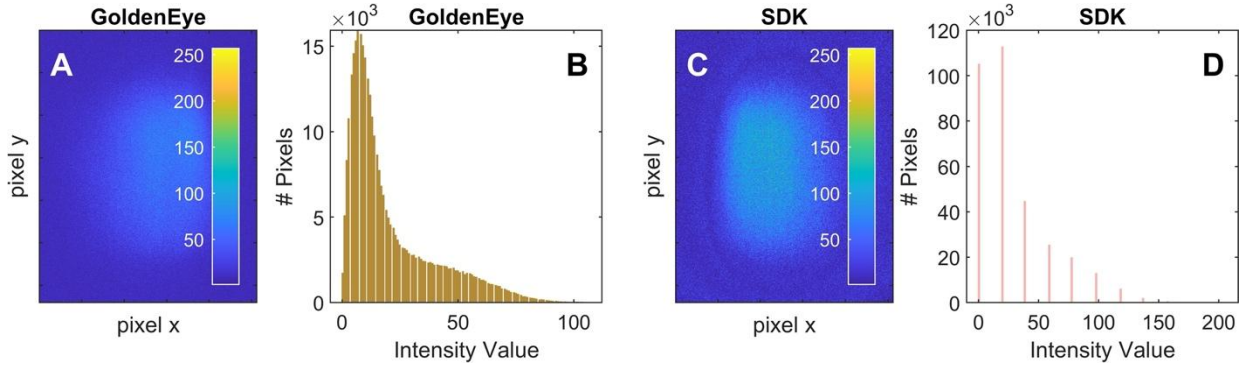

Figure 4.8. Data density of images acquired using GoldenEye software and SDK with the BaySpec camera Illumination by 548 nm light through a white matte business card, lens not in focus, f/3, 200 frames, gain 10, exposure time 30 ms. (A, C) show intensity summed from all 141 channels, (B, D) histograms of intensity values for all the pixels in (A, C).

Data Density and Normalization

The images obtained through the Python SDK have lower data density than those acquired with the GoldenEye™ software, and are normalized before transmission, removing much of the intensity information between images. The GoldenEye™ software acquires images in uint16 format, with a nearly continuous distribution of values across the range of intensity values. The SDK provides images in uint8 format, with intensity values that appear to be normalized to the maximum value (255 for uint8 data).

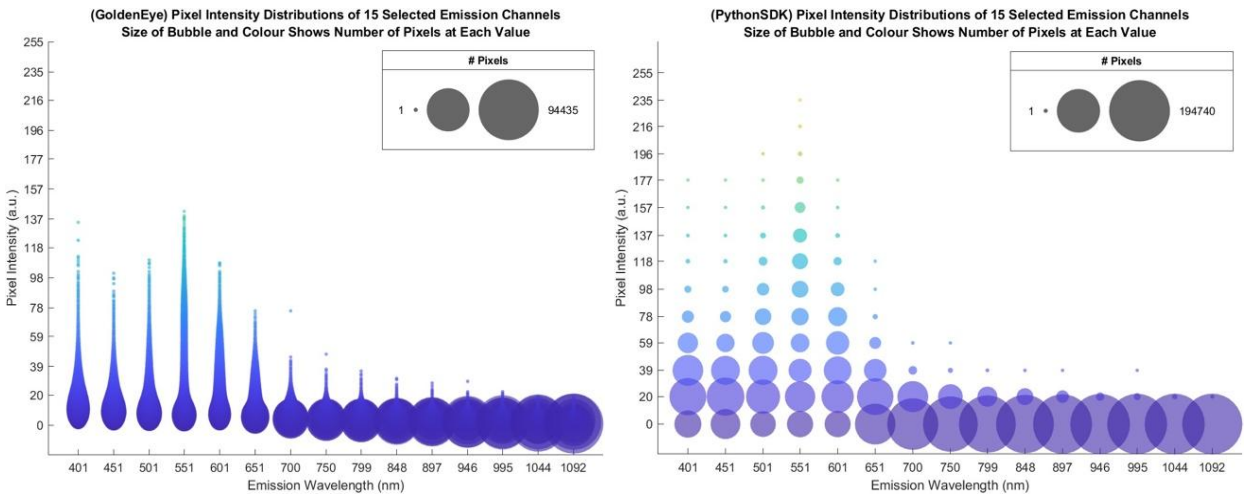

Figure 4.9. Data density and normalization of images acquired with BaySpec camera using the GoldenEye software and the SDK. Illumination by 548 nm light through a white matte business card, lens not in focus, f/3, 200 frames, gain 10, exposure time 30 ms. Bubble size indicates the number of pixels with a unique pixel intensity value. Pixel intensity is shown by a colour scale from purple to yellow, and by the y-axis. Only 15 evenly spaced emission wavelengths of the 141 available emission bands are shown for clarity.

This can be seen in the histogram (Figure 4.8d) and bubble chart (Figure 4.9, right) as data are missing from most of the intensity values, though the shape is similar to Figure 4.8b. This suggests we are missing valuable information when our data is converted from uint16 to uint8 and normalized to a value of 1. To combat this, I worked around the limitations in the SDK, described in Section 4.2.3. We suspect that the Python SDK software normalizes the data because the highest intensity value does not change for different exposure times or different gain, whereas they increase for the images acquired with the GoldenEye™ software. That is, when using the GoldenEye™ software, the exposure time increases proportional to the exposure time as expected. When increasing gain, the intensity increases according to the power law—again, as expected.

4.2.3 Software Control

As mentioned, the BaySpec HSC can be used with the custom GoldenEye™ software developed by BaySpec, or through an additional SDK which can be used through Python, and which is also created by BaySpec. Above we demonstrate that the SDK is quite limited in its functionality with only a few parameters that can be set on the camera (exposure time per frame, number of frames, gain) and functionality to take an image. The SDK code is almost entirely obscured which has made modifications difficult, and the SDK manual is quite sparse. Although the GoldenEye™ software can be used to acquire a single image, when we attempt to acquire images using a

Hadamard-multiplexed illumination, we require a MATLAB-compatible SDK so that the programmable light sources and spectrometer can be controlled together.

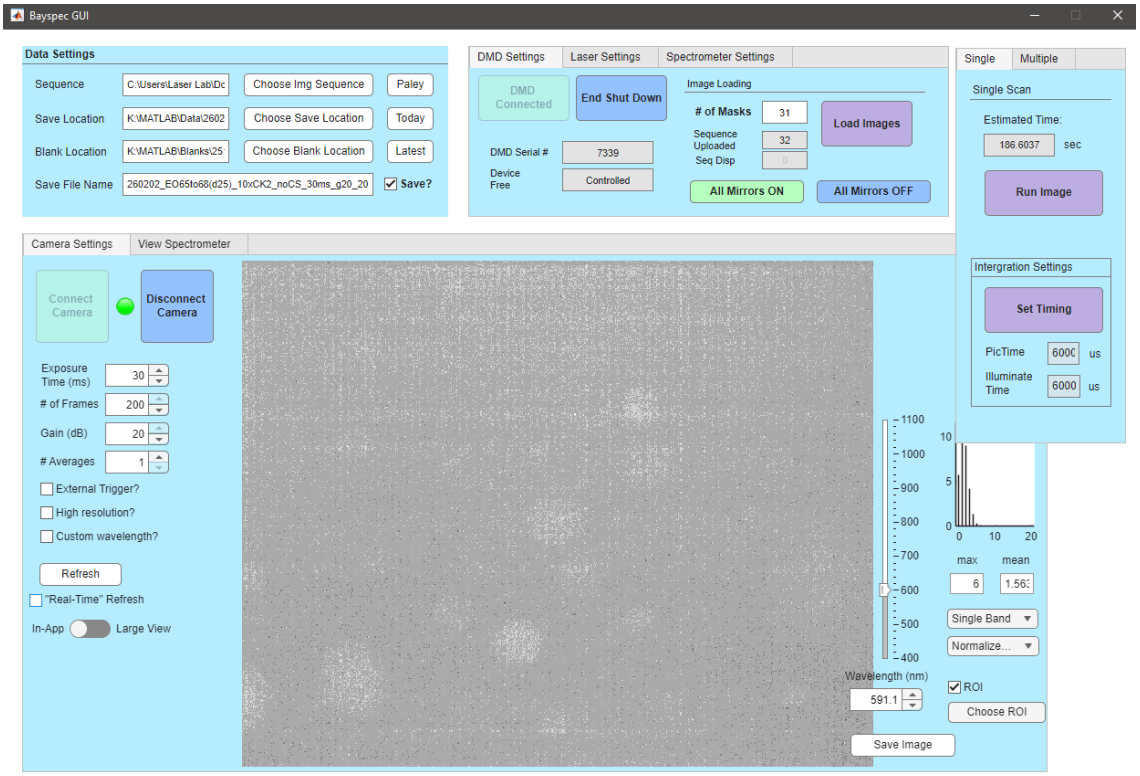

Figure 4.10. Interface used for F-EEM image acquisition with the hyperspectral camera.

Communication with MATLAB

Because the available controls for the BaySpec camera are quite different than those for the MSC from Spectral Devices, we built a new interface to use the camera with our programmable light sources in MATLAB (Figure 4.10). The app was designed using AppDesigner (MATLAB), and the camera control used functions that could be accessed through the SDK supplied by BaySpec. Because the SDK can only be used in Python, a virtual Python environment was created in MATLAB. The code for this is shown in Appendix A.7.

Using the SDK, the exposure time per frame, number of frames (spectral resolution), software gain, and resolution (512 × 640 or 1024 × 1280) can be set for an image. We added controls such as number of averages and some display options such as the selection of a wavelength band, but these are functionalities created in the image acquisition GUI and are not communicated to the camera. For microscopy or other purposes in which a live video of the image scene is useful, a "real-time refresh" button is included which begins a constantly refreshed image which may have

no voltages applied to the LC layers to allow the maximum light through to the detector. No image can be acquired in this way, but it is used for alignment to visualize the scene.

Integration with Programmable Light Sources

The GUI allows a user to connect either the DMA-PLS or the LDA-PLS and turn those sources on when needed for alignment purposes. The LDA-PLS and DMA-PLS are controlled the same way as described in Section 4.1.2 and in Oren Katz' thesis [286], respectively.

Integration with a Spectrometer

As with the MSC, an emission spectrum is acquired using a fiber-coupled spectrometer (AvaSpec-ULS2048XL-EVO, Avantes) simultaneously with each image, and again a panel is included in the GUI to connect the spectrometer and set its timing.

Image Acquisition

After parameters are set on the camera using the appropriate controls in the window (integration time, number of frames, gain), and the timing is set, the "Run Image" button begins an F-EEM image acquisition. See Appendix A.7 for the image acquisition timeline. Similarly to EEM image acquisition using the MSC, a background image is taken first, with the light source turned off, then the Hadamard-encoded masks illuminate the sample, and an image is taken with each unique illumination.

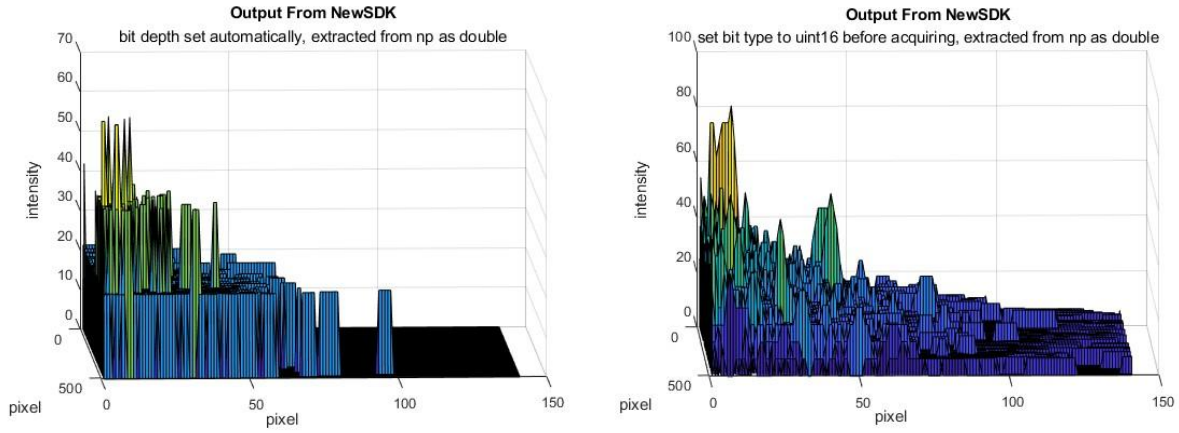

Figure 4.11. Pixel values of uint8 and uint16 images acquired with the BaySpec camera. Images were taken using the supplied SDK from BaySpec. All pixel values for the image are shown for bit depths set to uint8 (**left**) or uint16 (**right**).

As was discussed in the previous section (Section 4.2.2), images seemed to be normalized and lowered to an 8-bit intensity resolution, when acquired using the SDK, compared with the GoldenEye™ software.

Acquiring Images in uint16 Format

The bit depth of the camera object was changed in the Python SDK to 16-bit manually, which seemed to override the uint8 setting. Pixel values from a small region of an image are shown in Figure 4.11, for the former (uint8) and current (uint16) images of the same scene. The characterization of the bit depth of the camera was done with Dr. Swapnil Daxini, a former group member with experience in computer science. Although this conversion appears simple, finding information about even the most basic functions of the provided software was quite challenging with blocked access to most of its functionality.

These results were presented to BaySpec, and an updated version of the SDK was created which no longer normalized the images to a value of 1. However, the other problems—maximum 30 ms exposure time and images acquired in uint8 format instead of uint16 were not updated. The BaySpec HSC is currently only useful for bright fluorophores which can be excited using the laser diode array in the configuration described in Section 7.6 , however for the DMA system, the images are not bright enough with our current attempts.

The excitation sources (LDA and DMA-PLS) and emission detectors (MSC and HSC) used to acquire F-EEM images have been described in Chapter 3 and Chapter 4, and the next chapter will discuss the methods for analysis of those images.

Chapter 5 Four-Dimensional Fluorescence Data Analysis

New datasets require new methods for analysis—to analyze F-EEM images, modifications are required to a typical F-EEM analysis workflow. This includes the selection of only the most information-rich pixels from an F-EEM image and the optimization of code to run efficiently with these new and much larger datasets. The analyses here used a Dell OptiPlex 5000 with a 12th Gen Intel® Core™ i7-12700 (2.10 GHz), 32 GB RAM, 512 GB storage, with a 12-core GPU (Intel® UHD Graphics 770). The operating system was Windows 11 Enterprise and MATLAB R2024b was primarily used for analysis. MATLAB through Digital Alliance Canada was not used, though would be valuable to pursue if faster processing speeds or analysis of larger datasets are required. Some plots shown in this work used *cmocean* [315] and *crameri* [316, 317] colour palettes.

Although some modifications were made to analyze the data acquired using the MSC and DMA-PLS, the replacement of the MSC with the HSC led to more significant analysis requirements due to the size. Since an F-EEM image acquired with the HSC has 141 emission channels instead of the eight from the MSC, the dataset has the dimensions 512 × 640 × 141 × 31, or 1.4 billion points with 16 bits (2 bytes) per point for a total of 2.8 GB per F-EEM image. Here we assume that the DMA-PLS generates 31 distinct wavelength bands—a typical size used for our experiments.

Note that 2.8 GB per frame corresponds to a low-resolution image; we can also acquire a high-resolution image of 1024 × 1280 × 141 × 31, for 5.7 billion points, corresponding to 11.4 GB. Consequently, many of the previous versions of the functions used for demultiplexing and image analysis were no longer effective for the size of this data hypercube. I therefore re-wrote many functions with better memory and speed optimization principles. These have already been discussed briefly in Section 4.1.3. In this section I will describe general principles used for optimizing functions for running with large datasets and provide examples for image saving and Hadamard demultiplexing.

Additionally, an F-EEM image—compared with an F-EEM spectrum or dataset—requires that additional preprocessing be done before multivariate analysis for fluorescent component separation. Methods described in this section include the removal of Rayleigh-scattered light, which is common to all F-EEM PARAFAC analysis, and pixel selection. The pixel selection

reduces the size of the analyzed dataset and improves the quality of the fit. Two primary methods for pixel selection will be discussed; filtering pixels based on statistical parameters such as minima, maxima, and variance along the excitation or emission dimensions, and creating a threshold based on a component from PCA fit. Additionally, the use of PARAFAC for fluorescent component separation in the F-EEM images is explained.

5.1 Optimization for Large Datasets

Several functions are frequently used for data analysis in our group and had to be optimized for these large datasets, if they were inefficient in run speed and/or memory usage. Examples include demultiplexing F-EEM spectra acquired using a Hadamard-modulated excitation source, loading data into a MATLAB workspace, and formatting F-EEM data for PARAFAC analysis. Optimization in MATLAB can be assisted using the Profiler function, which times the code being run and provides a breakdown of the time spent on each line, section, and function. This was used to find the bottlenecks in the code.

For example, using MATLAB built-in functions, especially vectorized operations in place of for-loops, can decrease processing time [318, 319] as previously mentioned. An example is shown in Section 4.1.3 and 5.1.2. Considering the format of the data being saved or processed can also reduce processing time or used space by a variable. This will be described for image format when saving and for the excitation-demultiplexing process.

5.1.1 Image Saving

Although the compression that occurs in the 7.3 version of the save function in MATLAB reduces image size, that compression step can take a long time. This caused experimental problems, as we could not adjust the camera settings or start new image acquisition started until the previous image had been compressed and saved. Even moderate stacks of "small" images acquired using the 8-channel MSC (*e.g.*, 10 F-EEM images with dimensions 256 × 256 × 8 × *nEx* × 10) often took over 15 minutes to save. Dr. Deniz Aydin—a former student and post-doctoral researcher in our group—and I decreased that time to seconds by saving the images as binary files instead of .mat files. The trade-off is the file size—the binary files are larger than compressed .mat files.

For images acquired with the HSC, the .mat file compression is valuable as the HSC data cubes are much larger than MSC data cubes. Because image acquisition takes much longer than that of

the MSC—for example, a single excitation wavelength takes over 6 seconds to acquire where the MSC takes 0.3 seconds—the extra time required for saving the file is not critical. This may change when large stacks of F-EEM images are acquired, though.

To save binary image files in MATLAB we use the functions *fopen / write / fclose.* To open a binary file, the functions *fopen / fread / fclose are* used, followed by a reshape of the data which requires the dimensions of the original dataset. These dimensions are saved in a separate variable in the folder with the image (*camSettings*)—a structured variable ("struct" in MATLAB) which contains a dimensions field, among other camera and acquisition parameters. For F-EEM images, a demultiplexing function follows, if the image was acquired as an F-EEM using a Hadamard-modulated excitation source.

5.1.2 Hadamard Demultiplexing

When many images are acquired sequentially, for example following a sample change through time, if real-time analysis is required, memory allocation and processing time can limit the size of the data cube that can be acquired. Therefore, we implemented several data- and memory-handling improvements to the demosaicing process described in Section 4.1.3 and demultiplexing, described in this section.

For the F-EEM images acquired using the Hadamard-multiplexed excitation light sources (LDA-PLS and DMA-PLS), each F-EEM must be demultiplexed as described in Section 4.1.3. An F-EEM image acquired with the MSC and DMA-PLS with dimensions $256 \times 256 \times 8 \times 31$ is described in this section as an example. To demultiplex the Hadamard-encoded excitation dimension of this F-EEM image, each of the 65,536 pixels is multiplied by the inverse of the Hadamard matrix that was used to multiplex the excitation light. To optimize the usage for this process, the demosaiced unsigned 16-bit integer format should be preserved whenever possible.

However, the inverse of a Hadamard matrix is composed of signed (±) non-integer values, so when the uint16 values (pixel emission values at each excitation, 8×31) are demultiplexed by multiplying by these non-integer values, the result is non-integer values which must be stored as double precision in MATLAB. In this case—an $N = 31$ matrix—the magnitudes of each entry in the inverse Hadamard matrix are ± 0.0625. The magnitude of these values differs for different matrix sizes. To maintain the uint16 format, each demultiplexed F-EEM (each pixel) is then multiplied by the magnitude of the entry value which re-creates the integer value.

$$\mathbf{H}^{-1} = \begin{pmatrix} H_{11} & H_{21} & \cdots & H_{n1} \\ H_{12} & H_{22} & \cdots & H_{n2} \\ \vdots & \vdots & \ddots & \vdots \\ H_{1n} & H_{2n} & \cdots & H_{nn} \end{pmatrix}^{-1} = \begin{pmatrix} 0.0625 & -0.0625 & \cdots & 0.0625 \\ 0.0625 & 0.0625 & \cdots & 0.0625 \\ \vdots & \vdots & \ddots & -0.0625 \\ -0.0625 & -0.0625 & 0.0625 & 0.0625 \end{pmatrix} \quad [5.1]$$

Because the multiplexed pixel values must be multiplied by non-integer values, they are converted first to a double for this step only, after which the division by the magnitude of each entry is done and the values are converted back to uint16. Finally, negatives are set to zero after this step, which is done automatically upon conversion to a uint16 as the values are *unsigned* integers—all values below zero (negatives) are set to zero. An example of this demultiplexing step is shown in code below for an $N = 31$ matrix.

```
Build the Hadamard S-Matrix
H = paleyI(N+1);                    % creates Paley-type Hadamard matrix
H = H(2:end,2:end);                 % removes first row and column (all ones)
H(H==1) = 0;                        % changes ones to zeros
H(H==-1) = 1;                       % changes -1 to 1
H = H^-1;                           % take inverse of Hadamard matrix
H = H';                             % transpose matrix
repH = repmat(H,[1 1 256 256]);     % replicate matrix for all px
maxH = max(H,[],'all');             % get value to divide by for integers

Demultiplex using Array Operations (time = 0.101 seconds)
img = double(permute(img,[3 4 1 2])); % rearrange W for use in pagemtimes
dimg = pagemtimes(img,repH);        % multiply by inverse Hadamard matrix
if strcmp(datatype, 'uint16')       % convert back to integer
    dimg = dimg /maxH;              % divide by max to get back to integers
    dimg = uint16(dimg);            % convert to uint16 and remove zeros
else
    dimg(dimg<0) = 0;               % set all negatives to 0 for double
end
dimg = permute(dimg,[3 4 1 2]);     % rearrange into the (256,256,8,#ex)

Previous Version of Demultiplexing (time = 1.621 seconds)
dimg = zeros(size(img));
for r = 1:256 % demodulate pixel by pixel
    for c = 1:256
        dimg(r,c,:,:) = squeeze(W(r,c,:,:))*(H^-1)';
    end
end
dimg(dimg<0) = 0; % set all negatives to 0
```

Optimizations

Improvements to the processing time and temporary memory size while demultiplexing images were especially important for multi-image acquisitions such as monitoring a sample change through time.

1. Static values were set and modified outside any loops. For example, the static Hadamard S-matrix was inverted and transposed before the loop instead of inside the loop each time, and array-based operations replaced the previous loop for the demultiplexing step in which pixels are multiplied by the inverse Hadamard S-matrix. These steps reduced the time from ~1.621 seconds to ~0.101 seconds (≈18× faster).
2. Using array-based operations (MATLAB vectorized functions)—*pagemtimes* replaced *mtimes* (short form "*" in MATLAB) in a loop for multiplying the pixel values with the inverse transposed Hadamard matrix, shown in the code above.
3. Variables were re-assigned new values when the dimensions matched, to avoid that new variables had to be added. This reduced the memory requirements.

The modifications to the demosaicing (Section 4.1.3) and demultiplexing steps resulted in a processing time of 0.541 seconds, reduced from 2.709 seconds (≈5× faster), to convert a raw, excitation-multiplexed MSC image with dimensions 2048 × 2048 × 32 to an F-EEM image with dimensions 256 × 256 × 8 × 31. Each process was timed in triplicate to reduce timing effects from other system activity. Although this dataset is small in comparison to others we analyze, and larger datasets suffer from extra speed decreases from the memory load, this single F-EEM image is used as an example of the improved speed. The demultiplexed F-EEM image from a raw uint8-format excitation-multiplexed image with dimensions (2048 × 2048 × 32), occupies 32 megabytes (MB) and 130 MB, when processed with the new integer-friendly code and the previous doubles-only code, respectively. The result using each process is identical, verified using *isequal* along all dimensions of the dataset, in MATLAB.

5.2 Removing Rayleigh-Scattered Light

The Rayleigh-scattered light in a fluorescence EEM, also called the "Rayleigh line" represents elastically scattered excitation light. In an EEM spectrum the Rayleigh line appears as a diagonal, *i.e.,* when $\lambda_{ex}=\lambda_{em}$. This line is typically removed in F-EEMs because it can be much stronger than the detected fluorescence contains little information, though consult the work by Ferguson and Bernicky for an extraction of the absorption spectrum from the Rayleigh light [34, 285, 293]. Additionally, it cannot be modelled by PARAFAC analysis, so it must be removed prior to this

type of multivariate analysis [17, 270]. In MATLAB, this is done using one of two functions: *EEMCut* or *cutRayleighAndBelow.*

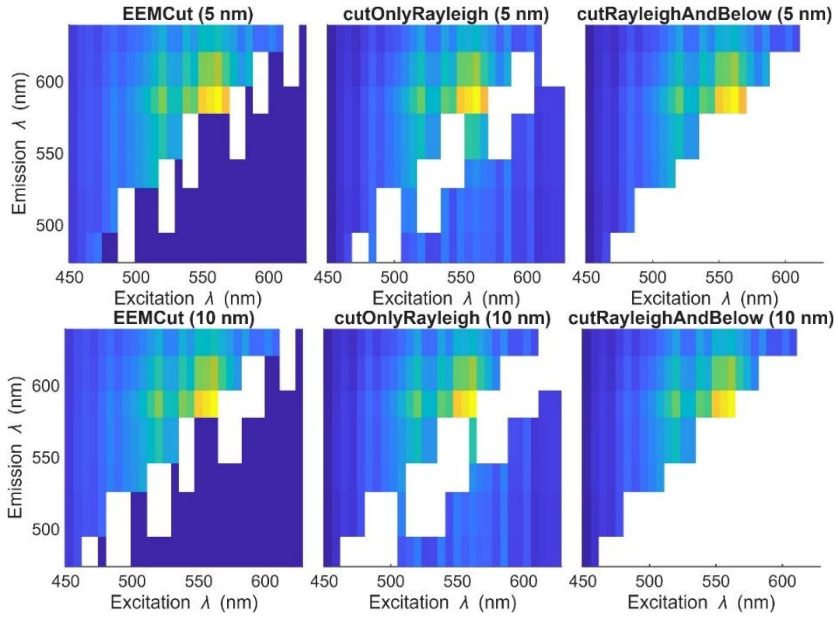

Figure 5.1. Comparison of Rayleigh cut functions on F-EEMs using different cut sizes. Data acquired using the 8-channel multispectral camera and DMA-PLS.

The first is provided by the authors of the *drEEM* toolbox for PARAFAC analysis in MATLAB [320] and requires the data format to match that of the input for PARAFAC—a structure with specific fields—which is not always convenient for simple visualization of an F-EEM. *EEMCut* removes any emission values within a set distance from each excitation wavelength by setting those values to "not a number" (NaN). I created the second function *cutRayleighAndBelow* to use simple inputs—an F-EEM and the corresponding excitation and emission wavelengths—to remove any excitation within a set distance from each emission channel. This works particularly well for F-EEMs acquired using the coarse emission of the MSC. The removed values can be set as NaN when conducting subsequent PARAFAC analysis, and to zero for PCA analysis. PARAFAC interprets NaN values as missing, not as zero, which is important for fitting F-EEM spectra which might have a sudden drop in the excitation or emission spectra when the Rayleigh line has been removed [17]. The difference between *EEMCut* and *cutRayleighAndBelow* are shown in Figure 5.1.

When values are instead set as zero, the datatype can remain as an unsigned integer instead of converting to a double, which is useful when further processing is to be done for large datasets. This can be useful for preliminary examinations of the F-EEMs of, for example, the HSC, before converting the large dataset into a double-precision format.

5.3 Loading Fits

PARAFAC analysis for F-EEM datasets is frequently done as described in Section 1.5 above (see also Murphy [18]). The algorithms implemented in the *drEEM* toolbox and others require user input for parameter optimization and typically some knowledge of the system being analyzed. The term "blind fit" refers to a PARAFAC analysis which does not require any knowledge about the EEM spectra of the components. Nevertheless, it requires an estimate of the number of components (*e.g.,* fluorophores) expected in the system, setting constraints such as non-negativity or unimodality, initialization type, and convergence value. Typically, numerous blind fits will be performed on a dataset, usually having a different number of components and some optimization to any of the following parameters: constraints, initialization, and convergence criteria. [270] These values are changed until a model is found which sufficiently explains the entire F-EEM hypercube without overfitting the data.

An inadequate model can be identified using statistical metrics as well as user knowledge about the system. Numerically, low values of "core consistency" and percentage of explained variance ("percent explained") suggest a poor fit [18]. For example, if the core consistency drops steeply as an additional component is added to the fit, this usually indicates that the model is now overfit [18]. Human-interpreted parameters to suggest a poor fit include EEMs that appear unphysical and—for F-EEM imaging—component images (or scores vectors) which appear nearly identical for multiple components.

There are mathematical challenges in obtaining reliable fits such as significant noise or residual scatter in a dataset, instrumental challenges such as artifacts or inconsistent pixel responses, as well as physical limitations such as inner filter effects, solvatochromism, and signal intensity differences between components.

When components cannot be accurately extracted from a dataset using a blind fit, prior knowledge of the system, can be incorporated into the model using loading vectors. Vectors corresponding to the excitation, emission, or spatial locations of the expected fluorophores in a system can be introduced either as an initial estimate or as fixed constraints for a PARAFAC model.

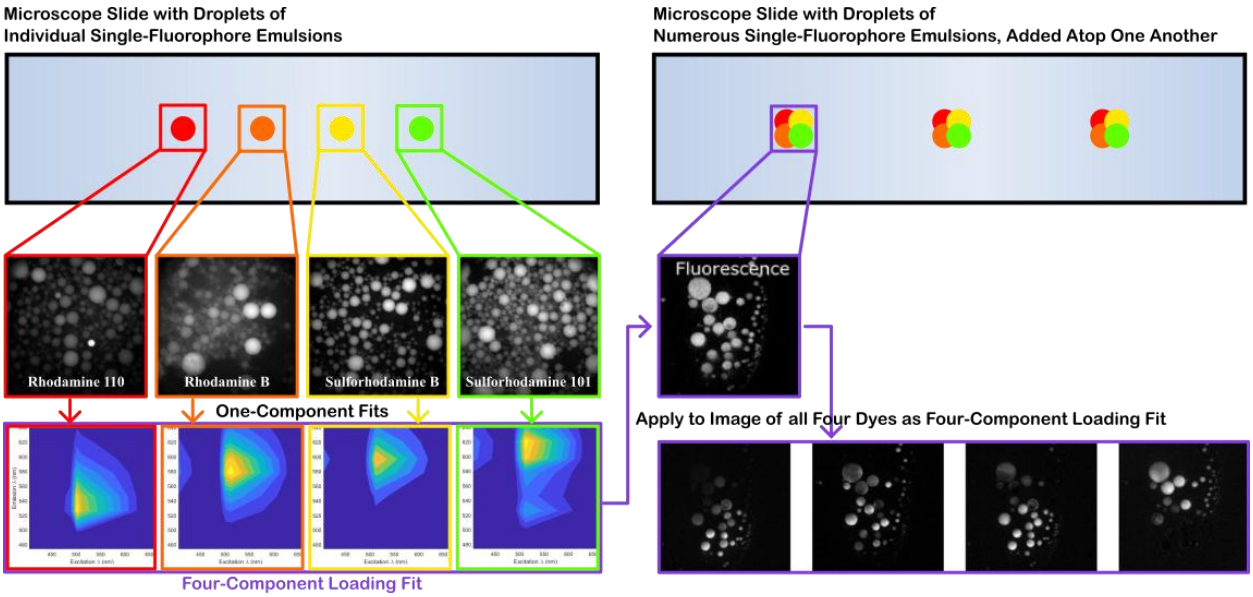

Figure 5.2. Creation of a loading fit using single-fluorophore emulsions. One-component PARAFAC analyses of images acquired using the MSC and LDA-PLS are performed for four neat fluorophore emulsions, then combined to use as a four-component loading fit. The four-component loading fit is used on an F-EEM image containing all four dyes, to spatially locate each dye.

When loading vectors are used as fixed constraints in a PARAFAC analysis of a large F-EEM dataset, the speed of an analysis is increased considerably. As an example, we use an F-EEM image taken with the MSC and DMA-PLS, which creates a dataset of size 256 × 256 × 8 × 31, reshaped to 65,536 × 8 × 31—or some permutation of this dataset depending on the PARAFAC model used [86]. A blind fit can take between five minutes and many hours, depending on many factors, described further in Section 7.4, whereas fitting the entire image using a loading fit with fixed excitation and emission dimension takes only seconds. These vectors can be created using a successful blind fit of a different dataset containing the fluorophores which are expected in the current dataset or by combining single-component fits of neat fluorophores, which is shown in Figure 5.2.

This very quick analysis can be used as an initial step in an F-EEM image analysis to see if all the expected components are present in an image before proceeding with blind PARAFAC analysis. Obtaining datasets with single components is straightforward in many practical settings, particularly when fluorophores have well-established signatures. For example, in microscopic fluorescence imaging many biological samples which are stained or contain fluorescence tags.

Alternatively, loading vectors can be created using a blind fit of a small sub-section of pixels in an F-EEM image. Using only those pixels exhibiting the strongest fluorescence and removing those which represent primarily noise can reduce the size of the dataset (decreasing fit time) and provide

cleaner data for an accurate decomposition using PARAFAC. This fit can then be applied to the full image, to visualize locations and relative abundances of the components within that image.

Absolute concentration cannot be determined this way without comprehensive data pre-treatment or post-treatment, such as pixel variability correction, division by fluorophore quantum yields and interactions with other fluorophores in the system, excitation source uniformity, and other factors which fall beyond the scope of this work but present a valuable direction for future investigation.

The following section will describe methods used to select data to use for an initial or loading PARAFAC analysis, which is then applied to a full image.

5.4 Pixel Selection

Pixel selection is an important preprocessing step for F-EEM image analysis using PARAFAC decomposition. A typical F-EEM dataset contains *n* spectra, each with an excitation and emission dimension, usually acquired using a fluorometer, with spectra either as replicates or as samples taken along a varying parameter. In an F-EEM image, however, not every spectrum (pixel) contains fluorescence. Additionally, with 65,536 spectra per F-EEM image taken using the MSC, and 327,680 pixels per F-EEM image taken using the HSC at low-resolution, selecting only those pixels containing the most reliable data is important to create a better loading fit more quickly. Additionally, PARAFAC cannot accurately model noise or scatter as it is the wrong order [18, 93]. Reducing the number of pixels which contribute primarily background and/or noise and/or scatter allows for the PARAFAC decomposition to focus on the most meaningful fluorescent components. I have attempted many methods for reducing the size of the dataset and/or choosing only the pixels exhibiting the most meaningful fluorescence from an image to obtain a high-quality initial fit, and these will be discussed in the following sub-sections.

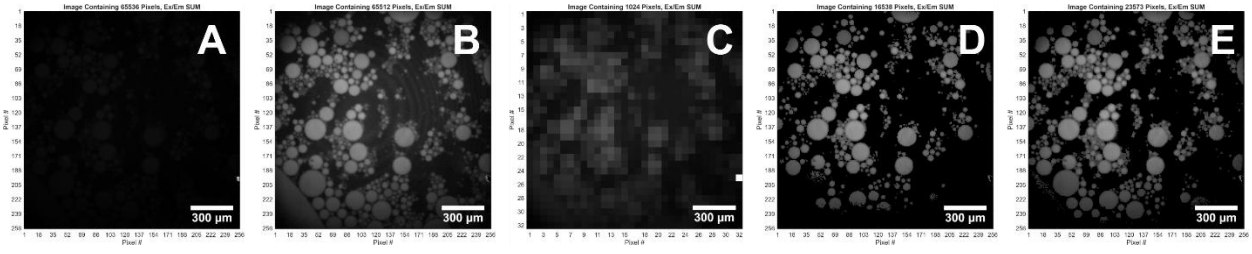

Figure 5.3. Application of different preprocessing methods on an F-EEM image. A) Original image, B) pixels below a maximum threshold are set to NaN (removes brightest pixels), C) groups of 8 pixels summed in both x and y pixel dimensions, and pixels above a D) minimum threshold and E) above a difference in excitation and emission variance, are set to zero.

5.4.1 Pixel Group and Image Region

Pixel Grouping

The first technique uses spatial groups of pixels, choosing either a representative value from one of those pixels or their sum. This reduces the dataset size by the number of pixels per group, $1/n$ and increases the SNR when pixels are averaged or summed. This works well for images which have features larger than the size of the groups (Figure 5.4). For example, if pixels are separated into groups of $n=8$ (8 × 8) and the smallest feature size is 4 × 4, the signals from different objects are added together and cause a more difficult fit. However, if the largest object size is approximately the order of the pixel groupings, this reduces the size of the dataset and leads to a faster and more accurate fit. When objects are large enough, this is a fast and simple way to reduce an F-EEM image from 32 MB [256 × 256 × 8 × 31] to 8 MB [64 × 64 × 8 × 31]. The optimal size of the group may be obtained using a spatial Fourier transform, although in this work it was done by estimation.

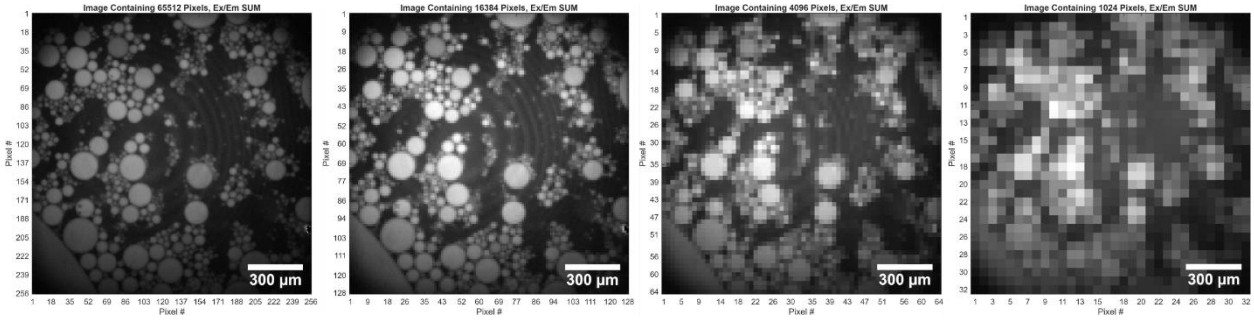

Figure 5.4. Effect of differing number of summed pixels per group. From left to right, the number of summed pixels per group in the x and y directions is 1, 2, 4, 8. With 8 pixels in each direction (64 pixels total per group), the features cannot be properly resolved and the spectra become difficult to decompose.

To demonstrate the time advantage of using fewer pixels to analyze data using PARAFAC using differing numbers of pixels, a piece of agarose gel containing fluorescein and rhodamine B was placed in an acidic solution and monitored over time. In this case, the object is much larger than the pixel sections and the images were acquired using the MSC with the DMA-PLS as the excitation illumination (Appendix A.19).

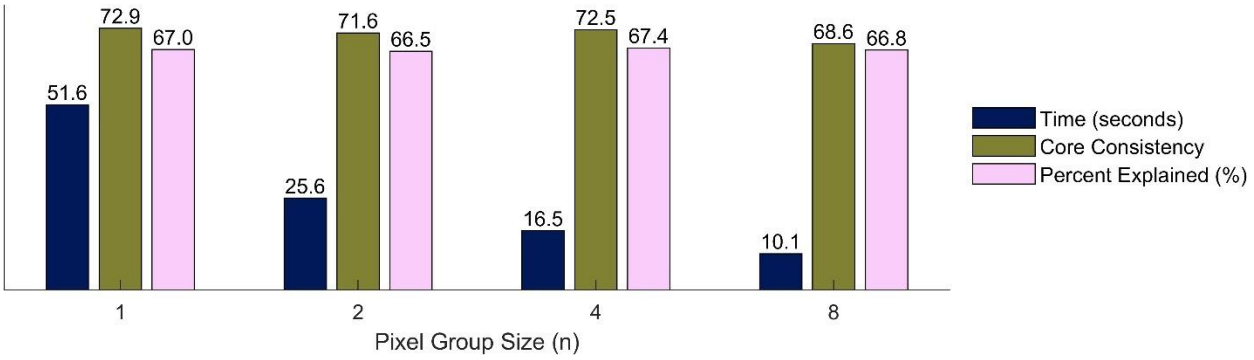

Figure 5.5. Effect of differing numbers of pixels used in an initial blind PARAFAC fit.

Fits were done using the same parameters and the data used every n^{th} pixel, where the fits differed in the number *n* pixels. The time in minutes and the fit quality checks core consistency (CC) and percentage explained variance (PE) are shown in Figure 5.5. This demonstrates that even with every 8^{th} pixel used, the fit remains similar in quality, shown by the PE and CC values, while the fit time is reduced greatly using a smaller dataset.

Image Region. Selecting a small region of interest (ROI) of an image is another simple method for reducing the size of the original dataset to use in a PARAFAC analysis of an F-EEM image. An ROI is chosen from a 2D image representing the mean excitation and emission dimensions of an F-EEM image and those coordinates are applied to the whole dataset. Use of an ROI is limited to situations in which each fluorophore in the entire image is also present in the smaller region. When this condition is satisfied, using the reduced-size dataset from the ROI is a very simple way to create a loading fit which can then be applied to the full image.

5.4.2 Filtering by Statistical Parameters

Statistical parameters guided the next approach for reducing the dataset size by retaining only the most information-rich pixels. The minimum, maximum, median, mean, mode, overall variance, variance in excitation and emission, and standard deviation were calculated for each pixel in an F-EEM image. Select EEMs with the parameters displayed were shown for a user to manually examine and choose which parameters would best filter the data, as shown in Figure 5.6.

Additionally, an image with removed pixels shown in white is displayed as well as an EEM of the mean over all the remaining pixels. The user can then set a filter to retain pixels either above or below a threshold for that parameter. A few parameters are described to illustrate the process.

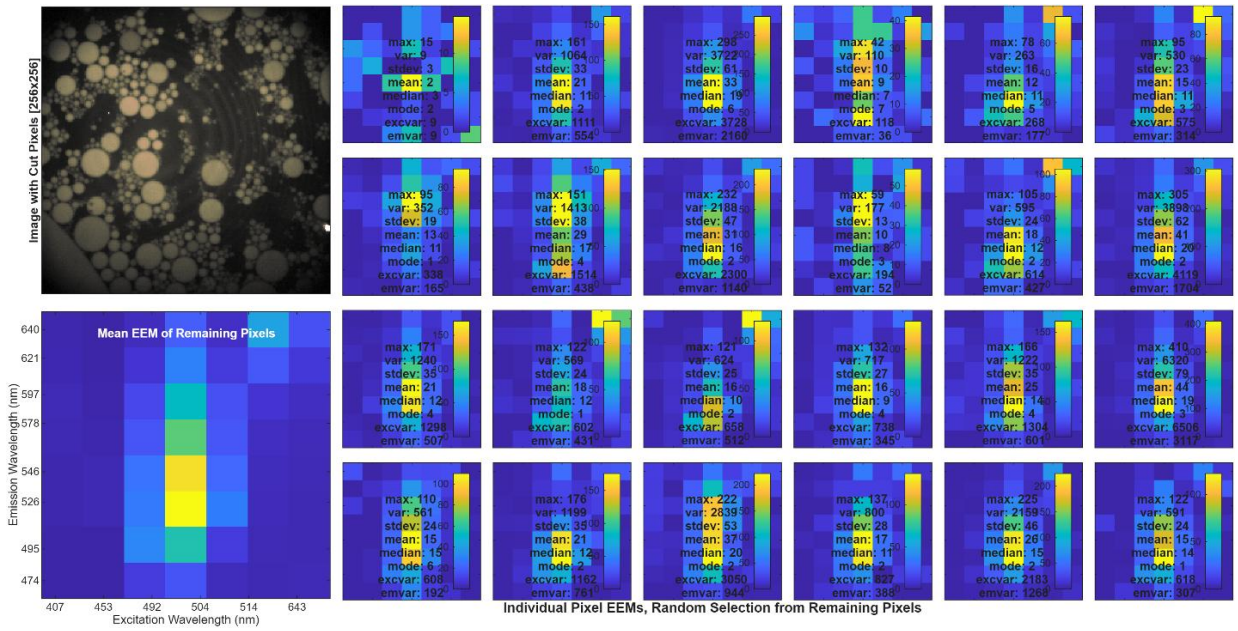

Figure 5.6. Pixel EEMs and their associated parameters to display the result of and to aid in the choosing of statistical parameters to use for pixel selection using the *preprocessing_pixels* function. In this example, pixels above a value of 750 have been set to NaN and appear white in the image.

Examples. The simplest measure, an intensity threshold, will remove pixels above or below a given value to remove noise or strongly scattering artefacts, respectively. Noisy pixels should be removed as they do not contribute to the fluorescence signal, while pixels with strong scatter, often caused by pieces of dust or imperfections in a glass slide for a microscope image should be removed as they strongly affect the intensity scaling of the remaining pixels, which affects the quality of the PARAFAC analysis. Pixels with a small signal based on intensity are removed in Figure 5.7, as are a few pixels which were very brightly scattering.

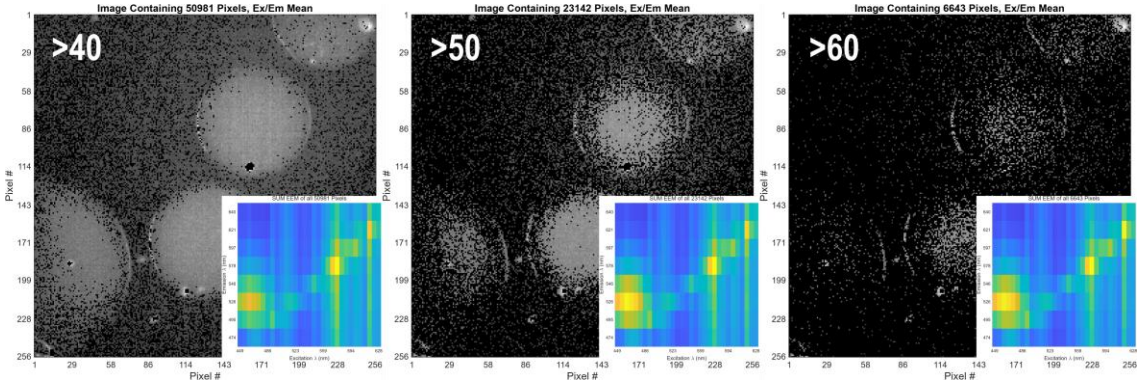

Figure 5.7. Threshold using a maximum value. Remaining pixels are above the threshold value shown in each image. The mean EEM for each image (the remaining pixels) is shown overlain on the black and white image. The brightest pixels are also removed (the small central dot on the droplets). Images were acquired using the MSC and DMA-PLS of a fluorescent emulsion under Olympus CK2 microscope with a 10x objective lens.

Other parameters, such as the variance in the excitation and/or emission dimension, are useful in identifying pixels which consist primarily of either noise or optical scatter, which will typically both have low or high variance. Pixels with stronger fluorescence signals will often have different variance in the excitation and emission dimensions, so this can be a method for selecting those pixels with stronger fluorescence. The difference between setting pixels below a simple minimum value threshold and using the difference between the excitation and emission variances is shown in the comparison of Figure 5.3d and Figure 5.3e, respectively.

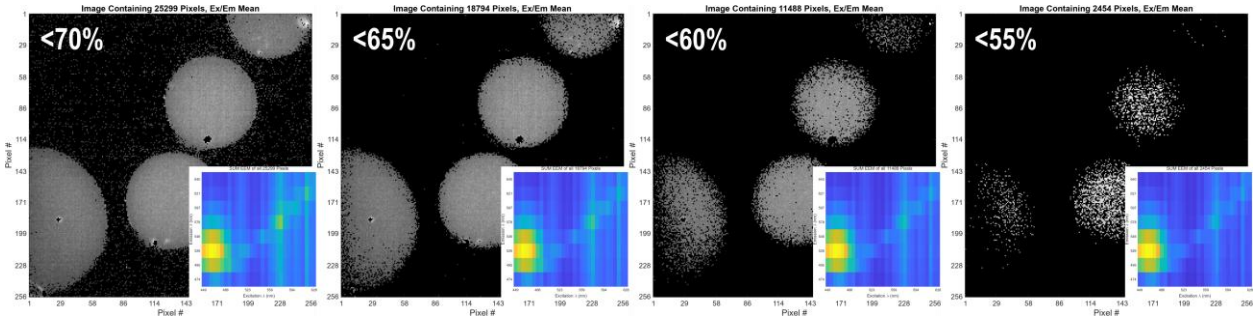

Figure 5.8. Threshold using a difference in original to Rayleigh-removed data. Thresholds are shown in percentage of difference between the original and the Rayleigh-cut datasets. Multiple values demonstrate the effect of various values of the threshold. Images were acquired using the MSC and DMA-PLS of a fluorescent emulsion under Olympus CK2 microscope with a 10x objective lens.

Another parameter differentiating noise, scatter, and fluorescence uses the difference in the mean of the raw and Rayleigh-removed datasets. When that difference is low, the contribution of the Rayleigh-scattered light to the overall EEM was low, suggesting either a noisy or strongly fluorescent pixel. This is demonstrated in Figure 5.8 for different threshold values (percentages). Comparison of Figure 5.8 and Figure 5.7 shows how useful the difference in the Rayleigh-cut data can be as a threshold for choosing pixels containing good fluorescence data pixels for an initial fit.

Functions. The function for applying these parameters is *preprocessing_pixels* and uses an F-EEM image shaped as pixels × emission × excitation and variable arguments passed as 'parameter', 'above/below value', 'value'. The function has the following outputs: 1) an image of the same dimensions as the input image using NaN or zero values for removed pixels, 2) an image containing only the pixels that were not removed—often used for the reduced size PARAFAC analysis, and 3) a binary mask of the image size specifying which pixels are to be kept. The *preprocessing_pixels* function uses a function, *statParamsCampic* which calculates statistical and other parameters. The inputs are the same reshaped image, a specification of NaN or zero values to be used for any zeros in the input image which can affect the application of some parameters such as mean. Two additional optional parameters are images with matching dimensions to the

input, one with the Rayleigh-scatter removed, and the other containing only the removed Rayleigh-scatter. These are used to determine the difference between the cut and non-cut data.

Demonstration of Parameters. The function *plotImg_meanEEM_25pxEEMs* is used to display the EEMs from 25 pixels with select parameters overlain, along with an image of the remaining pixels and their average EEM. The function takes the original reshaped image size as an input, along with the pixel mask and wavelengths for the excitation and emission dimensions. Figure 5.6 shows the function output.

Graphical User Interface. These methods have been combined in a GUI developed in MATLAB for image processing.

5.4.3 Pixel Mapping with Principal Component Analysis

The final method for pixel selection discussed uses a threshold value obtained using a principal component analysis (PCA) fit of an F-EEM image.

The dimensions of the raw image will have to be changed to use a PCA fit. For an F-EEM image containing *N* pixels, each pixel EEM is a matrix represented by:

$$X_n \in \mathbb{R}^{I \times J}, n = 1, ..., N \quad [5.2]$$

where *I* and *J* are the number of excitation and emission wavelengths, respectively, and $X_n(i, j)$ is the fluorescence intensity at excitation i and emission j. The full dataset can then be described as a third-order tensor $X \in \mathbb{R}^{N \times I \times J}$. To satisfy the 2D requirement of a matrix for PCA, each EEM is unfolded or vectorized into a single vector $x_n = vec(X_n)$, where $x_n \in \mathbb{R}^{IJ}$. This provides excitation-emission pairs:

$$x_n = \left[X_n(1,1) \quad X_n(1,2) \quad \ldots \quad X_n(I,J) \right] \in \mathbb{R}^{IJ} \quad [5.3]$$

The PCA input matrix stacks each sample row vector where each row represents one sample, and each column corresponds to a specific excitation-emission wavelength pair.

$$X_{PCA} = \begin{bmatrix} x_1 \\ x_2 \\ \vdots \\ x_N \end{bmatrix} \in \mathbb{R}^{N \times IJ} \quad [5.4]$$

Effectively, each excitation-emission matrix with original dimensions $I \times J$ is vectorized by unfolding the excitation and emission dimensions into a vector with length $I \cdot J$. These vectorized

EEMs are assembled into an $N \times IJ$ matrix where each row corresponds to a sample and each column represents a specific excitation-emission wavelength pair.

Pixels containing the most information-rich signals are often grouped into the first one or two components, followed by less meaningful data such as scatter and noise (Figure 5.9). PCA preselection of information-rich pixels works best with raw data—once the Rayleigh light has been removed, PCA explains the actual variations in the sample EEMs, which is not what it is being used for at this step.

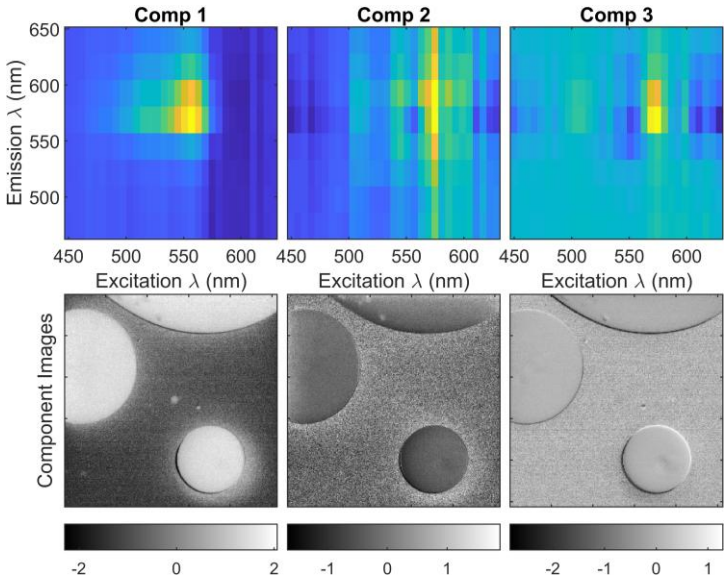

Figure 5.9. Principal component analysis on a raw F-EEM image. Top row shows a 1st order approximation of the spectral components, and the bottom row shows the scores reshaped as images.

A threshold, below which pixel values will be discarded or set to zero or NaN, is chosen based on the values provided in the PCA fit. To apply this to an image, a binary mask is created containing the pixels to be kept and discarded, of the original size of the image dimensions, in this case 256 × 256. In the example shown in Figure 5.9, a value of 1 might be chosen, which would produce an image and EEM as shown in Figure 5.10.

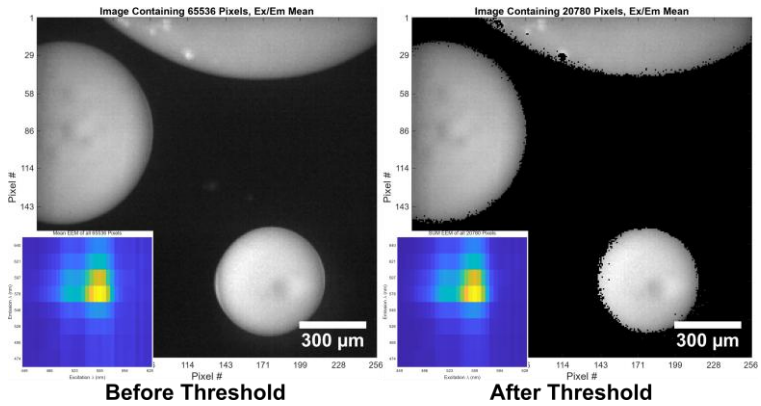

Figure 5.10. Principal component analysis (PCA) as a pixel threshold. Black and white images represent the mean excitation and emission of each pixel, and the coloured inset represents the mean F-EEM for all the pixels in the image. (**left**) Raw image taken with the DMA-PLS and 8-channel multispectral camera, (**right**) after a threshold using scores from a PCA fit.

Creating a binary mask of pixel values to be kept or discarded is a consistently successful method to remove noisy pixels to keep only the fluorescence or information-rich pixels in an F-EEM image. Figure 5.10 shows the data contained within a raw F-EEM image (left) and one which has used the PCA map threshold method to remove pixels with significant noise. The difference in the mean F-EEMs demonstrates the higher-quality pixels that remain after the threshold has been applied. Additionally, the creation of a mask in this form allows one to re-map the removed pixels onto images as shown here, even though the spatial element would otherwise be destroyed.

Conclusion

Selecting only those pixels containing the most valuable information is a useful way to reduce the size of a large dataset for PARAFAC analysis, resulting in better and faster fits. These fits using a selection of pixels are then applied as loading vectors for an analysis of the entire *unprocessed* image. Other methods of loading vectors for PARAFAC analysis of F-EEM images are shown, as were optimization methods for the large datasets in MATLAB. Preprocessing the data in the ways shown in this chapter have allowed us to obtain well-separated fluorophores in F-EEM images using multi- and hyperspectral cameras and Hadamard-multiplexed excitation light sources using the DMA-PLS and the LDA, as will be demonstrated in Chapter 7.

Chapter 6 Applications—Macroscopic Imaging

To demonstrate the separation ability of the 8-channel multispectral camera (MSC) and DMA-PLS for spatially overlapping fluorophores, we examined dye mixtures in capillaries. This work was performed after using the initial setup of the camera by Oren Katz and is described in his M.Sc. thesis [286]. Sarah Klose and I performed this experiment to further demonstrate the separation ability of the system. Our work has been published [219] and this chapter of the dissertation uses several images similar to those which appear in the paper. In our F-EEM imaging systems, we vary the number of both emission and excitation bands. This experiment demonstrates that the 8-channel MSC with a 31-channel DMA-PLS allows for distinction of up to three spatially overlapping fluorophores. Because the emission dimension is very coarse in comparison to a typical spectrometer used for fluorescence, we use numerous excitation bands to aid with the distinction of fluorophores. Four rhodamine dyes were mixed to create primary, secondary, and ternary solutions in separate glass capillaries. The capillaries were placed side-by-side and illuminated using the DMA-PLS described in Section 3.2 and the emission was captured by the MSC described in Section 4.1. Figure 6.1 shows the instrumentation and data were analyzed using PARAFAC [219].

6.1 Experimental Setup

Rhodamines 6G (R6G), B (RB), 110 (R110), and sulforhodamine 101 (SR101) dyes were selected based on their excitation and emission wavelengths, similar fluorescence quantum yield, and their solubility in ethanol. Neat solutions of the dyes in ethanol (200 μM) were added to separate 1 mm (outer) diameter glass capillaries. To create dye mixtures each with a concentration of 200 μM in the remaining six capillaries, equal aliquots of 400 μM and 600 μM solutions were used to create secondary and ternary mixtures, respectively. The combinations are shown in Table 6.1.

Table 6.1. Dyes in each capillary in the macroscopic F-EEM imaging setup. Total concentration of each dye in each of the ten capillaries is 200 μM in ethanol.

		Capillary #									
		1	2	3	4	5	6	7	8	9	10
Dye	R6G	•				•	•		•	•	•
	RB		•			•			•	•	
	SR101			•			•	•		•	•
	R110				•			•	•		•

The ten capillaries were held side-by-side using marking tape and suspended in front of the MSC using a cylindrical lens mount (CH1A, Thorlabs). The capillary setup was illuminated using the DMA-PLS to spectrally disperse and select wavelengths of a white and blue light-emitting diode (LED). The blue LED (M470F4, Thorlabs) was added to fill the gap left by the emission spectrum of the phosphor coating over the blue LED used to create the white LED (MCWHF2, Thorlabs). The fiber bundle uses linearly aligned 100 µm core fibers (FVP100110125 Polymicro Technologies) to enter the spectral dispersion portion of the DMA system, as described in Oren Katz' thesis [286]. The chosen spectral regions are reflected from the DMA to a second fiber bundle, as described in Section 3.2.4. For this setup, a size 31 Hadamard Paley S-matrix was chosen for the illumination, because it provides acceptable values for both FWHM and acquisition time (31 masks × 500 ms exposure time = 15.5 seconds). The MSC was equipped with a 50 mm fixed focal length lens (V5024-MPZ, Computar) and a +7 diopter to increase the lens magnification. Images were taken with no adjustments to either the gain or black level of the camera.

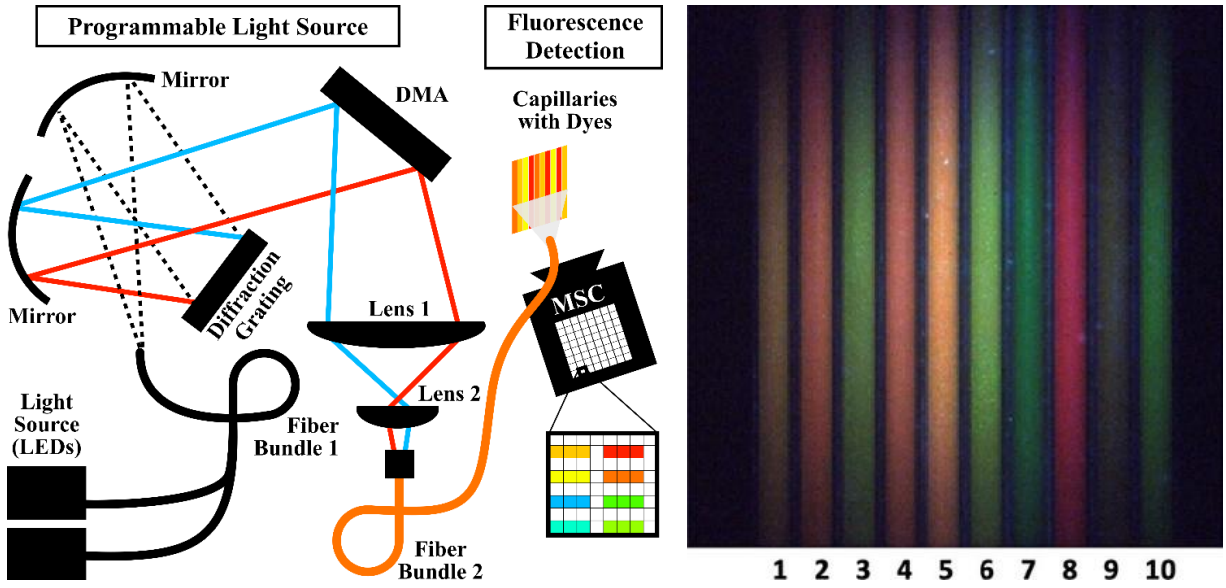

Figure 6.1. Instrument setup: DMA-PLS and multispectral camera for F-EEM imaging. Excitation via the digital micromirror array programmable light source, DMA-PLS, using white and blue LEDs as the white-light source. Emission collection and imaging of capillaries containing dyes via a multispectral camera (MSC) with eight colour channels (**left**). False-coloured image of the 10-capillary dataset, illuminated via flashlight, and displayed using a single red, green, and blue channel from the MSC image (**right**).

To visualize the differences in colour of the capillaries, Figure 6.1 (right) was created by choosing a single red, green, and blue channel from the eight channels of the multispectral camera, to simulate a colour image. The sample for the false-coloured image was illuminated using a flashlight for greater colour definition, as the programmable light source provides a dimmer image.

6.2 Data Analysis and Results

The raw F-EEM spectra of each dye acquired using the MSC, chosen from ROIs in the analyzed image for capillaries 1, 2, 3, and 4 (R6G, RB, SR101, R110, respectively) are shown in Figure 6.2.

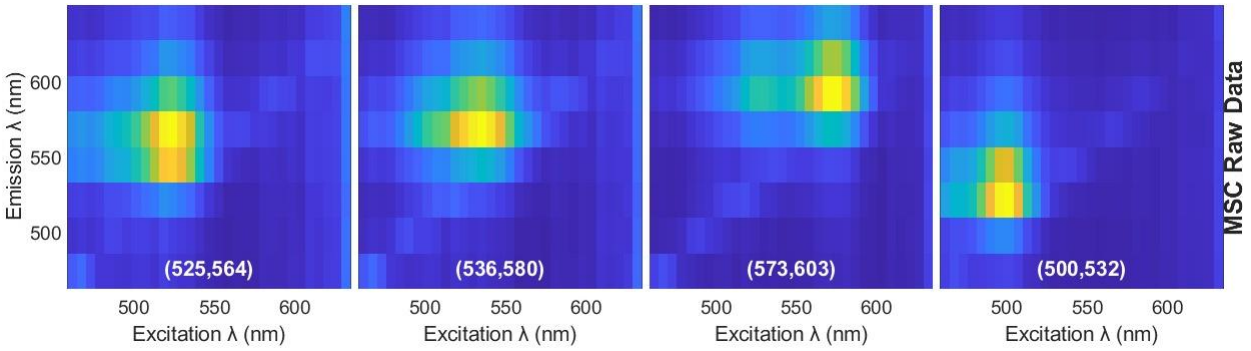

Figure 6.2. F-EEM signatures of the neat dyes used in the 10-capillary dataset taken with a multispectral camera (MSC). The mean F-EEM of all the pixels in a capillary region corresponding to that dye are shown. F-EEM images were taken using a programmable light source (DMA-PLS). All spectra were excitation corrected, described further in Figure 6.4.

The data from all the capillaries were fit as a sum of four components using a PARAFAC (parafac2) [321] model, after the Rayleigh light had been removed within 20 nm of each excitation wavelength. The intensities of the spectra were corrected using the relative intensities of the excitation wavelengths obtained from an alignment file, before the fit was performed. EEMs of each component found by the PARAFAC analysis are shown in Figure 6.3.

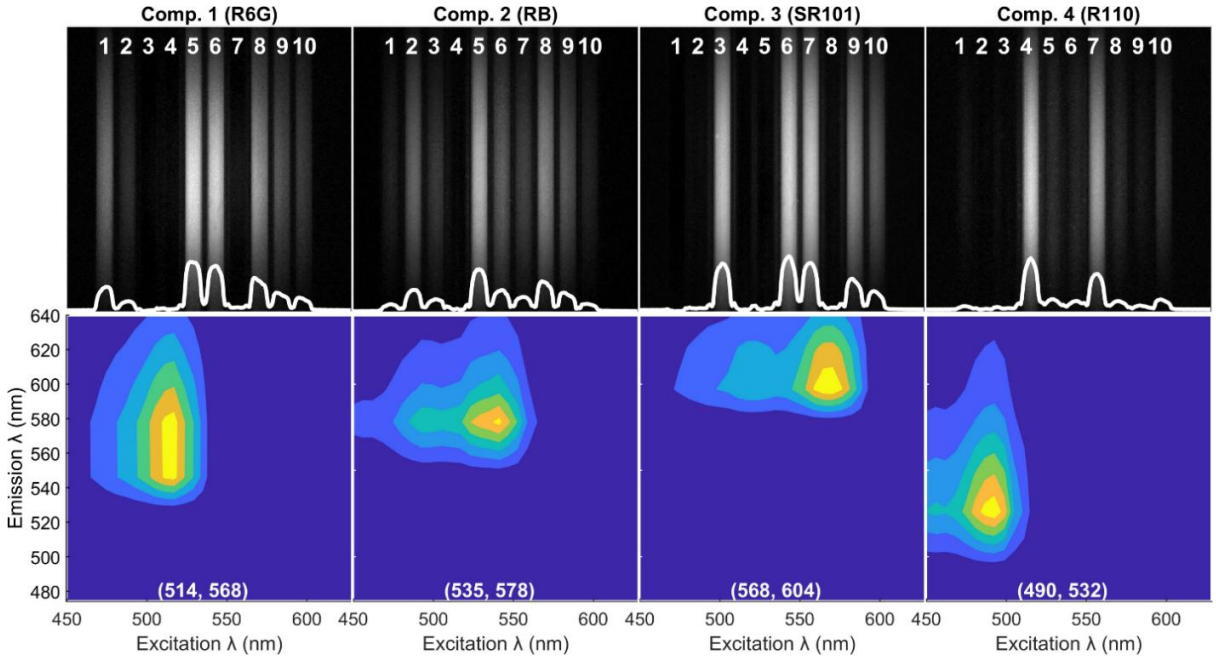

Figure 6.3. PARAFAC analysis of 10-capillary dataset. Image taken with MSC of capillaries containing mixtures of four dyes. Four-component PARAFAC analysis of ten capillaries of mixtures of R6G, RB, SR101, SRB (Table 6.1). (**top**) component scores for each pixel to demonstrate in which capillary each component (dye) appears, white line is a plot of the summed pixel intensities for each column of the above four component score images. (**bottom**) Component EEMs.

Based on the F-EEM spectra of neat 200 μM solutions of the dyes in ethanol (Figure 6.3) components A, B, C, and D are assigned as R6G, RB, SR101, R110, respectively.

The amount a particular component EEM contributes to the EEM of a pixel is given by the "score". Plotting the scores for each component provides the spatial distribution—in this case, which of capillaries 1–10 the dye is present in. Overlain on the black and white component images is a white line plot showing the summed intensity values for each column of pixels in the image.

In theory, it is possible to use this technique for quantitative measurements, if experimental and post-processing corrections are made. First, each pixel must be illuminated evenly, so that each pixel receives the same excitation intensity spectrum. This would allow for pixels to be corrected for accurately using the excitation corrector. For the purposes of identifying components, it seems that having slight variation in the illumination at different areas does not impact the fit, however if it were to be quantitative, an even illumination would be required. Second, because the MSC uses a CMOS sensor, each pixel has its own readout electronics, each associated with varying levels of signal and noise. The differences between the pixels would have to be corrected for, in a "white field" correction, which would also account for any variations in differences in the filters.

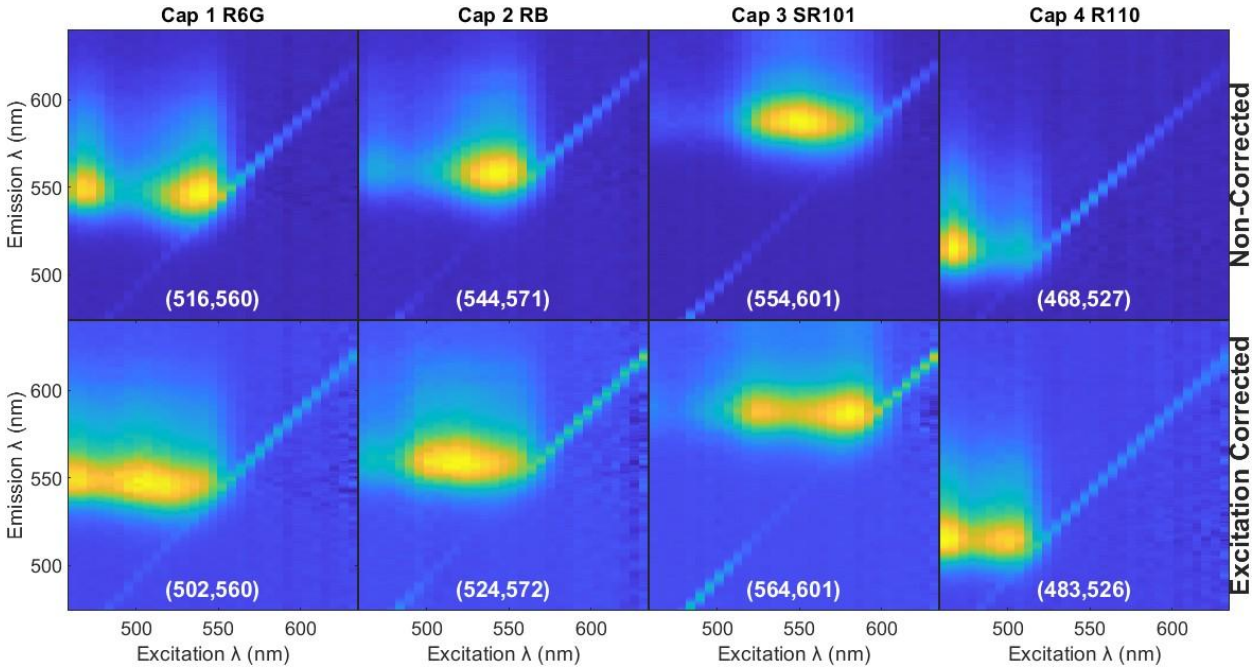

Figure 6.4. Effect of excitation correction on raw EEM spectra collected using a spectrometer. Centroids of the top 30% of the peaks are shown in white text in the form (excitation wavelength, emission wavelength) (nm). Spectra were collected using DMA-PLS source with a bifurcated fiber bundle to an Avantes spectrometer. Excitation corrected spectra were divided by the alignment file containing the intensities for each excitation wavelength.

Correcting the excitation wavelength intensities is important for creating an F-EEM with an accurate excitation dimension. Figure 6.4 shows F-EEM spectra after before and after correcting for the excitation spectrum of the neat dyes used to fill capillaries 1, 2, 3, and 4.

The difference in the excitation-corrected spectra demonstrates the importance of the excitation correction leading to more complex and in some cases bimodal F-EEM spectra. Expected excitation and emission values for the four dyes studied here, in ethanol, are shown in Table 6.2.

Table 6.2. Literature values for maximum excitation and emission wavelengths of fluorophores in ethanol. These values were obtained from online spectral databases, referenced in the table.

	Maximum Excitation λ (nm)	**Maximum Emission λ (nm)**
Rhodamine 6G [322]	530	551
Rhodamine B [323]	546	567
Rhodamine 110 [324]	500	522
Sulforhodamine 101 [325]	576	590

The excitation correction can be flawed when the emission fibers are collecting a region of the sample that was illuminated non-uniformly. A non-uniform excitation may occur when fibers are pressed closely to a vial, and the light in each fiber is different—as may have been the case for the collection of the neat F-EEM spectra by the Avantes spectrometer through the bifurcated fiber bundle, shown in Figure 6.4. The uneven illumination and sampling results in an excitation corrector with inaccurate values, demonstrated in Figure 6.4, where application of the excitation correction results in a distortion of the excitation spectrum. This distortion is evidenced by the deviation from the expected values in Table 6.2 and the F-EEM spectra acquired of the capillaries illuminated evenly (Figure 6.2).

Whether the excitation correction is done before or after a PARAFAC fit does not make a difference to the component EEMs, as shown in Figure 6.5. This is because the correction is a simple division, so does not affect the weighting for fitting. Component EEMs from the PARAFAC analysis without excitation correction and with correction before and after running the PARAFAC fit are compared in Figure 6.5.

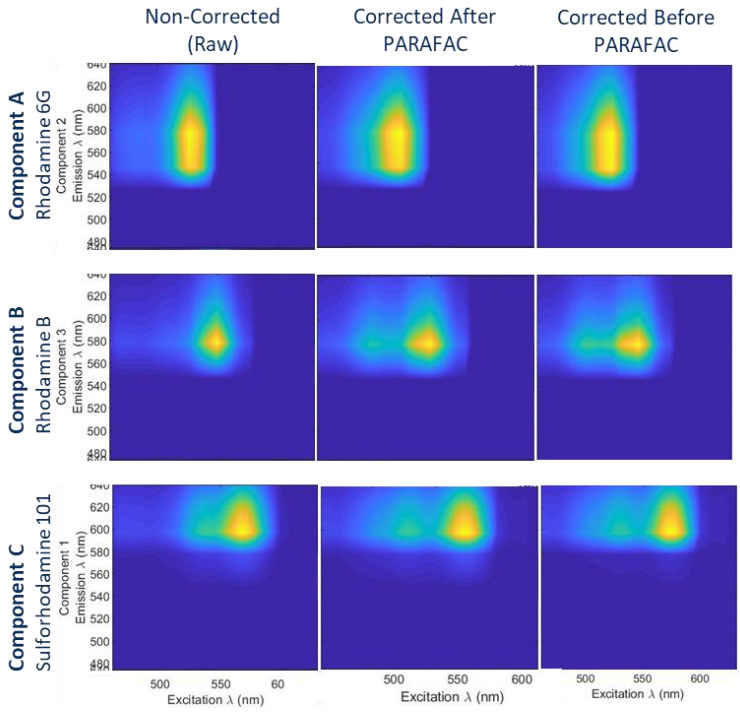

Figure 6.5. Effect of excitation correction on EEMs before and after a PARAFAC fit. Spectra are plotted using contourf which smooths levels. PARAFAC fit used F-EEMs acquired using the 8-channel MSC and DMA-PLS source, and only the first three components (first three capillaries) are shown in this plot.

Based on the component EEMs similarity to the expected excitation and emission maximum values, and the capillaries in which each component appears, we conclude that the analysis demonstrates that we can identify the correct locations for each component. We also note that inner-filter effects generate fluorescence signatures of components in capillaries in which they are not in. This likely arises from overlap of component signatures, and of scatter and transmission through the sides of the capillary walls, and of absorption of emitted fluorescence of another component, such as SR101 absorbing the emitted fluorescence from R110.

Conclusion

This test of the MSC and DMA-PLS demonstrated that the system could distinguish four spatially overlapping and spectrally separate components. Many of the potential applications of FLEEMSI are on a microscopic scale, so we adjusted the system to allow for microscopic imaging, and those results are demonstrated in Chapter 7.

Chapter 7 Applications—Microscopy

Fluorescence EEM spectral imaging (FLEEMSI) microscopy is a novel extension of the EEM imaging approach described in the previous chapters. We think that the advantages of this method for identifying complex mixtures of fluorophores will provide a valuable research tool to aid in areas focusing on, for example, medical samples, agriculture, and the environment. Any field of imaging science in which a sample is fluorescent and heterogeneous on a microscopic scale may be studied, which includes most of conventional fluorescence (biological and medical) imaging. To obtain F-EEM images through a microscope objective, the two programmable light sources discussed previously were used—the digital micromirror, DMA-PLS and the laser diode array, LDA-PLS. This chapter describes several illumination configurations, including brightfield-, darkfield-, frustrated total internal reflection-, and shallow angle-illumination, and follows with a comparative analysis on the spectral resolution and memory requirements of data obtained using different light sources and emission detectors (Section 7.1). Then, the usefulness of F-EEM microscopic imaging is demonstrated for fluorescent powder analysis (Section 7.2) and the separation ability of the multi- and hyperspectral cameras using emulsions (Section 7.3). Post-processing computational approaches to improving the temporal and spectral resolution of the MSC are described in Section 8.1 and Section 8.2, respectively.

7.1 Microscopy Instrumentation

This section describes different sample illumination techniques for F-EEM microscopic imaging using our homebuilt programmable light sources. For each method I will describe the contributions made by me and collaborators to application of the technique for F-EEM imaging and will refer the reader to the relevant background described in the introduction. Part of this work was done in collaboration with other group members who will be credited in the respective sub-sections.

The simplest illumination method is brightfield illumination—common for conventional microscopic imaging. It is not expected to work well in fluorescence imaging due to the large light background. Nevertheless, we tested brightfield illumination to ensure the simplest option would not work before proceeding with more complicated options. We do not describe this failed attempt.

Illumination via frustrated total internal reflection using fiber-coupled light in a microscope slide is described first, followed by darkfield illumination using a ring of fiber-optic emitters. We finally describe shallow angle illumination via a liquid core waveguide. Application of these light sources to different F-EEM microscopy and multi- or hyperspectral camera systems, and the associated spectral resolution of the acquired data, follows the description of the different light sources.

7.1.1 Frustrated Total Internal Reflection

Frustrated Total Internal Reflection, FrTIR, was briefly described in the introduction Section 1.3.3. Light is delivered to a sample area via total internal reflection, in a planar waveguide such as a microscope slide. In most total internal reflection fluorescence microscopy (TIRFM) setups the refractive index of the sample is intentionally lower than that of the substrate so that most of the waveguided light remains trapped in the waveguide. Excitation of fluorescence in the sample would then only be possible by interaction of the fluorophores in the sample with the evanescent wave of the guided light. This is the case for aqueous samples (n=1.33) on a glass microscope slide (n=1.52). Light undergoes refraction into the sample when the sample has a higher refractive index than the waveguide or substrate—when the angle of refraction is higher than the critical angle in the waveguide. Although some light (below the critical angle) may still create an evanescent field, a much greater portion of the fluorescence excitation will instead arise from the refraction into the sample from the slide. This section describes how the materials were chosen and practical applications of each setup using the two HT programmable light sources.

FrTIR illumination was used because an epifluorescence configuration (Figure 1.22) proved too complex for effectively aligning all fibers from the light source into a single location, due to the requirements for collinearity and the inclusion of filters. Alternative approaches, such as free-space coupling may have been possible, but because we were retrofitting a microscope, this presented many practical challenges. We required a relatively simple way to illuminate the sample without directing excitation light through the objective lens. One way of doing this for fluorescence microscopy is illumination of the sample via the evanescent field generated upon TIR of light at the glass (microscope slide)-sample interface. We also note that this approach reduces the risk of photobleaching because of the comparably small intensities incident on the sample.

Total Internal Reflection

Light rays with incidence angles above the critical angle (θ_c) will undergo TIR at the glass-air, glass-water, or glass-oil interfaces. Figure 1.25 shows the difference in the angle below which TIR occurs for these three interfaces with different refractive indices (n_i). For the interface between glass (n_1 = 1.52) and air (n_2 = 1.00), the critical angle is calculated as $\theta_c = \sin^{-1}(n_2 / n_1) = 41°$, whereas for the glass-water (n_2 = 1.33) interface it is $\theta_c = 61°$, and for glass-mineral oil (n_2 = 1.47) it is $\theta_c = 75°$. This means that only light at glancing angles (90°-75°=15°) is guided by TIR at a glass-oil interface.

This is important because the (acceptance) cone angle, θ_a of the excitation light exiting the fibers does not all fall within the 15° condition. From Equation [3.5], $\theta_a = \sin^{-1}(NA_{fiber} / n_m)$ where n_m is the n of the medium the light exits into.

$$\begin{aligned} \theta_{a(\text{air})} &= \sin^{-1}(0.39 / n_{air}) = \sin^{-1}(0.39 / 1.00) = 23° \\ \theta_{a(\text{glass\_slide})} &= \sin^{-1}(0.39 / n_{glass}) = \sin^{-1}(0.39 / 1.52) = 14.9° \\ \theta_{a(\text{idx\_gel})} &= \sin^{-1}(0.39 / n_{gel}) = \sin^{-1}(0.39 / 1.4646) = 15.4° \end{aligned} \qquad [7.1]$$

The calculations shown in [7.1] demonstrate that the angles at which light exits the fibers into air, a glass slide, and index matching gel (G608N3, Thorlabs) are 23°, 15°, and 15°, respectively. So, fluorescence excitation of an oil-based sample on a glass microscope slide using light coupled from a glass fiber first through air, occurs via refraction for light rays with θ_a between 15° and 23° and via evanescent illumination for angles between 0° and 15°. When index-matching gel is used, nearly all angles of light exiting the fiber ($\theta_{a(\text{idx\_gel})}$ = 15°) falls within the angles required for TIR from the glass slide to the oil sample (θ_c = 75° from the surface normal = 15°).

Experimentally, we observe that some amount of excitation light is refracted into the sample medium (*e.g.*, mineral oil). This indicates that excitation does not occur exclusively through evanescent illumination when the refractive index of the sample medium exceeds 1.47, *e.g.,* the oil samples. The sample medium could be changed to alter the illumination method—for example, a medium with a higher n could be used for more refraction through the sample while one with a lower n could be used for primarily evanescent illumination.

FrTIR Illumination using Fiber-Coupled Light Sources

Fibers carrying excitation light are held side-by-side at the short end of a glass microscope slide (25 × 75 × 1 mm) using an aluminum slide and fiber holder custom-built by machinist Chris Secord at the UVic Faculty of Science Machine Shop. The slide was conceptualized by Dr. Klose and me who created the initial designs, Dr. Klose guided the iterations of the holder designs and builds by the machine shop, and Yasaman Shahrestani characterized the impact the part had on fluorescence excitation. There are approximately ~5% Fresnel reflection losses at each of the glass-to-air and air-to-glass interfaces as the light exits the cleaved fiber end and enters the glass slide, respectively. To reduce the reflection losses, index matching gel (G608N3, Thorlabs) (n = 1.4646) was placed between the fiber ends and glass slide.

FrTIR Illumination using the DMA-PLS

The light from the DMA-PLS was coupled into a fiber bundle of 22 fibers arranged as a [6,5,6,5] hexagonal-packed rectangle (Figure 3.11). We could not detect fluorescence in this configuration using either the MSC or HSC. This may be in part due to the sample used to test the setup—an agarose gel containing fluorescein. The agarose (n=1.33) would have allowed for evanescent illumination instead of FrTIR, supplying a much weaker illumination than the oil-based emulsions that were tested with later setups. It would be interesting to test this setup once again with the oil-based emulsions we are using currently. At the time this was investigated, darkfield illumination was attempted as an alternative that would allow more light from the source to be used for sample excitation.

FrTIR Illumination using the LDA-PLS

Our FrTIR setup for fluorescence imaging through a microscope is shown in Figure 7.1. The seven laser diodes in the laser diode array (LDA) are individually fiber-coupled using 400/440 μm multimode fiber (FT400UMT, Thorlabs) and SMA connectors on the input (laser) side. The output (excitation) side of each fiber is cleaved and bare, to be held in the slide holder described below.

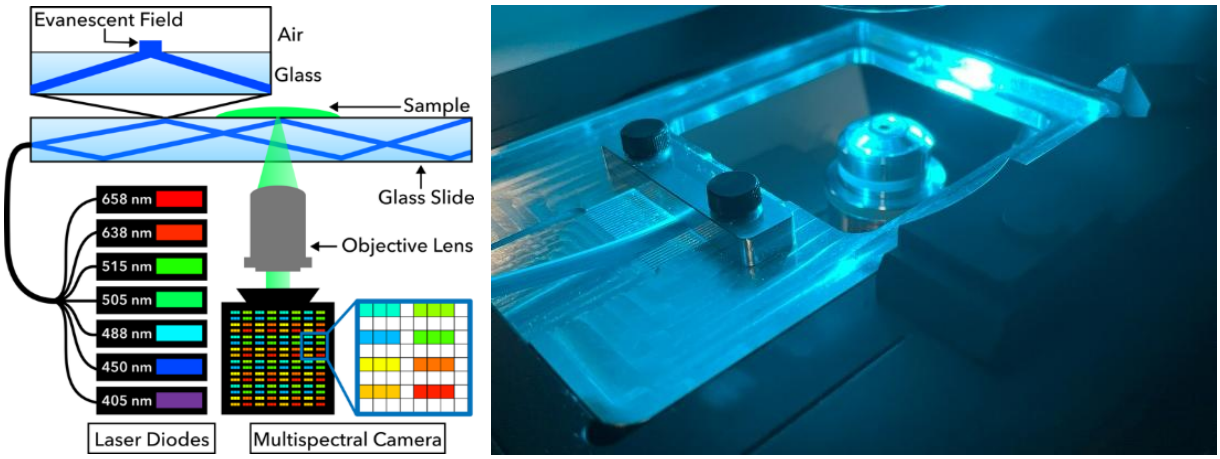

Figure 7.1. Instrument setup: evanescent illumination on a microscope using a laser diode array, for F-EEM imaging using a multispectral camera (Section 4.1). (right) Aluminum holder for cleaved fibers of the light source and for the microscope slide, used for evanescent illumination, mounted on a Zeiss Axiovert 200 inverted microscope.

The reflectivity of the aluminum appears to reduce light loss at the sides of the microscope slide, as the light escaping the slide from the short end opposite the fiber entrance is reflected back into the slide. Yasaman Shahrestani demonstrated that the aluminum slide holder reduced light loss at the sides of the microscope slide, increasing the overall light within the slide available for evanescent illumination of the sample. The results of these tests will appear in her M.Sc. thesis.

7.1.2 Darkfield Illumination

As discussed in Section 1.3.1, darkfield illumination directs only oblique light rays onto a sample, so all light entering the objective is either scattered by the sample or due to luminescence. The excitation light is angled such that it does not enter the objective lens for imaging. When the DMA-PLS was used in a typical darkfield illumination configuration, I found that removing the large portion of the input light beam resulted in a source that was too dim for fluorescence detection. To lessen that loss of expensive photons in blocking the center of the light beam, we instead used a ring of fibers coupled to the source to simulate the ring created in darkfield illumination. To reduce the losses associated with fiber-coupling the DMA-PLS we used shallow angle illumination—not a true darkfield illumination technique, but one which employs similar principles. These experiments are briefly described below.

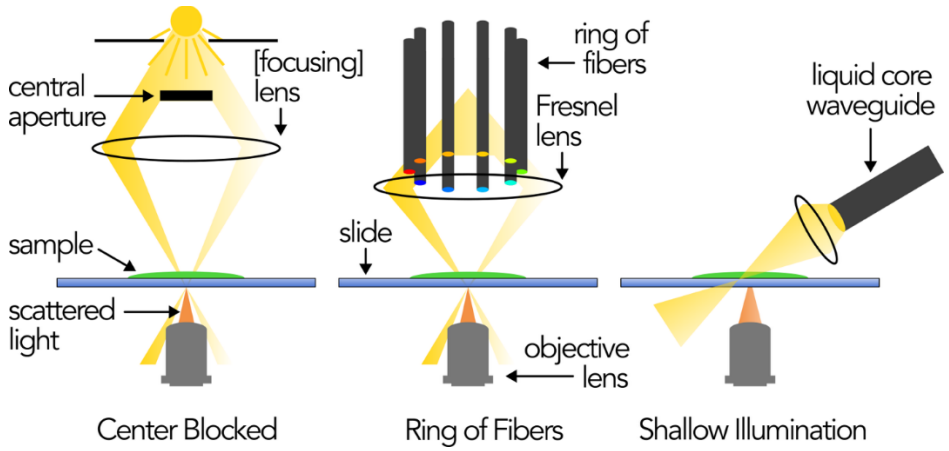

Figure 7.2. Darkfield illumination configurations for microscopy. Note that "scattered light" in this case could be the same for fluorescence. Only the general light path is shown—optics for collimation, focusing, and flat-field correction are omitted.

Typical Darkfield Illumination

Darkfield illumination was first tested using an Olympus CK2 inverted microscope with a standard circular aperture to block the central light rays, leaving only the outer rays for sample illumination (Figure 7.2, left). We observed weak fluorescence for a bright fluorescent dye using the microscope's built-in halogen lamp.

The white light from the halogen lamp cannot provide information about the excitation spectrum of the sample, and to acquire F-EEM spectra, we therefore replaced the halogen lamp with the fiber-coupled DMA-PLS. Unfortunately, we could not detect any measurable fluorescence with the DMA-PLS and the circular aperture setup. This is likely because the central aperture simply blocked too much of the excitation light. Note that the DMA-PLS is significantly dimmer than the halogen lamp. Because we were able to detect fluorescence in a macroscopic imaging setup (Chapter 6) and the images acquired with brightfield illumination were saturated, it seemed likely that the sample could be effectively excited without discarding such a large fraction of the light.

Darkfield Illumination using a Ring of Fibers

To avoid wasting photons by blocking the central portion of the light to form a ring of oblique rays, the fibers from a fiber-coupled source were instead arranged in a ring. This work was done in collaboration with two group members—Dr. Klose, a former post-doctoral researcher and Yasaman Shahrestani, a current master's student. The optical simulations and practical tests for different combinations of ring diameters and various collimation and focusing optics will be

included in the M.Sc. thesis of Yasaman Shahrestani, and only the final version and my contributions will be included here.

Setup Overview

Dr. Klose tested different ring diameters and lens combinations to produce a small focal spot on the sample to approximately match the field of view and maintained a sufficient divergence such to prevent the excitation light from entering the objective lens. Based on these results, a 12 mm ring diameter and a Fresnel lens were chosen.

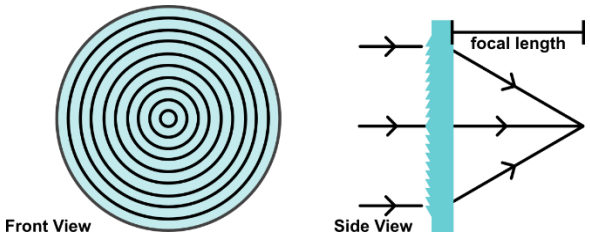

Figure 7.3. Diagram of a Fresnel lens showing the front and side views.

Fresnel Lenses

Perhaps best known as the lenses used in lighthouses, Fresnel lenses essentially take the curvature of a spherical lens at a number of points along that surface and place each of those surfaces on a plane, creating a thin lens that simulates a very high-curvature (high NA) spherical lens (Figure 7.3). These lenses allow for a tight focus with a much smaller physical footprint than what could be achieved using a typical spherical lens. The Fresnel lens allowed a short distance to the sample and a quick divergence from the sample to the objective lens. The Fresnel lens used here is a 50.0 × 50.0 mm, 10 mm focal length acrylic Fresnel lens (13-457, Edmund Optics). The lens has extra material around the circular lens portion to form a square, and is held in a custom-built lens holder, designed and created by Chris Secord in the UVic Machine Shop. The work on the lens holder was done by Yasaman Shahrestani, and details of holder iterations and the optimization process will appear in her thesis.

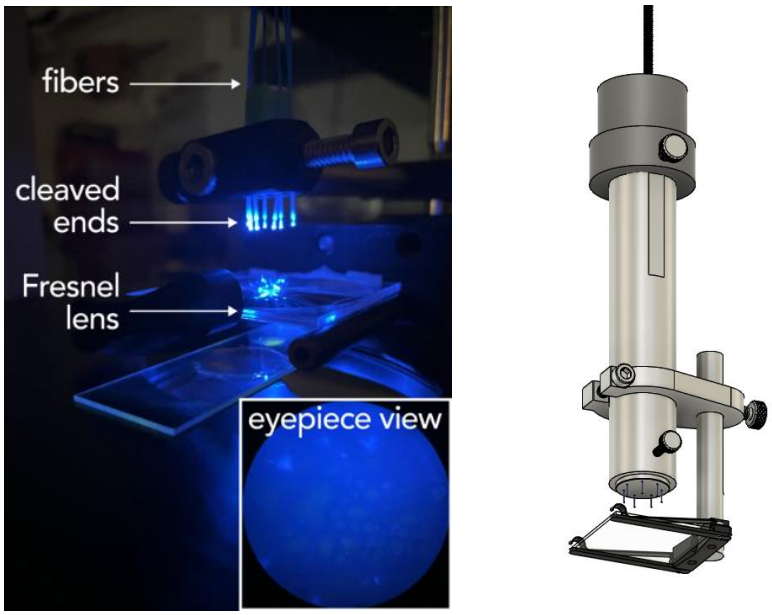

Figure 7.4. Darkfield illumination setup. (**left**) Initial test of fibers in a ring using a fiber-coupled blue LED, inset is an image of an emulsion taken with this light source (dim fluorescence seen), (**right**) render of the Fresnel lens holder shown in the left setup.

Darkfield Illumination Tests using a Blue LED

To test the setup without interfering with ongoing experiments with the DMA-PLS, a 470 nm blue LED (M470F4, Thorlabs), a custom-built fiber bundle containing seven 400/440 µm fibers (FT400UMT, Thorlabs) was used. The side of the bundle coupled to the LED had the seven fibers arranged hexagonally in a 1.275 mm SMA ferrule, and the side of the fibers used for excitation were cleaved and unattached.

Although we observed dim fluorescence with the seven-fiber blue LED darkfield illumination (Figure 7.4, left inset), a blue background indicated that excitation light was collected by the objective lens. Additionally, the spot size of approximately 1 cm is much larger than the field-of-view (FOV) of the objective lens, which creates a significant loss of available excitation light. Specifically, from the estimated ratio of the FOV (1 mm^2) and the irradiated area (80 mm^2), one may estimate that only 1 in 80 photons, or 1.2% of the fluorescence illuminated can be detected.

The same arrangement using the DMA-PLS with 22 fibers in place of the blue LED was similarly characterized. Again, the resulting fluorescence intensity was nearly undetectable and showed a bright background. To match the irradiation spot size on the sample to the FOV of the objective lens, ball lenses were used at the ends of the excitation fibers to collimate the divergent light from the fiber output (NA = 0.39) before focusing onto the sample by the Fresnel lens.

Ball Lenses—Preliminary Test

Figure 7.5 demonstrates that a large (Ø = 1.5 mm) silica bead which acts as a ball lens, can effectively collimate the output light of a 400 µm cleaved fiber (NA = 0.39).

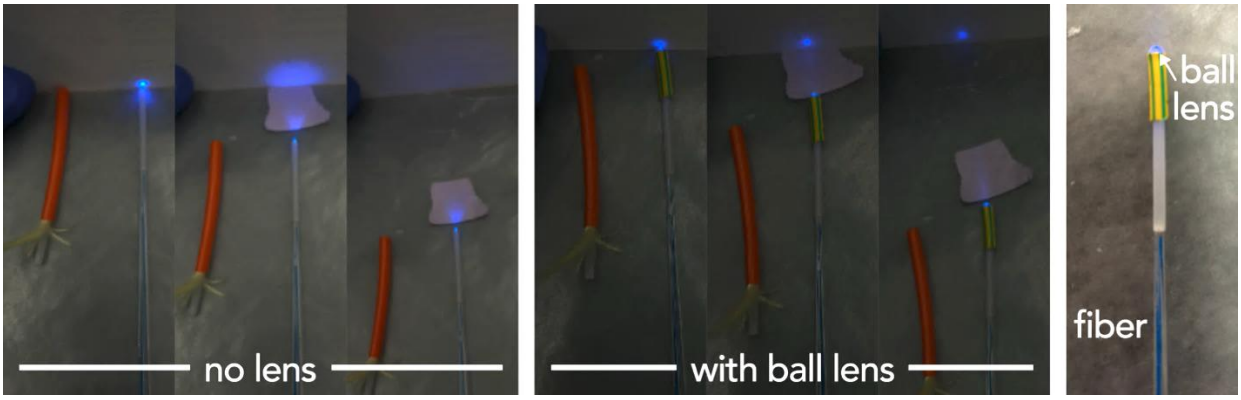

Figure 7.5. Effect on focus of a ball lens at the end of a fiber. The ball lens is placed at different distances from a white sheet of paper. (right) Ball lens setup used in the preliminary test, containing the ball lens held onto the plastic tubing containing an unstripped 400 µm fiber (FT400UMT, Thorlabs) surrounded by six stripped 200 µm fiber pieces (FT200UMT, Thorlabs).

The setup for the preliminary test is shown in Figure 7.5 (right). A silica bead approximately 1.5 mm in diameter (Silica Gel Desiccant, 6-14 Mesh, Grade 40, Fisher Chemical) was friction fit into a piece of heat-shrink tube, which was then shrunk around a piece of the plastic from furcation tubing (FT030, Thorlabs). The plastic tubing held a cleaved 400 µm fiber (FT400UMT, Thorlabs) of the fiber-coupled 470 nm LED, and six ~30 mm pieces of 200 µm (FT200UMT, Thorlabs) fiber to keep the 400 µm fiber aligned with the center of the lens. Index matching gel (G608N3, Thorlabs) was used to couple the light more effectively from the fiber end into the bead. Although this worked for collimation, lenses of this size would not work for 22 fibers because the ring diameter of 12 mm (37.7 mm circumference) cannot practically accommodate 22 × 1.5 mm lenses in individual holes. Additionally, this configuration was difficult to align precisely. Lastly, the bead itself caused significant light loss. For all these reasons, we required a more permanent solution.

Fiber Holder for Darkfield Illumination

A more robust version to hold 1 mm ball lenses in place was created by Chris Secord from the UVic Machine Shop and consists of a 12 mm Delrin cylinder with 24 tapered through-holes to hold individual fibers from the DMA-PLS. A shorter cylinder with 24 holes holding the 1 mm ball lenses is attached to the bottom of the cylinder holding the fibers. I cleaved each fiber to create flat and smooth end faces to reduce scattering and distortions at the glass-air interface. The cleaved fibers are secured in the fiber holder, which is then inserted into the microscope illumination lens

mount with the optical elements removed, and held in place by set screws. The other end of the fiber bundle is a rectangular array of 11 × 2 fibers, glued in place in a metal fiber holder made by the machine shop and assembled by Yasaman Shahresatni.

We observed weak fluorescence through the microscope eyepiece in this updated version, however neither the 8-channel MSC and the HSC are sensitive enough to detect this fluorescence. The increase of the light throughput is still subject to ongoing improvements. microscope assembly requires precise alignment with many degrees of freedom, which is quite time-consuming and prone to human errors. In ongoing work, the light throughput improved by adjusting the distance of the ball lenses from the fiber end faces, by replacing the Fresnel lens with another Fresnel lens having a shorter focal length to reduce the spot size onto the sample, and by increasing the brightness of the DMA-PLS by using a larger entrance slit. This project has potential to be a useful technique and work on it is ongoing by Yasaman Shahrestani.

7.1.3 Liquid-Core Waveguide Illumination

The light throughput of the DMA-PLS may also be increased by replacing the fiber bundle with a liquid-core waveguide, LCW, or liquid light guide. LCWs are expected to have much lower coupling losses at the entrance facet and comparable transmission losses. In our experiments, the LCW was directed at the sample at a shallow angle, such that the sample would be illuminated but the transmitted excitation light would not be collected by the objective lens.

Shallow angle illumination using the LCW provided a much brighter excitation source than using the bifurcated fiber bundle. For the LCW setup, a single 400 μm core fiber patch cord is placed above the sample to collect fluorescence emission, which is detected by a fiber-coupled spectrometer (AvaSpec-ULS2048XL-EVO, Avantes), simultaneously as the fluorescence images are acquired (see Appendix A.6 for a timing diagram of these processes). The probe is placed above the sample, at a shallow angle from the surface plane, and the large core and better placement, provides a brighter fluorescence signal for the spectrometer, compared to the bifurcated bundle at shallow-angle illumination. Using the MSC, we collected F-EEM images through the Olympus CK2 inverted microscope using the LCW with shallow angle illumination, as demonstrated in Section 7.7.

The light from the DMA was coupled into an LCW as described in Section 3.2.4. The light output from the LCW was focused and directed to the microscope slide at ~60° from the surface normal.

The incidence angle was adjusted for maximum brightness when a sample was placed under a coverslip. The light from the LCW was collimated then focused using a by a Ø25.4 mm lens with a long focal length (f=250 mm). A short focal length (f=15 mm) Ø12.7 mm biconvex lens placed approximately 30 mm from the previous lens then focuses the light to the slide. The smaller diameter lens allows for a shallower illumination angle than a Ø25.4 mm lens. Many other configurations of optics to collimate and focus the LCW output work equally well and should be optimized for each experimental setup. Longer focal length lenses were also tested, up to f=50 mm resulting in similar fluorescence intensities, though these were qualitative tests only, based on intensity values in collected images. Lenses with focal lengths longer than these resulted in spot sizes larger than the objective FOV and had lower intensity than the short focal length versions in many instances, though not all. It appears that the setup is quite robust—if light does not strike the objective lens after illuminating the sample, the method provides sufficient excitation intensity.

The LCW and previous fiber probe are compared in Section 7.2 (Figure 7.10) where the LCW illumination shows a more accurate excitation peak when compared to the spectrometer data and a much brighter signal than the fiber probe version acquired using the same parameters.

7.1.4 Data Density

With two options for programmable light sources—the LDA-PLS and the DMA-PLS—and two emission imaging detectors—the MSC and HSC—the trade-off between spectral resolution on one hand, and the associated costs (time, intensity, wavelength range, storage and processing memory) on the other, should be considered. One might not need the resolution of the HSC when doing a simple fluorescence experiment using dyes with known spectral signatures and distinct emission peaks. Similarly, many excitation bands may not be required to separate fluorophores which have distinct emission spectra, reducing the cost associated with acquisition time, intensity, and size.

Figure 7.6 shows two F-EEM spectra acquired using different excitation sources. When separation is more important than accuracy in the excitation dimension, the 7 × 8 F-EEM is acceptable to detect the emission peak, whereas if the excitation wavelength identification is important, the 31 × 8 F-EEM is more useful.

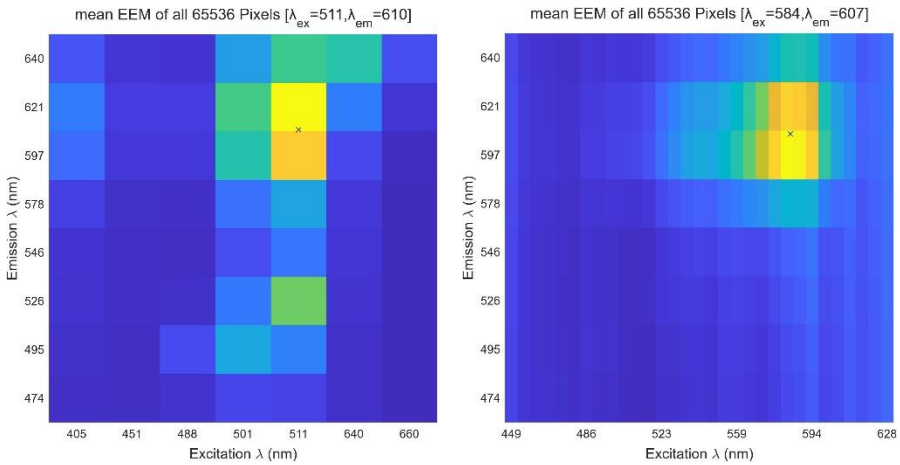

Figure 7.6. F-EEMs using different excitation sources and the multispectral camera (MSC). Fluorescence emission collected with the 8-channel MSC and excitation by (**left**) seven laser diodes (LDA-PLS) or (**right**) 31-channel DMA-based source (DMA-PLS).

For the DMA-PLS, increasing the excitation spectral resolution equates to longer integration times due to the greater number of masks or channels. The way the masks are programmed on the DMA, increasing the number of channels (number of masks, size of Hadamard matrix) results in narrower wavelength bands, as shown in Figure 7.7. The FWHM of each channel decreases with larger mask size and consequently smaller channels.

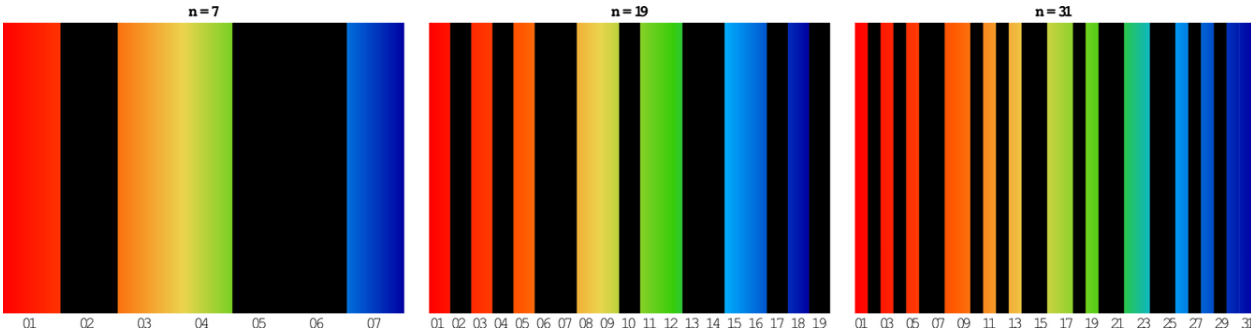

Figure 7.7. Representation of spectrally dispersed light on a DMA. Black regions represent light not chosen to illuminate the sample for this mask. This shows the relative amount of light for each channel when different size masks are used. Channel numbers are labelled below each, and mask size (n) is labelled above.

By contrast, for an array of discrete-wavelength light sources—the LDA or UV-LEDs—new light sources must be added to increase the excitation spectral density or wavelength range. This increases the complexity and cost of the setup not just due to the light sources, but also to their controls added to the driver board and fiber bundles. On the other hand, F-EEM images of the same sample will take less time to acquire using the LDA-PLS compared to the DMA-PLS, because the laser diodes are much brighter than the DMA-PLS and consequently require a lower integration time of the camera per mask. Additionally, the LDA-PLS has only seven light

sources—a mask size of 7—requiring only 7 acquisitions to create an F-EEM, compared with the DMA-PLS which often uses a mask size of 31—requiring 31 image acquisitions.

When fluorophores have similar emission, the increased spectral resolution in the emission or excitation dimensions gained by using the HSC in place of the MSC or the DMA-PLS in place of the LDA, respectively, may allow for separation of those peaks. In this case, the slower acquisition time and decreased sensitivity of the HSC may be worthwhile.

An additional option for increasing the emission resolution of an F-EEM image acquired using the MSC is spectral upscaling, discussed in Section 8.2, where the costs for increased resolution are only due to the size of the data, but not in sensitivity or acquisition time. The range and intensity of the fluorescence emission by the fluorophores can also determine which system may perform better. The DMA-PLS is limited to visible wavelengths above approximately 430 nm and it has lower overall intensity than the LDA-PLS, which ranges from 405–658 nm. The MSC is limited in range to ~464–650 nm—a fluorophore must emit within those wavelength limits to be detected, whereas the HSC detects wavelengths between 395–1100 nm.

Table 7.1. Memory required for combinations of excitation sources and emission detectors. [1]Avantes AvaSpec-ULS2048XL-EVO, [2]Spectral Devices 8-channel multispectral camera, [3]BaySpec up-to 141-channel hyperspectral camera.

Excitation Source	# Excitation Channels	Emission Detector	# Emission Channels	# Pixels	Bit Depth	Total Storage
Lasers	7	Spectrometer[1]	2048	1	16	115 KB
DMA-based	31	Spectrometer[1]	2048	1	16	508 KB
Lasers	7	MSC[2]	8	65,536	8	29 MB
DMA-based	31	MSC[2]	8	65,536	8	130 MB
Lasers	7	HSC[3]	141 (200 frames)	327,680	16	1.4 GB
DMA-based	31	HSC[3]	141 (200 frames)	327,680	16	11 GB

A final consideration is the size of the stored data and the computational cost for the analysis of that data. Table 7.1 lists typical storage sizes using different fluorescent detectors—a spectrometer, MSC, and HSC—with the two HT-programmable light sources.

This has hopefully outlined the considerations that should be made to select the optimal excitation source and emission detector for a particular fluorescence application. Some of these applications will be discussed in the following sections.

7.2 Fluorescent Powder

A fluorescent powder, carbazole-bromobenzothiodiazole (CBB), first described and synthesized by the group of Dr. Erin Chernick [326] was examined using FLEEMSI microscopy.

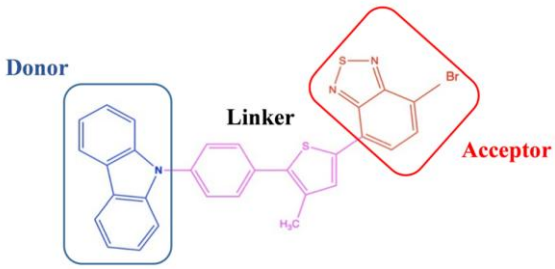

Figure 7.8. Structure of carbazole-bromobenzothiadiazole (CBB) [326].

Simulations of the excited-state behaviours of CBB (Figure 7.8) were performed by Sara Joulai, a former student in our group, to solvatochromic shifts of the fluorescence excitation and emission maxima as a function of solvent polarity [2, 327]. The CBB powder is of a vibrant orange colour and fluoresces both when dry and in solution.

Since the powder shows spatial structure on a microscopic scale and exhibits a simple F-EEM spectrum, it serves as a useful test for the illumination system. We illuminated the sample using the DMA-PLS using either the bifurcated fiber bundle or the LCW and imaged it through an inverted Olympus CK2 microscope with the 8-channel MSC. The emission was also collected simultaneously through a fiber-coupled array spectrometer (AvaSpec-ULS2048XL-EVO, Avantes). The emission peaks found using the MSC were found to be consistent with those acquired using the spectrometer.

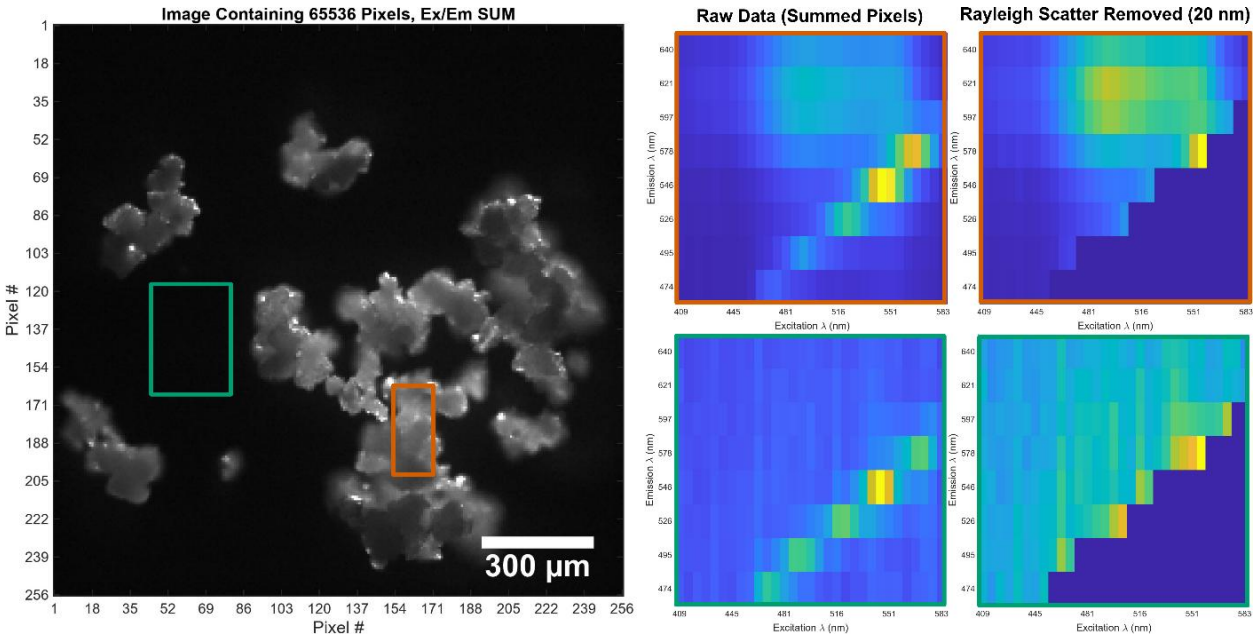

Figure 7.9. F-EEM microscopy image of carbazole–bromobenzothiadiazole powder. The F-EEM image was taken using an 8-channel multispectral camera through an inverted Olympus CK2 microscope using a 10x magnification objective lens. The powder was placed on a glass microscope slide and illuminated by the DMA-PLS using the bifurcated fiber bundle. The grayscale image (**left**) is the sum of all excitation and emission channels in the F-EEM image. The summed F-EEMs of each pixel in the two regions shown in green and orange in the grayscale image are shown on the right, shown using the raw data (**center** column) and with Rayleigh light removed within 20 nm of the excitation bands (**right** column). The green (bottom) represents the background (glass slide) and orange (top) represents the powder. The brightest pixels have been set to 1 (white) to increase visibility.

In image regions where the powder is present (orange ROI in Figure 7.9), fluorescence emission is observed, whereas in other regions (green ROI) only scatter from the microscope slide is observed. The emission maxima found using the MSC and Avantes spectrometer were 607 and 615 nm, respectively. Emission maxima are from the calculated centroid of the top 30% of the F-EEM maximum (*findCentroid* function, Appendix A.10). F-EEM were preprocessed by removing scattered light within a 20 nm band (Section 5.2).

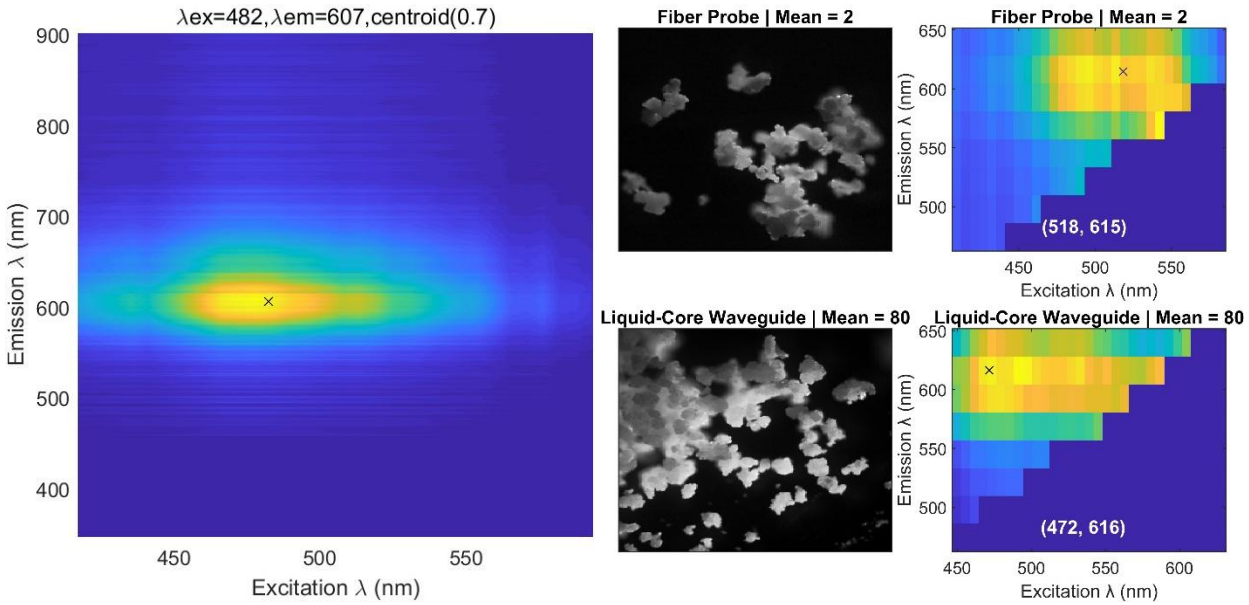

Figure 7.10. Effect of coupling the DMA-PLS through a bifurcated fiber bundle (BFB) or a liquid-core waveguide (LCW). (left) F-EEM acquired using a fiber-coupled spectrometer (AvaSpec-ULS2048XL-EVO, Avantes) and the DMA-PLS via the bifurcated fiber bundle. (center and right) F-EEM images acquired using the MSC through an Olympus CK2 microscope with a 10x objective lens with illumination by the DMA-PLS using the BFB (top) and LCW (bottom). Grayscale images are the mean of all excitation and emission channels of the F-EEM image. F-EEM spectra (right) are the mean of all pixels in the image, with Rayleigh light removed within 30 nm of the excitation bands. Centroids were found using the top 30% of the F-EEM are shown above the F-EEM (left) and in white as (λ_{ex}, λ_{em}) on the F-EEM spectra (right).

The mean values of all excitation and emission channels of the F-EEMs acquired using the MSC show that the DMA-PLS coupled to the LCW provides brighter illumination (mean = 80) compared to the bifurcated fiber probe (mean = 2). The LCW-coupled DMA-PLS also provides a more accurate excitation peak (λ_{ex} = 472 nm) compared to the bifurcated fiber probe (λ_{ex} = 518 nm). These values may be compared to the F-EEM acquired using the spectrometer (λ_{ex} = 482 nm), as shown in Figure 7.10. The emission maxima detected by the MSC using the LCW (λ_{em} = 616 nm) and fiber probe (λ_{em} = 615 nm) were close to the maximum found using the spectrometer (λ_{em} = 607 nm).

This simple demonstration shows that FLEEMSI microscopic imaging could be useful in identifying mixtures of fluorescent powders or other dry samples, especially for non-homogeneous samples. To demonstrate that the MSC and DMA-PLS microscopy imaging system can identify multiple fluorophores both spectrally and spatially, we use dye emulsions, discussed in the following section.

7.3 Emulsions—Experimental Setup

Fluorescent dye emulsions are used to determine the spectral and spatial separation abilities of the FLEEMSI microscopy systems described in this work. The emulsions are used as a proof-of-concept for complex fluorescent samples such as stained tissues which might be used in biological imaging fields. I describe the method for producing the dye emulsions and the adjustments that were made to select for properties of those emulsions. Spatial fluorescence emission from the dye emulsions under a microscope is detected with three instrumentation setups—illumination by the LDA-PLS or DMA-PLS and fluorescence imaging by the MSC or HSC. These three setups are described along with the preparation method of the emulsions on the microscope slides in Section 7.3.2. The spectral separation abilities of the three setups are demonstrated in Sections 7.5, 7.6, and 0, and a typical data analysis workflow used for analyzing these FLEEMSI datasets is described in Section 7.4.

7.3.1 Emulsion Preparation

Emulsions containing various fluorescent dyes were used to demonstrate the spectral resolving power of the 8-channel multispectral camera (MSC) in conjunction with the LDA-PLS and DMA-PLS. To create an emulsion with the properties we required, numerous emulsions were prepared with varying ingredients and preparation methods. The effects on droplet size, strength, and fluorescence of adjustments to the solvent viscosity and density, surfactant(s), dyes, stir speed, and method of addition, are described briefly below.

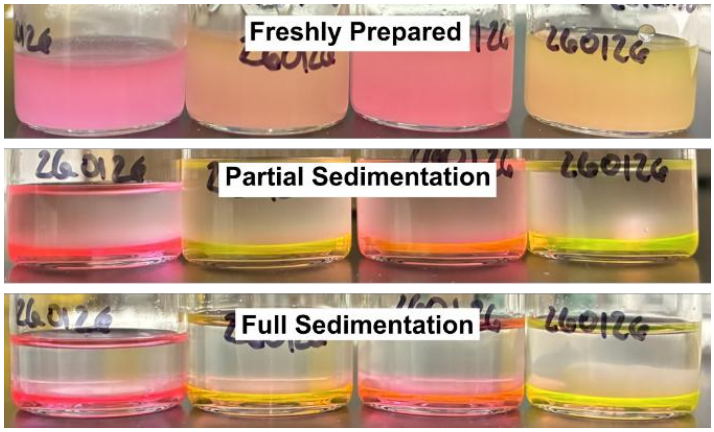

Figure 7.11. Four ethanol-in-oil emulsions at various stages of sedimentation. From left to right, the dyes in the emulsions are sulforhodamine 101, acid red 87, acid red 92, and rhodamine 19. Emulsions were prepared as described for the EO#65 emulsions.

The following reflects my personal experience and observations in preparing emulsions with the required properties and should not be taken as definitive evidence of the behaviour of these systems

or their ingredients. Many of the emulsions were prepared only once, and parameters were not tightly controlled.

The emulsions were optimized to create large droplets with strong fluorescence within the droplets (in the dispersed phase, DP) and minimal background fluorescence (in the continuous phase, CP), low edge scattering, and which did not coalesce too quickly. We did not try to prevent sedimentation and creaming, as the droplets could be easily and effectively re-dispersed before imaging. The ideal *droplet size* was chosen using the pixel dimensions of the MSC and magnification of the microscope. The size represented by a single image pixel was found to be 1.7 × 1.7 μm for the MSC through a 10x objective lens on the Olympus CK2 microscope, and the pixel size was found by manually counting pixels in an image of a micrometer disk as shown in Appendix A.18. The ideal droplet diameter was chosen as a minimum of 17 μm (10 pixels) to give adequate spatial resolution and a representative fluorescence signal. An additional benefit of larger droplets is their lower scatter compared to smaller droplets due to the smaller surface area to volume ratio. Reducing scatter was essential to improve the quality of the data, because the signal from scatter can be bright in the shallow-angle, evanescent, and FrTIR illumination microscopy methods used in this work.

Below we discuss first the preparation methods and formulations which affect the droplet size, then those affecting barrier strength. The effect of formulations on background fluorescence in an emulsion is discussed next, followed lastly by factors which affect the fluorescence properties of the droplets in an emulsion.

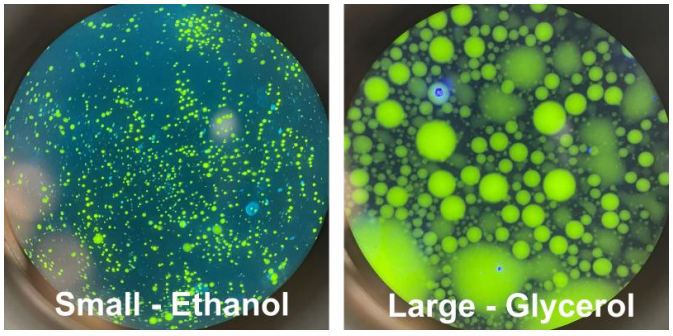

Figure 7.12. Droplet size using different dispersed phase solvents. Adding 80 wt% glycerol to the ethanol and dye (right) created much larger droplets. Photos taken through the eyepiece of a Zeiss Axiovert 200 microscope with a 10x objective lens and illumination using a 450 nm laser.

Droplet Properties—Size

Both preparation and formulation affected the droplet sizes. The viscosity, density, and solubility of each phase impacted droplet size and dispersity significantly during preparation.

Shear Force in Emulsification. Droplet sizes were reduced when a faster stir speed during preparation was used. This is likely caused by the higher shear force created in the continuous phase with a faster stir speed. Decreasing the stir speed can cause larger droplets, however the speed must be sufficient for proper emulsification.

Density of Continuous and Dispersed Phases. The densities of each phase determined the method of dispersion and if the dispersed phase (DP) should be added from above or below the surface of the continuous phase (CP). In ethanol-in-oil (E/O) emulsions, the density of the DP (ethanol, 0.789 g/mL) is lower than the density of the CP (mineral oil, 0.82 g/mL). In E/O emulsions, slower addition was required if the DP (ethanol and oil) was added from above the CP (mineral oil and surfactant), so the liquid on the top had time to be emulsified. When the DP was added beneath the surface of the CP, the droplets were smaller than when added above the surface. For a DP consisting of dye and a mixture of ethanol and PEG400 (1.13 g/mL), the bulk density of a 50/50 wt% mixture of EtOH/PEG is (1.13 g/mL × 0.5) + (0.789 g/mL × 0.5) = 0.96 g/mL. This bulk density is larger than mineral oil, so the DP is added from above the surface of the CP and is dispersed into (emulsified by) the CP more readily than the E/O emulsions.

Viscosity of Continuous and Dispersed Phases. Droplet sizes decreased when the viscosity of the CP was increased. This was tested using heavy mineral oil in place of light mineral oil. Larger droplets were created when the viscosity of the DP was increased, holding other parameters constant. Figure 7.12 shows that larger droplets are formed in an E/O emulsion made with a DP of dye in ethanol compared to a DP of dye in an 80/20 wt% mixture of ethanol to glycerol.

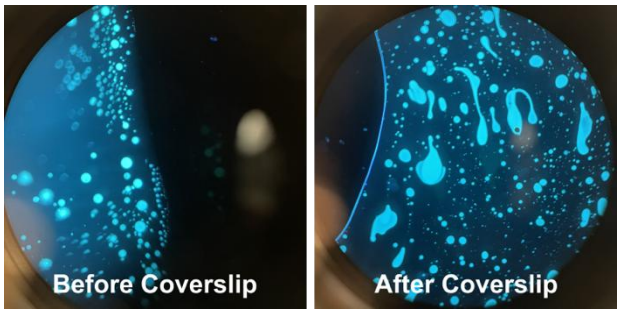

Figure 7.13. Weak droplet barrier when a coverslip is added to a droplet of the emulsion. Photos taken through the eyepiece of a Zeiss Axiovert 200 microscope with a 10x objective lens and illumination using a 450 nm laser.

Droplet Properties—Barrier Strength

Strong interfacial barriers between the DP and CP were required so that the droplets (DP) did not break when a coverslip was added atop a droplet of an emulsion on a microscope slide. The coverslip was added because an image of the droplet contained out-of-focus fluorophores which contributed to the background fluorescence and made identification of spectra more difficult. The force imposed on the droplets when a coverslip was added caused droplets with weaker interfacial barriers to break apart then re-form smaller droplets. This created smaller droplets than desired, and the breaking and re-forming was effective for mixing the numerous different dye emulsions that were on a slide, shown in Figure 7.13. Additionally, blurred images resulted from droplets with weaker interfacial barriers combining (*coalescing*) more quickly than the total acquisition time of the F-EEM image.

Viscosity of Continuous and Dispersed Phases. When the viscosity of the DP was increased, the droplets were better able to maintain their shape under the force of an added coverslip and joined less quickly when in contact with nearby droplets.

Surfactant in the Dispersed Phase. The addition of Tween 20 (T20) to the DP seemed to increase the interfacial barrier strength, shown by a decrease in droplet distortion under strain and a decreased rate at which neighbouring droplets joined.

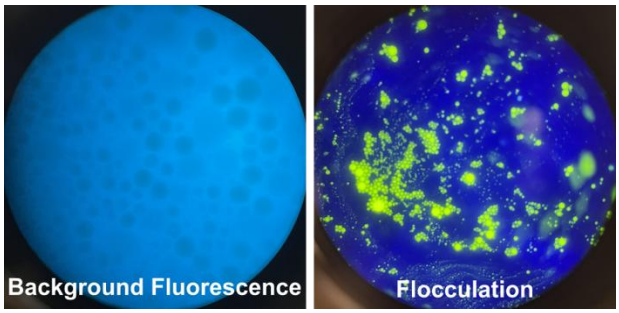

Figure 7.14. Photos of background fluorescence and flocculation in emulsions. Photos taken through the eyepiece of a Zeiss Axiovert 200 microscope with a 10x objective lens and illumination using a 450 nm laser. (**left**) Coumarin 153 emulsion five minutes after initial emulsification, demonstrating a dye which has a higher solubility in the continuous (mineral oil) phase than the dispersed (ethanol/glycerol) phase. (**right**) Flocculation in an ethanol-in-oil emulsion.

Emulsion Properties—Background Fluorescence

When the dyes from the DP are solubilized in the CP (mineral oil), a fluorescent background can appear.

Solvent Properties. Fluorescence in the dispersed phase from the dye can arise because ethanol is slightly miscible with mineral oil, and it can bring with it some of the dye as it moves across the droplet barrier. The dye is then slightly solubilized into the mineral oil, in E/O emulsions. The background fluorescence surrounds the droplets and makes spectral and spatial separation of the fluorophores more difficult. In addition, a dye-containing matrix may give rise to inner filter effects.

Dye Solubility. Dyes which are more soluble in the CP than the DP tend to dissolve into the CP quite quickly. Coumarin 153—a relatively hydrophobic dye, more soluble in mineral oil than ethanol—has moved into the oil phase in less than ten minutes, as shown in Figure 7.14 (left).

Droplet Properties—Fluorescence

Droplets in emulsions with a dispersed phase of dye in ethanol showed stronger fluorescence than DPs of glycerol, water, or mixtures of ethanol with glycerol or water.

Dispersed Phase Solvent. Many strong dyes such as rhodamines and coumarins have reduced fluorescence in water and glycerol due to quenching from the aggregates that form in solution [328]. Ideally, we would use only ethanol in the DP for the increased fluorescence signal. Unfortunately, the droplets in the E/O emulsions have weak interfacial barriers,

while the droplets in emulsions using glycerol or water as the DP have much stronger barriers.

Oil-in-Water Emulsions. To circumvent the E/O barrier strength problem entirely, we tested oil-soluble fluorescent dyes, in oil-in-water (O/W) emulsions. Though these ultimately produced droplets of a sufficient size and brightness, the availability of oil-soluble dyes with differing excitation and emission wavelength were limited, so we pursued E/O type.

Additional Solvent in the Dispersed Phase. To increase the barrier strength of the droplets of the DP while maintaining strong bright fluorescence, we added glycerol or PEG400 to the dye and ethanol solution. The fluorescence of the droplets in the glycerol/ethanol DP was between that of the pure glycerol and pure ethanol but was bright enough for some applications. A mixture of ethanol/PEG400 as the DP produced brighter droplets than those of the glycerol/ethanol mixture and prevented dye solubilizing into the CP better than the glycerol/ethanol mixture.

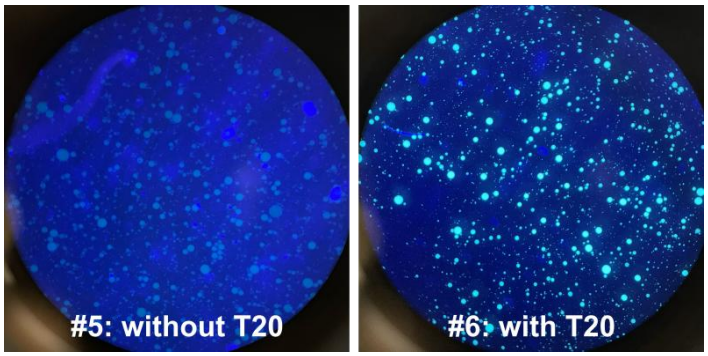

Figure 7.15. Effect on droplet brightness of adding Tween 20 to the dispersed phase of two ethanol-in-oil emulsions. A droplet of emulsion was placed on a microscope slide with a glass coverslip and illuminated via FrTIR using a 450 nm laser. Images were taken using a cellphone camera through the microscope eyepiece of a Zeiss Axiovert 200 through a 10x objective lens.

Surfactant in the Dispersed Phase. Adding Tween 20 (1 drop per mL dye solution) to the DP before emulsification resulted in droplets with brighter fluorescence. Two E/O emulsions using coumarin 6 dye both with and without T20 in the DP are shown in Figure 7.15. The increased fluorescence allowed the glycerol/ethanol-in-oil (GE/O) emulsions to be easily detectable with the MSC and DMA-PLS.

The properties of different dispersed and continuous phase solvent compositions are shown in Table 7.2. Using ethanol in the DP allowed for the selection of many soluble dyes, compared with a hydrophobic DP. Mixtures of ethanol with either glycerol or PEG400 were found to have a

sufficiently strong interfacial barrier for the purposes of these experiments. The ethanol-PEG400 mixture was ultimately chosen due to decreased solubilization of the dye into the mineral oil.

Table 7.2. Observed properties of different types of emulsions. The green checkmarks, orange crosses, yellow lines, and black question marks represent an affirmative, negative, in-between, and unknown, respectively.

	Droplet Strength	Less Dye Transfer	Strong Dye Fluorescence	Availability of Soluble Dyes
Water-in-Oil	–	✓	✗	✗
Glycerol-in-Oil	✓	✓	✗	✗
Ethanol-in-Oil	✗	✗	✓	✓
Ethanol/Glycerol-in-Oil	✓	–	✓	✓
Ethanol/PEG-in-Oil	✓	✓	✓	✓
Oil-in-Water	?	?	✓	✗

The emulsions used for demonstrating the FLEEMSI systems described in this dissertation were prepared using various fluorescent dyes—rhodamines 19, 110, B, 6G, coumarins 6, 7, 30, 153, 343, 453, 481, sulforhodamines B and 101, and acid reds 87 and 92. The continuous phase was hydrophobic—mineral oil and the surfactant Span 80, and the dispersed phase was hydrophilic—a mixture of ethanol with glycerol or PEG400, dye, and the surfactant Tween 20. Different mixtures were used for various instrumentation demonstrations, but all are described in Table 7.3 for referencing in later figures.

Table 7.3. Emulsion ingredients for the emulsions used in this work, for referencing datasets. Values are listed in weight percentages, the % mass of the total emulsion mass.

	Continuous Phase			Dispersed Phase				
Emulsion	**Total**	**Mineral Oil**	**Span 80**	**Total**	**Ethanol**	**Glycerol**	**PEG400**	**Tween 20**
GE/O #8	80%	75%	5%	20%	4%	16%	-	2%
GE/O #45	80%	75%	5%	20%	2%	18%	-	2%
E/O #65	80%	75%	5%	20%	10%	-	10%	2%

Preparation: 5 g emulsions were prepared with the ingredient proportions as listed in Table 7.3. Span 80 (Sorbitan Monooleate, S0060, TCI America) was dissolved in light mineral oil (330779-1L, Sigma Aldrich) on a stir plate in a 4-dram glass vial. Tween 20 (BP337-500, Fisher Bioreagents) was dissolved in a dye solution (0.1 mM dye in spectral-grade ethanol), which was added to glycerol (BP229-1, Fisher Bioreagents) or PEG400 (Poly-(ethylene glycol), average M.W. 400 g/mol, 25322-68-3, Acros Organics) and mixed manually by shaking and inverting then

immersed in an ultrasonic bath to remove bubbles. The mineral oil solution (continuous phase) was stirred at ~250 rpm using a 2 × 7 mm magnetic stir bar while the dye solution (dispersed phase) was slowly dropped in using a 100–1000 µL micropipette. Each drop was dispersed into the continuous phase before the next drop was added.

7.3.2 Experimental Setup

F-EEM are acquired using three different FLEEMSI microscopy setups described in this section, specified in Table 7.4, and shown in Figure 7.16.

Setup A—MSC and LDA-PLS—coarse excitation and coarse emission.

Setup B—HSC and LDA-PLS—coarse excitation and well-resolved emission.

Setup C—MSC and DMA-PLS—well-resolved excitation and coarse emission.

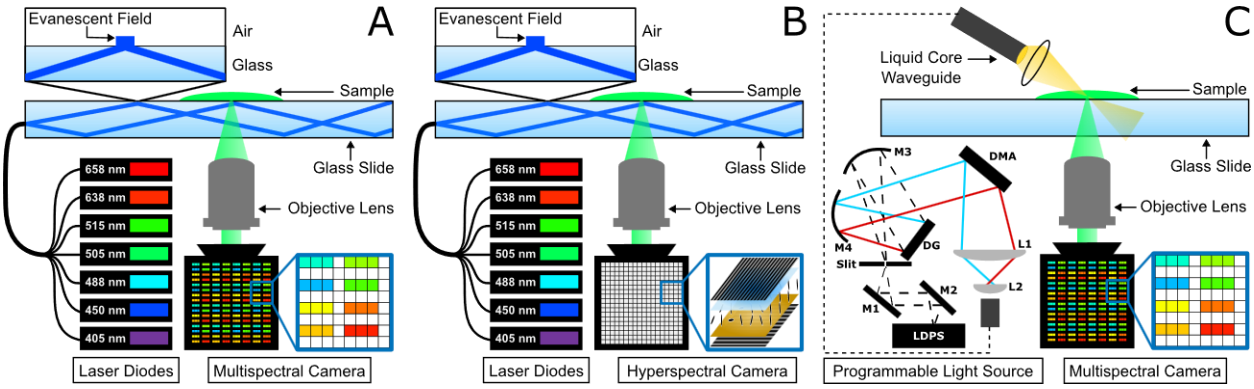

Figure 7.16. Instrumentation schematics for F-EEM micrography. The components of each setup are described in Table 7.4.

Illumination with the LDA-PLS uses FrTIR on a Zeiss Axiovert 200 inverted microscope. Shallow-angle illumination using a liquid-core waveguide is used with DMA-PLS on the Olympus CK2 inverted microscope. All microscope configurations use a 10x objective lens.

Table 7.4. Components of three F-EEM microscopic imaging setups. Excitation illumination via the laser diode array, LDA- or digital micromirror array, DMA-programmable light source, PLS. Fluorescence emission is imaged using either the 8-channel multispectral camera, MSC, or the hyperspectral camera, HSC. Excitation method is either frustrated total internal reflection fluorescence (FrTIR) or shallow-angle illumination.

	Excitation Source	**# Excitation Channels**	**Excitation Method**	**Imaging Detector**	**# Emission Channels**	**Microscope**
Setup A	LDA-PLS	7	FrTIR	MSC	8	Zeiss Axiovert 200
Setup B	LDA-PLS	7	FrTIR	HSC	141	Zeiss Axiovert 200
Setup C	DMA-PLS	31	Shallow-Angle	MSC	8	Olympus CK2

Dye emulsions were prepared as described in Section 7.3.1. Glass capillaries or micropipette tips were used to drop a small amount of a freshly re-agitated emulsion (by swirling, to disperse the sedimented/creamed droplets into the continuous phase) either onto a bare glass slide or into a droplet of mineral oil on the slide. Emulsions added to a mineral oil droplet were allowed to settle for a few minutes to reduce scatter from the droplet edges, especially for smaller droplets. Emulsions are added nearly on top of one another for the mixed images, and for individual (neat) emulsion images, the emulsions are added to different locations on a microscope slide and imaged separately, as shown in Figure 7.17. A coverslip can be added to reduce out-of-focus fluorescence of a thicker layer of droplets and to reduce movement of the droplets. When using a coverslip, the volume of emulsion to add to the microscope slide was calculated using the volume of a rectangular prism or cylinder, depending on the coverslip shape. The surface area of the coverslip and the depth of the solution as the size of the largest droplet we would expect or desire—usually 100 µm—were multiplied to obtain the volume in e.g., mm^3. This value was converted to millilitres using 1000 mm^3 per 1 mL.

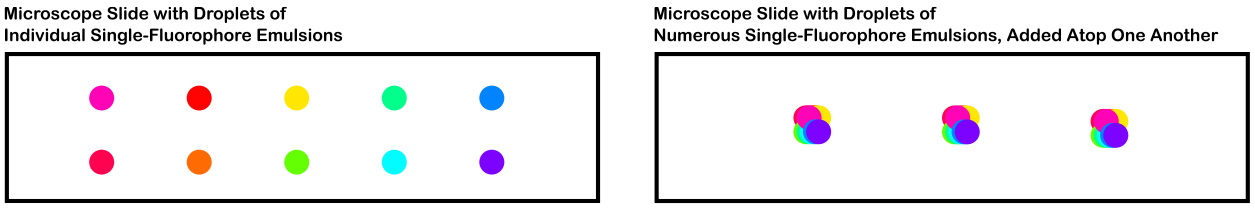

Figure 7.17. Preparation of emulsions on slides and individual and mixtures. (**left**) A single droplet of an emulsion is placed on a glass microscope slide, shown are 10 different emulsion droplets, (**right**) droplets of different dye emulsions are placed on top of or near-enough to overlap, to obtain images containing numerous different dyes.

7.4 Data Analysis—Example Workflow

F-EEM images of dye emulsions—both neat and mixtures thereof—were taken using one of the three FLEEMSI microscopy setups described in Section 7.3.2. The pixels containing the strongest fluorescence are selected to obtain a high-quality PARAFAC decomposition, as discussed in Sections 5.3 and 5.4. A workflow for the selection of those pixels and the following PARAFAC analyses is described in this section and shown in Figure 7.18. The method shown has been quite successful for analyzing F-EEM images acquired using the MSC and DMA-PLS (Setup C). Other methods for pixel pre-selection and analysis (Sections 5.3 and 5.4) are better suited for data acquired using the MSC and LDA-PLS.

In this section, the F-EEM images were acquired using the MSC and DMA-PLS (Setup C, Figure 7.16) and contain four E/O#65 dye emulsions—rhodamine 19 (R19), acid red 87 (AR87), acid red 92 (AR92), and sulforhodamine 101 (SR101), made as described in Section 7.3.1 and prepared on microscope slides as described in Section 7.3.2. Images were acquired with an exposure time of 350 ms per image for a total of 11 seconds total acquisition time for an excitation-modulated F-EEM image.

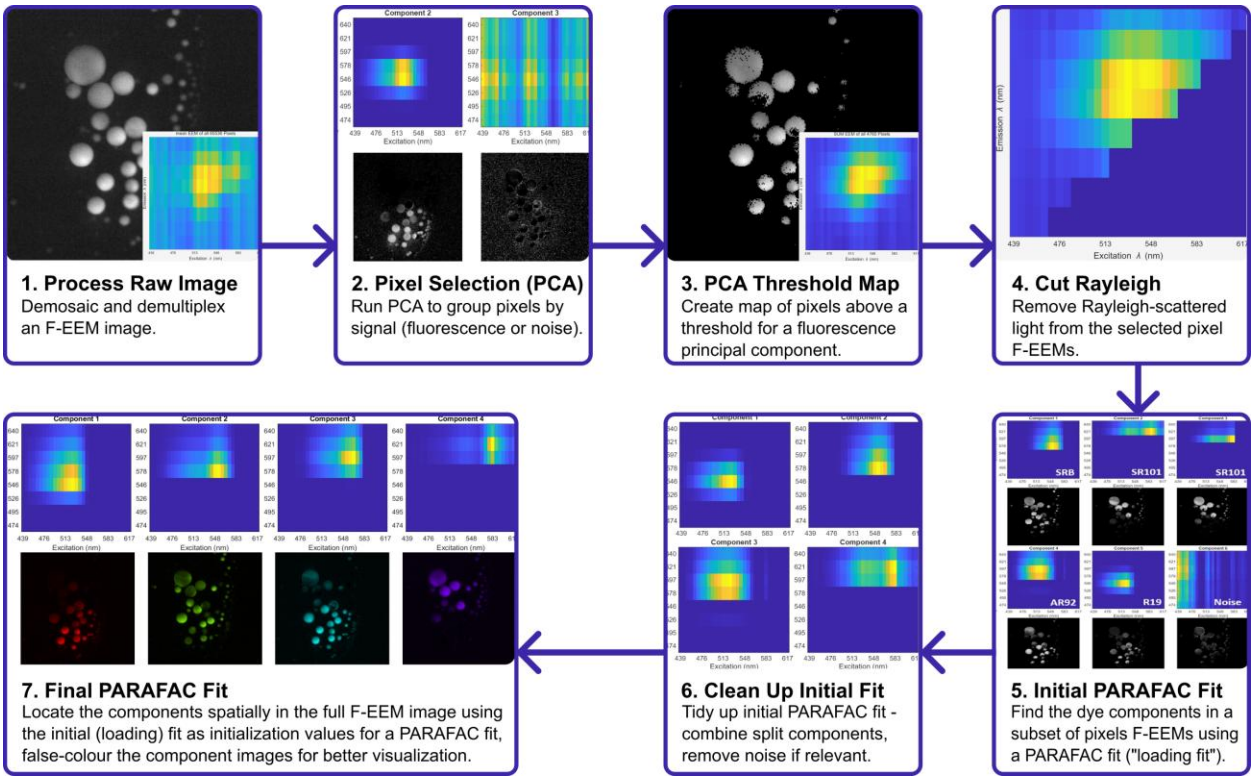

Figure 7.18. Workflow for pixel selection and PARAFAC analysis of an F-EEM image.

Pixel Selection & Analysis Overview. The pixels containing the strongest fluorescence signals in an F-EEM image were selected using a threshold of PCA component scores as described in Section 5.4.3. An initial PARAFAC analysis was performed on the F-EEMs of the selected pixels. The spatial distributions of each fluorescent component in the full image were identified using a PARAFAC analysis of the full F-EEM using the initial fit as an initialization.

Step 1: Process Raw Image. Raw F-EEM images acquired using the MSC and DMA-PLS with dimensions $2048 \times 2048 \times nEx$ were binned into eight spectral (emission) channels ("demosaiced", Section 4.1.3) and demultiplexed (Section 5.1.2) to create a $256 \times 256 \times 8 \times nEx$ F-EEM image.

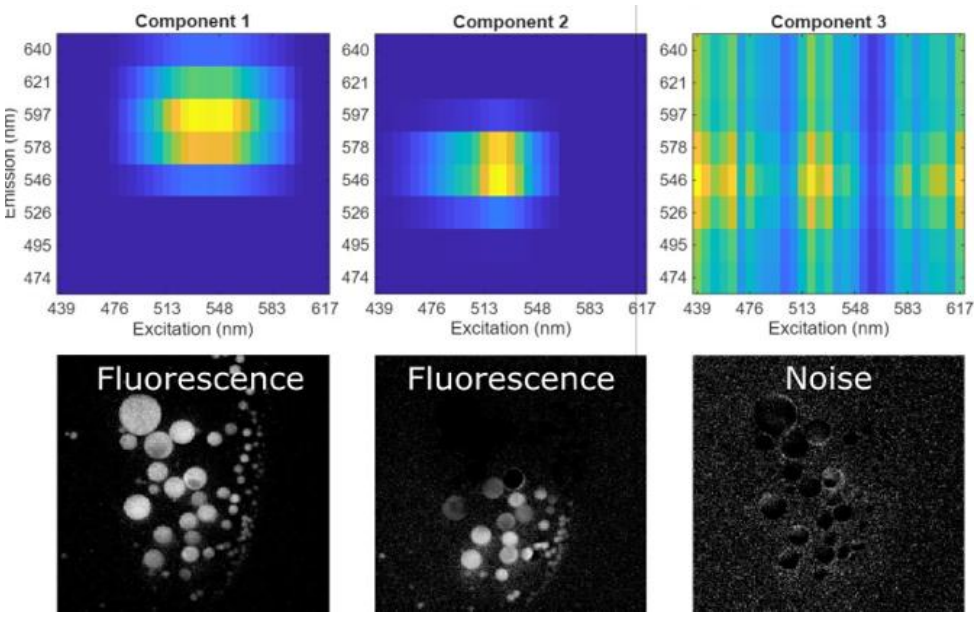

Figure 7.19. Principal component analysis of an F-EEM image taken with Setup C (Figure 7.16) of E/O#65 emulsions.

Step 2: Pixel Selection (PCA). Principal Component Analysis, PCA, is used to identify the pixels most strongly representing fluorescence. Removing noisy and non-meaningful data is an important step for a good PARAFAC fit, as described in Section 5.3 and 5.4. For an F-EEM image, this includes removing pixels which have no meaningful fluorescence signal—background pixels where no signal is expected and some very bright pixels which consist primarily of scattered light. This can be done effectively using a simple PCA fit of the raw data, as described in Section 5.4.3.

An example of a PCA fit of raw data is shown in Figure 7.19, where the first two components describe fluorescence and the third describes noise. The first two components seem to represent fluorescence signals, based on the peak shapes in the EEM spectra and on the locations of those components in the image (inside the droplets). The third component appears to be noise, as the EEM spectrum is somewhat uniform, signal appears both above and below the Rayleigh line, and the spatial location of the signal appears primarily in the background.

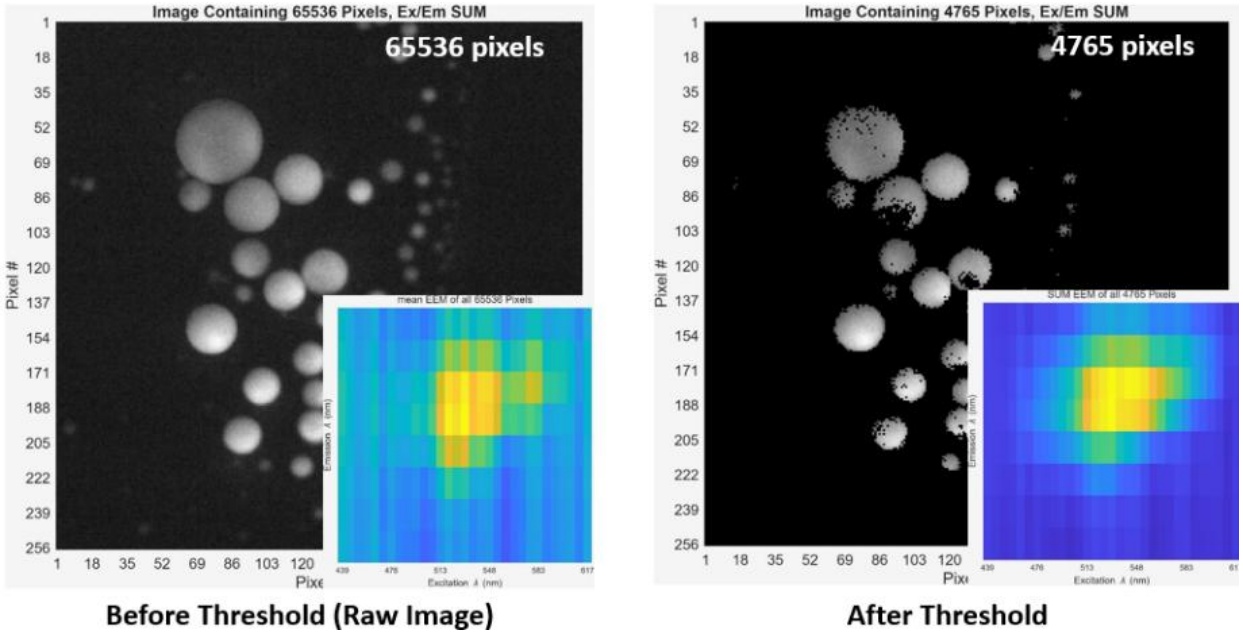

Figure 7.20. F-EEMs of pixels selected using a principal component threshold. Black and white images represent the summed excitation and emission dimensions of the 256 × 256 pixels. Insets show the EEM resulting from the mean of all pixels. (**Left**) is the raw data and (**right**) shows the pixels remaining after removing those represented by noise, as determine by the PCA fit in Figure 7.19.

Step 3: PCA Threshold Map. The pixels which are most strongly represented by the fluorescence components of the PCA fit (Figure 7.19) are selected for further analysis using a manually chosen threshold value. In the example shown, both components 1 and 2 represent fluorescence, so pixels representing either component are kept above respective thresholds. The remaining pixels which are not selected are removed from the dataset and are shown in black on the image in Figure 7.20. A pixel map—a logical array—is created so that pixels can be mapped back onto the original-sized 256 × 256 image for visualization of the selected pixels (Figure 7.20, right) and of later analysis. The selection of these pixels allows for a better and more accurate fit by PARAFAC, because the model is not required to explain a large amount of noise. The number of pixels in the dataset is reduced in this example from 65,536 to just 4765, corresponding to a reduction from 130 MB to 9 MB for the 4765 × 8 × 31 (linearized pixel dimension × emission × excitation) dataset.

Step 4: Cut Rayleigh. Rayleigh-scattered light must be removed before PARAFAC analysis, as it cannot be modelled by PARAFAC [17, 93]. Cut data should be set to NaN so that PARAFAC does not interpret the missing data as zeros which would be spectrally meaningful [17, 93]. This is described in Section 5.2. Different amounts of light can be cut from around the Rayleigh line, and the choice of value can impact the fit. It is important to remove all the Rayleigh-scattered light, however removing too large a region around the Rayleigh line can also remove fluorescence signals.

Step 5: Initial PARAFAC Fit. A PARAFAC decomposition of the 4,765 selected pixel F-EEMs identifies the fluorescence components (Figure 7.21). This will be referred to as the "initial fit" or the "loading fit". The initial fit is first run with the expected number of components, however component EEMs can be split or missing depending on the dataset and model, so more components may be required to identify all the expected components. In this example, although only four components are expected, a six-component fit (two additional components) was required to identify the spectral signatures of all four expected components. The additional components were required because one component (SR101) was split into components 2 and 3, and a noise component was also modelled, before all four components were found.

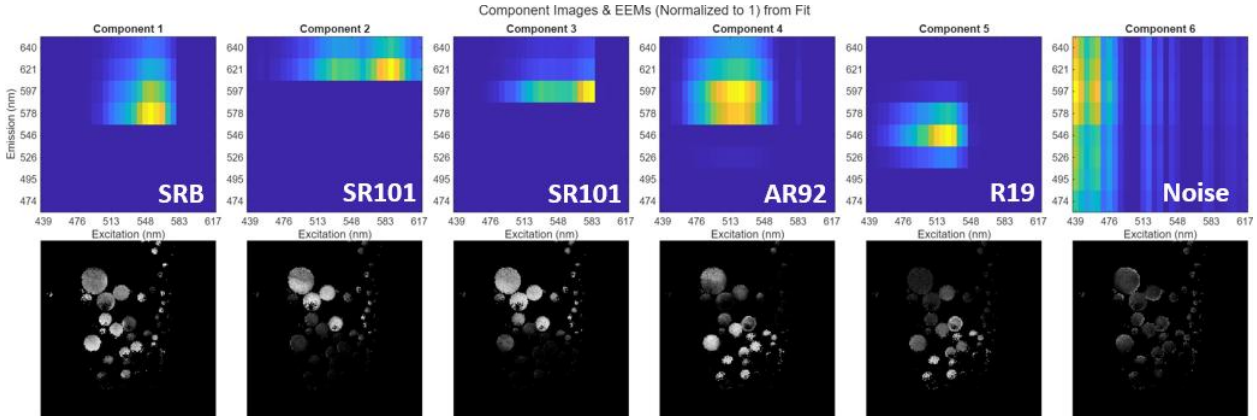

Figure 7.21. Results of an initial PARAFAC fit using chosen pixels from an F-EEM image. Rayleigh line was removed and data were smoothed in this example.

Compare Components to Expected Data. Component EEMs found in the initial fit are compared to F-EEMs from individual emulsions taken simultaneously using the MSC and an array spectrometer, with excitation with the DMA-PLS. The higher-resolution emission spectrum of the entire FOV of the sample is recorded simultaneously to supplement the coarse emission spectral resolution of the MSC. Component EEMs from the initial fit are compared with the F-EEMs of neat emulsions acquired separately using an array spectrometer and the MSC (Figure 7.22).

The centroids of the component EEMs from the initial fit for R19, AR92, and SR101 (Figure 7.22, bottom) are close to those of the EEMs from the neat dye emulsions imaged and analyzed individually, obtained by both the spectrometer (Figure 7.22, top) and the MSC (Figure 7.22, middle), suggesting a good fit for those components.

The component labelled SRB is possibly due to inner-filter effects with the R19—indicated by the similar excitation of both R19 and SRB in contrast to the typical SRB excitation at approximately

the emission peak of R19. It seems that the SRB component could represent an inner-filter effect of these components, which indicates that another component may be required or parameters such as nonnegativity adjusted. The purpose of this section is to demonstrate a method for analysis, and complete analyses of datasets are shown in Sections 7.5, 7.6, and 0.

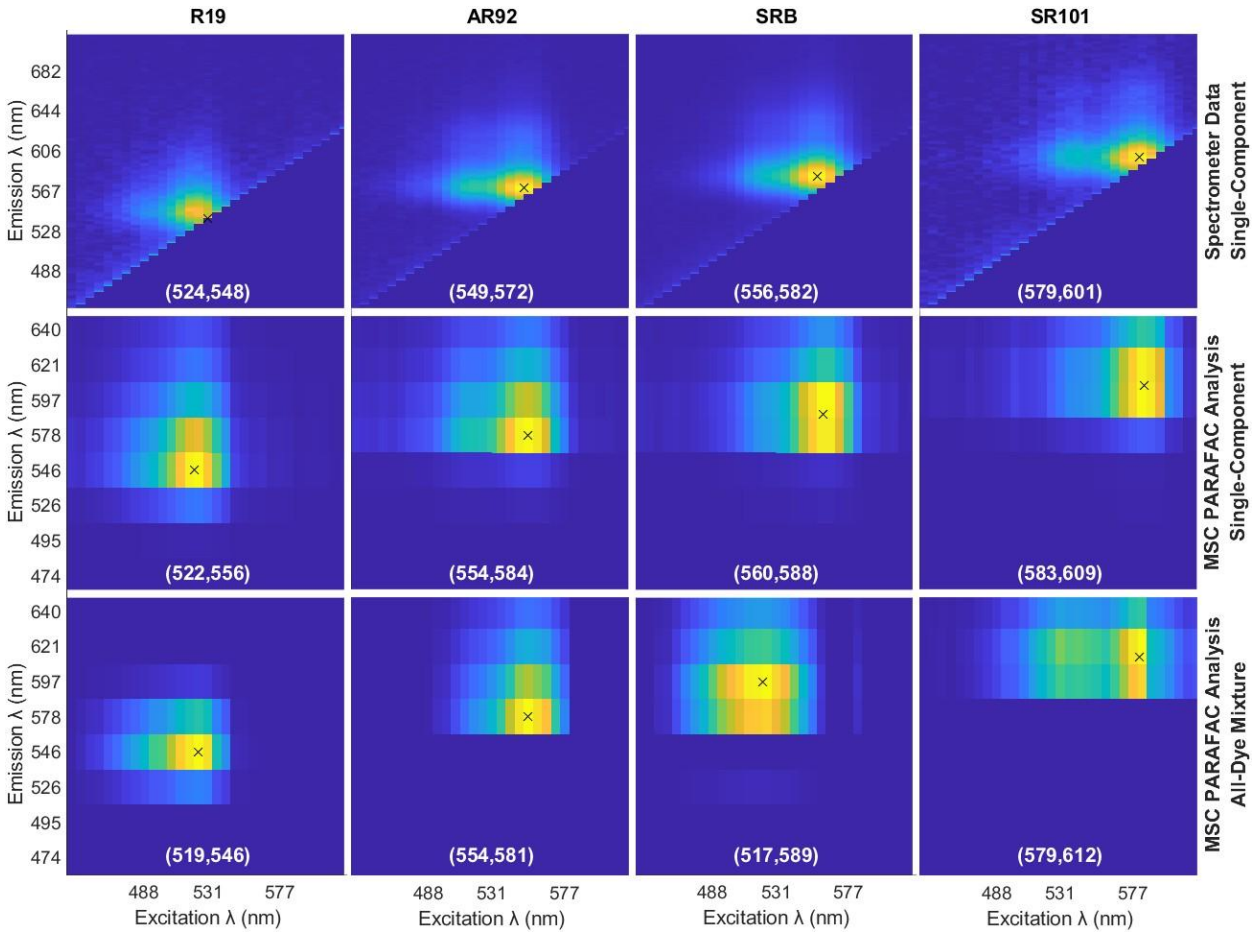

Figure 7.22. Validation of component EEMs to neat dye emulsions. F-EEM spectra of the four individual emulsions on a glass microscope slide acquired using a fiber-coupled spectrometer (AvaSpec-ULS2048XL-EVO, Avantes) and the DMA-PLS are shown in the top row. The component EEMs found in PARAFAC analyses of F-EEM images acquired using the MSC and DMA-PLS in Setup C are shown in the middle and bottom rows. (middle) Individual one-component PARAFAC analyses of each neat dye emulsion, (bottom) the selected component EEMs from the 6-component fit shown in Figure 7.21. Centroids of the top 30% of each EEM are overlain the respective spectra in white, displayed as (λ_{ex}, λ_{em}) (nm).

Step 6: Clean Up Initial Fit. The noise component is removed from the initial fit because we are more interested in the locations of the fluorophores than finding the noise. Components 2 and 3 are identified as a single split component identified as SR101 using the neat F-EEMs acquired using both the MSC and array spectrometer (Figure 7.22). When components two and three are combined into a single component, the EEM of the combined component more closely resembles that of a neat SR101 emulsion. There can be a physical reason for shifted spectra of a single dye—solvatochromism gives rise to different F-EEM spectra in different solvent environments (for

example, if the dye was partially solubilized into the mineral oil). In that case, the two components would no be co-located in the F-EEM image. We attribute the split spectra to bias of the fit by random variations in the spectra.

The "cleaned-up" initial fit of the 4,765-pixel dataset is shown in Figure 7.23 (top and middle rows). Note that the 4,765 pixels are mapped using the pixel map described above to display a 256 × 256 size image for meaningful visualization of component score location, as viewing a line plot of pixel intensities is not especially useful for an image.

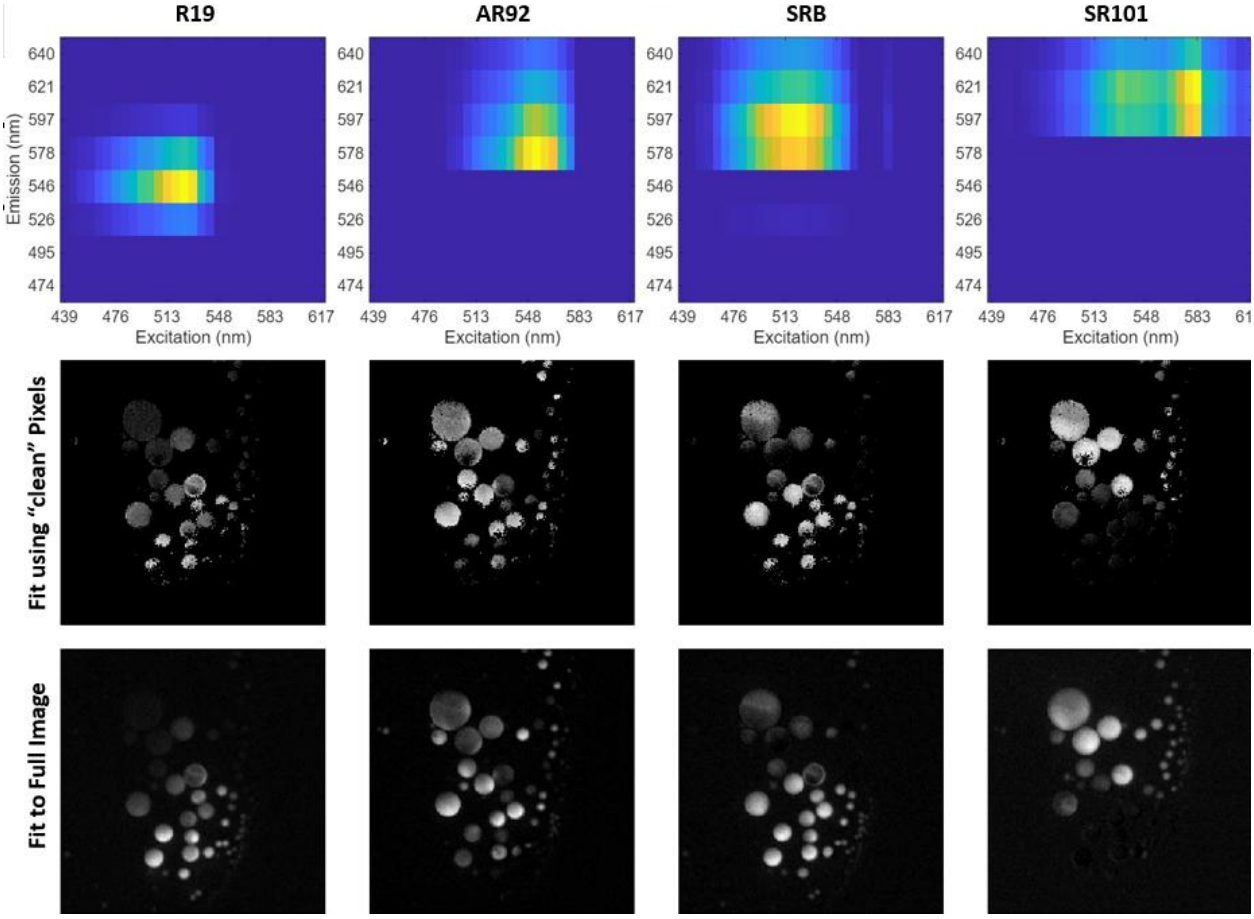

Figure 7.23. Full PARAFAC fit of an F-EEM image using scores from an initial fit. The initial PARAFAC fit was the six-component fit in Figure 7.21 with the noise component removed and split component combined. (Top) Component EEMs, (middle) component scores of the initial fit (4,765-pixel dataset) assigned onto a pixel map to represent a 256 × 256 image, (bottom) component scores of the PARAFAC fit of the full (Rayleigh-removed) F-EEM image using the initial fit EEMs as fixed initializations (excitation and emission dimensions were fixed).

Step 7: Final PARAFAC Fit. The spatial distributions of the fluorescent components in the 65,536-pixel dataset are found through a PARAFAC analysis of the full F-EEM image. Rayleigh light is removed before PARAFAC analysis. A final fit is run using a previous PARAFAC fit as an initialization. In this example, the previous PARAFAC fit was the modified ("cleaned up") fit from

Step 6. The final fit held the excitation and emission dimensions fixed, and only the relative contributions of these components are found per pixel, shown in Figure 7.23. Alternatively, a final fit can be run with no fixed dimensions—the initial fit is then used as a starting point with all dimensions (pixel, excitation, emission) free to fit.

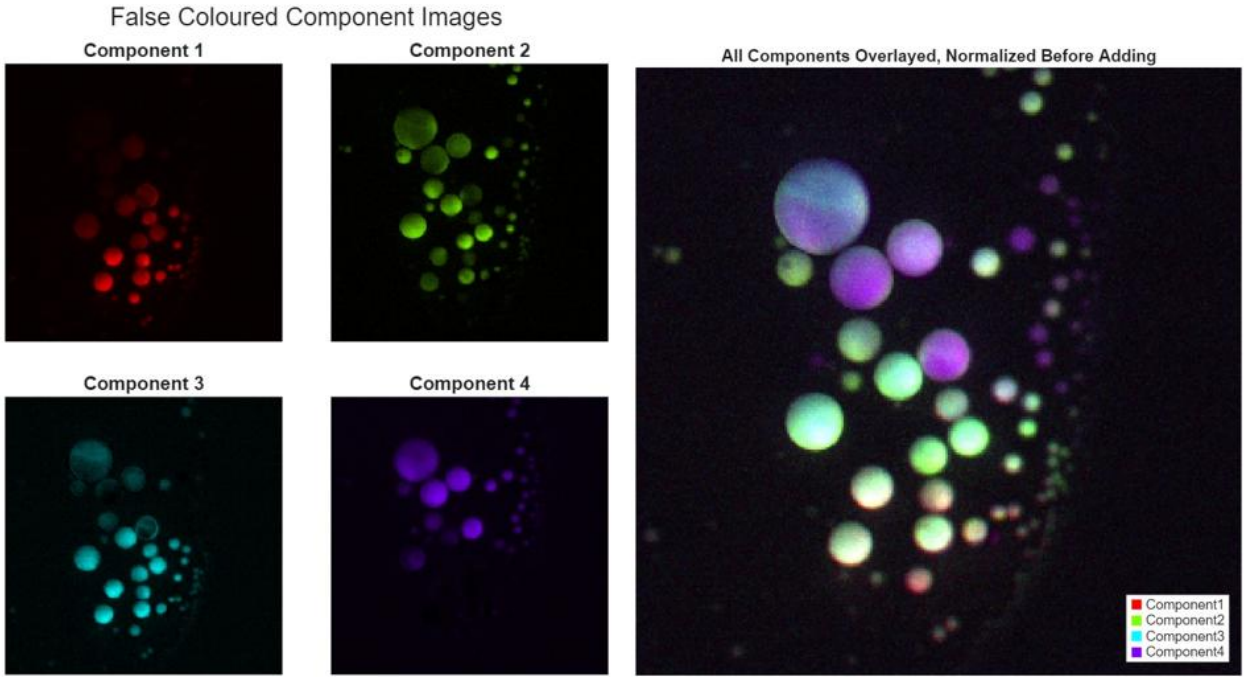

Figure 7.24. False-coloured image of full PARAFAC fit of an F-EEM image. Colours represent different components, shown in the legend on the right image. Individual components are shown in the left and middle columns, while the image on the right shows the four individual component images each normalized to 1 and overlain.

To visualize locations of fluorescence dyes in the sample, each component is assigned a colour (Figure 7.24 left, middle), and those image intensities are each normalized to 1 and superimposed (Figure 7.24 right).

This data processing flow was applied to F-EEM images acquired Setup C (MSC and DMA-PLS) and to Setup A (MSC and LDA-PLS) with a few modifications. The results are shown in the following sections.

7.5 FLEEMSI Microscopy using Multispectral Camera and LDA-PLS

A FLEEMSI microscopy setup with a coarse emission (8-channel MSC) and coarse excitation (7-channel LDA-PLS) could separate 10 fluorescent components using loading fits of neat dyes. Blind fits of the F-EEM images, however, were unsuccessful—instead, the EEM spectra had to be known, and the final fit required fixed excitation and emission dimensions. This type of analysis

is similar to that done for stained or tagged fluorophores in biological samples, such as multiplexed immunofluorescence but extended to more fluorophores compared to what is usually possible.

A loading fit of 10 dyes was created by combining one-component fits of F-EEM images of 10 individual single-dye emulsions (E/O#8, Table 7.3). The individual F-EEM images were acquired using the MSC and LDA-PLS through a Zeiss Axiovert 200 inverted microscope (Setup A, Figure 7.16). The 10 one-component fits are shown in Figure 7.25.

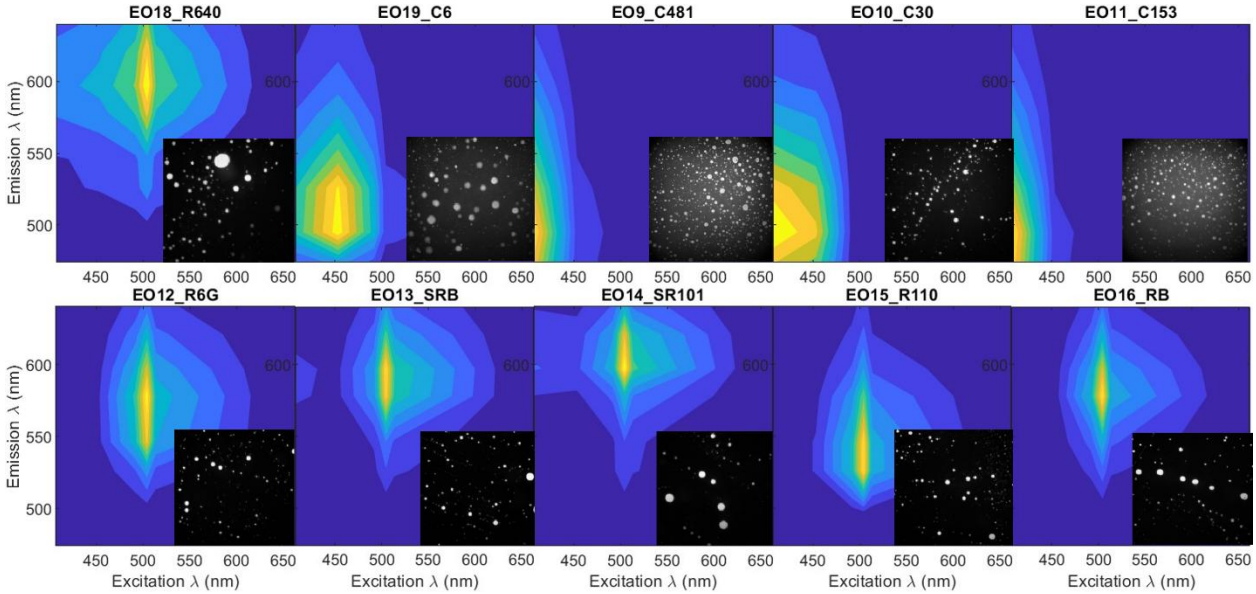

Figure 7.25. Loading vectors for a 10-component PARAFAC analysis. F-EEM images taken with Setup C were analyzed using a single-component PARAFAC decomposition, and those scores were added together to create a 10-component fit. This is used as loading scores for the excitation and emission dimensions of an F-EEM image containing all 10 emulsions.

The excitation and emission scores from the 10-component loading fit were used as fixed dimensions in a 10-component PARAFAC decomposition of an F-EEM image acquired using Setup A and containing all 10 dye emulsions. The false-coloured component images of the 10 components are shown in Figure 7.26, and the component EEM spectra are shown in Figure 7.25.

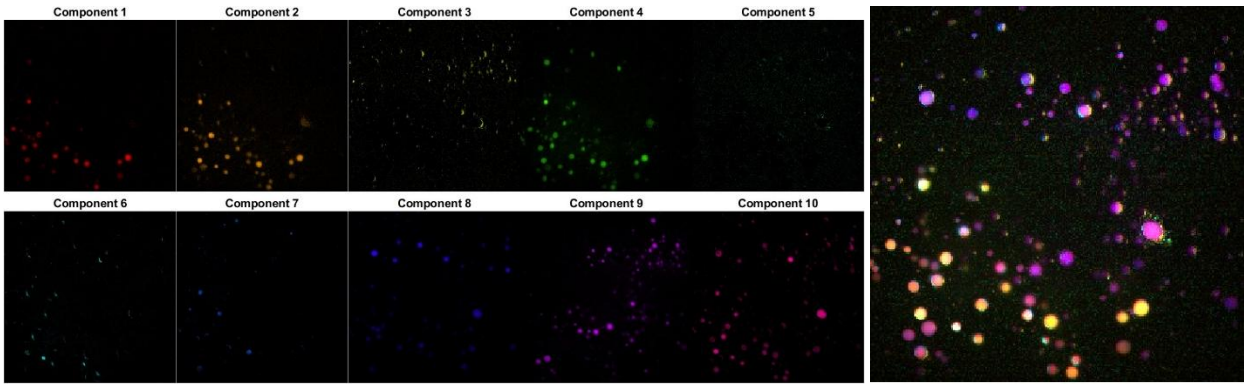

Figure 7.26. False-coloured image of the 10-component PARAFAC analysis. Image contained 10 dye emulsions and the PARAFAC analysis was run using fixed excitation and emission scores, found through single-component fits of neat dye emulsions shown in Figure 7.25.

The multispectral camera and laser diode array are shown to be capable of separation of at least 10 fluorophores with emission peaks between 474–640 nm. FLEEMSI microscopy imaging of samples containing many fluorescent stains without the requirement of many filter cubes on a microscope is a promising direction for a future student's work on this project.

A FLEEMSI microscopy system which replaces the coarse emission dimension of the MSC with a higher-resolution HSC is described in the following section.

7.6 FLEEMSI Microscopy using Hyperspectral Camera and LDA-PLS

The hyperspectral camera (HSC) (GoldenEye™, BaySpec) provides 141 emission wavelength channels in the range 400–1100 nm. The higher-resolution emission spectra for the inside and outside regions of a droplet in a Nile Red dye emulsion are shown in Figure 7.27. The two regions of interest (ROIs) of an F-EEM image acquired using the HSC to image samples on a Zeiss Axiovert 200 inverted microscope illuminated using the LDA-PLS (Setup B, Figure 7.16) are shown in green and orange in the grayscale image in Figure 7.27. We can observe that the inner and outer parts of the droplet appear to have differing emission spectra.

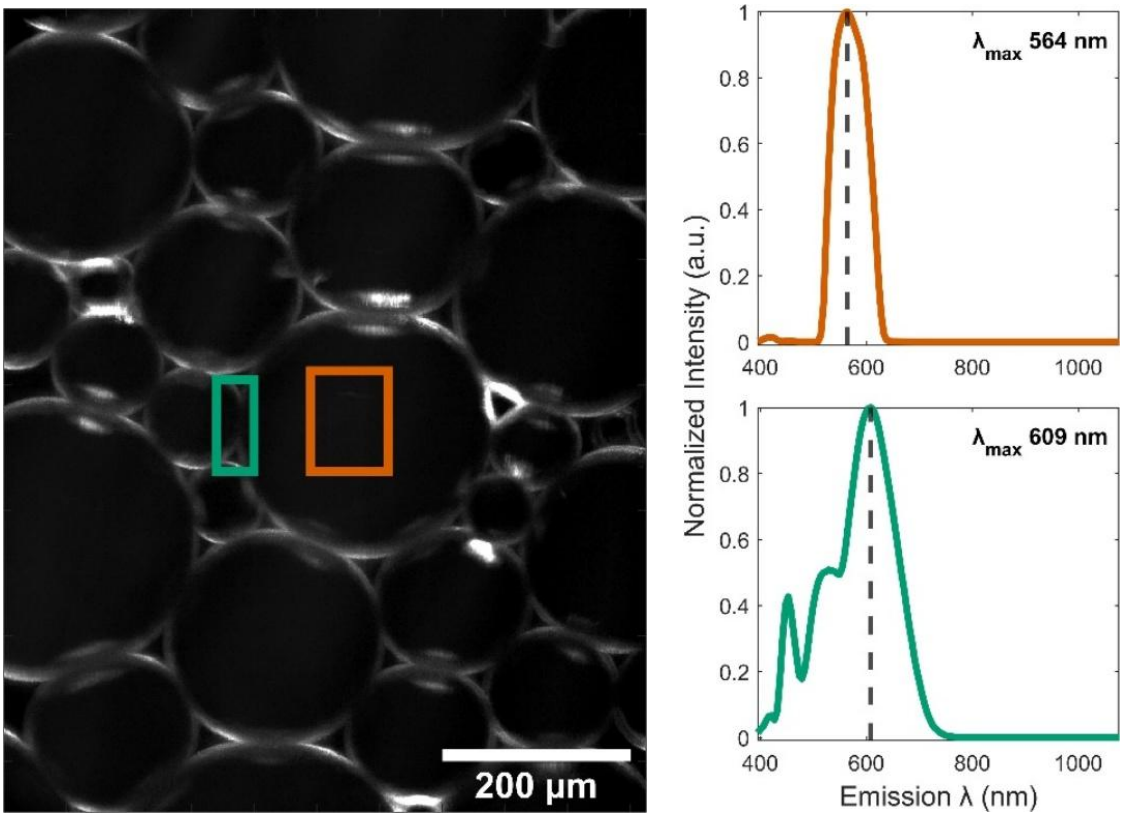

Figure 7.27. F-EEM image and emission spectra acquired using the hyperspectral camera and the laser diode array programmable light source (LDA-PLS) (Setup B, Figure 7.16). The sample was an emulsion of Nile Red on a microscope slide, imaged through a Zeiss Axiovert 200 inverted microscope with a 10x objective lens. The grayscale image (**left**) is the mean of the excitation and emission dimensions of the F-EEM, where the brightest pixels were set to 1 for better contrast of the dimmer features. Integrated emission spectra (**right**) over all seven excitation channels are shown normalized to 1 and with peak maxima for two regions of the F-EEM image, corresponding to the regions indicated on the grayscale image, of the inside (orange, top) and outside (green, bottom) of the droplets.

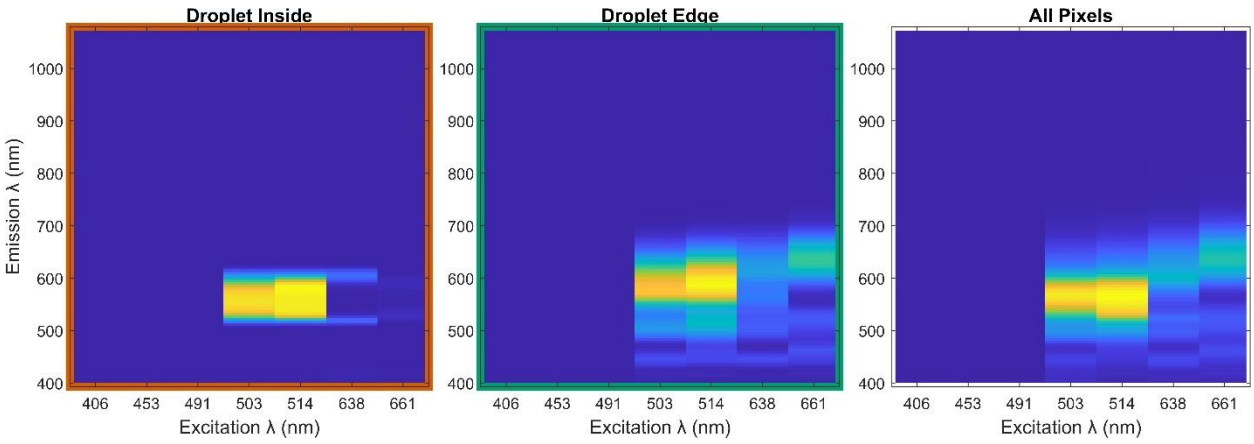

Figure 7.28. F-EEMs acquired using the hyperspectral camera and LDA-PLS (Setup B, Figure 7.16). The sample was an emulsion of Nile Red on a microscope slide, imaged through a Zeiss Axiovert 200 inverted microscope with a 10x objective lens. Mean F-EEMs correspond to the regions indicated on the grayscale image in Figure 7.27, and the whole image.

The shifted emission peak appears also in the mean F-EEMs of the ROIs shown in **Error! R eference source not found.**. The F-EEMs demonstrate that the shifted peak is not simply due to differing excitation or Rayleigh scatter, though the droplet edge does scatter more strongly than the droplet center.

Additionally, the ability to detect the shifted peak easily demonstrates a potential for use with the LDA-PLS as an illumination source for FLEEMSI FrTIR microscopy. When combined with the DMA-PLS for illumination, the intensity is too weak to observe fluorescence. The higher emission spectral resolution than that of the 8-channel MSC would be advantageous in a sample with small differences in emission spectra of components, and where the sample excitation matches that of the LDA-PLS.

In some applications, the LDA-PLS source is advantageous, such as plant or cell fluorescence, and the HSC would be able to resolve small changes in the emission spectra for *e.g.,* different chlorophyll derivatives and for fluorescent tags in different biological environments. It would be interesting to compare the spectral separation abilities of the MSC with the DMA-PLS and the HSC with the LDA-PLS, to determine the effect of a coarse spectral resolution in either the emission or excitation dimension, respectively.

7.7 FLEEMSI Microscopy using Multispectral Camera and DMA-PLS

This section presents a FLEEMSI microscopy system with a coarse emission dimension and a well-resolved excitation dimension. The fluorescence of dye emulsions excited by the DMA-PLS is imaged through an Olympus CK2 inverted microscope using the 8-channel MSC (Setup C, Figure 7.16).

Ethanol-in-oil (E/O) emulsions (EO#65, Table 7.3) were made as described in Section 7.3.1 using the dyes rhodamine 19 (R19), acid red 87 (AR87), acid red 92 (AR92), and sulforhodamine 101 (SR101). A small portion of each freshly re-agitated emulsion was added to a microscope slide on a droplet of mineral oil using a glass capillary. F-EEM images were acquired with an exposure time of 350 ms per image for a total of 11 seconds total acquisition time for the excitation-multiplexed F-EEM image.

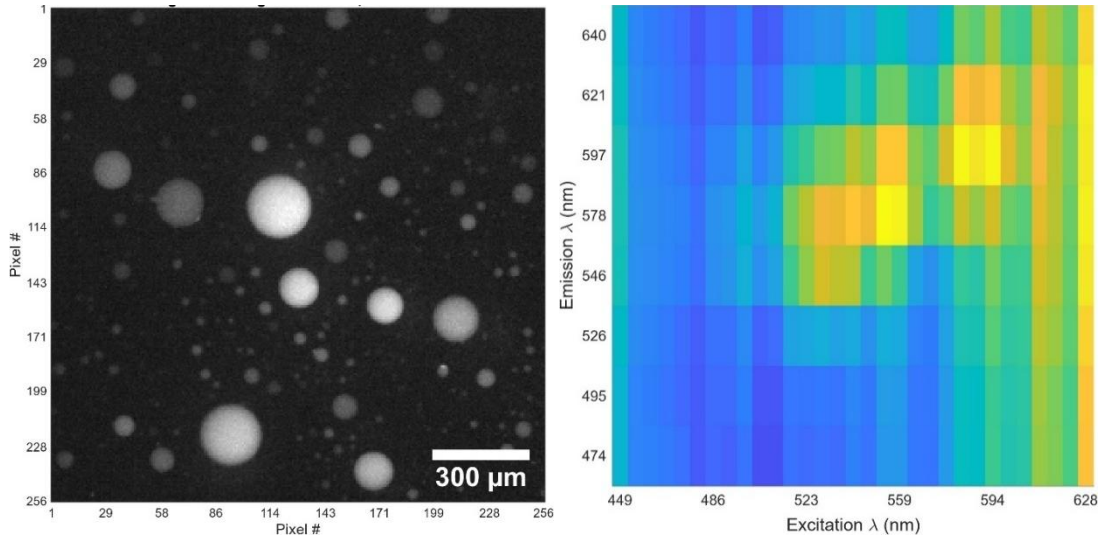

Figure 7.29. F-EEM image acquired using the multispectral camera and digital micromirror array programmable light source (DMA-PLS), through an Olympus CK2 microscope (Setup C, (Figure 7.16) using 350 ms integration time per image and 11 s total acquisition time. The image contains four E/O#65 dye emulsions. The grayscale image of the pixels in the F-EEM image (**left**) was summed over the excitation and emission dimensions. The F-EEM (**right**) is the mean of all pixels in the image.

An F-EEM image acquired with this setup—Setup C—is shown in Figure 7.29. The grayscale image containing the mean of the excitation and emission dimensions (256 × 256 pixels) shows the spatial distribution of the emulsions. The F-EEM is the mean F-EEM (8 × 31) of all the pixels in the image.

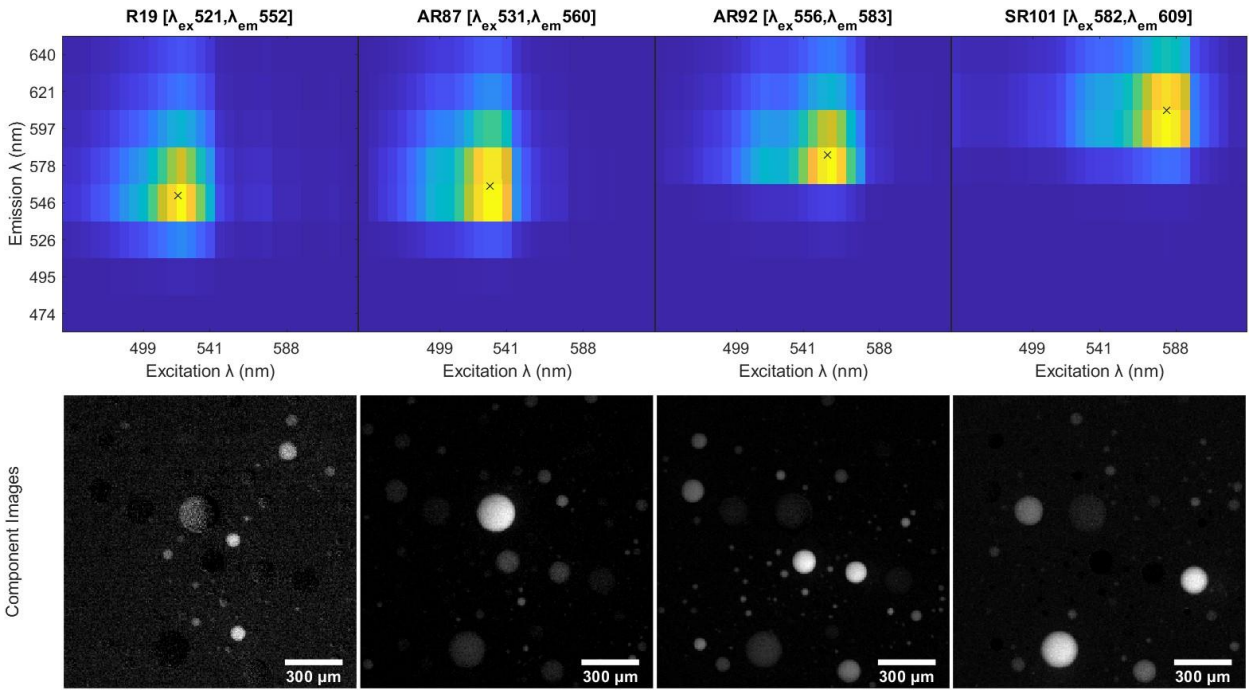

Figure 7.30. Component EEMs (top) and images (bottom) of a PARAFAC fit of an F-EEM image of four E/O#65 emulsions were added to a microscope slide taken with the 8-channel MSC and DMA-PLS through a microscope (Setup C) (Figure 7.16). Full fit used fixed loading vectors for the excitation and emission dimensions with the pixel dimension was free.

The four fluorophores can be separated using a blind PARAFAC analysis of a FLEEMSI microscopy image acquired using the 8-channel MSC with the 31-channel DMA-PLS. The F-EEM image was analyzed using the method outlined in Section 7.4. First, a PCA fit was used as a threshold to select pixels for an initial blind four-component PARAFAC. The spatial distributions of the four components were determined using fixed excitation and emission initializations from the initial fit. The component EEMs and images of this four-component fit of the full image are shown in Figure 7.30.

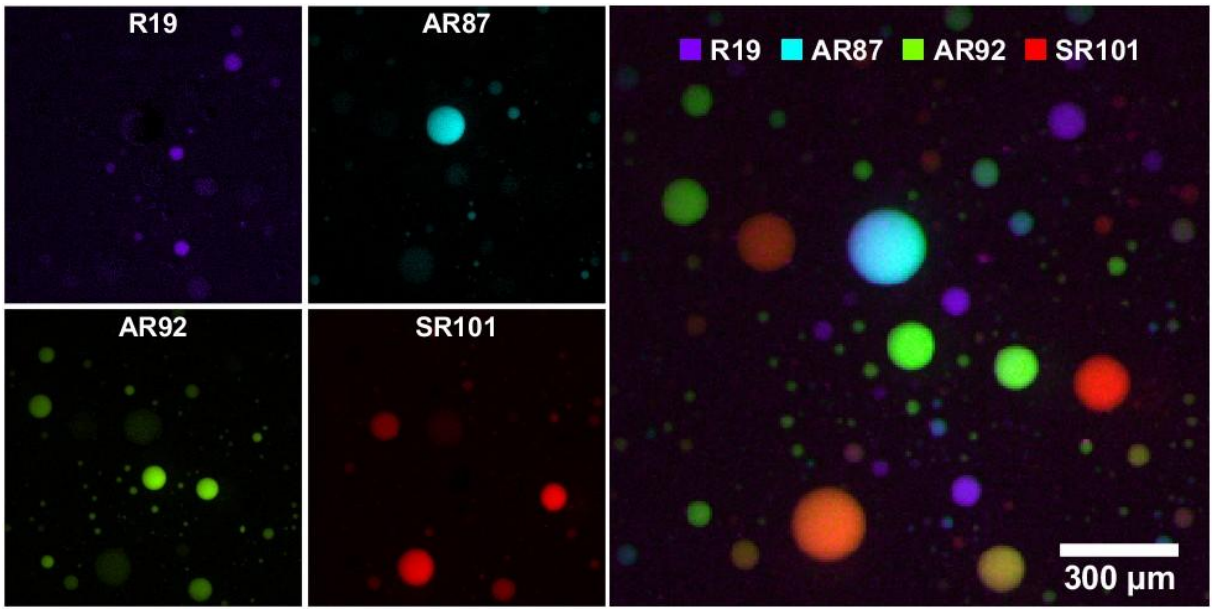

Figure 7.31. False coloured component images of the PARAFAC fit shown in Figure 7.30. Images show four different E/O dye emulsions (EO#65), and the F-EEM image was taken using Setup C (Figure 7.16).

To visualize the spatial locations of each component (dye) more clearly, false-coloured images are shown in Figure 7.31. Additional components will be imaged using this system to find the maximum number that can be identified using various combinations of spectral similarities in the dyes, and with various numbers of excitation channels with the DMA-PLS. Using a stitched image composed of neat dyes, such as the one which will be described in Section 8.2, will be an experimentally straightforward method of testing the limitations of the spectral separation ability of the 8-channel MSC and DMA-PLS FLEEMSI microscopy system.

This dataset demonstrates that the quickly acquired (11 seconds) F-EEM image obtained using the DMA-PLS and MSC system through a microscope can effectively separate four fluorophores in a blind PARAFAC analysis with no previous knowledge of the system. When the fluorophore signatures are known, based on the results shown in Section 7.5, we expect to be able to separate at least as many components as the LDA-PLS and MSC system (10 signatures). Ongoing work has shown separation of additional components using both blind and loading vector PARAFAC fits, both of which will appear in an upcoming publication.

The time resolution and the spectral resolution of F-EEM images acquired using a Hadamard-modulated excitation source can be increased using algorithms during dataset analysis. Both algorithms, developed by Dr. Travis Ferguson, are described in the next chapter.

Chapter 8 Increasing Time and Spectral Resolution

8.1 Supercycle—Increasing Time Resolution

The acquisition of a Hadamard-multiplexed F-EEM requires that the emission from all masks be recorded. Only when N different combinations of wavelengths have been used to excite the sample (N = 7 for the LDA-PLS and 31 for the DMA-PLS) the inverse Hadamard transform can be performed to obtain an F-EEM. The process of acquiring an entire "cycle" of masks takes between 500 ms to 11 s for exposure times between 50–350 ms range. Increasing the time resolution can not only increase the data available for analysis but also improve the image quality as it can reduce the blurring which occurs when the 7 or 31 images are demultiplexed—essentially averaged—over the time frame. Rapid changes within a single Hadamard cycle can also result in artifacts in the demultiplexed EEMs.

The Hadamard Paley S-matrices are composed in a way that the values in each row of the matrix shift by one to the right for each subsequent row (Figure 8.1). Usually F-EEM images are acquired sequentially—one full cycle of *e.g.,* 7 or 31 masks would be completed—then the next cycle would be started again with mask #1.

Assume that we want to acquire a dataset containing five full F-EEM images with N = 7 different wavelength bands and 8 emission bands I (256 × 256 × 8 × 7 × 5). We propose that the first *frame (F)* is demultiplexed as usual using the first seven masks ($M_{1–7}$), but that the second *frame* takes $M_{2–7}$ from the first cycle, I_1 and M_1 from the second cycle, I_2. Equivalently, one can rearrange the dataset as a 256 × 256 × 8 × 35 hypercube and select 7 consecutive masks to obtain one F-EEM frame. Each of these *frames* with dimensions 256 × 256 × 8 × 7 is then demultiplexed by their respective inverse Hadamard matrix. The matrix used for demultiplexing F_1 and F_2 would then be the inverse of those shown in Figure 8.1.

This should create $n_{frames} = \left(n_{images} \times n_{excitation}\right) - n_{excitation} = (5 \times 7) - 7 = 28$ *frames*, each with dimensions 256 × 256 × 8 × 7.

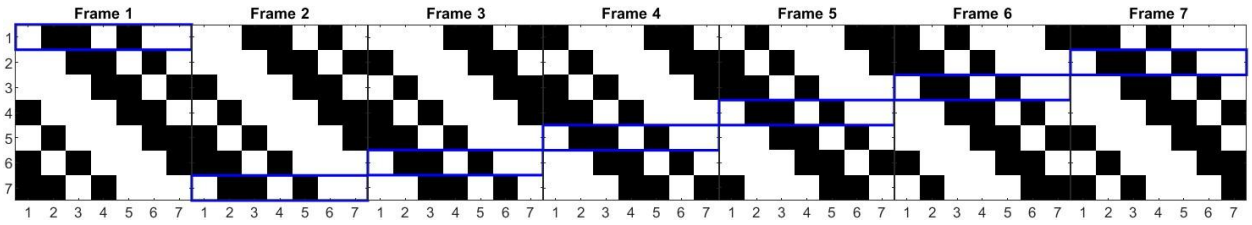

Figure 8.1. Matrices used for EEM acquisition for a rolling average-style Supercycle. This is for an n=7 size dataset, as shown in the other theoretical examples. The blue box shows the "first" mask which is used for excitation, as it is changed in position as a "rolling average" is moved through the sequentially acquired F-EEM images (*e.g.*, for a 256 × 256 × 8 × 7 × 5 dataset).

In practice, we require fixed loading vectors—known PARAFAC spectral components, an initial fit—to perform a PARAFAC fit to find the component scores for each pixel. A blind PARAFAC analysis becomes too unstable and forbiddingly complex. This to say—we use a final fit as described in Section 7.4.

Modelling the dataset containing the demultiplexed *frames* (256 × 256 × 8 × 7 × 28) using fixed excitation and emission loading vectors obtained from an initial fit, we can obtain the scores of those components at each of the 28 times. The time resolution is therefore much higher than before, approximately by a factor of N (here, 28 timesteps instead of 5). The spectral PARAFAC components (the loading vectors or initial fit) can be created using the 256 × 256 × 8 × 7 × 5 demultiplexed dataset or another dataset which includes the components in the 5-image dataset (for example, a static sample of the components), or using fits of the neat components. This is demonstrated in Figure 8.2 with data acquired using the DMA-PLS with 31 channels for a dataset of size 256 × 256 × 8 × 31 × 5.

An afterimage seems to trail behind the droplets as they move through space. While the repetition rate has been increased, each F-EEM is still the result of 31 masks that are illuminated sequentially—each F-EEM is a rolling average of 31 consecutive exposures and is consequently blurred if objects move at a higher rate.

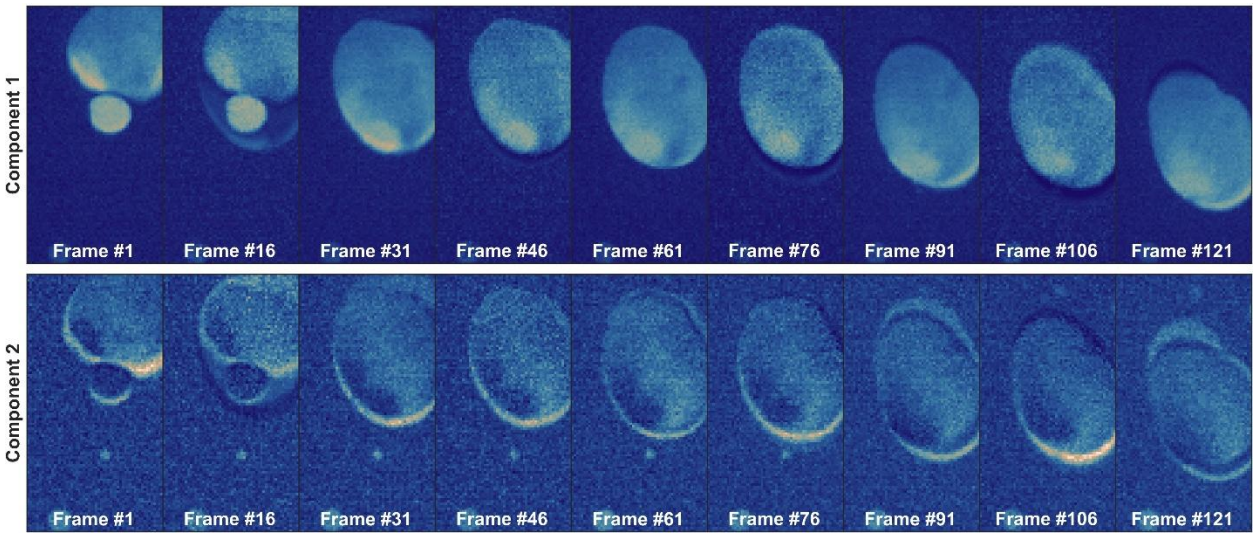

Figure 8.2. Frames of a rolling-average demultiplexed F-EEM image. F-EEM acquisition used 8-channel MSC, DMA-PLS with 31 multiplexed excitation channels (size 31 matrix), at 300 ms exposure time per excitation, for a scan of 5 F-EEM images, analysis was done on a 56 × 106-pixel region of the image to reduce processing time. F-EEMs were demultiplexed using a rolling-average style where excitation masks 1:31 were used for the first frame, 2:32 were used for the second, until frame #124 (the final 31 excitation wavelengths). Each frame was fit using a PARAFAC fit of known component EEMs, with the excitation and emission vectors set as fixed, and nonnegativity set in all dimensions.

The "Supercycle" algorithm was developed by Dr. Travis Ferguson and is described in the refenced paper for the case of fast fluorescence detection in an HPLC column [276]. In this paper, he suggests an alternative method which does not rely on a rolling average of subsequent exposures. Instead, the algorithm uses multiplexed component loading vectors *directly* for a PARAFAC fit on each of the multiplexed masks. To this end, arrays of the original matrix size—N = 7 for consistency with previous examples—are created using NaN values *except* for the individual mask associated with a particular *frame* (Figure 8.3).

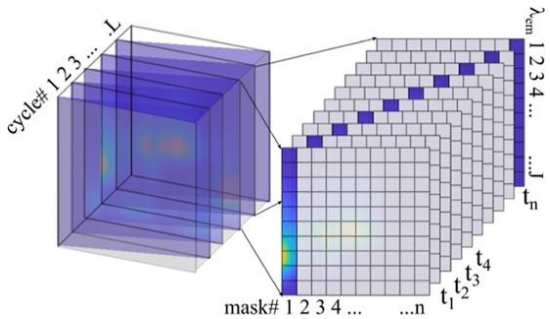

Figure 8.3. Graphical representation of NaN data-cube obtained by a sparse-NaN-expansion[276].

Multiplexed component spectra (Figure 8.4) are created by multiplying a component EEM spectrum with the Hadamard Paley S-matrix used to acquire each of the images in the analyzed dataset.

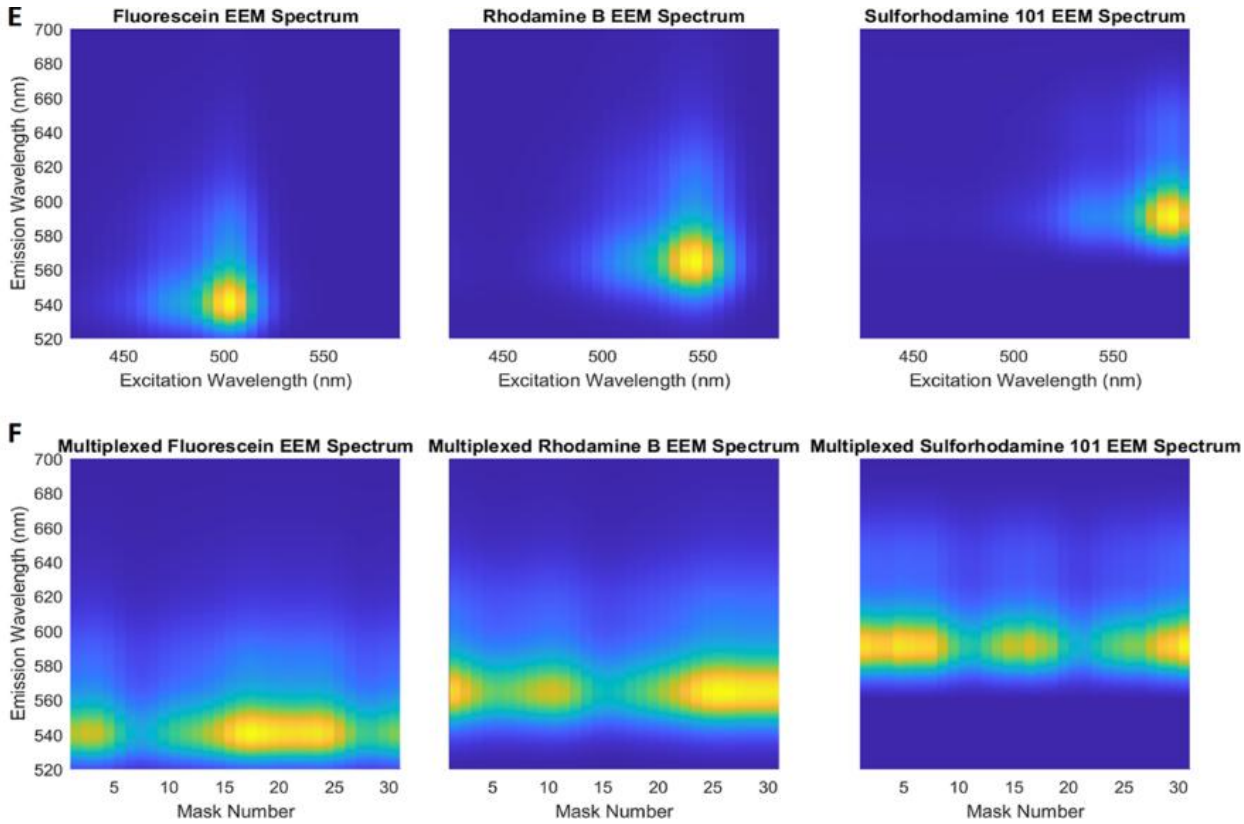

Figure 8.4. F-EEM signatures of fluorophores and their excitation-multiplexed equivalents[276]

This process was tested on both a simulated and a previously obtained experimental dataset and published in the paper explaining the algorithm [276] (Figure 8.5). The article demonstrates that applying the Supercycle to a sparse simulated dataset (Figure 8.5B) (down sampled from the simulated dataset in Figure 8.5A) allowed for accurate reconstruction of the spectral responses at intermediate time steps (Figure 8.5C).

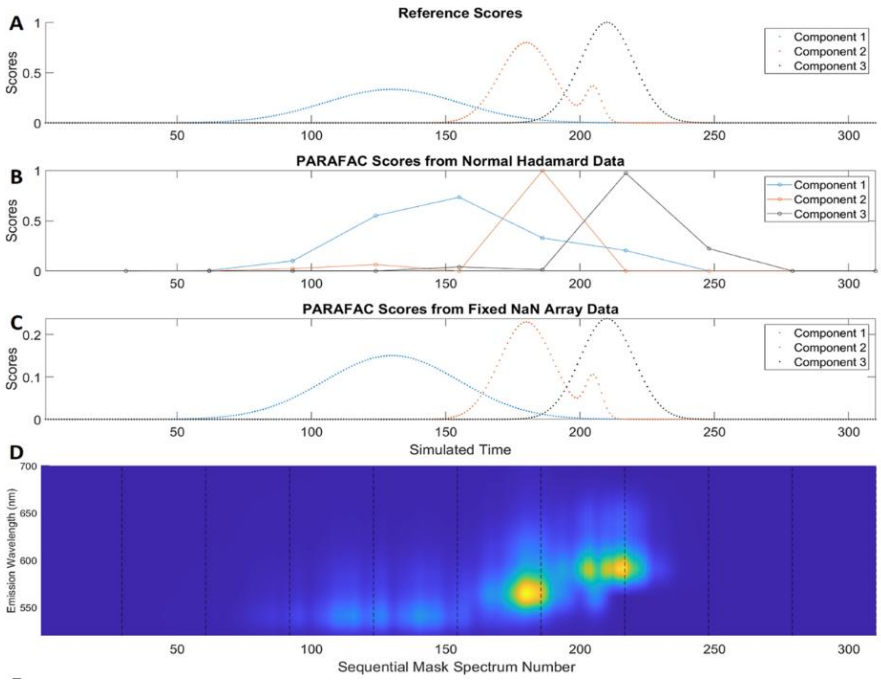

Figure 8.5. Application of Supercycle algorithm on simulated chromatographic data. (A) Simulated chromatogram for three fluorophores used to create a data cube for PARAFAC analysis. (B) PARAFAC scores from the HT- multiplexed simulated dataset using a cycle-by-cycle approach. (C) Scores from PARAFAC results from PARAFAC modeling the F^{NaN} data-cube. (D) Dimensionality-reduced unfolded data cube F, referred to as F* in the text. The vertical, black-dashed lines indicate a completed cycle of *n* masks[276].

In this work, we applied the NaN-array Supercycle algorithm (SCA) to the F-EEM image shown in the rolling average method above (Figure 8.2), with dimensions 256 × 256 × 8 × 31 × 5. Figure 8.6 shows the 31 masks of a raw F-EEM image, where each mask represents a Hadamard-multiplexed excitation pattern as described 0, and the grayscale image shows the mean of the 8 emission channels.

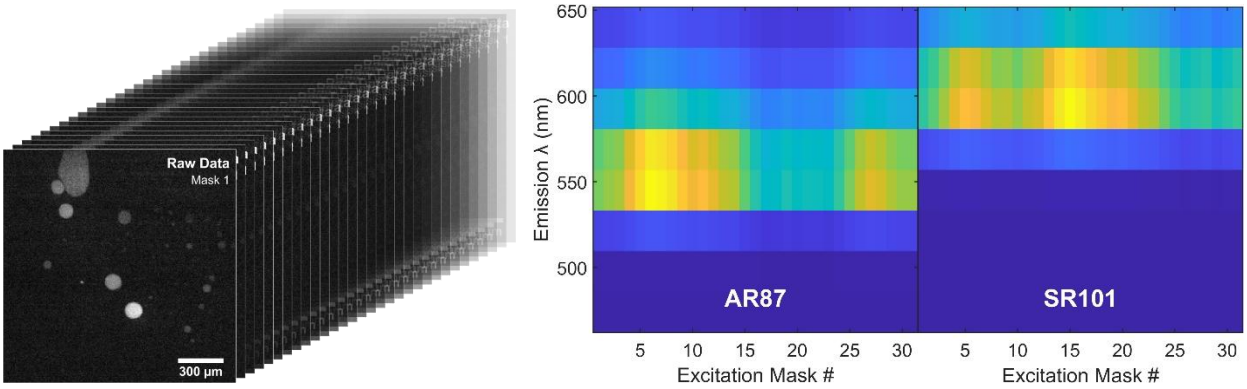

Figure 8.6. Raw excitation-multiplexed F-EEM frames and the component spectra used for fitting using the Supercycle algorithm. The component spectra are shown for each mask, instead of each excitation channel as would typically be seen. The 31 frames (**left**) (256 × 256 × 8) will be fit with the spectra (**right**) using the Supercycle algorithm.

These five multiplexed F-EEM images, each consisting of 31 individual acquisitions with Paley S-type excitation masks, are converted to 155 frames where each frame represents a 31 × 31 array of NaN values with the single mask used for illumination in that frame. The component EEMs were created using one-component PARAFAC fits of the neat components (recorded previously) and multiplied by the Hadamard matrix used to obtain the images for the multiplexed emission spectrum for each excitation mask.

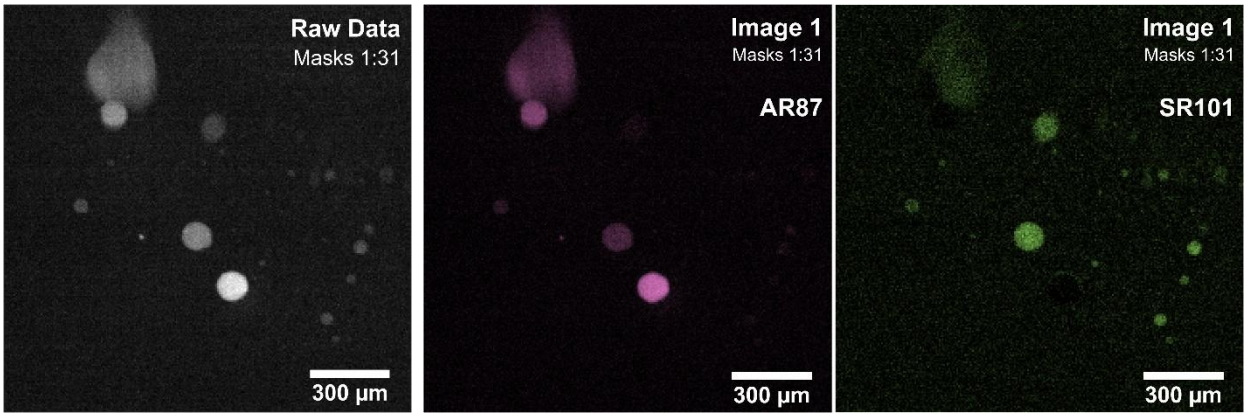

Figure 8.7. Application of the Supercycle algorithm to the first image in a time series. (**left**) Raw image, mean of masks 1 to 31, mean emission, (**right**) after Supercycle has been applied to each frame in that image.

Figure 8.6 shows the mean emission and excitation of the first 31 masks in the dataset—the first multiplexed image. The same set of masks are shown averaged after application of the SCA, where the component EEMs from Figure 8.6 have been applied to all 31 masks. The image is false coloured with arbitrary colours chosen for the two components—AR87 (pink) and SR101 (green).

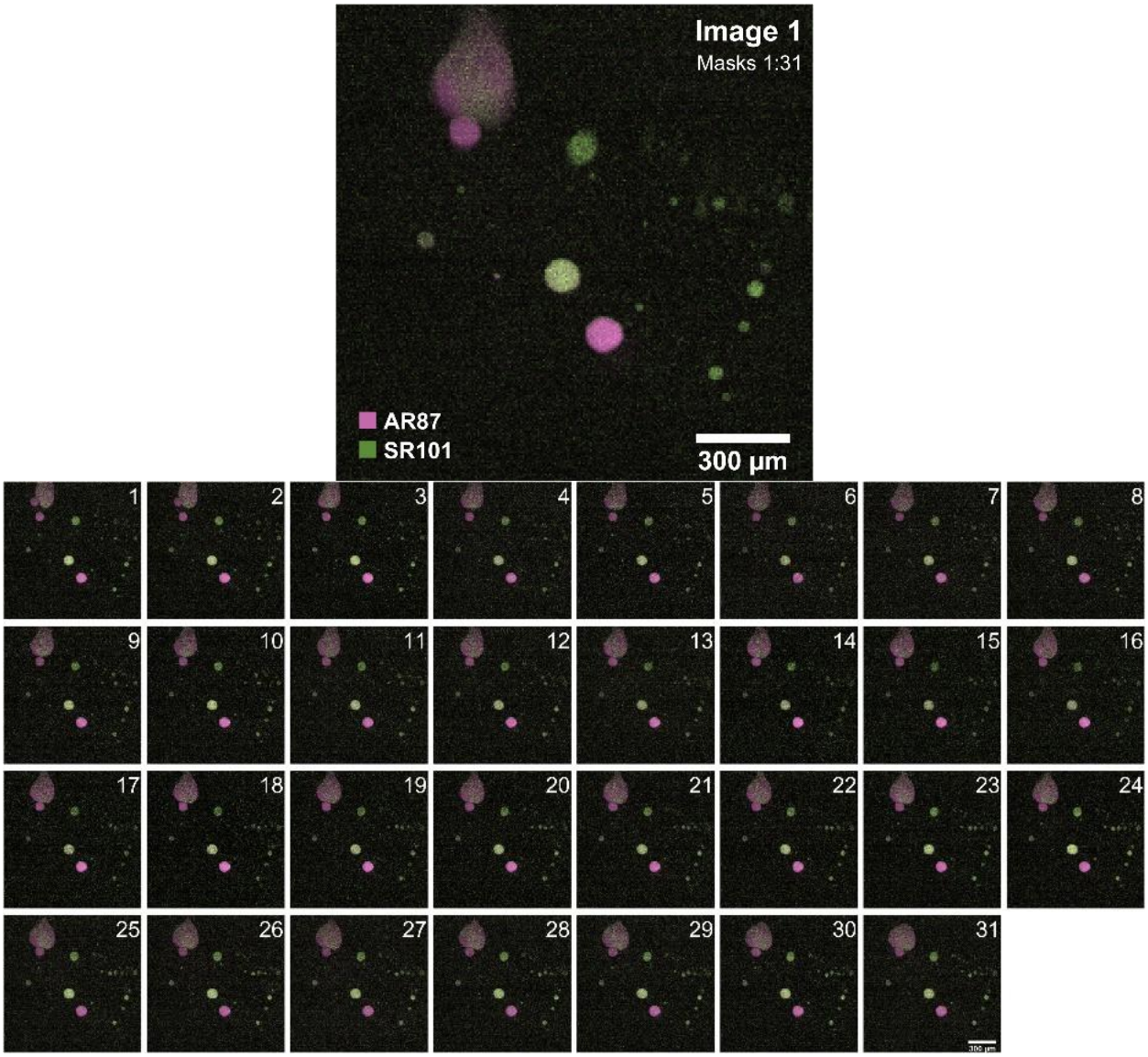

Figure 8.8. Single multiplexed F-EEM image after application of the Supercycle algorithm. Image size 256 × 256 × 8 × 31. (top) Overlain false coloured image of the two component images shown in Figure 8.6, mean of the 31 masks, (bottom) individual single-mask images after application of the Supercycle.

Although a video demonstration is more convincing, flat images are used for print to demonstrate the increased time resolution achieved using the Supercycle algorithm on an F-EEM acquired using a Hadamard-modulated excitation light source in Figure 8.8. The false coloured images of the two component images from Figure 8.6 are overlain (Figure 8.8, top), and the 31 frames representing the two overlain false-coloured component images for each multiplexed mask (masks 1–31) are shown in Figure 8.8 (bottom). Figure 8.9 shows the increased time resolution in video form, of the five images of the dataset.

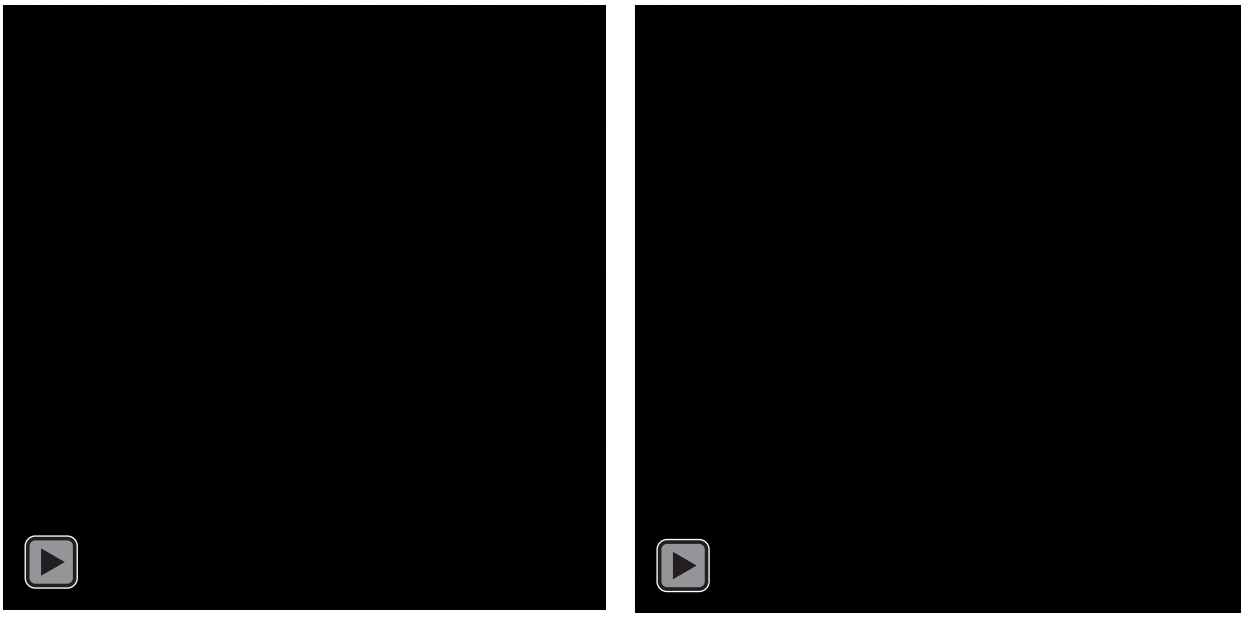

Figure 8.9. Increased time resolution using the Supercycle algorithm on an F-EEM image. Image size 256 × 256 × 8 × 31. (**left**) Greyscale image showing the regular, demultiplexed five-image dataset, where each image contains 31 excitation masks (wavelength bands), and each set of 31 frames represents a single F-EEM acquisition. (**right**) The 31 × 5 (155) frames of the still-multiplexed F-EEM dataset, after application of the Supercycle algorithm. Each frame represents an overlay of the component score vectors from a two-component PARAFAC analysis, shown in Figure 8.6.

The large droplet in the top left can be seen engulfing smaller droplets as it moves through the image. Interestingly, the small droplet to the left of the large droplet in the top left corner of the first and second frames is engulfed by the larger droplet by the third frame. This small droplet cannot be separated in the mean of the 31 frames (Figure 8.8, top) which demonstrates the usefulness of the increased time resolution.

Using the Supercycle algorithm on F-EEM images, we reduce the time interval between fluorescence observations from 11 seconds (every 31 masks) to 350 ms—*i.e.,* to every mask. This increases the time resolution by a factor of N, where N is the size of the Paley S-matrix used for the multiplexed excitation source. Additionally, the ability to use these intermediate frames of a multiplexed F-EEM image demonstrates an additional advantage over a traditional sequentially scanned F-EEM spectrum. The SCA allows for monitoring systems in which the analyte moves faster than the acquisition time required for a complete F-EEM to take place, such as droplet systems, Just as importantly, there is no longer a time penalty for using larger Hadamard matrices—for our DMA-PLS, the temporal resolution remains the same even if the Paly S-matrix and the associated number of wavelength bands is increased from 7 to 127. As opposed to any of

the conventional multiplex methods—conventional Hadamard- or Fourier-Transforms—the spectral resolution can be increased *without* a commensurate decrease in the data acquisition rate.

This section described how one could use a modified data processing routine to increase the time resolution of the image acquisition process by more than an order of magnitude. The following section describes a method to circumvent the hardware limitations of spectral resolution on a multispectral camera using a machine-learning approach to spectral upscaling. Both are, in essence, software solutions around hardware limitations, and have proven to be simple to implement and highly effective.

8.2 Spectral Upscaling—Increasing Emission Spectral Resolution

We rely on multispectral or hyperspectral imaging to obtain the fluorescence emission spectrum for each pixel in an image. Unfortunately, these cameras all exhibit trade-offs between spectral resolution, spatial resolution, and brightness—increasing either spectral or spatial resolution usually comes at a cost to the intensity and/or the respective other resolution.

An MSC using a colour filter array (CFA) has an inherent limitation to the number of colour channels that can be added while maintaining acceptable spatial resolution and intensity. With a Bayer CFA (RGGB), the red pixels make up one-quarter of the coloured pixels and will consequently see only 25% of the incoming light. In an 8-channel MSC, such as the one by Spectral Devices [204], each colour channel registers at most one-eighth the incoming light, and in fact significantly less. Since border pixels surround each of the eight three-pixel colour channels, only 3/64 of the incoming light is detected per channel and $64-(3\times 8)/64=62.5\%$ is not detected at all. As the number of colours is increased, the spatial resolution decreases for a given imaging sensor, and the sensitivity decreases with the lower light throughput.

In principle, interferometric image detection as advertised for our hyperspectral camera, should circumvent this issue. Ideally, each frame of an interferometric image sensor should contain 50% of the incoming light, and the light throughput and spatial resolution should not depend on the spectral resolution. In practice, the transmission losses through the complicated optical setup of the GoldenEye™ (BaySpec) camera were very high. Combined with less-than-optimal software controls such as too-low allowed exposure times, the camera fell short of this idea. This led us to look for increased spectral resolution using postprocessing rather than new hardware.

This fundamental limitation of snapshot cameras—increased spectral resolution implies decreased spatial resolution and lower light throughput—belies a circumvention of these parameters using computational solutions. Although we cannot easily increase the emission spectral resolution of an imaging sensor using hardware, we looked instead to software. Previous work by a group member showed that machine learning algorithms (MLAs) were able to identify and quantify components of atomic emission spectra far better than was initially thought possible[329, 330]. This success, along with the large body of recent work on RGB upscaling recently [331-333], led us to attempt spectral upscaling of our 8-channel MSC emission data using a convolutional neural network MLA which was trained on high-resolution fluorescence emission spectra. In essence, we combine the high spatial resolution / low spectral resolution output of the MSC with the *no* spatial resolution / high spectral resolution of a fiber-coupled array spectrometer that collects fluorescence from the entire FOV of the sample.

This work has been done collaboratively with Dr. Travis Ferguson, a post-doctoral researcher in our group, who created the MLAs for the spectral upscaling process. My contribution has been the collection, analysis, and application of the upscaling models on F-EEM images. Demonstration of spectral upscaling on fluorescence emission collected using the 8-channel MSC is shown using the laser diode array (LDA) as the excitation source (Setup B) and the DMA-PLS (Setup C) (Figure 7.16, Section 7.3.2).

8.2.1 Model Development

A convolutional neural network, CNN, is trained on fluorescence emission spectra of various fluorophores and scattered light to create a model. The training uses fluorescence emission spectra of various fluorophores and single-wavelength scattered light collected by the 8-channel MSC and an Avantes spectrometer (AvaSpec-ULS2048XL-EVO) simultaneously. The model learns to upscale the 8-channel emission spectra to the ground truth emission spectra collected by the spectrometer. Fluorescence spectra were acquired as F-EEM images with the MSC using the DMA-PLS, though once demultiplexed, the emission spectra were provided to the model independent of excitation information.

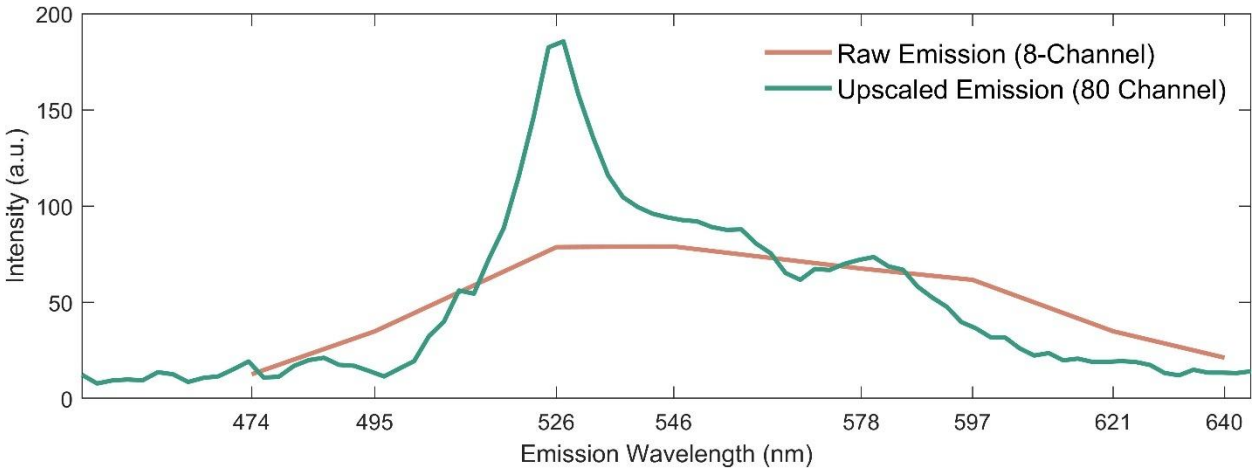

Figure 8.10. Raw (8-channel) and upscaled (80-channel) emission spectra. Sample is a mixture of glycerol-in-oil emulsions on a glass microscope slide. Images were taken through a Zeiss Axiovert 200 inverted microscope with an 8-channel multispectral camera using one excitation wavelength (504 nm). Emission spectra are the mean of all pixels in the raw or upscaled image.

We had an abundance of fluorescence emission spectra, as each pixel in an image acquired with the 8-channel MSC contains 65,536 spectra. Since the images are acquired with N different excitation bands, a total of $N \times 65{,}536$ emission spectra were acquired per F-EEM image. Because the sample illumination method did not take advantage of the full field of view of the camera, only a portion of the pixels in each image were used. The dataset was further divided into training, testing, and validation spectra. Details on the training and validation are described in the manuscript in progress, and this work focuses on the application of the trained model on new F-EEM images.

8.2.2 Application to Excitation-Multiplexed Fluorescence Images

The model is applied to each of the demultiplexed excitation bands for each of the 256 × 256 pixels in an F-EEM image acquired with the MSC. Figure 8.11 shows the mean EEM over all pixels for the raw and upscaled datasets.

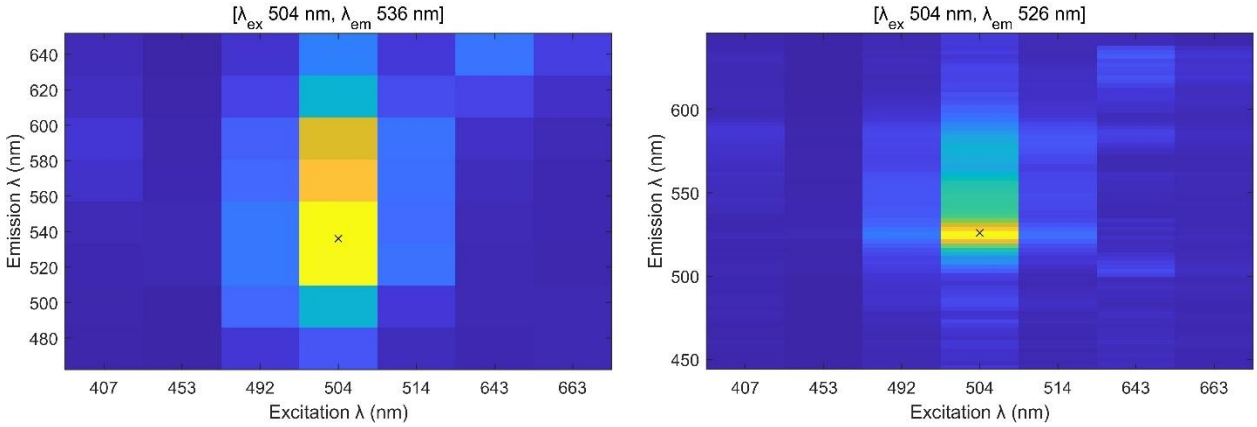

Figure 8.11. F-EEM before and after upscaling spectral emission. F-EEMs are the mean of all the pixels in an F-EEM image acquired using an 8-channel multispectral camera with the laser diode array for excitation. Upscaling performed by normalizing pixel emissions and applying the Supercycle algorithm, then correcting for excitation intensity and pixel intensity from the original image. Centroids are taken from the top 10% of the peak found using a mesh grid in MATLAB (Appendix A.10).

The pixels are linearized for easier indexing, which is how they will be referred to from here. Each upscaled emission spectrum is then represented by $U_{p,i} = f_\theta(S_{p,i}), f_\theta : \mathbb{R}^n \to \mathbb{R}^m$ where M is the model from the neural net and S_p is the 8-value emission spectrum at each pixel p and excitation wavelength i. Each S is normalized to 1 before applying the model to prevent incorrect CNN predictions based on spectral intensity. Because this also amplifies noise and maintains none of the original intensity information in the image, the data are corrected after the model is applied. The intensity of each EEM in the upscaled image U is normalized using the sum of the intensities in the original pixel EEM R and the upscaled pixel EEM.

$$U_p^{corr} \approx U_p \times \left(I_p^R / I_p^U \right) \quad [8.1]$$

Where I_p^U is the intensity of a pixel in the upscaled image:

$$I_p^U = \sum_{em,ex} U(p, em, ex) \quad [8.2]$$

And I_p^R is the intensity of a pixel in the original image:

$$I_p^R = \sum_{em,ex} R(p, em, ex) \quad [8.3]$$

The spectral response of the EEM is then corrected using the mean excitation channel intensities for each pixel in the original and upscaled datasets.

8.2.3 Demonstration of Technique

We find that upscaling the 8-channel MSC emission data to 80 channels allows us to spectrally separate a greater number of fluorophores than was possible with the raw 8-channel data.

This is first demonstrated using Setup B—excitation via the LDA-PLS and emission detection via the MSC through a Zeiss Axiovert 200 microscope—imaging a mixture of G/O dye emulsions. Three-component PARAFAC fits of the raw and upscaled data are shown in Figure 8.12 and Figure 8.13. Spectral upscaling of the 7 × 8 F-EEM spectra acquired using the MSC and LDA allowed for a PARAFAC analysis to find the third fluorescent component. This was not possible with the raw data, as shown in Figure 8.13, where the additional component appears as a split component overlapping nearly exactly with the first component.

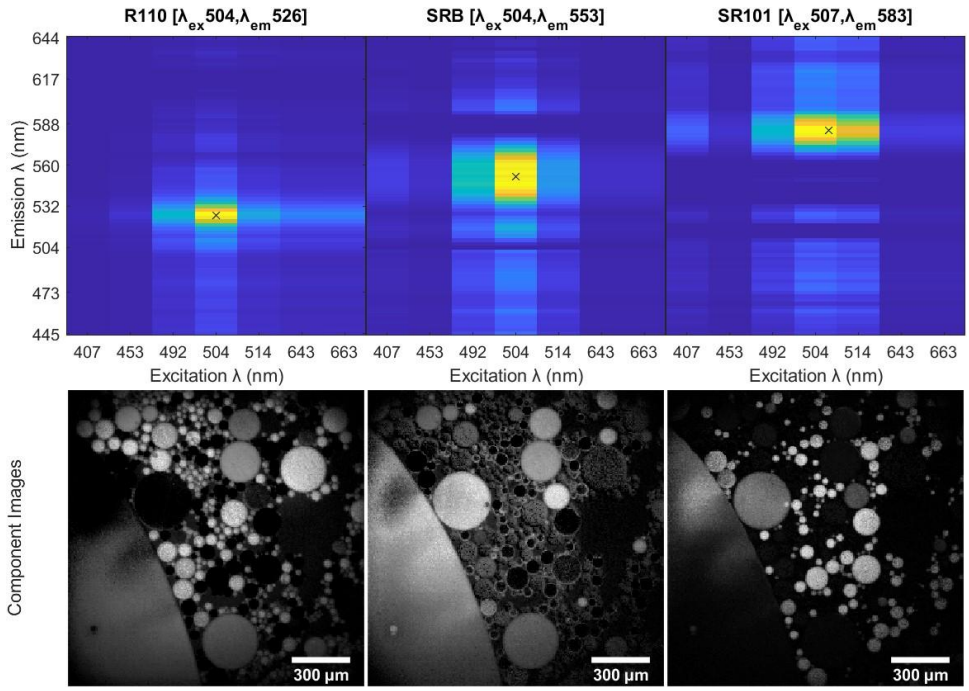

Figure 8.12. Three-component PARAFAC analysis using upscaled emission data. F-EEM images were acquired with an 8-channel multispectral camera and seven laser diodes and upscaled data were created by applying an upscaling neural network to the raw data. Component EEMs and component images from a three-component PARAFAC fit are shown on the top and bottom rows, respectively.

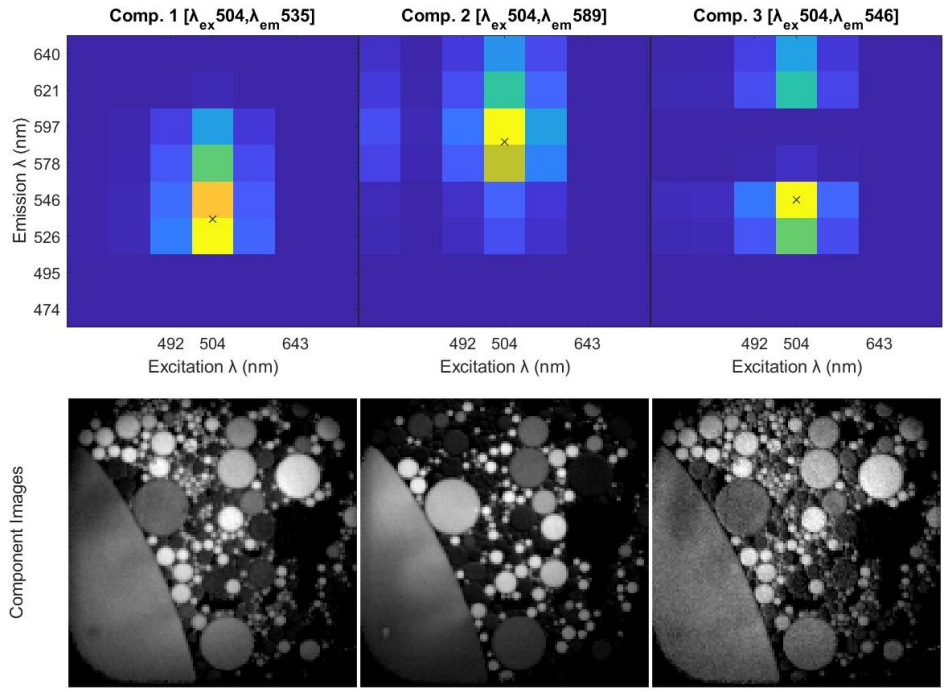

Figure 8.13. Three-component PARAFAC analysis using raw emission data. F-EEM images were acquired with an 8-channel multispectral camera and seven laser diodes. Component EEMs and component images from a three-component PARAFAC fit are shown on the top and bottom rows, respectively.

Using spectral upscaling on a coarse-emission and coarse-excitation F-EEM acquired using an 8-channel MSC can allow for component identification using a blind PARAFAC analysis which had not been possible with the raw data. While this experiment provides a useful test, there is greater potential for spectral upscaling when using a large excitation dimension such as the DMA-PLS and combining that with spectrally upscaled emission spectra.

The DMA-PLS and MSC can already separate four components with similar excitation and emission maxima as those shown in this section without difficulty, and we require a more complex test case to illustrate the advantage of the technique when using the DMA-PLS.

The ability of upscaled F-EEM images to identify fluorophores in a sample was demonstrated using a stitched image composed of six images, each showing an emulsion of a neat dye. These six images of single-fluorophore emulsions were taken using Setup C and pixels representing the strongest fluorescence in each of those images were selected using a PCA threshold (Section 5.4.3). Individual masked images containing the selected pixels are shown in Figure 8.14, where black pixels are NaN values used only to create an image of the correct dimensions for visualization. A stitched image (Figure 8.14, right) was created using slices (30 × 240 pixels) of each masked image.

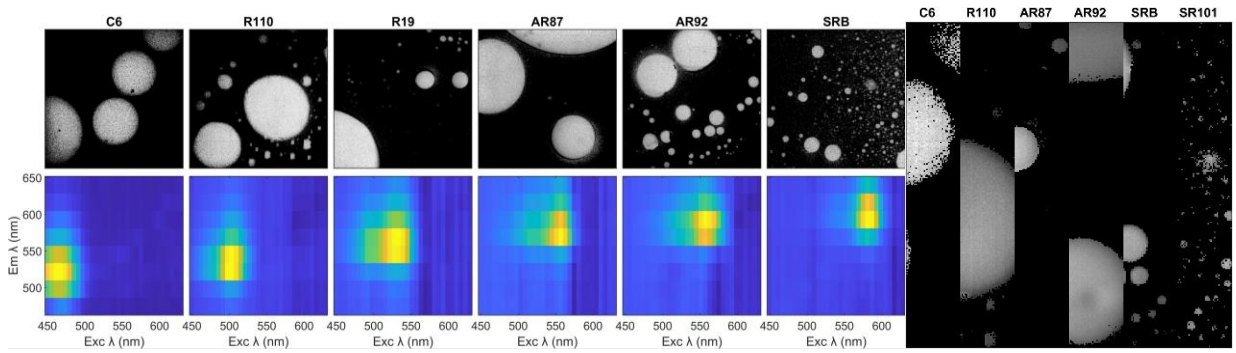

Figure 8.14. Creation of a stitched image as a ground truth in an analysis of upscaled emission spectra. Individual images of single-dye emulsions were acquired using Setup C with an exposure time of 350 ms per mask for a total of 11 seconds per F-EEM image. PCA threshold maps (top) were created for each of the six images by keeping only pixels with a score above 1 for the first principal component in a PCA of the neat image, and the mean F-EEMs of the remaining pixels is shown on the bottom. Slices of 30 × 240 pixels of each mapped image were added to create the stitched image shown on the right. Black pixels are NaN values and are not used in the PARAFAC analyses shown.

The stitched image was an alternative to using images containing all six dyes, as adding the dyes to a slide together was practically difficult. Although our simple computational experiment does not account for inner-filter effects or other experimental difficulties such as fluorophore quantum yields, it serves as a useful benchmark for the technique. Each component should appear in only one slice of the image, so it should work well as a method to characterize the quality of each fit and the crosstalk between components. Crosstalk between components cannot be verified in an image made up of multiple emulsions on the same slide as the droplets combine. Finding a ground truth is then not possible without an entirely different experimental setup. Analysis of F-EEM images acquired using mixtures of dye emulsions on slides is ongoing by myself, Mackenzie McNiven, and Dr. Ferguson, and will appear in a future publication.

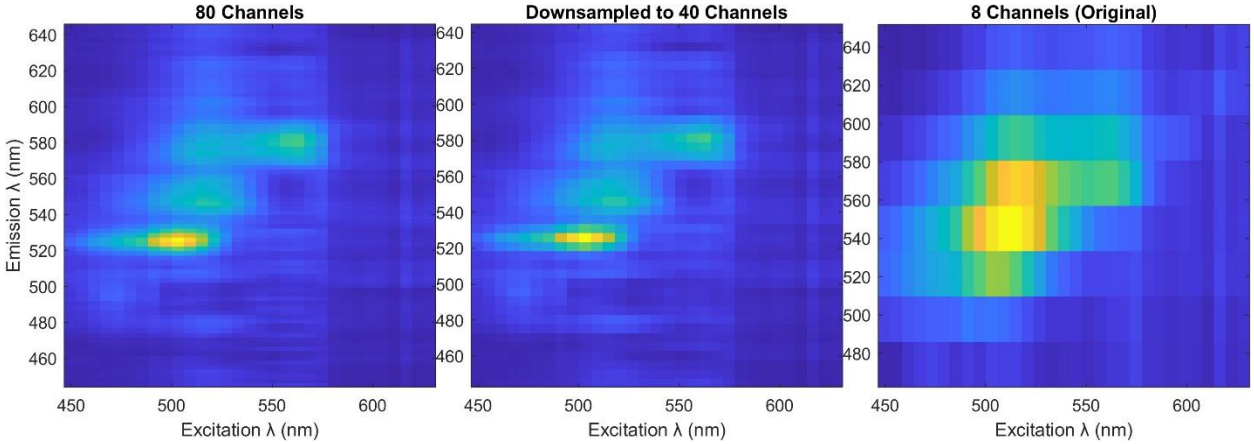

Figure 8.15. F-EEMs of upscaled and raw emission spectra from an 8-channel multispectral camera (MSC). The F-EEMs are the mean of all F-EEMs in the stitched image in Figure 8.14. The 80-channel data was upscaled from 8-channel MSC using an upscaling neural net model, and the 40-channel data was "down-sampled" using every 2nd emission channel from the 80-channel dataset. The 8-channel data is the original (raw) MSC dataset which was emission-upscaled.

The F-EEMs of the emission-upscaled MSC data for 80 and 40 emission channels are shown in Figure 8.15 along with the original 8 emission channels of the raw MSC data. Figure 8.15 shows that by "down-sampling" the emission channels from 80 to 40 the spectral resolution is largely maintained, while reducing the dataset size by half for faster processing and lesser demands on memory.

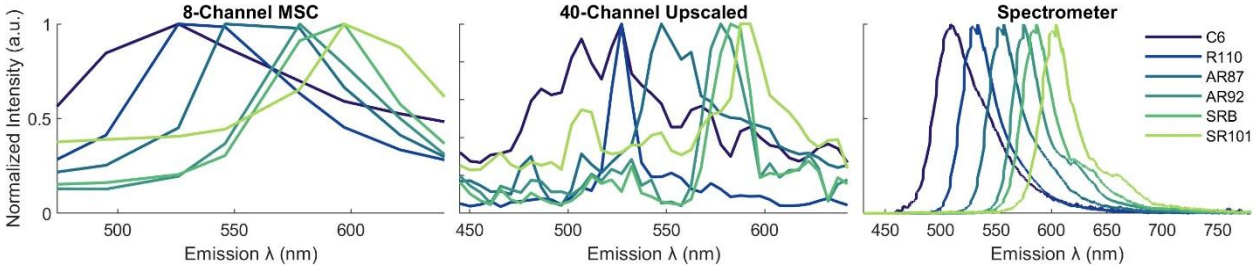

Figure 8.16. Emission spectra of raw and upscaled multispectral camera data compared with that from a spectrometer (AvaSpec-ULS2048XL-EVO, Avantes).

A comparison of the emission spectral resolution of raw- and emission-upscaled data from the MSC with data acquired using an Avantes spectrometer are shown in Figure 8.16.

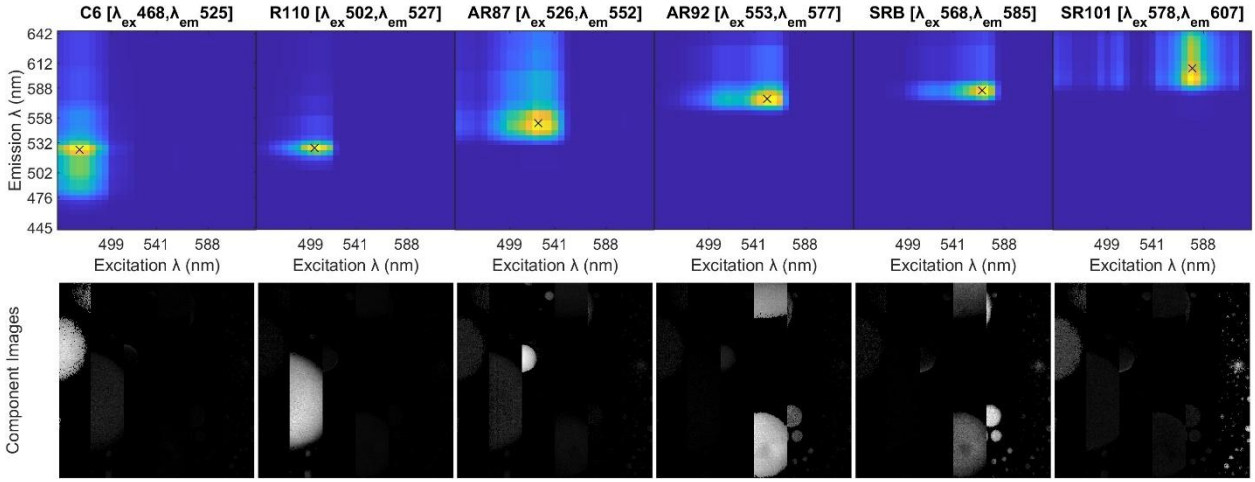

Figure 8.17. Six-component PARAFAC analysis of an emission-upscaled F-EEM image. Component EEMs (top) and images (bottom) of a blind six-component PARAFAC fit of the stitched image shown in Figure 8.14 after a 15 nm Rayleigh cut (*EEMCut)*. The *parafac* [321] function was used with convergence criteria 1E-10 and random orthogonalization initialization, with constraints: nonnegativity for sample (pixel) and excitation, unimodality and nonnegativity on emission. The fit converged after 72 iterations with an error of 2.8E4.

A six-component blind PARAFAC analysis of the emission-upscaled stitched image shown in Figure 8.14 and Figure 8.15 can accurately separate six fluorescent components (Figure 8.17), whereas only five components could be extracted using the 8-channel F-EEM image as shown in Figure 8.18.

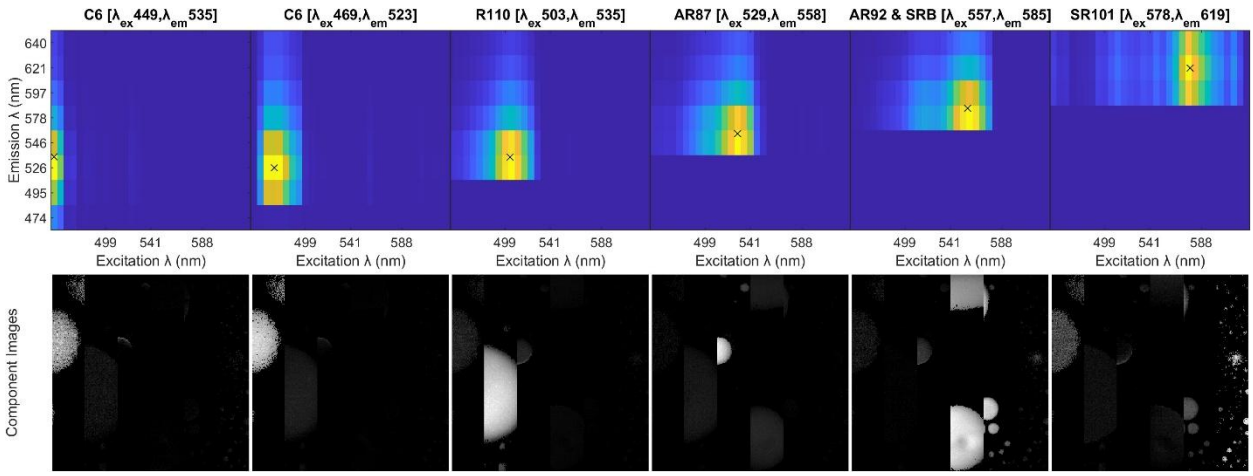

Figure 8.18. Six-component PARAFAC analysis of 8-channel F-EEM image. Component EEMs (top) and images (bottom) of a blind six-component PARAFAC fit of the stitched image shown in Figure 8.14 after a 15 nm Rayleigh cut (*EEMCut)*. The *parafac* [321] function was used with convergence criteria 1E-10 and random orthogonalization initialization, with nonnegativity constraint on sample (pixel), excitation, and emission dimensions. The fit converged after 56 iterations with an error of 3.8E4.

Figure 8.19 shows false-coloured images of the component scores of the six-component fit of the upscaled data shown in Figure 8.17, for visualization of spatial location of each component. Some crosstalk is seen between AR92 and SRB—the two components that could not be separated using a fit of the 8-channel data.

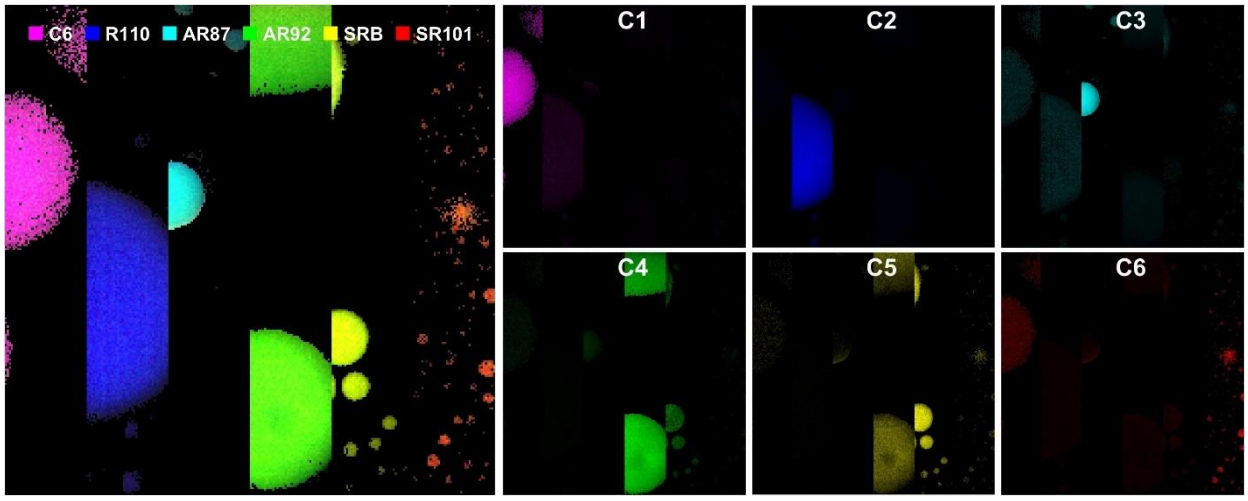

Figure 8.19. Location of fit components using an upscaled dataset. Images are false-coloured component images from the blind 6-component PARAFAC fit shown in Figure 8.17.

F-EEM images acquired with the MSC and DMA-PLS were upscaled from 8 to 80 channels using a neural network model for a dataset size of 256 × 256 × 40 × 31, then optionally down sampled to 40 channels. Using a stitched image created using individual images of neat emulsions, a blind PARAFAC analysis could quickly find six unique fluorescent components with distinct spatial

distributions. The peaks found in the PARAFAC fit are accurate when compared with F-EEM spectra taken with the Avantes spectrometer and the raw 8-channel F-EEM spectra.

A seven-component fit could not find seven fluorophores in an emission-upscaled stitched image containing an additional component (rhodamine 19) with an excitation peak at 535 nm and emission peak at 557 nm. The technique requires further refinement for complex mixtures with very similar fluorophores (within approximately 5 nm excitation and emission maxima). My ongoing work with Dr. Ferguson tests the spectral and spatial separation limitations of emission-upscaled F-EEM images acquired with the MSC, and that work will appear in a future publication.

Chapter 9 Conclusion & Future Work

9.1 Conclusion

In this dissertation I have demonstrated first-of-its-kind fluorescence excitation-emission matrix spectral imaging (FLEEMSI) microscopy, capable of spectrally and spatially separating fluorophores without the use of filters. The data acquired contain the excitation and emission spectra for each pixel in an image, with each image representing over 65,000 F-EEM spectra. We demonstrated the spectral and spatial separation ability of these microscopy systems through parallel factor analysis, allowing us to distinguish up to 10 fluorophores. We further demonstrated that emission spectral resolution upscaling—a computational approach based on convolutional neural networks that were trained using a high-resolution spectrometer—can further increase the number of distinguishable spectra. To improve the time resolution attainable using consecutive excitation-multiplexed F-EEM images, we applied the Supercycle algorithm to a dataset. This allowed us to observe the spatial variation of components through time at higher temporal resolution than otherwise possible.

All systems presented in this dissertation use Hadamard-multiplexed programmable excitation light sources combined with snapshot multispectral and hyperspectral cameras, through the camera ports of inverted microscopes. Similar light sources and cameras could be applied to other microscopes without difficulty—the concepts of Hadamard multiplexing, data preprocessing, PARAFAC analysis, spectral upscaling and “Supercycling” are readily transferred to other systems.

The potential for FLEEMSI application for biological systems is particularly promising and would allow scientists to conduct photomicrography of biological samples more quickly and with a greater number of distinguishable components. There are many interesting applications for FLEEMSI microscopy, and more work is required to further improve the limits of the spectral, spatial, and time-resolution of the systems.

This work has established a promising foundation for F-EEM microscopy and has left many avenues for students to continue along current paths and new directions with instruments that are working well as they are. A few of these opportunities are described in the following sections.

9.2 Future Work—Microscopy Applications

Biological Samples

Fluorescent tagging of biomarkers is frequently performed, and because these samples take time to prepare and image, multiple proteins are often tagged in multiplexed immunofluorescence microscopy. Fluorescent tags are typically designed to work with particular wavelengths that are common in microscopy and are often imaged through filters for excitation and emission. This limits the combinations of the tags that can be used to very distinct emission within the visible range (often used to avoid tissue autofluorescence). We demonstrated (Section 7.5) that we could separate 10 fluorophores in the visible range using the seven laser diodes and the MSC using a loading fit of known excitation and emission spectra. Consequently, we hope that we could identify a greater number of protein tags which have similar emission signatures, allowing for more biomarkers to be identified in a sample. Because the spatial resolution of the MSC imaging chip is not particularly high, stitched images taken at a slightly higher magnification may need to be used to observe the detail present in these samples. Alternatively, the bright LDA-PLS can be combined with the hyperspectral camera to observe fluorescence over a larger wavelength range and with a higher spatial and spectral resolution.

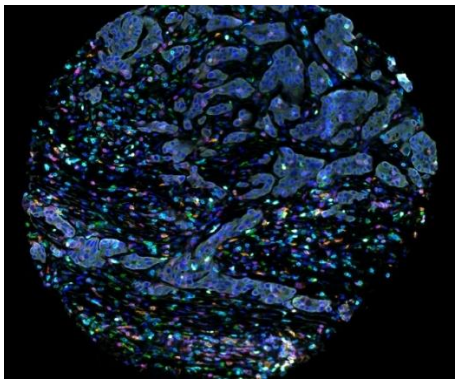

Figure 9.1. Multiplexed immunofluorescence microscope image, false-coloured. This sample was provided by BC Cancer of a mouse tumor and processed by Mackenzie McNiven.

Samples of mouse tumor tissue were provided by Dr. Julian Smazynski at BC Cancer for testing with our fluorescent imaging setups. These samples or similar ones would be a very interesting next step for the imaging systems described here. A student taking on a project such as this should find a collaboration with a lab willing to do the immunofluorescence labelling, as the procedure is not simple, and a microscope capable of identifying the markers present as a ground-truth would also be necessary to validate the results.

Hyperspectral Camera

The hyperspectral camera has the potential to separate many fluorescent compounds in a microscope sample, and a test to determine the upper limit of that separation would be interesting. This could be tested as demonstrated in Section 8.2 for the stitched images—images of neat emulsions could be taken and either superimposed or stitched together to form an image containing each of those dyes, and that image could be fit using a PARAFAC analysis.

Ongoing work by Mackenzie McNiven using the hyperspectral camera and laser diode array aims to mathematically separate fluorophores in fluorescent-tagged plant lines. The hyperspectral camera and laser diode array or an array of ultraviolet LEDs could be useful in identifying the variation of the lignin content in cross-sections of trees.

Programmable White Light Source—Higher Spectral Resolution

In the work shown here, the excitation source was programmed to have a maximum of 31 excitation bands. A higher spectral resolution is possible using Hadamard matrices of larger size and we have demonstrated up to 127 wavelength bands before. While the higher spectral resolution did not make a difference in distinguishing the broad fluorescence features in the EEM spectra one can conceive a scenario in which a much narrower excitation band exhibits solvatochromic behaviour. For example, many polycyclic aromatic hydrocarbons, PAH, have narrow vibronic excitation spectra and some conjugated aromatics show large solvatochromic responses [2, 327]. It can then be quite valuable to use a light source with high spectral resolution and probe the polarity of the fluorophore environment through the spatially resolved solvatochromic shift. Since the F-EEM spectra of many fluorophores depend on the molecular environment, it could be interesting to monitor multiple fluorophores over space and time using the MSC and a programmable light source.

9.3 Future Work—Macroscopic Applications

Programmable White Light Source—Superhydrophobic Slides

Using superhydrophobic slides from the Oleschuk at Queen's University, one could monitor the fluorescence of solutions as they evaporate or are added to other solvents. Preliminary tests with the MSC and DMA-PLS have shown that there may be merit in this approach. The Oleschuk group coated glass microscope slides with a superhydrophobic coating. This film is laser-etched to create

circular patches that are more hydrophilic. When these slides are dip-coated in a dye solution, droplets remain on the etched regions of the slide. The fluorescence of these localized and well-defined droplets can then be monitored for changing fluorescence wavelengths or intensities as they dry. Oleschuk's group already studied the interactions of droplets as they merge, move, evaporate, and more [334]. Our method would add additional information on these drying droplets allowing us to apply chemometrics on small-volume samples, with a high-throughput of reaction conditions. We anticipate that the setup would have to be modified for this work so that the white light is scrambled for a uniform full-field illumination, and corrections for the individual pixels in the CMOS imaging detector would be required to obtain quantitative or semi-quantitative results.

Additionally, we think that there could be some potential uses of this and similar setups in chromatography.

Programmable White Light Source—Reaction Monitoring in a Multi-Well Plate

Very small samples can also be confined using a multi-well plate. A collaboration with the group of Dr. David Leitch at UVic is anticipated. The Leitch team could provide the chemical system design, while we provide the instrumentation setup and acquisitions for the fluorescent monitoring. Very preliminary tests were done using a fluorescent solution in four and nine glass vials of a 96-well plate. We did not use a microscope for magnification but used the objective lens with the MSC that had a 50 mm focal length and added +7 diopters to increase magnification.

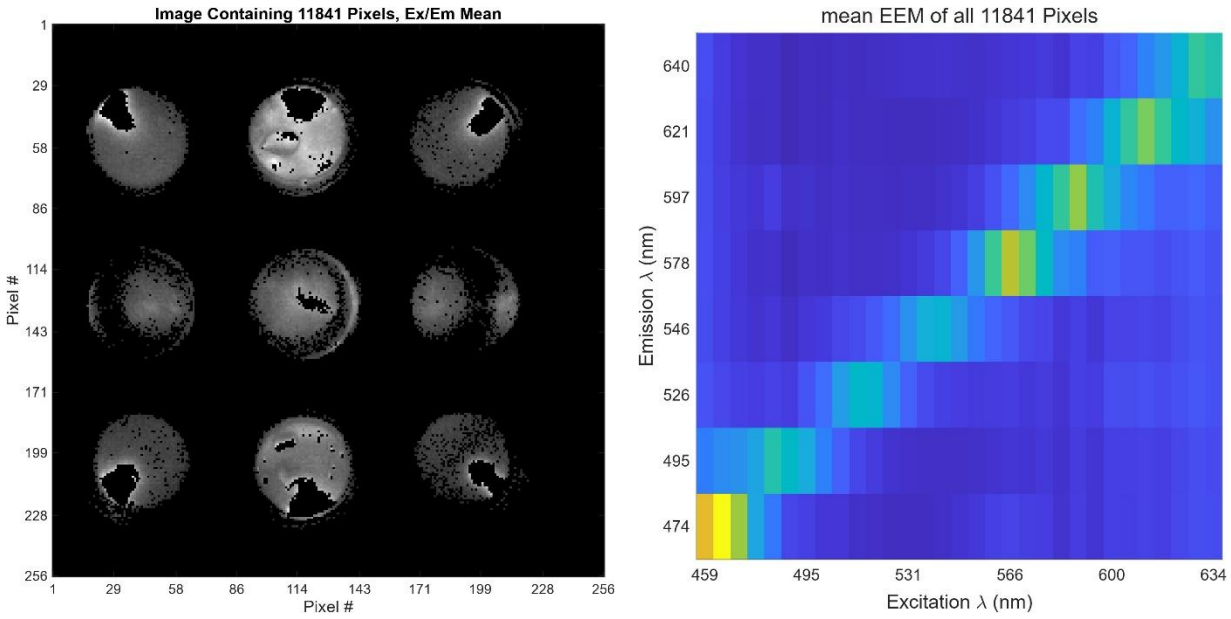

Figure 9.2. F-EEM image of 9 wells in a 96-well plate. Image was acquired using the 8-channel multispectral camera with a 50 mm lens and +7 diopters, positioned below a 96-well plate. The DMA-PLS with 31 excitation channels was used for illumination, and two layers of KimWipes were placed above the vials to diffuse the excitation light. The exposure time was 15 ms per mask. A principal component analysis threshold (Section 5.4.3) on the F-EEM image was used to select the pixels that showed the vials, and the brightest pixels were set to zero. (**left**) Mean of excitation and emission dimensions, (**right**) mean of all remaining pixels.

The MSC was placed below the 96-well plate and the DMA-PLS was placed above the plate for sample illumination (Figure 9.2). We also placed both the MSC and DMA-PLS above the plate. We used both a clear plastic plate and a metallic plate to hold the glass vials of fluorescent solution. Vials were imaged either bare or with a black paper covering to reduce reflections from the sides of the plate and scatter from the plastic, metal, and glass from other vials. It was found to be quite difficult to illuminate the fluorescent solution in the vials primarily because of the intense scattering from the glass and plate material (plastic or metal) and the depth of the vials which necessitated a nearly straight-on illumination. The illumination straight through the vials caused oversaturation on the camera detector from the incident light more than the fluorescence. Various apertures with the camera lens were tested to reduce light intensity however this has been so far unsuccessful.

Changes to the setup for it to be feasible would include a method to illuminate the solution in the vials without too much scatter, and an additional method of scatter-reduction for the glass vials, perhaps using index-matching gel, a different material, or a different shape. It is possible that the plastic 396-well plates are better-suited to the instrumental setup as the illuminated area would be smaller and the material may be less prone to significant scatter, though at the cost of lower fluorescence. Additionally, the sample volume may be not practical to monitor chemical reactions.

9.4 Future Work—Multiplexed Raman Spectroscopy

As described in Section 1.4.3, multiplexed SERS spectra using multiple excitation wavelengths could generate 2D Raman EEM spectra, which would show a clear distinction between the narrow Raman features forming narrow lines akin to the Rayleigh line, and the broad fluorescence features. The technique can then overcome one of the problems in Raman detection—the distinction from the fluorescence background.

The laser diode array (LDA) of seven LDs was originally created for this purpose, and with some modifications, would be a very interesting and potentially useful instrument. The instrumentation design for this type of instrument is described in Section 9.4.3. The steps taken so far on this project have been the LDA (Section 3.3), the synthesis of the SERS substrates, and preliminary tests and results of the system and of the SERS substrates (Section 9.4.2).

9.4.1 Synthesis & Characterization of Silver Nanostars

Silver nanoparticles were chosen as SERS substrates since the resonant frequencies of silver occur at visible wavelengths—matching the wavelengths of the LDA. We chose to use nanostars instead of one of the many other nanoparticle shapes given their record for Raman signal enhancement and reproducibility using a colloidal nanoparticle suspension. In nanospheres and some other shapes, the distance between particles is essential in creating hot spots, and solutions rely on aggregation [262, 263], while in nanostars, hot spots are created both on the tips of the arms and between the arms [248, 265]. Aggregation is not required, which could improve reproducibility of SERS measurements when used in solution. If the substrates are to be dried, as I will show in the next section, there are other issues with reproducibility, primarily stemming from the drying of the substrate on a flat surface, and the drying of an analyte onto that surface.

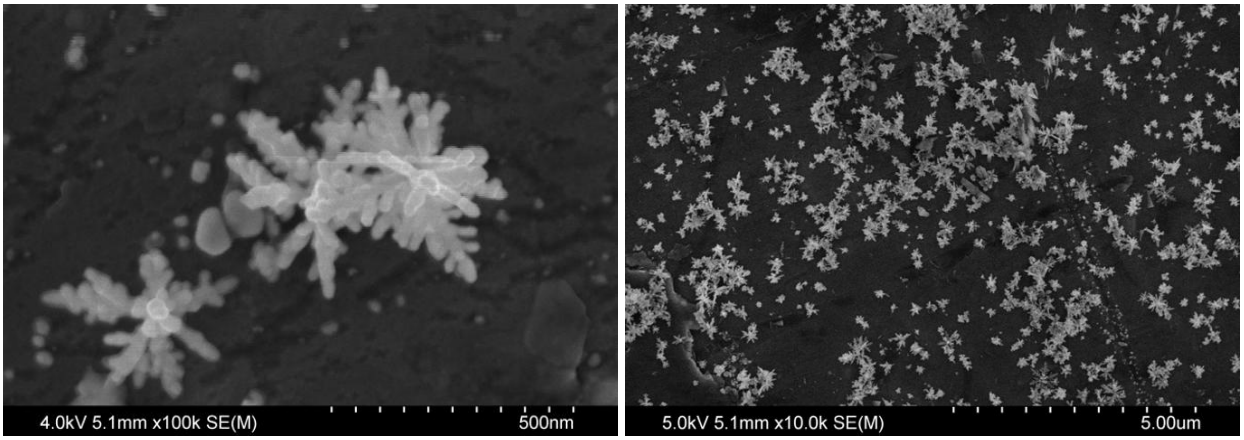

Figure 9.3. Image of silver nanostars through a scanning electron microscope. Images were taken with the Hitachi S-4800.

9.4.2 Preliminary Results of Enhanced Raman

Preliminary tests for SERS enhancement used rhodamine 6G adsorbed on a dried AgNS substrate. AgNS were prepared as described by Garcia-Leis *et al* [335], and characterized using absorption spectroscopy and scanning electron microscopy (SEM). The SEM images shown in Figure 9.3 show that on average, the nanostars had eight arms with a diameter of approximately 300 nm.

The dried substrate was prepared by dropping AgNS solution on aluminum foil and allowing to dry in a covered dish. Once dry, a droplet of 0.1 mM solution of rhodamine 6G in (R6G) in ethanol was added to the surface and allowed to dry. R6G was chosen as the analyte because it produces a strong Raman and strong fluorescence signal and adsorbs well to the metallic nanoparticles [336].

Aluminum foil was chosen because it is reflective in the wavelength region of interest and does not interfere with the Raman signal.

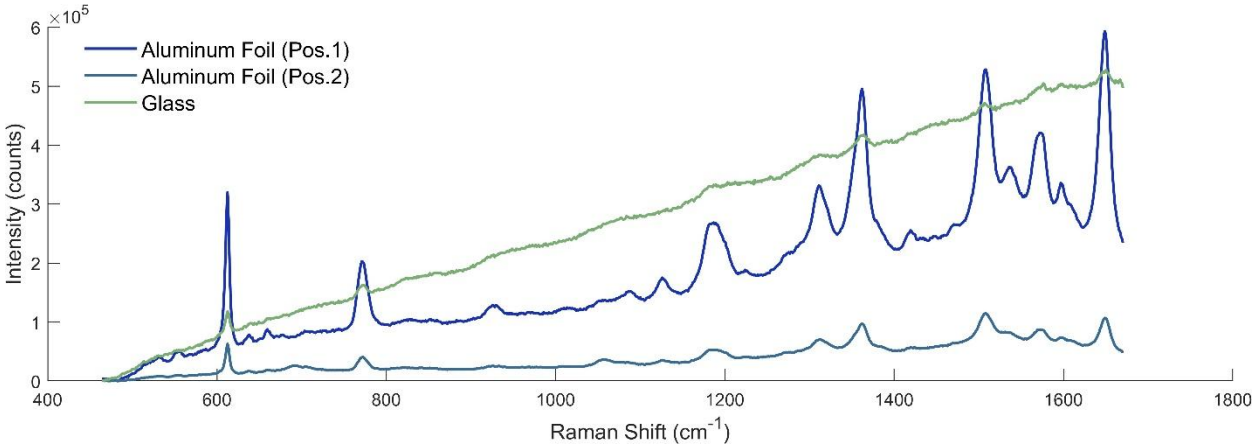

Figure 9.4. SERS spectra of rhodamine 6G on glass and on silver nanostars (AgNS). Substrate is a dried droplet of AgNS on a glass slide or aluminum foil. Spectra are the average of 10 (glass) and 3 (aluminum foil) acquisitions, taken on a Raman microscope with a 10x objective lens, 532 nm laser at 5% and 1% power for the glass and aluminum foil respectively, using 1 second integration with an Andor camera detector and a 2400 lines/mm grating. Removal of spikes due to cosmic rays striking the detector was done using the instrument software.

Figure 9.4 shows a significant increase in the intensity of the Raman signal with the nanostars and a spectrum which agrees with that of the literature [337]. Additionally, Figure 9.4 shows the difference in signal using a glass slide compared with aluminum foil for the AgNS deposition and the difference in signal at different locations on the aluminum foil. These demonstrate both that the aluminum foil provides a much stronger signal enhancement than the glass slide, but also that the reproducibility of the AgNS on the aluminum foil is not high, likely due to the uneven drying of both the AgNS and the R6G solution. The Raman microscope used to collect the spectra in Figure 9.4 was accessed through CAMTEC at UVic. The spectra were acquired using a 532 nm laser for illumination and a high-resolution detector (2400 lines/mm grating).

The AgNS were tested for a Raman signal in solution with R6G, however an emission spectrometer with low spectral resolution was used, as were the laser diodes which are not ready for Raman spectroscopy, so no signal was observed. Once modifications to the system are made to work for Raman spectroscopy, analysis of the analytes in solution would be valuable to test again.

9.4.3 Instrumentation Design for Multiplexed Raman

Possible detectors that could be used for this experiment are shown and steps are described to overcome the many non-optimized parameters that would need to be included in a multiplexed Raman experiment, as worked out with Dr. Stanislov Konorov.

Detector for Multiplexed Raman Spectroscopy

Only one design for the spectrometer side of the setup is shown, however many other options exist. The two largest problems are the high wavelength resolution of the grating required for Raman, with a wide excitation wavelength range (405–658 nm), and rejecting the numerous Rayleigh-scattered light bands. Using filters for each wavelength is difficult, as the numerous wavelengths illuminated at once. If their contribution was removed using band-stop filters, large gaps in the Raman spectrum will be observed. The best option is one which does not exist as of my current knowledge—a CMOS array detector capable of selectively not detecting the pixels on which the excitation light falls. This could be done by setting certain pixels to acquire at a much faster rate than the rest so the pixel wells are continuously refreshed and not filled up quickly with the strong Rayleigh light, which can cause bleeding and other problems in the detector. A visual representation of a spectrum on a detector like this is shown in Figure 9.5.

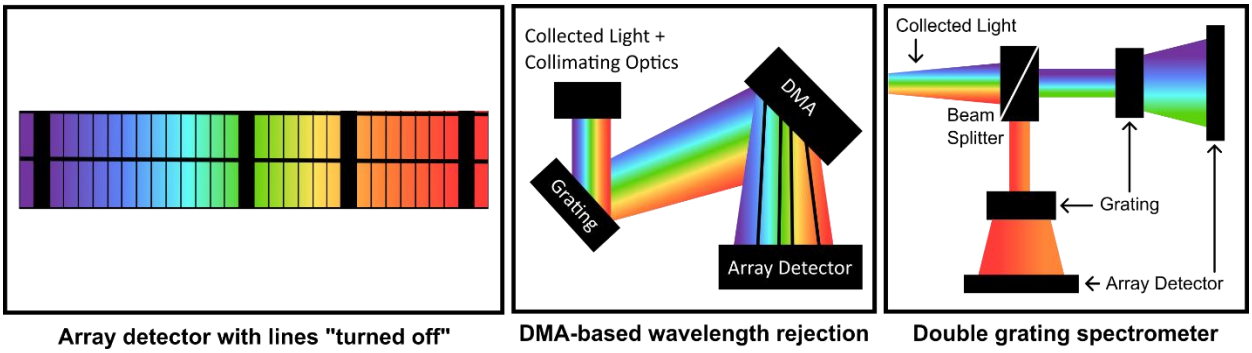

Figure 9.5. Spectrometer and detector designs for multiplexed Raman spectroscopy. (**left**) Array detector with lines blocked or "turned off" to reject Rayleigh-scattered light, (**middle**) a Digital Micromirror Array (DMA)-based rejection of Rayleigh-scattered light, could also be used for multiplexing, (**right**) a two-grating spectrometeter system where shorter-wavelength light uses one detector and longer-wavelegnth light uses a second detector, to allow for high-resolution Raman spectroscopy at numerous wavelengths. With careful alignment, the top and bottom halves of the DMA should be able to be used for two different beams at one (for example, for two gratings).

Another option could be to use a DMA to direct Rayleigh-scattered light away from the detector (Figure 9.5, middle) [338, 339]. Should a DMA be implemented for excitation light rejection, one might also consider Hadamard-multiplexing the detection side. Li [340] described a multiplexed approach to fluorescence detection using a DMA, and Mazhar [106] described multiplexing the dispersed light using a single pixel detector, such as a photomultiplier tube.

An option for the spectral resolution could be to use multiple gratings and array detectors for the different spectral regions (for example, one for 405–500 nm light, another for 500–660 nm light).

Steps to Work through this Project:

These are incremental steps to build up the system starting with an optimized system, then replacing one non-ideal component at a time—the fibers, numerous wavelengths, and laser diodes.

Free-Space, Single Wavelength

Detect a Raman signal using a high-resolution spectrometer, stable laser (Helium-Neon, 633 nm), band stop filter, and a molecule with a strong and distinct Raman spectrum such as cyclohexane. The system can be aligned using a fluorescent dye—for a 633 nm laser, Nile Blue works well. This should demonstrate that a Raman signal can be detected using the chosen detector and orientation. SERS could be tested at this point to determine if the in-solution and dried substrates work to enhance the Raman signal.

Free-Space, Single Laser Diode

Collect a Raman spectrum with excitation via a laser diode in place of a stable single-wavelength laser. The LD should be cooled and may have to be etalon-narrowed to reduce the FWHM to produce a higher-quality Raman spectrum. The paper by Muller[310] describes etalon-narrowing of an LD using an etalon and a prism. The LDs should be cooled or the very least temperature stabilized more than they are currently, to reduce peak shifts due to operating temperature. The components are described in lab notes and not included here for brevity. This step should demonstrate that the laser diodes have a sufficient peak width and low enough fluctuation that they can be used to obtain Raman spectra.

Fiber-Coupled, Single Laser Diode

Fiber-couple the single etalon-narrowed and cooled LD from the previous step and collect a Raman spectrum. Fibers can introduce additional peaks, so this step should demonstrate that using the LD fiber-coupled does not reduce the quality of the acquired Raman spectrum. This may sound like a simpler step, but I have been assured that it is not. If this step is unsuccessful, another method of combining multiple beams should be attempted.

Multiple Laser Diodes

Each cooled and narrowed LD to be used in the multiplexed setup should be tested individually to ensure they can each produce a Raman spectrum using the setup. This step should then test the laser diodes together for Raman signal, with whatever discrimination method has been chosen to remove the Rayleigh-scattered light.

Multiple Laser Diodes, SERS

The SERS enhancement using AgNS and an analyte should be tested at this step, to see which method (solution or dried substrate) works for signal enhancement and reproducibility. This should be tested with the lasers in sequential and multiplexed illumination.

This project would hopefully demonstrate that SERS using multiple-wavelength multiplexed excitation would produce a better Raman signal and the fluorescence signal can be identified both for compound identification and for removal from the Raman signal. This is an interesting, fun, and challenging project that will involve optical configurations (simulations would be advantageous) and alignments, as well as some data analysis on the resulting spectra, and lots of problem solving.

References

1. Kasha, M. Characterization of electronic transitions in complex molecules. *Discussions of the Faraday Society* **1950**, (9), 14-19. doi: 10.1039/df9500900014.
2. Joulaei-Zonouz, S.; Wiebe, H.; Prüfert, C.; Loock, H.-P. Twisted-internal charge transfer (TICT) state mechanisms may be less common than expected. *New Journal of Chemistry* **2024**, *48* (9), 4077-4087. doi: 10.1039/d4nj00047a.
3. Monago-Maraña, O.; de la Peña, A. M.; Al-Tameemi, M.; Galeano-Díaz, T.; Campiglia, A. Feasibility of Multidimensional Fluorescence at Low Temperature in Shpol'skii Matrices Combined with PARAFAC for the Quantitation of Polycyclic Aromatic Hydrocarbons. *Int J Exp Spectroscopic Tech* **2018**, *3*, 1-11.
4. Donaldson, R. Spectrophotometry of fluorescent pigments. *British Journal of Applied Physics* **1954**, *5* (6), 210. doi: 10.1088/0508-3443/5/6/303.
5. Bowman, R. L.; Caulfield, P. A.; Udenfriend, S. Spectrophotofluorometric Assay in the Visible and Ultraviolet. *Science* **1955**, *122* (3157), 32-33. doi: 10.1126/science.122.3157.32.
6. Udenfriend, S. Development of the spectrophotofluorometer and its commercialization. *Protein Science* **1995**, *4* (3), 542-551. doi: 10.1002/pro.5560040321.
7. Warner, I. M.; Callis, J. B.; Davidson, E. R.; Christian, G. D. Multicomponent analysis in clinical-chemistry by use of rapid scanning fluorescence spectroscopy. *Clinical Chemistry* **1976**, *22* (9), 1483-1492.
8. Johnson, D. W.; Callis, J. B.; Christian, G. D. Rapid scanning fluorescence spectroscopy. *Analytical Chemistry* **1977**, *49* (8), A747-&. doi: 10.1021/ac50016a008.
9. Leiner, M. J. P.; Wolfbeis, O. S. Biochemical applications of 3-dimensional fluorescence spectrometry. *Time-Resolved Laser Spectroscopy in Biochemistry. SPIE Proc.* **1988**, *909*, 134-138. doi: 10.1117/12.945377.
10. Gemperline, P. J. Mixture analysis using factor analysis I: Calibration and quantitation. *Journal of Chemometrics* **1989**, *3* (4), 549-568. doi: 10.1002/cem.1180030404.
11. Yang, L. Y.; Hur, J.; Zhuang, W. N. Occurrence and behaviors of fluorescence EEM-PARAFAC components in drinking water and wastewater treatment systems and their applications: a review. *Environmental Science and Pollution Research* **2015**, *22* (9), 6500-6510. doi: 10.1007/s11356-015-4214-3.
12. Sgroi, M.; Gagliano, E.; Vagliasindi, F. G. A.; Roccaro, P. Absorbance and EEM fluorescence of wastewater: Effects of filters, storage conditions, and chlorination. *Chemosphere* **2020**, *243*, 125292. doi: 10.1016/j.chemosphere.2019.125292.
13. Stedmon, C. A.; Markager, S.; Bro, R. Tracing dissolved organic matter in aquatic environments using a new approach to fluorescence spectroscopy. *Marine Chemistry* **2003**, *82* (3-4), 239-254. doi: 10.1016/S0304-4203(03)00072-0.
14. Sheng, G.; Yu, H. Characterization of extracellular polymeric substances of aerobic and anaerobic sludge using three-dimensional excitation and emission matrix fluorescence spectroscopy. *Water Research* **2006**, *40* (6), 1233-1239. doi: 10.1016/j.watres.2006.01.023.
15. Sciscenko, I.; Arques, A.; Micó, P.; Mora, M.; García-Ballesteros, S. Emerging applications of EEM-PARAFAC for water treatment: a concise review. *Chemical Engineering Journal Advances* **2022**, *10*. doi: 10.1016/j.ceja.2022.100286.

16. Khan, M. F. S.; Akbar, M.; Wu, J.; Xu, Z. A review on fluorescence spectroscopic analysis of water and wastewater. *Methods and Applications in Fluorescence* **2022**, *10* (1). doi: 10.1088/2050-6120/ac3d79.
17. Andersen, C. M.; Bro, R. Practical aspects of PARAFAC modeling of fluorescence excitation-emission data. *Journal of Chemometrics* **2003**, *17* (4), 200-215. doi: 10.1002/cem.790.
18. Murphy, K. R.; Stedmon, C. A.; Graeber, D.; Bro, R. Fluorescence spectroscopy and multi-way techniques. PARAFAC. *Analytical Methods* **2013**, *5* (23), 6557-6566. doi: 10.1039/c3ay41160e.
19. Yu, J. L.; Xiao, K.; Xue, W. C.; Shen, Y. X.; Tan, J. H.; Liang, S.; Wang, Y. F.; Huang, X. Excitation-emission matrix (EEM) fluorescence spectroscopy for characterization of organic matter in membrane bioreactors: Principles, methods and applications. *Frontiers of Environmental Science & Engineering* **2020**, *14* (2). doi: 10.1007/s11783-019-1210-8.
20. Obeidat, S.; Bai, B.; Rayson, G. D.; Anderson, D. M.; Puscheck, A. D.; Landau, S. Y.; Glasser, T. A multi-source portable light emitting diode spectrofluorometer. *Applied Spectroscopy* **2008**, *62* (3), 327-332. doi: 10.1366/000370208783759722.
21. Karoui, R.; Dufour, E. Development of a portable spectrofluorometer for measuring the quality of cheese. *Dairy Science & Technology* **2008**, *88* (4-5), 477-494. doi: 10.1051/dst:2008020.
22. Khoshmaram, L.; Mohammadi, M.; Babadi, A. A portable low-cost fluorimeter based on LEDs and a smart phone. *Microchemical Journal* **2021**, *171*. doi: 10.1016/j.microc.2021.106773.
23. Fabila, D. A.; de la Rosa, J. M.; Stolik, S.; Moreno, E.; López, T.; Álvarez, M.; Arellano, A.; de la Rosa, G.; Mercado, R.; Soto, J. L. Development of a spectrofluorometer with USB interface for in vivo measurements in surgical procedures. *2nd Circuits and Systems for Medical and Environmental Applications Workshop (CASME)*: Merida, Mexico, 2010; pp 1-4.
24. Chen, P.; Pan, D.; Mao, Z. Fluorescence measured using a field-portable laser fluorometer as a proxy for CDOM absorption. *Estuarine Coastal and Shelf Science* **2014**, *146*, 33-41. doi: 10.1016/j.ecss.2014.05.010.
25. Petryayeva, E.; Algar, W. A job for quantum dots: use of a smartphone and 3D-printed accessory for all-in-one excitation and imaging of photoluminescence. *Analytical and Bioanalytical Chemistry* **2016**, *408* (11), 2913-2925. doi: 10.1007/s00216-015-9300-3.
26. Hossain, M.; Canning, J.; Ast, S.; Rutledge, P.; Yen, T.; Jamalipour, A. Lab-in-a-Phone: Smartphone-Based Portable Fluorometer for pH Measurements of Environmental Water. *Ieee Sensors Journal* **2015**, *15* (9), 5095-5102. doi: 10.1109/JSEN.2014.2361651.
27. Tedetti, M.; Joffre, P.; Goutx, M. Development of a field-portable fluorometer based on deep ultraviolet LEDs for the detection of phenanthrene- and tryptophan-like compounds in natural waters. *Sensors and Actuators B-Chemical* **2013**, *182*, 416-423. doi: 10.1016/j.snb.2013.03.052.
28. Cucci, C.; Mignani, A. G.; Dall'Asta, C.; Pela, R.; Dossena, A. A portable fluorometer for the rapid screening of M1 aflatoxin. *Sensors and Actuators B-Chemical* **2007**, *126* (2), 467-472. doi: 10.1016/j.snb.2007.03.036.
29. Gu, H. Y.; Hu, L. J.; Dong, Y. N.; Chen, Q. S.; Wei, Z. J.; Lv, R. Q.; Zhou, Q. Evolving trends in fluorescence spectroscopy techniques for food quality and safety: A review. *Journal of Food Composition and Analysis* **2024**, *131*. doi: 10.1016/j.jfca.2024.106212.

30. Blockstein, L.; Yadid-Pecht, O. Lensless Miniature Portable Fluorometer for Measurement of Chlorophyll and CDOM in Water Using Fluorescence Contact Imaging. *IEEE Photonics Journal* **2014**, *6* (3). doi: 10.1109/JPHOT.2014.2326665.
31. Alam, M.; Wahid, K.; Goel, R.; Lukong, K. Development of a low-cost and portable smart fluorometer for detecting breast cancer cells. *Biomedical Optics Express* **2019**, *10* (2), 399-410. doi: 10.1364/BOE.10.000399.
32. Ferguson, T.; Bernicky, A.; Kozin, I.; Loock, H. P. HPLC-Detector Based on Hadamard-Transform Fluorescence Excitation-Emission-Matrix Spectroscopy. *Analytical Chemistry* **2021**, *93* (23), 8116-8121. doi: 10.1021/acs.analchem.1c01037.
33. He, Z. Q.; Ohno, T.; Wu, F. C.; Olk, D. C.; Honeycutt, C. W.; Olanya, M. Capillary electrophoresis and fluorescence excitation-emission matrix spectroscopy for characterization of humic substances. *Soil Science Society of America Journal* **2008**, *72* (5), 1248-1255. doi: 10.2136/sssaj2007.0305.
34. Bernicky, A.; Ferguson, T.; Denotter, S.; Rigg, A.; Loock, H. P. Simultaneous Double-Pass Absorption and Fluorescence Excitation-Emission Matrix Spectroscopy for Measurements of Reaction Kinetics. *Analytical Chemistry* **2020**, *92* (18), 12489-12497. doi: 10.1021/acs.analchem.0c02320.
35. Shcheslavskiy, V. I.; Shirmanova, M. V.; Yashin, K. S.; Rück, A. C.; Skala, M. C.; Becker, W. Fluorescence Lifetime Imaging Techniques-A Review on Principles, Applications and Clinical Relevance. *Journal of Biophotonics* **2025**. doi: 10.1002/jbio.202400450.
36. Zhao, M.; Li, Y.; Peng, L. L. Parallel excitation-emission multiplexed fluorescence lifetime confocal microscopy for live cell imaging. *Optics Express* **2014**, *22* (9), 10221-10232. doi: 10.1364/oe.22.010221.
37. Andrade-Eiroa, A.; Canle, M.; Cerda, V. Environmental Applications of Excitation-Emission Spectrofluorimetry: An In-Depth Review I. *Applied Spectroscopy Reviews* **2013**, *48* (1), 1-49. doi: 10.1080/05704928.2012.692104.
38. Coble, P. G. Characterization of marine and terrestrial DOM in seawater using excitation emission matrix spectroscopy. *Marine Chemistry* **1996**, *51* (4), 325-346. doi: 10.1016/0304-4203(95)00062-3.
39. Geng, T.; Wang, Y.; Yin, X. L.; Chen, W.; Gu, H. W. A Comprehensive Review on the Excitation-Emission Matrix Fluorescence Spectroscopic Characterization of Petroleum-Containing Substances: Principles, Methods, and Applications. *Critical Reviews in Analytical Chemistry* **2023**. doi: 10.1080/10408347.2023.2205500.
40. Sá, M.; Ferrer-Ledo, N.; Gao, F. Z.; Bertinetto, C. G.; Jansen, J.; Crespo, J. G.; Wijffels, R. H.; Barbosa, M.; Galinha, C. F. Perspectives of fluorescence spectroscopy for online monitoring in microalgae industry. *Microbial Biotechnology* **2022**, *15* (6), 1824-1838. doi: 10.1111/1751-7915.14013.
41. Booksh, K. S.; Muroski, A. R.; Myrick, M. L. Single measurement excitation/emission matrix spectrofluorometer for determination of hydrocarbons in ocean water 2. Calibration and quantitation of naphthalene and styrene. *Analytical Chemistry* **1996**, *68* (20), 3539-3544. doi: 10.1021/ac9602534.
42. Mahamuni, G.; He, J.; Rutherford, J.; Ockerman, B.; Majumdar, A.; Seto, E.; Korshin, G.; Novosselov, I. Solid-phase excitation-emission matrix spectroscopy for chemical analysis of combustion aerosols. *Plos One* **2021**, *16* (5). doi: 10.1371/journal.pone.0251664.

43. Karoui, R.; Blecker, C. Fluorescence Spectroscopy Measurement for Quality Assessment of Food Systems-a Review. *Food and Bioprocess Technology* **2011**, *4* (3), 364-386. doi: 10.1007/s11947-010-0370-0.
44. Sádecká, J.; Tóthová, J. Fluorescence spectroscopy and chemometrics in the food classification -: a review. *Czech Journal of Food Sciences* **2007**, *25* (4), 159-173. doi: 10.17221/687-CJFS.
45. Martín-Tornero, E.; Durán-Merás, I.; de la Peña, A. M.; Galeano-Díaz, T. Fiber optic fluorescence as non-invasive tool to monitor the ripening process of cheeses: Torta del casar and Queso de la Serena. *Lwt-Food Science and Technology* **2024**, *199*. doi: 10.1016/j.lwt.2024.116141.
46. Fan, Y. W.; Dong, R. Z.; Luo, Y. K.; Tan, Y. Q.; Hong, H.; Ji, Z. T.; Shi, C. Deep learning models with optimized fluorescence spectroscopy to advance freshness of rainbow trout predicting under nonisothermal storage conditions. *Food Chemistry* **2024**, *454*. doi: 10.1016/j.foodchem.2024.139774.
47. Guimet, F.; Ferré, J.; Boqué, R. Rapid detection of olive-pomace oil adulteration in extra virgin olive oils from the protected denomination of origin "Siurana" using excitation-emission fluorescence spectroscopy and three-way methods of analysis. *Analytica Chimica Acta* **2005**, *544* (1-2), 143-152. doi: 10.1016/j.aca.2005.02.013.
48. Suciu, R.; Zarbo, L.; Guyon, F.; Magdas, D. Application of fluorescence spectroscopy using classical right angle technique in white wines classification. *Scientific Reports* **2019**, *9*. doi: 10.1038/s41598-019-54697-8.
49. Airado-Rodriguez, D.; Galeano-Diaz, T.; Duran-Meras, I.; Wold, J. P. Usefulness of Fluorescence Excitation-Emission Matrices in Combination with PARAFAC, as Fingerprints of Red Wines. *Journal of Agricultural and Food Chemistry* **2009**, *57* (5), 1711-1720.
50. Gonzaga, L. S.; Bastian, S. E. P.; Capone, D. L.; Ranaweera, R. K. R.; Jeffery, D. W. Modelling Cabernet-Sauvignon wine sensory traits from spectrofluorometric data. *Oeno One* **2021**, *55* (4), 19-33. doi: 10.20870/oeno-one.2021.55.4.4805.
51. Mori, S.; Hall, C. R.; Bradley, S. J.; Smith, T. A. Multidimensional fluorescence spectroscopy of wine using synchronous excitation/emission matrices and time-resolved fluorescence interferometric detection. *Methods and Applications in Fluorescence* **2024**, *12* (4). doi: 10.1088/2050-6120/ad64a9.
52. Quatela, A.; Gilmore, A. M.; Gall, K. E. S.; Sandros, M.; Csatorday, K.; Siemiarczuk, A.; Ben Yang, B.; Camenen, L. A-TEEM™, a new molecular fingerprinting technique: simultaneous absorbance-transmission and fluorescence excitation-emission matrix method. *Methods and Applications in Fluorescence* **2018**, *6* (2). doi: 10.1088/2050-6120/aaa818.
53. Ranaweera, R. K. R.; Gilmore, A. M.; Capone, D. L.; Bastian, S. E. P.; Jeffery, D. W. Authentication of the geographical origin of Australian Cabernet Sauvignon wines using spectrofluorometric and multi-element analyses with multivariate statistical modelling. *Food Chemistry* **2021**, *335*. doi: 10.1016/j.foodchem.2020.127592.
54. Ríos-Reina, R.; Azcarate, S. M.; Camiña, J. M.; Goicoechea, H. C. Multi-level data fusion strategies for modeling three-way electrophoresis capillary and fluorescence arrays enhancing geographical and grape variety classification of wines. *Analytica Chimica Acta* **2020**, *1126*, 52-62. doi: 10.1016/j.aca.2020.06.014.

55. Suciu, R. C.; Zarbo, L.; Guyon, F.; Magdas, D. A. Application of fluorescence spectroscopy using classical right angle technique in white wines classification. *Scientific Reports* **2019**, *9*. doi: 10.1038/s41598-019-54697-8.
56. Vinciguerra, L. L.; Böck, F. C.; Schneider, M. P.; Reis, N.; Silva, L. F.; de Souza, K. C. M.; Guerra, C. C.; Gomes, A. D.; Bergold, A. M.; Ferrao, M. F. Geographical origin authentication of southern Brazilian red wines by means of EEM-pH four-way data modelling coupled with one class classification approach. *Food Chemistry* **2021**, *362*. doi: 10.1016/j.foodchem.2021.130087.
57. Andersen, C. M.; Vishart, M.; Holm, V. K. Application of fluorescence spectroscopy in the evaluation of light-induced oxidation in cheese. *Journal of Agricultural and Food Chemistry* **2005**, *53* (26), 9985-9992. doi: 10.1021/jf051143d.
58. Sádecká, J.; Urícková, V.; Májek, P.; Jakubíková, M. Comparison of different fluorescence techniques in brandy classification by region of production. *Spectrochimica Acta Part a-Molecular and Biomolecular Spectroscopy* **2019**, *216*, 125-135. doi: 10.1016/j.saa.2019.03.018.
59. Ríos-Reina, R.; Pérez-Bernal, J. L.; Azcarate, S. M.; Callejón, R. M. Usefulness of excitation-emission fluorescence spectralprint combined with chemometrics for authentication of PDO fortified wines. *Microchemical Journal* **2024**, *199*. doi: 10.1016/j.microc.2024.110067.
60. Al Riza, D. F.; Kondo, N.; Rotich, V. K.; Perone, C.; Giametta, F. Cultivar and geographical origin authentication of Italian extra virgin olive oil using front-face fluorescence spectroscopy and chemometrics. *Food Control* **2021**, *121*. doi: 10.1016/j.foodcont.2020.107604.
61. Guimet, F.; Boque, R.; Ferre, J. Application of non-negative matrix factorization combined with Fisher's linear discriminant analysis for classification of olive oil excitation-emission fluorescence spectra. *Chemometrics and Intelligent Laboratory Systems* **2006**, *81* (1), 94-106.
62. Guimet, F.; Ferre, J.; Boque, R.; Rius, F. X. Application of unfold principal component analysis and parallel factor analysis to the exploratory analysis of olive oils by means of excitation-emission matrix fluorescence spectroscopy. *Analytica Chimica Acta* **2004**, *515* (1), 75-85.
63. Lia, F.; Formosa, J. P.; Zammit-Mangion, M.; Farrugia, C. The First Identification of the Uniqueness and Authentication of Maltese Extra Virgin Olive Oil Using 3D-Fluorescence Spectroscopy Coupled with Multi-Way Data Analysis. *Foods* **2020**, *9* (4). doi: 10.3390/foods9040498.
64. Omwange, K. A.; Al Riza, D. F.; Saito, Y.; Suzuki, T.; Ogawa, Y.; Shiraga, K.; Giametta, F.; Kondo, N. Potential of front face fluorescence spectroscopy and fluorescence imaging in discriminating adulterated extra-virgin olive oil with virgin olive oil. *Food Control* **2021**, *124*. doi: 10.1016/j.foodcont.2021.107906.
65. Yuan, Y. Y.; Wang, S. T.; Wang, J. Z.; Cheng, Q.; Wu, X. J.; Kong, D. M. Rapid detection of the authenticity and adulteration of sesame oil using excitation-emission matrix fluorescence and chemometric methods. *Food Control* **2020**, *112*. doi: 10.1016/j.foodcont.2020.107145.
66. Nandyala, S.; Walsh, B.; Hungerford, G.; Santos, J.; Stamboulis, A. Time-resolved and fluorescence excitation-emission matrix measurements of lanthanide

(Gd³⁺, Tb³⁺and Dy³⁺) doped silver-zinc borate glasses. *Materials Letters* **2020**, *273*. doi: 10.1016/j.matlet.2020.127935.
67. Andrews, N. L. P.; Fan, J. Z.; Omrani, H.; Dudelzak, A.; Loock, H. P. Comparison of lubricant oil antioxidant analysis by fluorescence spectroscopy and linear sweep voltammetry. *Tribology International* **2016**, *94*, 279-287. doi: 10.1016/j.triboint.2015.08.023.
68. Omrani, H.; Dudelzak, A. E.; Hollebone, B. P.; Loock, H. P. Assessment of the oxidative stability of lubricant oil using fiber-coupled fluorescence excitation-emission matrix spectroscopy. *Analytica Chimica Acta* **2014**, *811*, 1-12. doi: 10.1016/j.aca.2013.10.019.
69. Omrani, H.; Barnes, J.; Dudelzak, A.; Loock, H.; Waechter, H. Fluorescence excitation-emission matrix (EEM) spectroscopy and cavity ring-down (CRD) absorption spectroscopy of oil-contaminated jet fuel using fiber-optic probes. *Analyst* **2012**, *137* (12), 2782-2790. doi: 10.1039/c2an35091b.
70. Divya, O.; Mishra, A. K. Chemometric study of excitation-emission matrix fluorescence data: Quantitative analysis of petrol-kerosene mixtures. *Applied Spectroscopy* **2008**, *62* (7), 753-758. doi: 10.1366/000370208784909454.
71. Tovstun, S. A.; Gadomska, A. V.; Spirin, M. G.; Razumov, V. F. Extracting the homogeneous and inhomogeneous linewidths of colloidal quantum dots from the excitation-emission matrix. *Journal of Luminescence* **2022**, *252*. doi: 10.1016/j.jlumin.2022.119420.
72. Ramsay, H.; Simon, D.; Steele, E.; Hebert, A.; Oleschuk, R. D.; Stamplecoskie, K. G. The power of fluorescence excitation-emission matrix (EEM) spectroscopy in the identification and characterization of complex mixtures of fluorescent silver clusters. *Rsc Advances* **2018**, *8* (73), 42080-42086. doi: 10.1039/c8ra08751b.
73. Finnie, P.; Ouyang, J.; Fagan, J. A. Broadband Full-Spectrum Raman Excitation Mapping Reveals Intricate Optoelectronic–Vibrational Resonance Structure of Chirality-Pure Single-Walled Carbon Nanotubes. *ACS Nano* **2023**, *17* (8), 7285-7295. doi: 10.1021/acsnano.2c10524.
74. Chung, Y. G.; Schwartz, J.; Gardner, C.; Sawaya, R.; Jacques, S. l.; Alfano, R. R.; Katzir, A. Fluorescence of normal and cancerous brain-tissues - the excitation emission matrix. *Advances in Laser and Light Spectroscopy To Diagnose Cancer and Other Diseases* **1994**, *2135*, 66-75. doi: 10.1117/12.176012.
75. Richardskortum, R.; Rava, R. P.; Petras, R. E.; Fitzmaurice, M.; Sivak, M.; Feld, M. S. Spectroscopic diagnosis of colonic dysplasia. *Photochemistry and Photobiology* **1991**, *53* (6), 777-786. doi: 10.1111/j.1751-1097.1991.tb09892.x.
76. Zangaro, R. A.; Silveira, L.; Manoharan, R.; Zonios, G.; Itzkan, I.; Dasari, R. R.; VanDam, J.; Feld, M. S. Rapid multiexcitation fluorescence spectroscopy system for in vivo tissue diagnosis. *Applied Optics* **1996**, *35* (25), 5211-5219. doi: 10.1364/AO.35.005211.
77. Zuluaga, A. F.; Utzinger, U.; Durkin, A.; Fuchs, H.; Gillenwater, A.; Jacob, R.; Kemp, B.; Fan, J.; Richards-Kortum, R. Fluorescence excitation emission matrices of human tissue:: A system for in vivo measurement and method of data analysis. *Applied Spectroscopy* **1999**, *53* (3), 302-311. doi: 10.1366/0003702991946695.
78. DaCosta, R. S.; Andersson, H.; Wilson, B. C. Molecular fluorescence excitation-emission matrices relevant to tissue spectroscopy. *Photochemistry and Photobiology* **2003**, *78* (4), 384-392.

79. Trevisan, M. G.; Poppi, R. J. Determination of doxorubicin in human plasma by excitation-emission matrix fluorescence and multi-way analysis. *Analytica Chimica Acta* **2003**, *493* (1), 69-81. doi: 10.1016/S0003-2670(03)00864-X.
80. Andrews, N. L. P.; Fan, J. Z.; Forward, R. L.; Chen, M. C.; Loock, H. P. Determination of the thermal, oxidative and photochemical degradation rates of scintillator liquid by fluorescence EEM spectroscopy. *Physical Chemistry Chemical Physics* **2017**, *19* (1), 73-81. doi: 10.1039/c6cp06015c.
81. Moberg, L.; Robertsson, G.; Karlberg, B. Spectrofluorimetric determination of chlorophylls and pheopigments using parallel factor analysis. *Talanta* **2001**, *54* (1), 161-170.
82. Sá, M.; Bertinetto, C. G.; Ferrer-Ledo, N.; Jansen, J. J.; Wijffels, R.; Crespo, J. G.; Barbosa, M.; Galinha, C. F. Fluorescence spectroscopy and chemometrics for simultaneous monitoring of cell concentration, chlorophyll and fatty acids in Nannochloropsis oceanica. *Scientific Reports* **2020**, *10* (1). doi: 10.1038/s41598-020-64628-7.
83. Cordella, C. PCA : The basic building block of chemometrics. In *Analytical Chemistry*, Ira, S. K. Ed.; IntechOpen, 2012; p 146.
84. Consonni, V.; Baccolo, G.; Gosetti, F.; Todeschini, R.; Ballabio, D. A MATLAB toolbox for multivariate regression coupled with variable selection. *Chemometrics and Intelligent Laboratory Systems* **2021**, *213*. doi: 10.1016/j.chemolab.2021.104313.
85. Eriksson, L.; Trygg, J.; Wold, S. A chemometrics toolbox based on projections and latent variables. *Journal of Chemometrics* **2014**, *28* (5), 332-346. doi: 10.1002/cem.2581.
86. Andersson, C. A.; Bro, R. The N-way Toolbox for MATLAB. *Chemometrics and Intelligent Laboratory Systems* **2000**, *52*, 5.
87. Andrews, N.; Ferguson, T.; Rangaswamy, A.; Bernicky, A.; Henning, N.; Dudelzak, A.; Reich, O.; Barnes, J.; Loock, H. Hadamard-Transform Fluorescence Excitation-Emission-Matrix Spectroscopy. *Analytical Chemistry* **2017**, *89* (16), 8554-8564. doi: 10.1021/acs.analchem.7b02400.
88. Aminfar, P.; Ferguson, T.; Steele, E.; Macneil, E. M.; Matus, M. F.; Malola, S.; Häkkinen, H.; Duchesne, P. N.; Loock, H. P.; Stamplecoskie, K. G. Accelerated size-focusing light activated synthesis of atomically precise fluorescent Au- 22 (Lys-Cys-Lys) 16 clusters. *Nanoscale* **2023**, *16* (1), 205-211. doi: 10.1039/d3nr04793h.
89. Liu, Z.; Zhao, H. Y.; Yang, G. L.; He, K. Y.; Sun, X. D.; Wang, Z. Y.; Wang, D.; Qiu, J. Study of photodegradation kinetics of aflatoxins in cereals using trilinear component modeling of excitation-emission matrix fluorescence data. *Spectrochimica Acta Part a-Molecular and Biomolecular Spectroscopy* **2020**, *235*. doi: 10.1016/j.saa.2020.118266.
90. Zhou, Z. Z.; Guo, L. D.; Shiller, A. M.; Lohrenz, S. E.; Asper, V. L.; Osburn, C. L. Characterization of oil components from the Deepwater Horizon oil spill in the Gulf of Mexico using fluorescence EEM and PARAFAC techniques. *Marine Chemistry* **2013**, *148*, 10-21. doi: 10.1016/j.marchem.2012.10.003.
91. de Bruyn, W.; Chang, D.; Bui, T.; Hok, S.; Clark, C. Photochemical degradation of oil products in seawater monitored by 3D excitation emission matrix (EEM) fluorescence spectroscopy: implications for coloured dissolved organic matter (CDOM) studies. *Environmental Science and Pollution Research* **2018**, *25* (34), 34777-34787. doi: 10.1007/s11356-018-3190-9.
92. Zhao, C.; Wang, Z. H.; Wang, C. Y.; Li, X.; Wang, C. C. Photocatalytic degradation of DOM in urban stormwater runoff with TiO2 nanoparticles under UV light irradiation: EEM-

PARAFAC analysis and influence of co-existing inorganic ions. *Environmental Pollution* **2018**, *243*, 177-188. doi: 10.1016/j.envpol.2018.08.062.
93. Bro, R. PARAFAC. Tutorial and Applications. *Chemometrics and Intelligent Laboratory Systems* **1997**, *38* (2), 149-171.
94. Chen, A.-Q.; Wu, H.-L.; Wang, T.; Wang, X.-Z.; Sun, H.-B.; Yu, R.-Q. Intelligent analysis of excitation-emission matrix fluorescence fingerprint to identify and quantify adulteration in camellia oil based on machine learning. *Talanta* **2023**, *251*, 123733. doi: 10.1016/j.talanta.2022.123733.
95. Hiraoka, Y.; Shimi, T.; Haraguchi, T. Multispectral imaging fluorescence microscopy for living cells. *Cell Structure and Function* **2002**, *27* (5), 367-374. doi: 10.1247/csf.27.367.
96. Levenson, R. M.; Mansfield, J. R. Multispectral imaging in biology and medicine: Slices of life. *Cytometry Part A* **2006**, *69A* (8), 748-758. doi: 10.1002/cyto.a.20319.
97. Hanley, Q. S.; Murray, P. I.; Forde, T. S. Microspectroscopic fluorescence analysis with prism-based imaging spectrometers: Review and current studies. *Cytometry Part A* **2006**, *69A* (8), 759-766. doi: 10.1002/cyto.a.20265.
98. Zhou, L. L.; El-Deiry, W. S. Multispectral Fluorescence Imaging. *Journal of Nuclear Medicine* **2009**, *50* (10), 1563-1566. doi: 10.2967/jnumed.109.063925.
99. Qin, J. W.; Chao, K. L.; Kim, M. S.; Lu, R. F.; Burks, T. F. Hyperspectral and multispectral imaging for evaluating food safety and quality. *Journal of Food Engineering* **2013**, *118* (2), 157-171. doi: 10.1016/j.jfoodeng.2013.04.001.
100. Guo, N.; Cheung, K. W.; Wong, H. T.; Ho, D. CMOS Time-Resolved, Contact, and Multispectral Fluorescence Imaging for DNA Molecular Diagnostics. *Sensors* **2014**, *14* (11), 20602-20619. doi: 10.3390/s141120602.
101. Kharbach, M.; Mansouri, M. A.; Taabouz, M.; Yu, H. W. Current Application of Advancing Spectroscopy Techniques in Food Analysis: Data Handling with Chemometric Approaches. *Foods* **2023**, *12* (14). doi: 10.3390/foods12142753.
102. Herman, B. *Fluorescence Microscopy*; Taylor & Francis Group, 1998.
103. Haisch, C. Photoacoustic spectroscopy for analytical measurements. *Measurement Science and Technology* **2012**, *23* (1). doi: 10.1088/0957-0233/23/1/012001.
104. Proskurnin, M.; Baudelet, M. Photothermal spectroscopy. *Laser Spectroscopy For Sensing: Fundamentals, Techniques and Applications* **2014**, (43), 313-361. doi: 10.1533/9780857098733.2.313.
105. Abbey, E. X.; Loock, H.-P.; McNiven, M. *Build your own Spectroscope!* Loock, H-P, 2025. https://www.loocklaserlab.com/home-page/2025/5/13/build-your-own-spectroscope (accessed 2026 March 01).
106. Mazhar, M. A.; Riza, N. A. 96 dB Linear High Dynamic Range CAOS Spectrometer Demonstration. *IEEE Photonics Technology Letters* **2020**, *32* (23), 1497-1500. doi: 10.1109/LPT.2020.3038062.
107. De Rosa, S. C.; Brenchley, J. M.; Roederer, M. Beyond six colors: A new era in flow cytometry. *Nature Medicine* **2003**, *9* (1), 112-117. doi: 10.1038/nm0103-112.
108. Adan, A.; Alizada, G.; Kiraz, Y.; Baran, Y.; Nalbant, A. Flow cytometry: basic principles and applications. *Critical Reviews in Biotechnology* **2017**, *37* (2), 163-176. doi: 10.3109/07388551.2015.1128876.
109. Muroski, A. R.; Booksh, K. S.; Myrick, M. L. Single-measurement excitation/emission matrix spectrofluorometer for determination of hydrocarbons in ocean water 1.

Instrumentation and background correction. *Analytical Chemistry* **1996**, *68* (20), 3534-3538. doi: 10.1021/ac960252b.
110. Scientific, T.-F. *Varioskan LUX Multimode Microplate Reader*. 2025. https://www.thermofisher.com/ca/en/home/life-science/lab-equipment/microplate-instruments/plate-readers/models/varioskan.html (accessed 2025 May 29).
111. Agilent. *Cary Eclipse Fluorescence Spectrometer*. 2025. https://www.agilent.com/en/product/molecular-spectroscopy/fluorescence-spectroscopy/fluorescence-systems/cary-eclipse-fluorescence-spectrophotometer (accessed 2025 May 29).
112. Instruments, E. *FS5 Spectrofluorometer*. 2025. https://www.edinst.com/product/fs5-spectrofluorometer/ (accessed 2025 May 29).
113. Shimadzu. *RF-6000 Spectrofluorophotometer*. 2025. https://www.shimadzu.com/an/products/molecular-spectroscopy/fluorescence/fluorescence-spectroscopy/rf-6000/spec.html (accessed July 18, 2025).
114. Horiba. *Fluorolog-QM Fluorometer*. 2025. https://www.horiba.com/int/scientific/products/detail/action/show/Product/fluorolog-qm-1997/ (accessed 2025 May 29).
115. Wang, W.; Wu, Z.; Zhao, J.; Lui, H.; Zeng, H. A rapid excitation-emission matrix fluorometer utilizing supercontinuum white light and acousto-optic tunable filters. *Review of Scientific Instruments* **2016**, *87* (6). doi: 10.1063/1.4954502.
116. Senga, Y.; Minami, S. Excitation-emission matrix scanning spectrofluorometer. *Applied Spectroscopy* **1991**, *45* (10), 1721-1725. doi: 10.1366/0003702914335346.
117. Destrampe, K. A.; Hieftje, G. M. New instrumentation for use in excitation-emission fluorescence-polarization measurements. *Applied Spectroscopy* **1993**, *47* (10), 1548-1554. doi: 10.1366/0003702934334741.
118. Li, H.; Zheng, W.; Huang, Z. Rapid near-infrared fluorescence excitation-emission matrix spectroscopy for multifluorophore characterization using an acousto-optic tunable filter technique. *Journal of Biomedical Optics* **2010**, *15* (2). doi: 10.1117/1.3374051.
119. Peng, L.; Gardecki, J. A.; Bouma, B. E.; Tearney, G. J. Fourier fluorescence spectrometer for excitation emission matrix measurement. *Optics Express* **2008**, *16* (14), 10493-10500. doi: 10.1364/OE.16.010493.
120. Yuan, J.; Peng, L.; Bouma, B. E.; Tearney, G. J. Quantitative FRET measurement by high-speed fluorescence excitation and emission spectrometer. *Optics Express* **2010**, *18*, 18839-18851. doi: 10.1364/OE.18.018839.
121. Griffiths, P. R.; De Haseth, J. A. Signal-to-Noise Ratio. In *Fourier Transform Infrared Spectrometry*, 2007; pp 161-175.
122. Jia, X.; Wei, Q.; Zhu, Y.; Zhang, W. Analysis of noise and its characteristics in avalanche photodiode. *AIP Advances* **2024**, *14* (9). doi: 10.1063/5.0229293.
123. Curtiss, C. F.; Hirschfelder, J. O.; Adler, F. T. The seperation of the rotational coordinates from the N-particle Schroedinger equation. *Journal of Chemical Physics* **1950**, *18*, 1638.
124. Dzsaber, S.; Negyedi, M.; Bernáth, B.; Gyüre, B.; Fehér, T.; Kramberger, C.; Pichler, T.; Simon, F. A Fourier transform Raman spectrometer with visible laser excitation. *Journal of Raman Spectroscopy* **2015**, *46* (3), 327-332. doi: 10.1002/jrs.4641.

125. Park, J.; Gao, L. Advancements in fluorescence lifetime imaging microscopy Instrumentation: Towards high speed and 3D. *Current Opinion in Solid State & Materials Science* **2024**, *30*. doi: 10.1016/j.cossms.2024.101147.
126. Gouzou, D.; Taimori, A.; Haloubi, T.; Finlayson, N.; Wang, Q.; Hopgood, J. R.; Vallejo, M. Applications of machine learning in time-domain fluorescence lifetime imaging: a review. *Methods and Applications in Fluorescence* **2024**, *12* (2). doi: 10.1088/2050-6120/ad12f7.
127. Torrado, B.; Pannunzio, B.; Malacrida, L.; Digman, M. A. Fluorescence lifetime imaging microscopy. *Nature Reviews Methods Primers* **2024**, *4* (1). doi: 10.1038/s43586-024-00358-8.
128. Datta, R.; Heaster, T.; Sharick, J.; Gillette, A.; Skala, M. Fluorescence lifetime imaging microscopy: fundamentals and advances in instrumentation, analysis, and applications. *Journal of Biomedical Optics* **2020**, *25* (7). doi: 10.1117/1.JBO.25.7.071203.
129. Poudel, C.; Mela, I.; Kaminski, C. High-throughput, multi-parametric, and correlative fluorescence lifetime imaging. *Methods and Applications in Fluorescence* **2020**, *8* (2). doi: 10.1088/2050-6120/ab7364.
130. Wang, Z.; Zheng, Y.; Zhao, D.; Zhao, Z.; Liu, L.; Pliss, A.; Zhu, F.; Liu, J.; Qu, J.; Luan, P. Applications of fluorescence lifetime imaging in clinical medicine. *Journal of Innovative Optical Health Sciences* **2018**, *11* (1). doi: 10.1142/S179354581830001X.
131. Borst, J. W.; Visser, A. Fluorescence lifetime imaging microscopy in life sciences. *Measurement Science and Technology* **2010**, *21* (10). doi: 10.1088/0957-0233/21/10/102002.
132. Chen, Y. C.; Clegg, R. M. Fluorescence lifetime-resolved imaging. *Photosynthesis Research* **2009**, *102* (2-3), 143-155. doi: 10.1007/s11120-009-9458-7.
133. Kennedy, G. T.; Elson, D. S.; Hares, J. D.; Munro, I.; Poher, V.; French, P. M. W.; Neil, M. A. A. Fluorescence lifetime imaging using light emitting diodes. *Journal of Physics D-Applied Physics* **2008**, *41* (9). doi: 10.1088/0022-3727/41/9/094012.
134. Suhling, K.; French, P. M. W.; Phillips, D. Time-resolved fluorescence microscopy. *Photochemical & Photobiological Sciences* **2005**, *4* (1), 13-22. doi: 10.1039/b412924p.
135. Wang, X. F.; Periasamy, A.; Herman, B.; Coleman, D. M. Fluorescence Lifetime Imaging Microscopy (FLIM) - Instrumentation And Applications. *Critical Reviews in Analytical Chemistry* **1992**, *23* (5), 369-395. doi: 10.1080/10408349208051651.
136. Yuan, Y.; Hwang, J. Y.; Krishnamoorthy, M.; Ye, K. T.; Zhang, Y.; Ning, J.; Wang, R. C.; Deen, M. J.; Fang, Q. Y. High-throughput acousto-optic-tunable-filter-based time-resolved fluorescence spectrometer for optical biopsy. *Optics Letters* **2009**, *34* (7), 1132-1134. doi: 10.1364/OL.34.001132.
137. Manning, H. B.; Kennedy, G. T.; Owen, D. M.; Grant, D. M.; Magee, A. I.; Neil, M. A. A.; Itoh, Y.; Dunsby, C.; French, P. M. W. A compact, multidimensional spectrofluorometer exploiting supercontinuum generation. *Journal of Biophotonics* **2008**, *1* (6), 494-505. doi: 10.1002/jbio.200810051.
138. Kirchner, F.; Lahme, S.; Riedle, E.; Baum, P. All-reflective UV-VIS-NIR transmission and fluorescence spectrometer for µm-sized samples. *Aip Advances* **2014**, *4* (7). doi: 10.1063/1.4891863.
139. Spriet, C.; Trinel, D.; Laffray, S.; Landry, M.; Vandenbunder, B.; Heliot, L.; Barbillat, J. Setup of a fluorescence lifetime and spectral correlated acquisition system for two-photon microscopy. *Review of Scientific Instruments* **2006**, *77* (12), 6. doi: 10.1063/1.2400015.

140. Horiba. *Duetta - A Versatile Spectrometer for Science and Industry*. 2025. https://www.horiba.com/int/scientific/products/detail/action/show/Product/duetta-1621/ (accessed 2025 2025 Sept 23).
141. Gao, F.; Dong, Y.; Xiao, W.; Yin, B.; Yan, C.; He, S. LED-induced fluorescence spectroscopy technique for apple freshness and quality detection. *Postharvest Biology and Technology* **2016**, *119*, 27-32. doi: 10.1016/j.postharvbio.2016.04.020.
142. Leonhardt, A.; Goldbrunner, M.; Hackett, B.; Schoenert, S. A novel cryogenic VUV spectrofluorometer for the characterization of wavelength shifters. *Journal of Instrumentation* **2024**, *19* (5). doi: 10.1088/1748-0221/19/05/C05020.
143. Suzuki, Y.; Hashigaya, N.; Kawakubo, S. Development of a Simple and Low-cost Device for Fluorometric Determination of Selenium in Water Samples. *Analytical Sciences* **2010**, *26* (6), 719-722. doi: 10.2116/analsci.26.719.
144. Ma, J. J.; Bock, W. J. Evanescent-Wave Fiber-Optic Fluorometer Capable of Dense Channel Multiplexing, Signal Enhancement and Stray Excitation Light Suppression. *2008 Ieee Instrumentation and Measurement Technology Conference, Vols 1-5* **2008**, 125-129. doi: 10.1109/IMTC.2008.4547016.
145. Panigrahi, S.; Mishra, A. Reflective walled sample compartment and optimization of data acquisition geometry towards sensitive fluorescence measurement in fiber-optic setup. *Measurement* **2019**, *139*, 277-283. doi: 10.1016/j.measurement.2019.02.076.
146. Sosnovski, O.; Suresh, P.; Dudelzak, A.; Green, B.; Soskind, Y.; Olson, C. Fluorescence Excitation-Emission Matrix Spectroscopy for Degradation Monitoring of Machinery Lubricants. *Photonic Instrumentation Engineering V* **2018**, *10539*. doi: 10.1117/12.2290637.
147. Puiu, A.; Fiorani, L.; Menicucci, I.; Pistilli, M.; Lai, A. Submersible Spectrofluorometer for Real-Time Sensing of Water Quality. *Sensors* **2015**, *15* (6), 14415-14434. doi: 10.3390/s150614415.
148. Shin, Y. H.; Gutierrez-Wing, M. T.; Choi, J. W. A field-deployable and handheld fluorometer for environmental water quality monitoring. Micro and Nano Syst Lett: 2018; Vol. 6, p 16.
149. Shin, Y.; Gutierrez-Wing, M.; Choi, J. Review-Recent Progress in Portable Fluorescence Sensors. *Journal of the Electrochemical Society* **2021**, *168* (1). doi: 10.1149/1945-7111/abd494.
150. Shin, Y.; Barnett, J.; Gutierrez-Wing, M.; Rusch, K.; Choi, J.; Gray, B.; Becker, H. A Portable Fluorescent Sensing System Using Multiple LEDs. *Microfluidics, Biomems, and Medical Microsystems Xv* **2017**, *10061*. doi: 10.1117/12.2261292.
151. Chen, X.; Du, J.; Kanwal, S.; Yang, Z. J.; Zheng, L. L.; Wang, J.; Wen, J.; Zhang, D. W. A low-cost and portable fluorometer based on an optical pick-up unit for chlorophyll-a detection. *Talanta* **2024**, *269*. doi: 10.1016/j.talanta.2023.125447.
152. Warner, I. M.; Callis, J. B.; Davidson, E. R.; Gouterman, M.; Christian, G. D. Fluorescence analysis: a new approach. *Analytical Letters* **1975**, *8* (9), 665-681.
153. Finnie, P.; Ouyang, J.; Lefebvre, J. Full Spectrum Raman Excitation Mapping Spectroscopy. *Scientific Reports* **2020**, *10* (1), 9172. doi: 10.1038/s41598-020-65757-9.
154. Nakamura, S.; Mukai, T.; Senoh, M. Candela-class high-brightness ingan/algan double-heterostructure blue-light-emitting diodes. *Appl. Phys. Lett.* **1994**, *64* (13), 1687-1689. doi: 10.1063/1.111832.

155. Kneissl, M.; Seong, T. Y.; Han, J.; Amano, H. The emergence and prospects of deep-ultraviolet light-emitting diode technologies. *Nat. Photonics* **2019**, *13* (4), 233-244. doi: 10.1038/s41566-019-0359-9.
156. Akasaki, I.; Amano, H. Crystal growth and conductivity control of group III nitride semiconductors and their application to short wavelength light emitters. *Jpn. J. Appl. Phys. Part 1 - Regul. Pap. Brief Commun. Rev. Pap.* **1997**, *36* (9A), 5393-5408. doi: 10.1143/jjap.36.5393.
157. Malik, M. A.; Gatto, E.; Macken, S.; DiNatale, C.; Paolesse, R.; D'Amico, A.; Lundström, I.; Filippini, D. Imaging fingerprinting of excitation emission matrices. *Analytica Chimica Acta* **2009**, *635* (2), 196-201. doi: 10.1016/j.aca.2009.01.018.
158. Alfano, R. R. *The Supercontinuum Laser Source: Fundamentals With Updated References*; Springer New York, NY, 2006. DOI: 10.1007/b106776.
159. Wadsworth, W. J.; Ortigosa-Blanch, A.; Knight, J. C.; Birks, T. A.; Man, T. P. M.; Russell, P. S. Supercontinuum generation in photonic crystal fibers and optical fiber tapers: a novel light source. *J. Opt. Soc. Am. B-Opt. Phys.* **2002**, *19* (9), 2148-2155. doi: 10.1364/josab.19.002148.
160. Horiba. *Aqualog - Benchtop Fluorometer for CDOM*. 2018. http://www.horiba.com/scientific/products/fluorescence-spectroscopy/steady-state/aqualog/aqualog-r-our-compact-benchtop-fluorometer-for-cdom-13031/ (accessed 2018 2018 March 28).
161. Gilmore, A. M.; Cohen, S. M. *Analysis of the chromophoric dissolved organic matter in water by EEMs with Horiba-Jobin Yvon fluorescence instrument called Aqualog*; 2013.
162. Kenar, N.; Lim, H.; Mirzaaghasi, A.; VoDinh, T.; MahadevanJansen, A.; Grundfest, W. Development of multiwavelength excitation light source for autofluorescence and photodynamic diagnosis systems. *Advanced Biomedical and Clinical Diagnostic and Surgical Guidance Systems Xii* **2014**, *8935*. doi: 10.1117/12.2039650.
163. Lim, H. S.; Kessel, D. H. Design and Evaluation of Excitation Light Source device for Fluorescence Endoscope. *12th World Congress of the International Photodynamic Association: Photodynamic Therapy: Back To the Future* **2009**, *7380*. doi: 10.1117/12.822808.
164. Weng, C.; Wang, L.; Chen, C.; Liu, D.; Hwang, C.; Chang, S. A novel filter wheel for multi-channel switching and polarization rotation. *Optik* **2020**, *200*. doi: 10.1016/j.ijleo.2019.163122.
165. Spibey, C. A.; Jackson, P.; Herick, K. A unique charge-coupled device/xenon arc lamp based imaging system for the accurate detection and quantitation of multicolour fluorescence. *Electrophoresis* **2001**, *22* (5), 829-836. doi: 10.1002/1522-2683()22:5<829::AID-ELPS829>3.0.CO;2-U.
166. Erdogan, T. Optical Filters for Wavelength Selection in Fluorescence Instrumentation. *Current Protocols in Cytometry* **2011**, *56* (1), 2.4.1-2.4.25. doi: 10.1002/0471142956.cy0204s56.
167. Johnson, S.; Annamdevula, N.; Rich, T. C.; Ballard, C.; Leavesley, S. J.; Tarnok, A.; Houston, J. P. High-speed fluorescence excitation-scanning hyperspectral imaging microscopy using thin-film tunable filters. *Imaging, Manipulation, and Analysis of Biomolecules, Cells, and Tissues Xxii* **2024**, *12846*. doi: 10.1117/12.3001600.

168. Gouzman, M.; Lifshitz, N.; Luryi, S.; Semyonov, O.; Gavrilov, D.; Kuzminskiy, V. Excitation-emission fluorimeter based on linear interference filters. *Applied Optics* **2004**, *43* (15), 3066-3072. doi: 10.1364/AO.43.003066.
169. Kieleck, C.; Bousquet, B.; Le Brun, G.; Cariou, J.; Lotrian, J. Laser induced fluorescence imaging: application to groups of macroalgae identification. J. Phys. D: Appl. Phys: 2001; Vol. 34, pp 2561-2571.
170. Taylor, T. A.; Jarvis, G. B.; Xu, H.; Bevilacqua, A. C.; Kenny, J. E. Laser-based fluorescence EEM instrument for in-situ groundwater monitoring. *Analytical Instrumentation* **1993**, *21* (3-4), 141-162.
171. Sivaprakasam, V.; Killinger, D. K. Tunable ultraviolet laser-induced fluorescence detection of trace plastics and dissolved organic compounds in water. *Applied Optics* **2003**, *42* (33), 6739-6746. doi: 10.1364/AO.42.006739.
172. Thériault, J.-F.; Yu, L.; Stephen, P.; Sheng, Y.; Lin, S.-X. Tunable ultraviolet laser induces high signal-to-noise ratio in intrinsic fluorescence titration for protein-ligand interaction studies. Results in Physics: 2023; Vol. 44, p 106120.
173. Owen, D. M.; Auksorius, E.; Manning, H. B.; Talbot, C. B.; de Beule, P. A. A.; Dunsby, C.; Neil, M. A. A.; French, P. M. W. Excitation-resolved hyperspectral fluorescence lifetime imaging using a UV-extended supercontinuum source. *Optics Letters* **2007**, *32* (23), 3408-3410. doi: 10.1364/OL.32.003408.
174. Dunsby, C.; Lanigan, P. M. P.; McGinty, J.; Elson, D. S.; Requejo-Isidro, J.; Munro, I.; Galletly, N.; McCann, F.; Treanor, B.; Önfelt, B.; et al. An electronically tunable ultrafast laser source applied to fluorescence imaging and fluorescence lifetime imaging microscopy. *Journal of Physics D-Applied Physics* **2004**, *37* (23), 3296-3303. doi: 10.1088/0022-3727/37/23/011.
175. Chen, B.; Shi, S.; Gong, W.; Xu, Q.; Tang, X.; Bi, S.; Chen, B. Wavelength selection of dual-mechanism LiDAR with reflection and fluorescence spectra for plant detection. Optics Express: 2023; Vol. 31, p 3660.
176. Chen, Y.; Li, W.; Hyyppä, J.; Wang, N.; Jiang, C.; Meng, F.; Tang, L.; Puttonen, E.; Li, C. A 10-nm Spectral Resolution Hyperspectral LiDAR System Based on an Acousto-Optic Tunable Filter. *Sensors* **2019**, *19* (7). doi: 10.3390/s19071620.
177. Perri, A.; Preda, F.; D'Andrea, C.; Thyrhaug, E.; Cerullo, G.; Polli, D.; Hauer, J. Excitation-emission Fourier-transform spectroscopy based on a birefringent interferometer. *Optics Express* **2017**, *25* (12), A483-A490. doi: 10.1364/OE.25.00A483.
178. Kiefer, J. Using a supercontinuum light source for instantaneous excitation-emission fluorescence mapping. *Measurement Science and Technology* **2017**, *28* (6). doi: 10.1088/1361-6501/aa6361.
179. Yu, Y.; Lee, A.; Wang, H.; Tang, S.; Zhao, J.; Lui, H.; Zeng, H. Imaging-guided two-photon excitation-emission-matrix measurements of human skin tissues. *Journal of Biomedical Optics* **2012**, *17* (7). doi: 10.1117/1.JBO.17.7.077004.
180. Esposito, A.; Bader, A.; Schlachter, S.; van den Heuvel, D.; Schierle, G.; Venkitaraman, A.; Kaminski, C.; Gerritsen, H. Design and application of a confocal microscope for spectrally resolved anisotropy imaging. *Optics Express* **2011**, *19* (3), 2546-2555. doi: 10.1364/OE.19.002546.
181. Kurtz, I.; Dwelle, R.; Katzka, P. Rapid scanning fluorescence spectroscopy using an acoustooptic tunable filter. *Review of Scientific Instruments* **1987**, *58* (11), 1996-2003. doi: 10.1063/1.1139506.

182. Zacharioudaki, D.-E.; Fitilis, I.; Kotti, M. Review of Fluorescence Spectroscopy in Environmental Quality Applications. *Molecules* **2022**, *27* (15), 4801.
183. Tran, C. D.; Furlan, R. J. Spectrofluorometer based on acoustooptic tunable filters for rapid-scanning and multicomponent sample analyses. *Analytical Chemistry* **1993**, *65* (13), 1675-1681. doi: 10.1021/ac00061a008.
184. Hueber, D. M.; Stevenson, C. L.; Vo-Dinh, T. Fast scanning synchronous luminescence spectrometer based on acoustooptic tunable filters. *Applied Spectroscopy* **1995**, *49* (11), 1624-1631. doi: 10.1366/0003702953965830.
185. Frank, J. H.; Elder, A. D.; Swartling, J.; Venkitaraman, A. R.; Jeyasekharan, A. D.; Kaminski, C. F. A white light confocal microscope for spectrally resolved multidimensional imaging. *Journal of Microscopy* **2007**, *227* (3), 203-215. doi: 10.1111/j.1365-2818.2007.01803.x.
186. Francisco-Cruz, A.; Parra, E. R.; Tetzlaff, M. T.; Wistuba, I. I. Multiplex Immunofluorescence Assays. In *Biomarkers for Immunotherapy of Cancer: Methods and Protocols*, Thurin, M., Cesano, A., Marincola, F. M. Eds.; Springer New York, 2020; pp 467-495.
187. Sheng, W.; Zhang, C.; Mohiuddin, T. M.; Al-Rawe, M.; Zeppernick, F.; Falcone, F. H.; Meinhold-Heerlein, I.; Hussain, A. F. Multiplex Immunofluorescence: A Powerful Tool in Cancer Immunotherapy. *International Journal of Molecular Sciences* **2023**, *24* (4), 3086.
188. Huang, Z.; Saito, Y.; Gao, T.; Al Riza, D. F.; Lu, R.; Cen, H.; Kondo, N.; Omwange, K. A. A review of fluorescence imaging system supported by excitation-emission matrix for fruit and vegetable quality estimation. *Food Control* **2025**, *169*, 111040. doi: 10.1016/j.foodcont.2024.111040.
189. Kanani, S. S.; Tsai, H. Y.; Algar, W. R. Quantitative and Multiplexed Chopper-Based Time-Gated Imaging for Bioanalysis on a Smartphone. *Analytical Chemistry* **2023**, *95* (35), 13258-13265. doi: 10.1021/acs.analchem.3c02397.
190. Baker, D. V.; Bernal-Escalante, J.; Traaseth, C.; Wang, Y. H.; Tran, M. V.; Keenan, S.; Algar, W. R. Smartphones as a platform for molecular analysis: concepts, methods, devices and future potential. *Lab on a Chip* **2025**, *25* (5). doi: 10.1039/d4lc00966e.
191. Xing, G.; Ai, J.; Wang, N.; Pu, Q. Recent progress of smartphone-assisted microfluidic sensors for point of care testing. *TrAC Trends in Analytical Chemistry* **2022**, *157*, 116792. doi: 10.1016/j.trac.2022.116792.
192. García Ramos, J.; de Souza Júnior, R. S.; Borges, E. M. How Digital Images Are Transforming Chemical Education: A Review of Laboratory-Based Applications. *ACS Omega* **2025**, *10* (30), 32651-32672. doi: 10.1021/acsomega.5c05125.
193. Garrido-González, J. J.; Trillo-Alcalá, M.; Sánchez-Arroyo, A. J. Lights, Camera, Spectroscope! The Basics of Spectroscopy Disclosed Using a Computer Screen. *Journal of Chemical Education* **2018**, *95* (5), 903-907. doi: 10.1021/acs.jchemed.7b00763.
194. Kovarik, M. L.; Clapis, J. R.; Romano-Pringle, K. A. Review of Student-Built Spectroscopy Instrumentation Projects. *Journal of Chemical Education* **2020**, *97* (8), 2185-2195. doi: 10.1021/acs.jchemed.0c00404.
195. Mool-am-kha, P.; Phetduang, S.; Ngamdee, K.; Surawanitkun, C.; Ren, X. K.; Ngeontae, W. A portable fluorescence detection device based on a smartphone employing carbon nanodots for Mn²⁺ sensing. *Analytical Methods* **2024**, *16* (14), 2101-2110. doi: 10.1039/d4ay00027g.

196. Wang, J.; Shen, Q.; Yu, X.; Kang, Q.; Shen, D. A smartphone-based ratiometric fluorescence and absorbance dual-mode device for Rhodamine B determination in combination with differential molecularly imprinting strategy and primary inner filter effect correction. *Microchemical Journal* **2022**, *183*. doi: 10.1016/j.microc.2022.108077.
197. Zheng, K.; Lin, H.; Hong, X.; Che, H.; Ma, X.; Wei, X.; Mei, L. Development of a multispectral fluorescence LiDAR for point cloud segmentation of plants. Optics Express: 2023; Vol. 31, p 18613.
198. Koenig, M.; Yi, E.; Sandridge, M.; Mathew, A.; Demas, J. "Open-Box" Approach to Measuring Fluorescence Quenching Using an iPad Screen and Digital SLR Camera. *Journal of Chemical Education* **2015**, *92* (2), 310-316. doi: 10.1021/ed500373d.
199. Arun, P. V.; Buddhiraju, K. M.; Porwal, A.; Chanussot, J. CNN based spectral super-resolution of remote sensing images. *Signal Processing* **2020**, *169*. doi: 10.1016/j.sigpro.2019.107394.
200. He, J.; Yuan, Q.; Li, J.; Xiao, Y.; Liu, D.; Shen, H.; Zhang, L. Spectral super-resolution meets deep learning: Achievements and challenges. *Information Fusion* **2023**, *97*, 101812. doi: 10.1016/j.inffus.2023.101812.
201. Arad, B.; Ben-Shahar, O.; Timofte, R.; Gool, L. V.; Zhang, L.; Yang, M. H.; Xiong, Z.; Chen, C.; Shi, Z.; Liu, D.; et al. NTIRE 2018 Challenge on Spectral Reconstruction from RGB Images. In *2018 IEEE/CVF Conference on Computer Vision and Pattern Recognition Workshops (CVPRW)*, 18-22 June 2018, 2018; pp 1042-104209. DOI: 10.1109/CVPRW.2018.00138.
202. Arad, B.; Timofte, R.; Yahel, R.; Morag, N.; Bernat, A.; Cai, Y.; Lin, J.; Lin, Z.; Wang, H.; Zhang, Y.; et al. NTIRE 2022 Spectral Recovery Challenge and Data Set. In *2022 IEEE/CVF Conference on Computer Vision and Pattern Recognition Workshops (CVPRW)*, 19-20 June 2022, 2022; pp 862-880. DOI: 10.1109/CVPRW56347.2022.00102.
203. Mukhtar, S.; Arbabi, A.; Viegas, J. Advances in Spectral Imaging: A Review of Techniques and Technologies. *IEEE Access* **2025**, *13*, 35848-35902. doi: 10.1109/access.2025.3544476.
204. Spectral Devices. *Snapshot Multispectral Cameras*. 2025. https://spectraldevices.com/collections/snapshot-multispectral-cameras (accessed 2025 May 30).
205. Yun, S.; Park, J.; Koo, S.; Park, C.; Kim, Y.; Kim, J. Cost-Effective Multiplex Fluorescence Detection System for PCR Chip. *Sensors* **2021**, *21* (21). doi: 10.3390/s21216945.
206. Lefcourt, A. M.; Kim, M. S.; Chen, Y. R.; Bennedsen, B. S.; Meyer, G. E.; Senecal, A. G.; Tu, S. I. Portable multispectral fluorescence imaging system for food safety applications. *Monitoring Food Safety, Agriculture, and Plant Health* **2004**, *5271*, 73-84. doi: 10.1117/12.516103.
207. Zhao, Y.; Zhu, D.; Baikejiang, R.; Li, C.; Tromberg, B.; Yodh, A.; SevickMuraca, E.; Alfano, R. Fluorescence molecular imaging system with a novel mouse surface extraction method and a rotary scanning scheme. *Optical Tomography and Spectroscopy of Tissue Xi* **2015**, *9319*. doi: 10.1117/12.2076476.
208. Morris, H. R.; Hoyt, C. C.; Treado, P. J. Imaging spectrometers for fluorescence and raman microscopy - acoustooptic and liquid-crystal tunable filters. *Applied Spectroscopy* **1994**, *48* (7), 857-866. doi: 10.1366/0003702944029820.

209. Liu, Q.; Chen, K.; Martin, M.; Wintenberg, A.; Lenarduzzi, R.; Panjehpour, M.; Overholt, B.; Vo-Dinh, T. Development of a synchronous fluorescence imaging system and data analysis methods. *Optics Express* **2007**, *15* (20), 12583-12594. doi: 10.1364/OE.15.012583.
210. Romier, J.; Selves, J.; Gastellu-Etchegorry, J. Imaging spectrometer based on an acousto-optic tunable filter. *Review of Scientific Instruments* **1998**, *69* (8), 2859-2867. doi: 10.1063/1.1149025.
211. Kasili, P. M.; Vo-Dinh, T. Hyperspectral imaging system using acousto-optic tunable filter for flow cytometry applications. *Cytometry Part a* **2006**, *69A* (8), 835-841. doi: 10.1002/cyto.a.20307.
212. Bouhifd, M.; Whelan, M. P.; Aprahamian, M.; Byrne, H. J.; Lewis, E.; MacCraith, B. D.; McGlynn, E.; McLaughlin, J. A.; OSullivan, G. D.; Ryder, A. G.; et al. Fluorescence imaging spectroscopy utilising acousto-optic tuneable filters. *Opto-Ireland 2005: Optical Sensing and Spectroscopy* **2005**, *5826*, 185-193. doi: 10.1117/12.605088.
213. Gupta, N.; Dahmani, R.; Choy, S. Acousto-optic tunable filter based visible- to near-infrared spectropolarimetric imager. *Optical Engineering* **2002**, *41* (5), 1033-1038. doi: 10.1117/1.1467936.
214. Gonzaga, F.; Pasquini, C. Near-infrared emission spectrometry based on an acousto-optical tunable filter. *Analytical Chemistry* **2005**, *77* (4), 1046-1054. doi: 10.1021/ac048656o.
215. Suo, J.; Bian, L.; Chen, F.; Dai, Q. Bispectral coding: compressive and high-quality acquisition of fluorescence and reflectance. *Optics Express* **2014**, *22* (2), 1697-1712. doi: 10.1364/OE.22.001697.
216. BaySpec. *Hyperspectral Imaging Cameras*. 2025. https://www.bayspec.com/product-category/hyperspectral-imagers/ (accessed 2025 May 30).
217. Heintzmann, R.; Lidke, K. A.; Jovin, T. M. Double-pass Fourier transform imaging spectroscopy. *Optics Express* **2004**, *12* (5), 753-763. doi: 10.1364/OPEX.12.000753.
218. Manning, H. B.; Owen, D. M.; Auksorius, E.; de Beule, P. A. A.; Oddos, S.; Talbot, C. B.; Dunsby, C.; Munro, I.; Magee, A. I.; Neil, M. A. A.; et al. Applications of rapid time-gated hyperspectral FLIM: live cell imaging of membrane order and 6-D microscopy. In *Conference on Confocal, Multiphoton and Nonlinear Microscopic Imaging III*, Munich, GERMANY, Jun 17-18, 2007; 2007; Vol. 6630.
219. Katz, O.; Ferguson, T.; Abbey, E.; Klose, S. J.; Prüfert, C.; Loock, H. P. Fluorescence Excitation-Emission-Matrix Imaging. *Analytical Chemistry* **2023**. doi: 10.1021/acs.analchem.3c00217.
220. Loock, H.-P.; Katz, O. Hadamard-Transform Fluorescence Excitation-Emission-Matrix Imaging Systems. US US 2023/0309834 A1, 2023.
221. Abbey, E.; Katz, O.; Ferguson, T.; Klose, S.-J.; Pruefert, C.; Loock, H.-P. Applications of Hadamard-Multiplexed Fluorescence Imaging using a Hyperspectral Camera. In *CLEO: Applications and Technology 2024*, Charlotte, North Carolina United States, 5–10 May 2024, 2024; Optica Publishing Group: p AM4A. 2. DOI: 10.1364/CLEO_AT.2024.AM4A.2.
222. Abbey, E. X.; Loock, H.-P. Hadamard-Multiplexed Multispectral Fluorescence Microscopy. In *2025 Conference on Lasers and Electro-Optics Europe & European Quantum Electronics Conference (CLEO/Europe-EQEC)*, Munich, Germany, 23-27 June 2025, 2025; IEEE: pp 1-1. DOI: 10.1109/CLEO/Europe-EQEC65582.2025.11110096.

223. Klose, S.-J.; Abbey, E.; Shahrestani, Y.; Ferguson, T.; Loock, H.-P. Fluorescence excitation-emission-matrix hyperspectral imaging for microscopy. In *Conference on Lasers and Electro-Optics/Pacific Rim 2024 (CLEO/PR 2024)*, Incheon Republic of Korea, 4–8 August 2024, 2024; IEEE: p We2G_3.
224. Mertz, J. *Introduction to optical microscopy*; Cambridge University Press, 2019.
225. Lichtman, J. W.; Conchello, J.-A. Fluorescence microscopy. *Nature Methods* **2005**, *2* (12), 910-919. doi: 10.1038/nmeth817.
226. Fish, K. N. Total Internal Reflection Fluorescence (TIRF) Microscopy. *Current Protocols* **2022**, *2* (8), e517. doi: 10.1002/cpz1.517.
227. Axelrod, D.; Long, J. C.; Davidson, M. W. *Evanescent Field Penetration Depth*. Evident Scientific, https://evidentscientific.com/en/microscope-resource/tutorials/tirf/penetration (accessed 2026.
228. Axelrod, D. Cell-substrate contacts illuminated by total internal reflection fluorescence. *Journal of Cell Biology* **1981**, *89* (1), 141-145. doi: 10.1083/jcb.89.1.141.
229. Stout, A. L.; Axelrod, D. Evanescent field excitation of fluorescence by epi-illumination microscopy. *Applied Optics* **1989**, *28* (24), 5237-5242. doi: 10.1364/AO.28.005237.
230. Zhu, S.; Yu, A. W.; Hawley, D.; Roy, R. Frustrated total internal reflection: A demonstration and review. *American Journal of Physics* **1986**, *54* (7), 601-607. doi: 10.1119/1.14514.
231. Vörös, Z.; Johnsen, R. A simple demonstration of frustrated total internal reflection. *American Journal of Physics* **2008**, *76* (8), 746-749. doi: 10.1119/1.2904473.
232. Tadros, T. F. *Emulsion formation, stability, and rheology*; Wiley-VCH Verlag GmbH & Co. KGaA, 2013. DOI: 10.1002/9783527647941.
233. Sharma, M. K.; Shah, D. O. *Introduction to macro-and microemulsions*; 1985.
234. Krstonošić, V.; Dokić, L.; Nikolić, I.; Milanović, M. Influence of xanthan gum on oil-in-water emulsion characteristics stabilized by OSA starch. *Food Hydrocolloids* **2015**, *45*, 9-17.
235. Taylor, P. Ostwald ripening in emulsions. *Advances in colloid and interface science* **1998**, *75* (2), 107-163.
236. Vengrenovitch, R. D. On the Ostwald ripening theory. *Acta metallurgica* **1982**, *30* (6), 1079-1086.
237. Kabalnov, A. Ostwald ripening and related phenomena. *Journal of Dispersion Science and Technology* **2001**, *22* (1), 1-12.
238. Koroleva, M. Y.; Yurtov, E. V. Effect of ionic strength of dispersed phase on Ostwald ripening in water-in-oil emulsions. *Colloid Journal* **2003**, *65* (1), 40-43.
239. Kent, P.; Saunders, B. R. The role of added electrolyte in the stabilization of inverse emulsions. *Journal of colloid and interface science* **2001**, *242* (2), 437-442.
240. Koroleva, M. Y.; Yurtov, E. V. Ostwald ripening in macro-and nanoemulsions. *Russian Chemical Reviews* **2021**, *90* (3), 293-323.
241. Tadros, T. F. Emulsion formation, stability, and rheology. *Emulsion formation and stability* **2013**, 1-75.
242. Friberg, S.; Jansson, P. O.; Cederberg, E. Surfactant association structure and emulsion stability. *Journal of Colloid and Interface Science* **1976**, *55* (3), 614-623.
243. *The HLB System: a time-saving guide to emulsifier selection*; ICI America, 1976.
244. Boyd, J.; Parkinson, C.; Sherman, P. Factors affecting emulsion stability, and the HLB concept. *Journal of Colloid and Interface Science* **1972**, *41* (2), 359-370.

245. Kopanichuk, I. V.; Vedenchuk, E. A.; Koneva, A. S.; Vanin, A. A. Structural properties of span 80/tween 80 reverse micelles by molecular dynamics simulations. *The Journal of Physical Chemistry B* **2018**, *122* (33), 8047-8055.
246. Aroca, R. *Surface-enhanced vibrational spectroscopy*; John Wiley & Sons, 2006.
247. Le Ru, E. C.; Etchegoin, P. G. Quantifying SERS enhancements. *MRS bulletin* **2013**, *38* (8), 631-640.
248. Shan, F.; Zhang, X.-Y.; Fu, X.-C.; Zhang, L.-J.; Su, D.; Wang, S.-J.; Wu, J.-Y.; Zhang, T. Investigation of simultaneously existed Raman scattering enhancement and inhibiting fluorescence using surface modified gold nanostars as SERS probes. *Scientific Reports* **2017**, *7* (1), 6813.
249. Fleischmann, M.; Hendra, P. J.; McQuillan, A. J. Raman spectra of pyridine adsorbed at a silver electrode. *Chemical physics letters* **1974**, *26* (2), 163-166.
250. Jeanmaire, D. L.; Van Duyne, R. P. Surface Raman spectroelectrochemistry: Part I. Heterocyclic, aromatic, and aliphatic amines adsorbed on the anodized silver electrode. *Journal of electroanalytical chemistry and interfacial electrochemistry* **1977**, *84* (1), 1-20.
251. Albrecht, M. G.; Creighton, J. A. Anomalously intense Raman spectra of pyridine at a silver electrode. *Journal of the american chemical society* **1977**, *99* (15), 5215-5217.
252. Xie, W.; Qiu, P.; Mao, C. Bio-imaging, detection and analysis by using nanostructures as SERS substrates. *Journal of materials chemistry* **2011**, *21* (14), 5190-5202.
253. Zheng, X.-S.; Jahn, I. J.; Weber, K.; Cialla-May, D.; Popp, J. Label-free SERS in biological and biomedical applications: Recent progress, current challenges and opportunities. *Spectrochimica Acta Part A: Molecular and Biomolecular Spectroscopy* **2018**, *197*, 56-77.
254. Zavaleta, C. L.; Smith, B. R.; Walton, I.; Doering, W.; Davis, G.; Shojaei, B.; Natan, M. J.; Gambhir, S. S. Multiplexed imaging of surface enhanced Raman scattering nanotags in living mice using noninvasive Raman spectroscopy. *Proceedings of the National Academy of Sciences* **2009**, *106* (32), 13511-13516.
255. Cialla, D.; Pollok, S.; Steinbrücker, C.; Weber, K.; Popp, J. SERS-based detection of biomolecules. *Nanophotonics* **2014**, *3* (6), 383-411.
256. Cheung, W.; Shadi, I. T.; Xu, Y.; Goodacre, R. Quantitative analysis of the banned food dye Sudan-1 using surface enhanced Raman scattering with multivariate chemometrics. *The Journal of Physical Chemistry C* **2010**, *114* (16), 7285-7290.
257. Xu, M.-L.; Gao, Y.; Han, X.-X.; Zhao, B. Innovative Application of SERS in Food Quality and Safety: A Brief Review of Recent Trends. *Foods* **2022**, *11* (14), 2097.
258. Jiang, L.; Hassan, M. M.; Ali, S.; Li, H.; Sheng, R.; Chen, Q. Evolving trends in SERS-based techniques for food quality and safety: A review. *Trends in Food Science & Technology* **2021**, *112*, 225-240.
259. Kneipp, K.; Wang, Y.; Kneipp, H.; Perelman, L. T.; Itzkan, I.; Dasari, R. R.; Feld, M. S. Single molecule detection using surface-enhanced Raman scattering (SERS). *Physical review letters* **1997**, *78* (9), 1667.
260. Lee, H. M.; Jin, S. M.; Kim, H. M.; Suh, Y. D. Single-molecule surface-enhanced Raman spectroscopy: a perspective on the current status. *Physical Chemistry Chemical Physics* **2013**, *15* (15), 5276-5287.

261. Li, L.; Hutter, T.; Steiner, U.; Mahajan, S. Single molecule SERS and detection of biomolecules with a single gold nanoparticle on a mirror junction. *Analyst* **2013**, *138* (16), 4574-4578.
262. Pilot, R.; Signorini, R.; Durante, C.; Orian, L.; Bhamidipati, M.; Fabris, L. A review on surface-enhanced Raman scattering. *Biosensors* **2019**, *9* (2), 57.
263. Langer, J.; Jimenez de Aberasturi, D.; Aizpurua, J.; Alvarez-Puebla, R. A.; Auguié, B.; Baumberg, J. J.; Bazan, G. C.; Bell, S. E.; Boisen, A.; Brolo, A. G. Present and future of surface-enhanced Raman scattering. *ACS nano* **2019**, *14* (1), 28-117.
264. Kim, J.; Jang, Y.; Kim, N.-J.; Kim, H.; Yi, G.-C.; Shin, Y.; Kim, M. H.; Yoon, S. Study of chemical enhancement mechanism in non-plasmonic surface enhanced Raman spectroscopy (SERS). *Frontiers in chemistry* **2019**, *7*, 582.
265. Giannini, V.; Rodríguez-Oliveros, R.; Sánchez-Gil, J. A. Surface plasmon resonances of metallic nanostars/nanoflowers for surface-enhanced Raman scattering. *Plasmonics* **2010**, *5*, 99-104.
266. Li, R.; Gao, L.; Wu, G.; Dong, J. Multiple marine algae identification based on three-dimensional fluorescence spectroscopy and multi-label convolutional neural network. *Spectrochimica Acta Part A: Molecular and Biomolecular Spectroscopy* **2024**, *311*, 123938. doi: 10.1016/j.saa.2024.123938.
267. Xu, R.-Z.; Cao, J.-S.; Feng, G.; Luo, J.-Y.; Feng, Q.; Ni, B.-J.; Fang, F. Fast identification of fluorescent components in three-dimensional excitation-emission matrix fluorescence spectra via deep learning. *Chemical Engineering Journal* **2022**, *430*, 132893. doi: 10.1016/j.cej.2021.132893.
268. Scott, S. M.; James, D.; Ali, Z.; O'Harea, W. T.; Rowell, F. J. Total luminescence spectroscopy with pattern recognition for classification of edible oils. *Analyst* **2003**, *128* (7), 966-973. doi: 10.1039/b303009a.
269. Harshman, R. A.; Lundy, M. E. PARAFAC: Parallel factor analysis. *Computational Statistics & Data Analysis* **1994**, *18*, 39-72. doi: 10.1016/0167-9473(94)90132-5.
270. Kolda, T. G.; Bader, B. W. Tensor Decompositions and Applications. *SIAM Rev.* **2009**, *51* (3), 455-500. doi: 10.1137/07070111x.
271. De Lathauwer, L.; De Moor, B.; Vandewalle, J. A Multilinear Singular Value Decomposition. *SIAM Journal on Matrix Analysis and Applications* **2000**, *21* (4), 1253-1278. doi: 10.1137/s0895479896305696.
272. Kompany-Zareh, M.; Akhlaghi, Y.; Bro, R. Tucker core consistency for validation of restricted Tucker3 models. *Analytica Chimica Acta* **2012**, *723*, 18-26. doi: 10.1016/j.aca.2012.02.028.
273. Kroonenberg, P. M. Three-mode principal component analysis illustrated with an example from attachment theory. In *Research methods for multi-mode data analysis*, H. G. Law, J. C., W. Snyder, J. A. Hattie & R. P. McDonald Ed.; Praeger, New York, 1986; pp 64-103.
274. Wise, B. M.; Gallagher, N. B.; Butler, S. W.; White, D. D.; Barna, G. G. A comparison of principal component analysis, multiway principal component analysis, trilinear decomposition and parallel factor analysis for fault detection in a semiconductor etch process. *Journal of Chemometrics* **1999**, *13* (3-4), 379-396. doi: 10.1002/(sici)1099-128x(199905/08)13:3/4<379::Aid-cem556>3.0.Co;2-n.
275. Anzai, H.; Joshi, N.; Fuyuki, M.; Wada, A. Fourier transform two-dimensional fluorescence excitation spectrometer by using tandem Fabry-Perot interferometer. *Review of Scientific Instruments* **2015**, *86* (1). doi: 10.1063/1.4905571.

276. Ferguson, T.; Loock, H.-P. Rapid Fluorescence EEM Spectroscopy Using Super-Cycle Hadamard-Transform Multiplexing. *Analytical Chemistry* **2023**. doi: 10.1021/acs.analchem.3c01245.
277. Thyrhaug, E.; Krause, S.; Perri, A.; Cerullo, G.; Polli, D.; Vosch, T.; Hauer, J. Single-molecule excitation–emission spectroscopy. *Proceedings of the National Academy of Sciences* **2019**, *116* (10), 4064-4069. doi: 10.1073/pnas.1808290116.
278. Decker, J. A., Jr.; Harwit, M. Experimental operation of a hadamard spectrometer. *Appl Opt* **1969**, *8* (12), 2552-2554. doi: 10.1364/ao.8.002552.
279. Decker, J. A. Experimental realization of the multiplex advantage with a Hadamard-transform spectrometer. *Applied Optics* **1971**, *10* (3), 510-514.
280. Ibbett, R. N. Digital Techniques in Measurement Instrumentation. *Measurement and Control* **1969**, *2*, T34 - T40.
281. Graff, D. K. Fourier- and Hadamard-transforms in spectroscopy. *Journal of Chemical Education* **1995**, *72* (4), 304-309. doi: 10.1021/ed072p304.
282. Harms, B. K.; Dyer, R. A.; Dyer, S. A.; Johnson, T. W.; Park, J. B. An introduction to hadamard spectrometry and the multiplex advantage. *IEEE Instrumentation and Measurement Technology Conference* **1989**, 434-437.
283. MacKinnon, N.; Stange, U.; Lane, P.; MacAulay, C.; Quatrevalet, M. Spectrally programmable light engine for in vitro or in vivo molecular imaging and spectroscopy. *Applied Optics* **2005**, *44* (11), 2033-2048. doi: 10.1364/ao.44.002033.
284. Mackinnon, N. B.; Macaulay, C. E.; Stange, U. Apparatus and methods relating to wavelength conditioning of illumination. United States 2004.
285. Ferguson, T. Hadamard-Transform Fluorescence Excitation-Emission-Matrix Spectroscopy: Rapid 3-Dimensional Fluorescence Data for Analytical and Industrial Applications. Queen's University, 2023.
286. Katz, O. G. Five-Dimensional Hadamard-Transform Fluorescence Imaging. University of Victoria, 2022.
287. Andrews, N. L. P. CHEMICAL SENSING USING THE LIFE, DEATH, AND REBIRTH OF A PHOTON. Queen's University, 2017.
288. Ferguson, T.; Bernicky, A.; Kozin, I.; Loock, H. HPLC-Detector Based on Hadamard-Transform Fluorescence Excitation-Emission-Matrix Spectroscopy. *Analytical Chemistry* **2021**, *93* (23), 8116-8121. doi: 10.1021/acs.analchem.1c01037.
289. Saleh, B. E. A.; Teich, M. C. *Fundamentals of Photonics*; John Wiley & Sons Inc., 1991.
290. Pereira, C.; Abreu, M.; Cabral, A.; Rebordão, J. M. Characterization of Light Diffraction by a Digital Micromirror Device. *Journal of Physics: Conference Series* **2022**, *2407* (1), 012048. doi: 10.1088/1742-6596/2407/1/012048.
291. Piotrowski, J.; Vorobiev, D.; Robberto, M.; Smee, S. *Optical diffraction simulation of a digital micromirror device*; SPIE, 2022.
292. Kearney, K.; Ninkov, Z. *Characterization of a digital micromirror device for use as an optical mask in imaging and spectroscopy*; SPIE, 1998.
293. Bernicky, A. THE ADVANCEMENT OF HADAMARD-TRANSFORM EXCITATION-EMISSION-MATRIX SPECTROSCOPY. Queen's University, 2020.
294. Sunada, T. Direct butt coupling type of LED module with multiple output fibers. *Electronics and Communications in Japan (Part II: Electronics)* **1989**, *72* (9), 39-47. doi: 10.1002/ecjb.4420720905.

295. Zimmermann, C. A.; Amouzou, K. N.; Ung, B. Recent advances in PDMS optical waveguides: Properties, fabrication, and applications. *Advanced Optical Materials* **2025**, *13* (1), 2401975.
296. Cai, Z.; Qiu, W.; Shao, G.; Wang, W. A new fabrication method for all-PDMS waveguides. *Sensors and Actuators A: Physical* **2013**, *204*, 44-47.
297. Amouzou, K. N.; Romero, A. A.; Sengupta, D.; Mishra, S. K.; Richard-Denis, A.; Mac-Thiong, J.-M.; Petit, Y.; Lina, J.-M.; Ung, B. Development of High Refractive Index Polydimethylsiloxane Waveguides Doped with Benzophenone via Solvent-Free Fabrication for Biomedical Pressure Sensing. *Photonics* **2022**, *9* (8), 557.
298. Prajzler, V.; Neruda, M.; Květoň, M. Flexible multimode optical elastomer waveguides. *Journal of Materials Science: Materials in Electronics* **2019**, *30* (18), 16983-16990.
299. Schneider, F.; Draheim, J.; Kamberger, R.; Wallrabe, U. Process and material properties of polydimethylsiloxane (PDMS) for Optical MEMS. *Sensors and Actuators A: Physical* **2009**, *151* (2), 95-99.
300. Hagen, N.; Tkaczyk, T. S. Compound prism design principles, I. *Applied Optics* **2011**, *50* (25), 4998-5011. doi: 10.1364/AO.50.004998.
301. Decker, J. A.; Harwitt, M. O. Sequential encoding with multislit spectrometers. *Applied optics* **1968**, *7* (11), 2205-2209.
302. Decker Jr, J. A. Hadamard-transform spectrometry. New analytical technique. *Analytical Chemistry* **1972**, *44* (2), 127A-134a.
303. Brayan, J. G.; Malcolme-Lawes, D. J.; Mew, C. D.; Xie, S. A Hadamard transform UV absorption detection for high performance liquid chromatography. Part I. Preliminary experiments. *Journal of Analytical Methods in Chemistry* **1995**, *17* (2), 257615. doi: 10.1155/S1463924695000137.
304. Ma, H.; Liu, X.; He, Q.; Chen, Y.; Qin, W. Theoretical Treatments for the Butt-Coupling Characteristics of Fibers. *International Journal of Optomechatronics* **2012**, *6* (1), 120-129. doi: 10.1080/15599612.2012.663461.
305. Sun, H. Laser Diode Beam Manipulations. In *A Practical Guide to Handling Laser Diode Beams*, Springer Netherlands, 2015; pp 53-104.
306. Kawano, K.; Mitomi, O. Coupling characteristics of laser diode to multimode fiber using separate lens methods. *Applied Optics* **1986**, *25* (1), 136-141. doi: 10.1364/AO.25.000136.
307. Best, G.; Sezerman, Ö. M. Shedding light on hybrid optics: A tutorial in coupling. *Optics and Photonics News* **1999**, *10* (2), 30-34.
308. Hempel, M.; La Mattina, F.; Tomm, J. W.; Zeimer, U.; Broennimann, R.; Elsaesser, T. Defect evolution during catastrophic optical damage of diode lasers. *Semiconductor Science and Technology* **2011**, *26* (7), 075020. doi: 10.1088/0268-1242/26/7/075020.
309. Hodgson, D.; Olsen, B. Protecting your laser diode. *ILX Lightwave Corporation* **2003**.
310. Muller, A. High-power diode laser spectrally narrowed with prism–etalon feedback. *Review of Scientific Instruments* **2024**, *95* (9). doi: 10.1063/5.0203666.
311. Safna Asiq, M. S.; Sam Emmanuel, W. R. Colour filter array demosaicking: a brief survey. *The Imaging Science Journal* **2018**, *66* (8), 502-512. doi: 10.1080/13682199.2018.1534388.
312. Hegyi, A.; Martini, J. Hyperspectral imaging with a liquid crystal polarization interferometer. *Optics Express* **2015**, *23* (22), 28742-28754. doi: 10.1364/OE.23.028742.

313. Hegyi, A. M., Joerg. Liquid Crystal Fourier Transform Imaging Spectrometer. United States US 10,250,823 B2, 2019.
314. Milston, R.; Madigan, M. C.; Sebag, J. Vitreous floaters: Etiology, diagnostics, and management. *Survey of Ophthalmology* **2016**, *61* (2), 211-227. doi: 10.1016/j.survophthal.2015.11.008.
315. Thyng, K. M.; Greene, C. A.; Hetland, R. D.; Zimmerle, H. M.; DiMarco, S. F. True colors of oceanography: Guidelines for effective and accurate colormap selection. *Oceanography* **2016**, *29* (3), 9-13.
316. Crameri, F. Scientific Colour Maps. Zenodo: 2019.
317. Crameri, F. Geodynamic diagnostics, scientific visualisation and StagLab 3.0. *Geoscientific Model Development* **2018**, *11* (6), 2541-2562.
318. Xue, D.; Pan, F. MATLAB Functions Programming. In *MATLAB and Simulink in Action: Programming, Scientific Computing and Simulation*, Springer Nature Singapore, 2024; pp 73-97.
319. Chen, H.; Krolik, A.; Lavoie, E.; Hendren, L. Automatic Vectorization for MATLAB. Cham, 2017; Springer International Publishing: pp 171-187.
320. Wünsch, U.; Esmaeeli, A.; Murphy, K.; Bro, R. *drEEM toolbox version 2*; 2025. DOI: 10.5281/zenodo.17182160.
321. *The N-way Toolbox*; 2026. https://www.mathworks.com/matlabcentral/fileexchange/1088-the-n-way-toolbox (accessed.
322. *Spectrum [Rhodamine 6G]*. AAT Bioquest Inc., 2026. https://www.aatbio.com/fluorescence-excitation-emission-spectrum-graph-viewer/rhodamine_6g (accessed 2026 March 9).
323. *Spectrum [Rhodamine B]*. AAT Bioquest Inc., 2026. https://www.aatbio.com/fluorescence-excitation-emission-spectrum-graph-viewer/rhodamine_b (accessed 2026 March 9).
324. *Spectrum [Rhodamine 110]*. AAT Bioquest Inc., 2026. https://www.aatbio.com/fluorescence-excitation-emission-spectrum-graph-viewer/rhodamine_110 (accessed 2026 March 9).
325. *Spectrum [Sulforhodamine 101]*. AAT Bioquest Inc., 2026. https://www.aatbio.com/fluorescence-excitation-emission-spectrum-graph-viewer/sulforhodamine_101 (accessed 2026 March 9).
326. Chernick, E. T.; Abdollahi, M. F.; Tabasi, Z. A.; Junge, M. J.; Zhao, Y. Study of a carbazole–bromobenzothiadiazole derived fluorescent molecular rotor: crystal structure, redox activity, and solvatofluorochromic effects. *New Journal of Chemistry* **2022**, *46* (2), 572-581. doi: 10.1039/D1NJ04274B.
327. Joulaei-Zonouz, S. Excitation Emission Matrix (EEM) Spectroscopy and Computational Evaluation of Excited States of Carbazole – Bromobenzothiadiazole (CBB). University of Victoria, 2023.
328. Hong, Y.; Lam, J. W. Y.; Tang, B. Z. Aggregation-induced emission. *Chemical Society Reviews* **2011**, *40* (11), 5361-5388. doi: 10.1039/C1CS15113D.
329. Bernicky, A. THROUGH THE FIRE AND FLAMES: Characterization of Solid Samples with Flame Emission Spectroscopy and Artificial Neural Networks. Queen's University, 2024.
330. Bernicky, A.; Davis, B.; Barnes, J.; Loock, H.-P. Spectroscopic characterisation of feedstock for copper smelters by machine-learning. *Canadian Metallurgical Quarterly* **2024**, *63* (2), 576-585. doi: 10.1080/00084433.2023.2215013.

331. Timofte, R.; Gu, S.; Wu, J.; Van Gool, L. Ntire 2018 challenge on single image super-resolution: Methods and results. In *Proceedings of the IEEE conference on computer vision and pattern recognition workshops*, 2018; pp 852-863.
332. Arad, B.; Timofte, R.; Ben-Shahar, O.; Lin, Y.-T.; Finlayson, G. D. Ntire 2020 challenge on spectral reconstruction from an rgb image. In *Proceedings of the IEEE/CVF conference on computer vision and pattern recognition workshops*, 2020; pp 446-447.
333. Zhang, J.; Su, R.; Fu, Q.; Ren, W.; Heide, F.; Nie, Y. A survey on computational spectral reconstruction methods from RGB to hyperspectral imaging. *Scientific Reports* **2022**, *12* (1), 11905. doi: 10.1038/s41598-022-16223-1.
334. Hermann, M.; Agrawal, P.; Koch, I.; Oleschuk, R. Organic-free, versatile sessile droplet microfluidic device for chemical separation using an aqueous two-phase system. *Lab on a Chip* **2019**, *19* (4), 654-664. doi: 10.1039/C8LC01121D.
335. Garcia-Leis, A.; Garcia-Ramos, J. V.; Sanchez-Cortes, S. Silver nanostars with high SERS performance. *The Journal of Physical Chemistry C* **2013**, *117* (15), 7791-7795.
336. Auguié, B.; Darby, B. L.; Le Ru, E. C. Electromagnetic interactions of dye molecules surrounding a nanosphere. *Nanoscale* **2019**, *11* (25), 12177-12187.
337. Watanabe, H.; Hayazawa, N.; Inouye, Y.; Kawata, S. DFT vibrational calculations of rhodamine 6G adsorbed on silver: analysis of tip-enhanced Raman spectroscopy. *The Journal of Physical Chemistry B* **2005**, *109* (11), 5012-5020.
338. Kristensson, E.; Ehn, A.; Berrocal, E. High dynamic spectroscopy using a digital micromirror device and periodic shadowing. *Optics Express* **2017**, *25* (1), 212-222. doi: 10.1364/OE.25.000212.
339. Sinjab, F.; Liao, Z.; Notingher, I. Applications of Spatial Light Modulators in Raman Spectroscopy. *Applied Spectroscopy* **2019**, *73* (7), 727-746. doi: 10.1364/AS.73.000727.
340. Li, Z.; Borggren, J.; Berrocal, E.; Ehn, A.; Aldén, M.; Richter, M.; Kristensson, E. Simultaneous multispectral imaging of flame species using Frequency Recognition Algorithm for Multiple Exposures (FRAME). *Combustion and Flame* **2018**, *192*, 160-169. doi: 10.1016/j.combustflame.2018.02.009.

Appendices

A.1 SNR Calculation for Hadamard-Multiplexed *versus* All-but-One Illumination.

Signal-to-noise ratio (SNR) was calculated for emission spectra acquired at various illumination wavelengths, using multiplexed (Hadamard matrix size 31) and all-but-one (30 out of 31 wavelengths illuminated). SNR was calculated using the root-mean-squared version, shown below.

$$SNR = \frac{S}{N} = \frac{S_{\max} - S_{\text{background}}}{N_{\text{rms,background}}}$$

$$N_{\text{rms,background}} = \sqrt{\frac{\sum_i^n (S_i - \bar{S})^2}{n}}$$

The result of this calculation is referenced in Section 2.1.3. The MATLAB code used to demultiplex each set of spectra is shown below.

```
load(strcat(filepath,"231127_RB_50ms_31m_Hadamard.mat"));
Exwave = RawEEM(1,2:end)';
Emwave = RawEEM(2:end,1);
nEx = length(Exwave);
nEm = length(Emwave);
F = Spec(:,3:nEx+2)-Spec(:,2);

% Demultiplex for Hadamard-Multiplexed Illumination
H = paleyI(nEx+1);
H=H(2:end,2:end);
H(H==1)=0;
H(H==-1)=1;
H = H^-1;
H=H';
M=F*H;
M(M<0)=0;
dmSpec = M;
F(F<0)=0;

% Demultiplex for All-but-One Illumination
allButOne = ones(nEx,nEx);
for n = 1:nEx
    allButOne (n,n) = 0;
end
allButOne = allButOne;
allButOne = allButOne ^-1;
M=F* allButOne;
M(M<0)=0;
dmSpec = M;
F(F<0)=0;

% Calculate SNR
meanspec = mean(dmSpec,2);
meanrms = rms(meanspec(1250:end-10))
snrH = (max(meanspec,[],'all')-mean(meanspec(1250:end-10),1))/meanrms
```

A.2 Arduino Control of Laser Diode Array

Laser diodes are attached to an Arduino Uno board through digital input/output (I/O) pins, and the board is connected to the desktop computer via USB as described in Section 3.3.3. MATLAB communicates with the Arduino board via serial communication, so a COM port (COM4) is opened at 9600 baud rate, and the terminator is configured to "CR" to match the style used by the Arduino compiler. The pins of the Arduino are programmed to send a ±5 V pulse, which trigger the laser drivers to turn that laser on or off. This code is written in the Arduino Integrated Development Environment which compiles in C++, and a simple portion of that code is shown here. Based on the code uploaded to the Arduino board, the commands to turn one or a group of lasers on is hardcoded, and should be called by "name", such as "l1" for the first laser (405 nm), or "m1" for the first mask in a Hadamard-multiplexed setup.

```
int myTimeout = 1000;
#define LD1 4  % define the pin numbers on Arduino Uno board each laser diode is connected to
...
#define LD7 12
#define en 3
const byte numChars = 32;
char receivedChars[numChars];

boolean newData = false;

void setup() {
    Serial.begin(9600);  % begin serial communication with baud rate 9600
    Serial.println("<Arduino is ready>");
    pinMode(LD1,OUTPUT); % define laser diode pins as outputs
    ...
    pinMode(LD7,OUTPUT);
    pinMode(en, INPUT);
    Serial.setTimeout(myTimeout); % set a time limit on response
}
void loop() {
    recvWithStartEndMarkers(); % communication received (such as a command to turn a laser on)
    showNewData(); % display that command sent
}
% receive communication - specify format
void recvWithStartEndMarkers() {
    static boolean recvInProgress = false;
    static byte ndx = 0;
    char startMarker = '<';
    char endMarker = '>';
    char rc;

    while (Serial.available() > 0 && newData == false) {
        rc = Serial.read();

        if (recvInProgress == true) {
            if (rc != endMarker) {
                receivedChars[ndx] = rc;
                ndx++;
                if (ndx >= numChars) {
                    ndx = numChars - 1;
                }
            }
            else {
                receivedChars[ndx] = '\0'; // terminate the string
                recvInProgress = false;
```

```
                ndx = 0;
                newData = true;
            }
        }
        else if (rc == startMarker) {
            recvInProgress = true;
        }
    }
}

void showNewData() {
    if (newData == true) {
        if (strcmp(receivedChars,"l1") == 0) { % when command "l1" is received (L1 = laser1)
          digitalWrite(LD1,HIGH); % turn LD1 on high (signal laser board to turn on)
          ...
          digitalWrite(LD7,LOW); % turn all other laser diodes off (low signal)
        }
        ... % repeat for all other single laser diodes to turn on
        % turn on a Hadamard mask of laser diodes ("m1" to "m7" for size-7 Hadamard matrix)
        else if (strcmp(receivedChars,"m1") == 0) {
          digitalWrite(LD1,HIGH);
          digitalWrite(LD2,LOW);
          digitalWrite(LD3,LOW);
          digitalWrite(LD4,HIGH);
          digitalWrite(LD5,LOW);
          digitalWrite(LD6,HIGH);
          digitalWrite(LD7,HIGH);
        }
      ... % repeat for all other masks and an "all on" mask
      % turn off all lasers

      else if (strcmp(receivedChars,"off") == 0) {
          Serial.println("off confirmed");
          digitalWrite(LD1,LOW);
          digitalWrite(LD2,LOW);
          digitalWrite(LD3,LOW);
          digitalWrite(LD4,LOW);
          digitalWrite(LD5,LOW);
          digitalWrite(LD6,LOW);
          digitalWrite(LD7,LOW);
        }
      newData = false;
    }
}
```

A.3 Laser Diode Array Integration in MATLAB

For MATLAB to communicate with the Arduino board, the "writeline" command is used. This example shows the way the lasers are turned on in a very simple control interface, made using MATLAB's AppDesigner.

```
a = serialport("COM4",9600);    % connect arduino
a.configureTerminator("CR");    % connect arduino (line terminator)
wavelengthChoices = ["408 nm" "450 nm" "488 nm" "505 nm" "515 nm" "638 nm" "658 nm" "All"];
laserChoices = ["<l1>" "<l2>" "<l3>" "<l4>" "<l5>" "<l6>" "<l7>" "<all>"];
i = matches(wavelengthChoices,Value); % creates logical array, matching string = 1
choice = laserChoices(i); % maps the logical array onto the string array of wavelength choices,
leaving only the value with "1" remaining
a.writeline(choice); % turns on the wavelength chosen
```

The laser diode array programmable light source is described in detail in Section 3.3

A.4 Multispectral Camera Image Acquisition Loop using DMA-PLS

The multispectral camera, MSC, is synchronized with the digital micromirror array programmable light source, DMA-PLS, using MATLAB code. The system is described in detail in Section 4.1.

```
campic = zeros(2048,2048,nEx+1,nAvg,'uint8');
spec = zeros(2048,nEx+2,nAvg);
for a = 1:nAverage
    for b = 1:nEx+1
        frameacquired = false;  % set flag to false (global variable)
        AlpProjStartError = calllib('alpV42','AlpProjStart',app.DevId,b); % call next sequence
(next mask) on DMD
        assert(AlpProjStartError == 0,'Display of Next Mask on DMD Failed'); % check mask
displayed
        app.cam.SoftTrigger; % trigger camera
        if useSpectrometerCheck == 1
            spectrometer('measure',1); % trigger spectrometer (won't continue until done)
            spec(:,b+1,a) = spectrometer('getdata');
        end
        k = 0;
        while ~frameacquired % waits for frameacquired to be true (a different script)
            pause(0.01); k = k+1;
        end
        pause(0.02); % required time to transfer image from buffer to camera
        campic(:,:,b,a) = data; % data is global variable, declared when a frame has been
acquired
        if b > 1 && (isequal(campic(:,:,b,a),campic(:,:,b-1,a)) | all(all(campic(:,:,b,a) == 0)))
            % stop camera acquisition if images are equal or equal to zero
            app.cam.set('Acquire',false);
            app.cam.unregisterallevents();
            app.cam.Trigger=false;
            app.cam.set('AcquisitionMode','Continuous');
            error('Data exactly matches previous data or is zeros') % error will halt loop
        end
        projwaiterror = calllib('alpV42','AlpProjWait',app.DevId);
    end
end

function frameAcquired(varargin)
% sets frameready = true when ready
% data is a global variable declared outside function, can access it once it has successfully
% grabbed the image

global frameacquired
global data
cam = varargin{1}[334];
data = cam.GetRawData(); % tries to get raw data, if it fails, the loop calling it will try again
frameacquired = true;

end
```

A.5 Multispectral Camera Image Acquisition Loop using Laser Diode Array

The multispectral camera, MSC, is also synchronized with the laser diode array programmable light source, LDA-PLS, using MATLAB code. The system is described in more detail in Section 4.1.

```
campic = zeros(2048,2048,nEx+1,nAvg,'uint8');
spec = zeros(2048,nEx+2,nAvg);
for a = 1:nAverage
    for b = 1:nEx+1
        frameacquired = false; % set flag to false (global variable)
        ard.writeline(hadamard{b}[229, 327]); % call next mask
        pause(0.01) % have to have at least 0.005 (5 ms) for command
        app.cam.SoftTrigger; % trigger camera
        if useSpectrometerCheck == 1
            spectrometer('measure',1); % trigger spectrometer (won't continue until done)
            spec(:,b+1,a) = spectrometer('getdata');
        end
        k = 0;
        while ~frameacquired % waits for frameacquired to be true (a different script)
            pause(0.01); k = k+1;
        end
        pause(0.02); % required time to transfer image from buffer to camera
        campic(:,:,b,a) = data; % data is global variable, declared when a frame has been
acquired
    end
    app.a.writeline('<off>');

end
```

A.6 Multispectral Camera Image using DMA-PLS Timing

These diagrams illustrate the triggering sequence and the time delays required to synchronize the two different cameras (MSC and HSC) with either of the two light sources (DMA-PLS or LDA-PLS). This programs which use these sequences are described in Section 4.1.2 and 4.2.3.

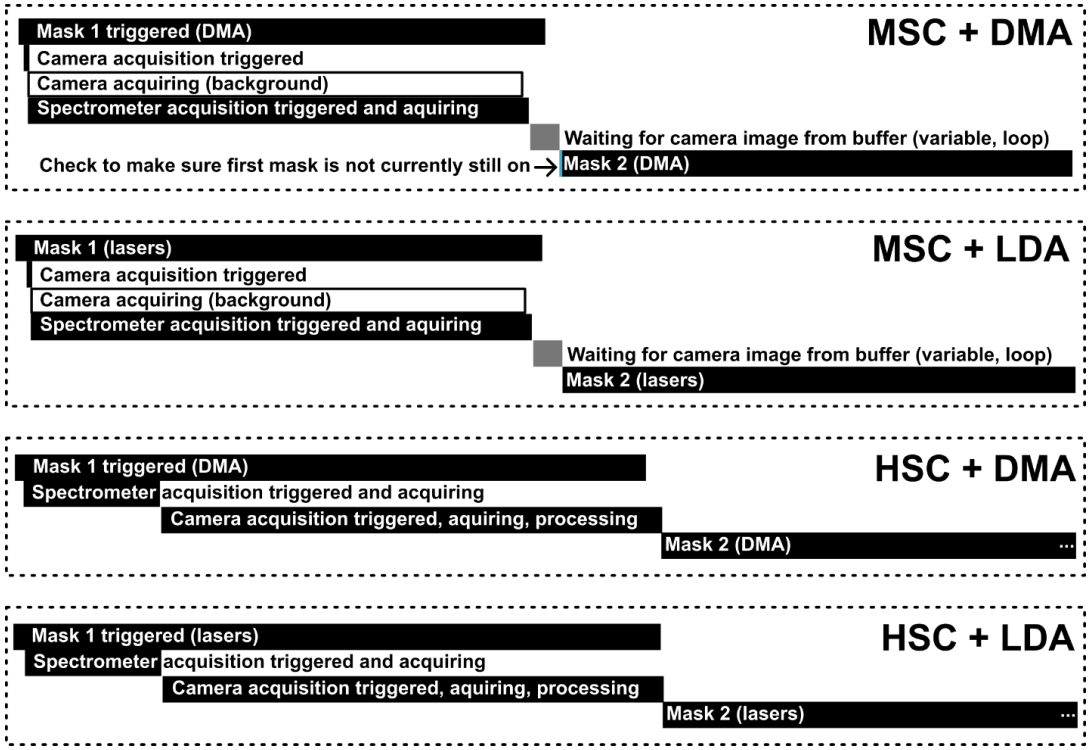

A pause of at least 0.005 seconds (5 milliseconds) is required for the communication from MATLAB through the Arduino to turn the lasers on, this is done using pause(0.01). Flipping mirrors on the DMA takes 44 microseconds and the communication time requires a short pause as well, so that the light source is illuminating the sample for the entire exposure time.

The spectrometer (Avantes) is triggered to acquire spectra and will pause the execution of further tasks until complete. This is used to pause for the correct integration time using the MSC and is done before image acquisition using the HSC. The MSC does not pause the program, a second command “GetRawData” is required to pull the data from the MSC after an image acquisition. This is done in a frameAcquired loop described in 0 and 0. The HSC pauses execution of other actions until it has finished acquiring and processing the data. The data processing time is approximately 1.2 seconds, so the DMA is set to illuminate for 0.5 seconds less than the acquisition time, to ensure illumination the entire time, as well as to ensure it has finished illuminating before the next mask is set to start.

A.7 Hyperspectral Camera Connection and Data Format Solution.

The following code describes a solution to obtain non-normalized uint16 data in place of the uint8 data, using the BaySpec GoldenEye™ camera with the developer-supplied SDK. The context for this is described in Section 4.2.3 (page 106).

```
app.pe=pyenv(Version='3.10'); % create python environment

% check if path is already in py.sys.path, if not, adds at index 0 (front)
PathforPyScripts = 'C:\Users\Laser Lab\Documents\loocklab_Hadamard\BaySpecSDK';
if count(py.sys.path,PathforPyScripts) == 0
    insert(py.sys.path,int32(0),PathforPyScripts); end

% set current directory as a folder containing xiapi64.dll
maindir = 'C:\Users\Laser Lab\Documents\loocklab_Hadamard'; % saving the current path
cd('C:\Users\Laser Lab\Documents\loocklab_Hadamard\BaySpecSDK') % set directory as SDK

% import python module for the camera settings and acquisition settings
setup_acquisition = py.importlib.import_module('setup_acquisition');

% reassign python classes imported from the module
MyCamera = setup_acquisition.MyCamera;
Setup_acquire = setup_acquisition.Setup_acquire;

% reassign the class for the acquisition settings
camfun = Setup_acquire();
app.camfun = camfun; % set camfun app variable for later use

cam_0 = MyCamera(); % camera identifier (connection to the camera)

cam_0.bit_depth = py.int(16); % set bit depth to uint16 (otherwise auto to uint8)

% set app properties for image acquisition
app.wavelengths_in.Value = app.np.linspace(int16(400),int16(1100),int16(141));
app.cam_0 = cam_0;

cd(maindir) % restore path previous folder (before GetCamImage)
[band_images,cube_info,calibrated_wavelengths] = GetCamImage(app,app.np, ...
    app.camfun,py.bool(app.ExternalTrigger.Value)); % acquire an image
```

A.8 Hyperspectral Camera Image Acquisition Loop using Programmable Light Source

The following code is used to acquire an image using the hyperspectral camera with excitation-modulated illumination by one of the two light sources (DMA-PLS or LDA-PLS). The relevant context for this code is described in Section 4.2.3.

```
size_temp=size(app.band_images.Value);
band_images_temp=zeros(size_temp(1,1),size_temp(1,2),size_temp(1,3),nAvg);
h = waitbar(0,'Acquiring Images...');
for j = 1:nAvg
    for i = 1:nEx+1
        AlpProjStartError = calllib('alpV42','AlpProjStart',DevId,i); % turns on next mask
            OR
        ard.writeline(hadamardmask{i}330); % turns on next mask

        spectrometer('measure',1);
        Spec(:,i+1) = spectrometer('getdata');
        pause(0.03)
        [band_images,cube_info,calib_wavelengths] = GetCamImage(app,np,camfun,Ext_trig);
        baypic(:,:,:,i,j) = band_images;
    end
end

[band_images,cube_info,calib_wavelengths,enviheaderinfo] = GetCamImage(app,np,camfun,Ext_trig)

if exist('C:\Users\Laser Lab\Documents\loocklab_Hadamard\BaySpecCamera\output.txt','file')
    delete('C:\Users\Laser Lab\Documents\loocklab_Hadamard\BaySpecCamera\output.txt');
end

%get camera image
diary('C:\Users\Laser Lab\Documents\loocklab_Hadamard\BaySpecCamera\output.txt');
res=cell(camfun.acquire_cube(Ext_trig));
diary off;

%read the output file constantly and stop reading, as soon as the data caputure complete.
while true
    fid = fopen('C:\Users\Laser Lab\Documents\loocklab_Hadamard\BaySpecCamera\output.txt','r');
    if fid > 0
        output=fread(fid,'*char')';
        fclose(fid);
    else
        disp('No file could be read.');
    end

    if contains(output,'Data capture complete')
        break
    end
end

%transform to MATLAB workspace variables
enviheaderinfo = res{1,1}334;
app.enviInfo = enviheaderinfo;
cube_information = cube_info_Struct(res{1,1});
app.cube_information.Value = cube_information;
calibrated_wavelengths=double(res{1,3});

%reshape images for bands
band_images_raw = np.ascontiguousarray(res{1,2}); %extract raw output from python image
acquisition
band_images1=double(band_images_raw); %transform raw data to a format usable by Matlab
band_images=flip(permute(band_images1,[3 2 1]),2); %rearrange to x,y,wl (image is flipped)
assignin('base','ImData',band_images);
```

A.9 Code to Open a Binary Image File

The following code is that which is used to open an image acquired with the MSC or HSC which was saved as a binary file. Saving the images in binary (.bin) format is described in Section 5.1.1. Here, the "campic" (image variable) dimensions are required to reshape the one-dimensional binary image into the correct dimensions. These are saved in a separate variable called "camSettings" in the folder containing the "campic" variable, with the same file name, with "_camSettings.mat" replacing the "_campic.bin" from the binary image file.

```
campicID = fopen([filePath fileName]);
campic = fread(campicID);
campic = reshape(campic,camSettings.campicDim);
fclose(campicID)
```

A.10 Code for Finding an EEM Centroid

The following code is that contained in a function used to find the centroid of an excitation-emission matrix (EEM). The MATLAB function I wrote with Dr. Swapnil Daxini is called *findCentroid*. The function accepts the excitation (*EX*) and emission (*EM*) wavelengths, or linearly increasing integers of the same length, and the EEM (*Z*). The function outputs the x and y values of the maximum of a specified percentage of the EEM, for example an input of 0.7 would find a centroid of the top 30% of the peak. This code is used throughout the dissertation to find the centroids of F-EEMs.

```
[x,y] = meshgrid(EX,EM);
exEm = [];

for k = 1:numComponents
    zmax = regionprops3(true(size(Z)),Z, "MaxIntensity"); % max of Z
    zmax = table2array(zmax); % puts maximum in readable format

    sum_numerator_ex = 0;
    sum_numerator_em = 0;
    sum_denom = 0;

    for i = 1:length(EX)
        for j = 1:length(EM)
            if Z(j, i) > zmax*peakCutoff
                sum_numerator_ex = sum_numerator_ex + EX(i)*Z(j, i);
                sum_numerator_em = sum_numerator_em + EM(j)*Z(j, i);
                sum_denom = sum_denom + Z(j, i);
            end
        end
    end

    cen_ex = sum_numerator_ex/sum_denom;
    cen_em = sum_numerator_em/sum_denom;

    EXEM = [cen_ex cen_em];
    exEm = [exEm; EXEM];
    peakCutoff = peakCutoff;
end

for i = 1:length(EX)
    for j = 1:length(EM)
        if Z(j, i) > zmax*peakCutoff
            sum_numerator_ex = sum_numerator_ex + EX(i)*Z(j, i);
            sum_numerator_em = sum_numerator_em + EM(j)*Z(j, i);
            sum_denom = sum_denom + Z(j, i);
        end
    end
end

cen_ex = sum_numerator_ex/sum_denom;
cen_em = sum_numerator_em/sum_denom;

EXEM = [cen_ex cen_em];
exEm = [exEm; EXEM];
peakCutoff = peakCutoff;
```

A.11 Peak Accuracy of Hyperspectral Camera using the DMA-PLS

To test the BaySpec GoldenEye™ hyperspectral camera, HSC, we recorded the reflected image of light from a business card. The reflection spectrum was generated by the DMA-PLS and recorded sequentially using the HSC. A vertical line at the expected wavelength is observed in each spectrum corresponding to the selected wavelength. This demonstrates that the camera can detect single wavelengths accurately within the spectral range of 460–629 nm. Three of these plots are shown in Figure 4.6 and the data are described in Section 4.2.2.

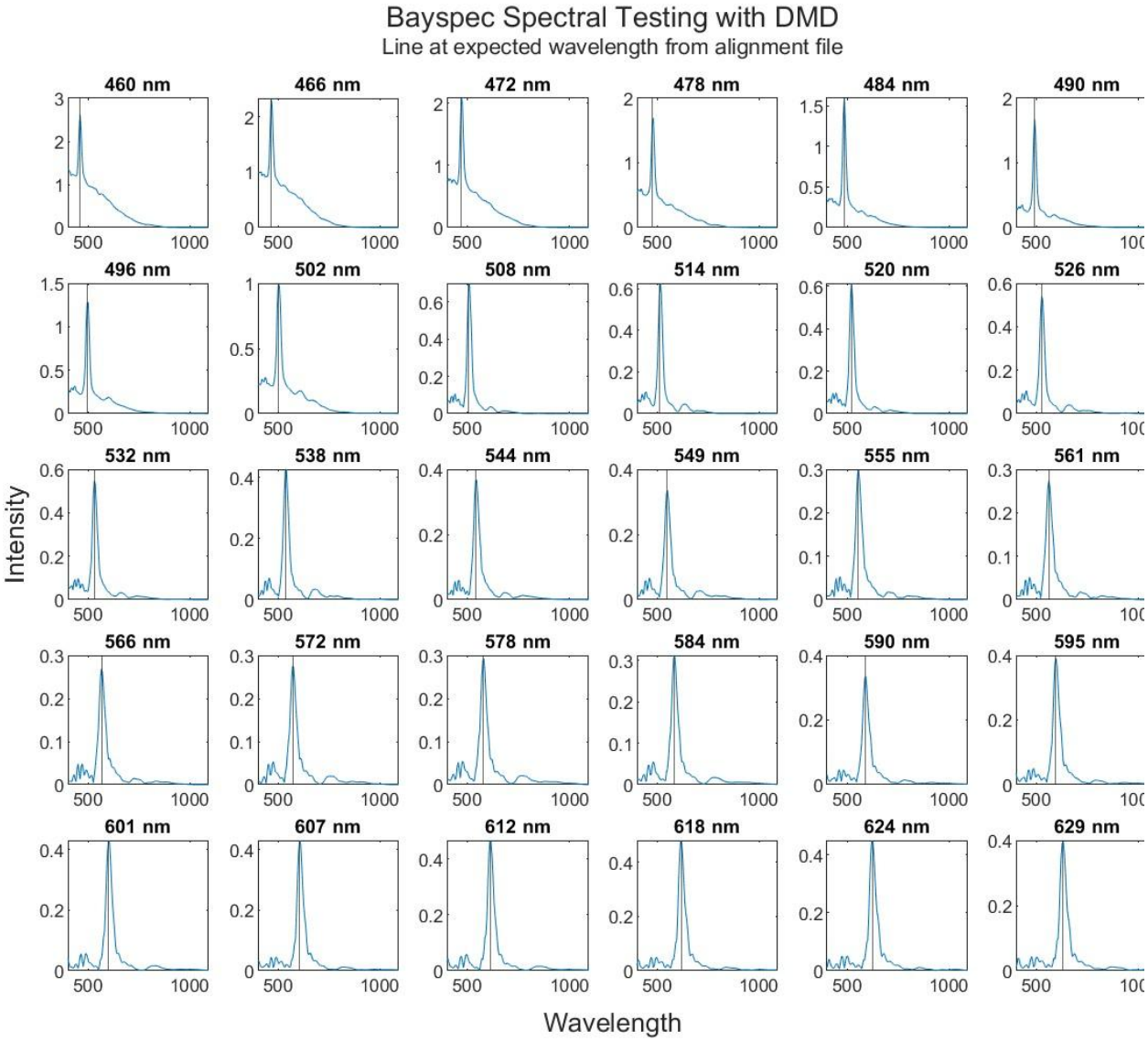

A.12 BaySpec Hyperspectral Camera Image Acquisition Timing Values

The timing values used in Figure 4.7 are shown in the following two tables, to characterize the expected and measured acquisition times of the BaySpec GoldenEye™ hyperspectral camera (HSC), described in Section 4.2.2.

Table A.1. Expected and measured acquisition times of the BaySpec GoldenEye™ HSC using the Python SDK through MATLAB.

Chosen Acquisition Time (ms)	# Frames	Expected Time (s)	Image Acquired (Python Readout, Automatic) (s)			Average Total Acquisition Time (s)	StDev Acquisition Time (s)
1	200	0.2	2.27148	2.256745	2.24409	2.26	0.01
2	200	0.4	2.212309	2.244441	2.281371	2.25	0.03
5	200	1	2.807097	2.920155	2.82835	2.85	0.06
10	200	2	3.74649	3.846608	3.813144	3.80	0.05
15	200	3	4.382243	4.365458	4.424721	4.39	0.03
30	200	6	7.229927	7.285986	7.25399	7.26	0.03
50	200	10	7.219462	7.320714	7.162369	7.23	0.08
70	200	14	7.337394	7.407582	7.206968	7.32	0.10
95	200	19	7.225232	7.273921	7.348736	7.28	0.06
100	200	20	7.202803	7.203716	7.289597	7.23	0.05

Table A.2. Expected and measured acquisition times of the BaySpec GoldenEye™ HSC using the GoldenEye™ software.

Chosen Acquisition Time (ms)	# Frames	Expected Time (s)	Total Acquisition Time (s)			Avg. Total Acquisition Time (s)	StDev Acquisition Time (s)
1	200	0.2	-	-	-	-	-
2	200	0.4	2.55	2.58	2.64	2.59	0.05
5	200	1	3.18	3.27	3.23	3.23	0.05
10	200	2	4.21	4.22	4.37	4.27	0.09
15	200	3	5.19	5.09	5.19	5.16	0.06
30	200	6	8.33	8.28	8.19	8.27	0.07
50	200	10	12.17	12.12	12.15	12.15	0.03
55	200	11	-	-	-	-	-
60	200	12	-	-	-	-	-
70	200	14	3.33	3.16	3.13	3.21	0.11
80	200	16	5.07	5.19	5.18	5.15	0.07
90	200	18	7.14	6.99	7.22	7.12	0.12
95	200	19	8.58	8.27	7.94	8.26	0.32
100	200	20	9.64	9.14	9.07	9.28	0.31

A.13 Characterization of the Laser-Driven Plasma Source used as a White-Light Source with the Digital Micromirror Array-Based Programmable Source

31 masks were illuminated sequentially using the DMA-PLS and directed to a photodetector and then to a spectrometer. A calibrated spectrometer was used to measure the center wavelength of the illuminated wavelength band, shown in the left column. A photodetector measured the power (shown in microwatts μW) in voltage, and a correction was done using the power meter reader for the responsivity at each of the set wavelengths to provide a value in watts. The full width at half-maximum (FWHM) of each wavelength band was measured from the spectrometer data for each wavelength band. The power in μW/nm was calculated by dividing the power in μW by the FWHM in nanometers (nm).

Table A.3. Measured properties of the DMA-PLS using the LDPS as the white light source.

Wavelength (nm)	**Power (μW)**	**FWHM (nm)**	**Power (μW/nm)**
468	11.6	3.62	**3.21**
475	12.9	3.62	**3.57**
482	12.4	3.9	**3.18**
489	12.4	3.9	**3.18**
497	12.1	3.62	**3.34**
504	11.6	3.62	**3.21**
511	11.3	3.62	**3.12**
518	11.5	3.9	**2.95**
525	11.3	3.9	**2.9**
532	11.4	3.34	**3.41**
540	11.2	3.62	**3.1**
547	10.9	4.48	**2.44**
560	9.8	4.49	**2.18**
567	9.3	4.77	**1.95**
574	9	4.21	**2.14**
581	8.6	4.63	**1.86**
588	8.1	4.92	**1.65**
594	8	5.21	**1.54**
601	7.7	4.92	**1.56**
608	7.4	4.92	**1.5**
615	7.2	5.5	**1.31**
622	6.8	5.79	**1.17**
628	6.7	5.5	**1.22**
635	6.5	5.5	**1.18**

A.14 Control Board for Laser Diode Array

The following pages contain the electronic diagrams for the laser diode driver board, designed by Nick Braam at the UVic Physics & Astronomy Electronics Shop, described in Section 3.3.3.

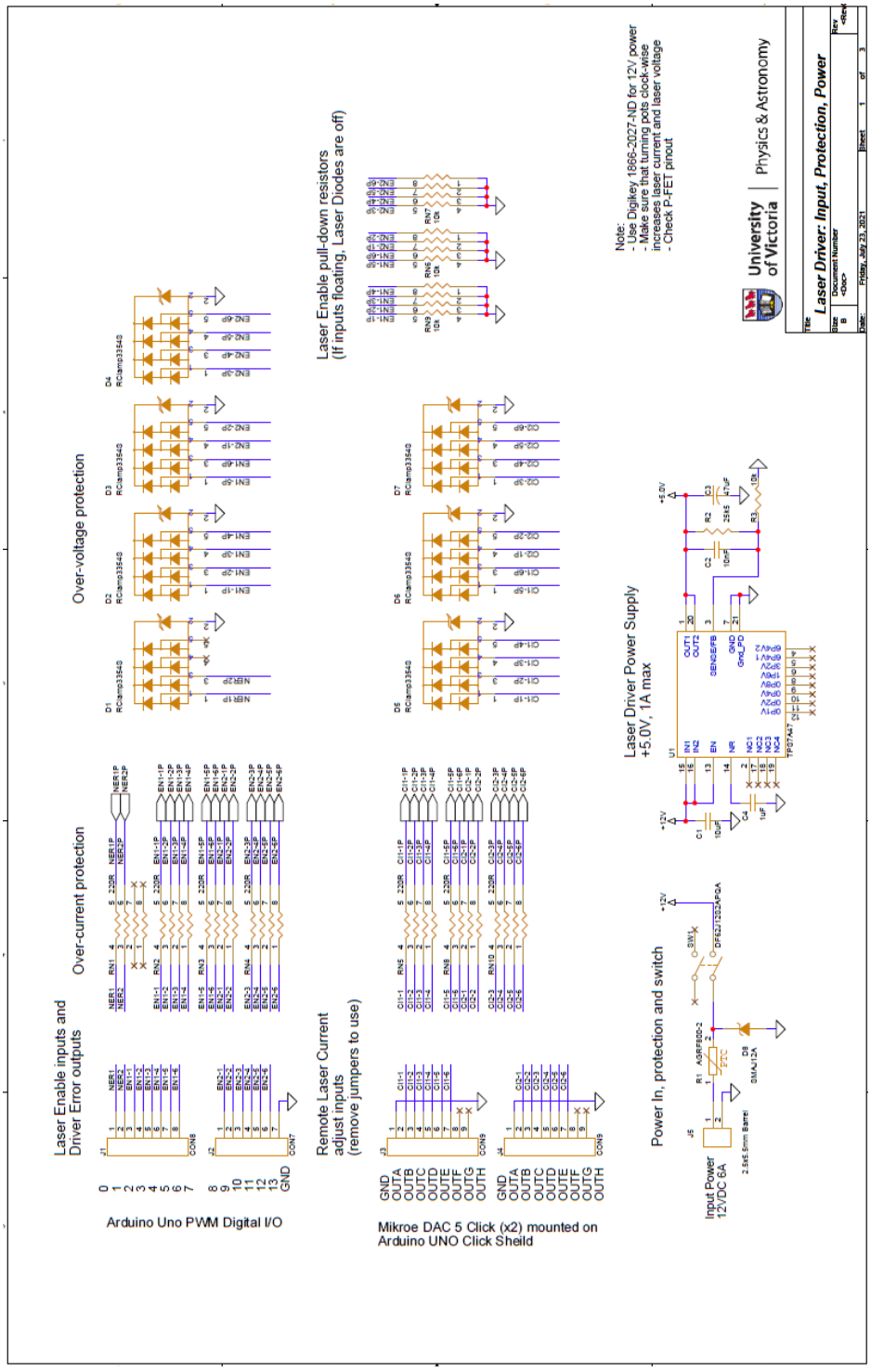

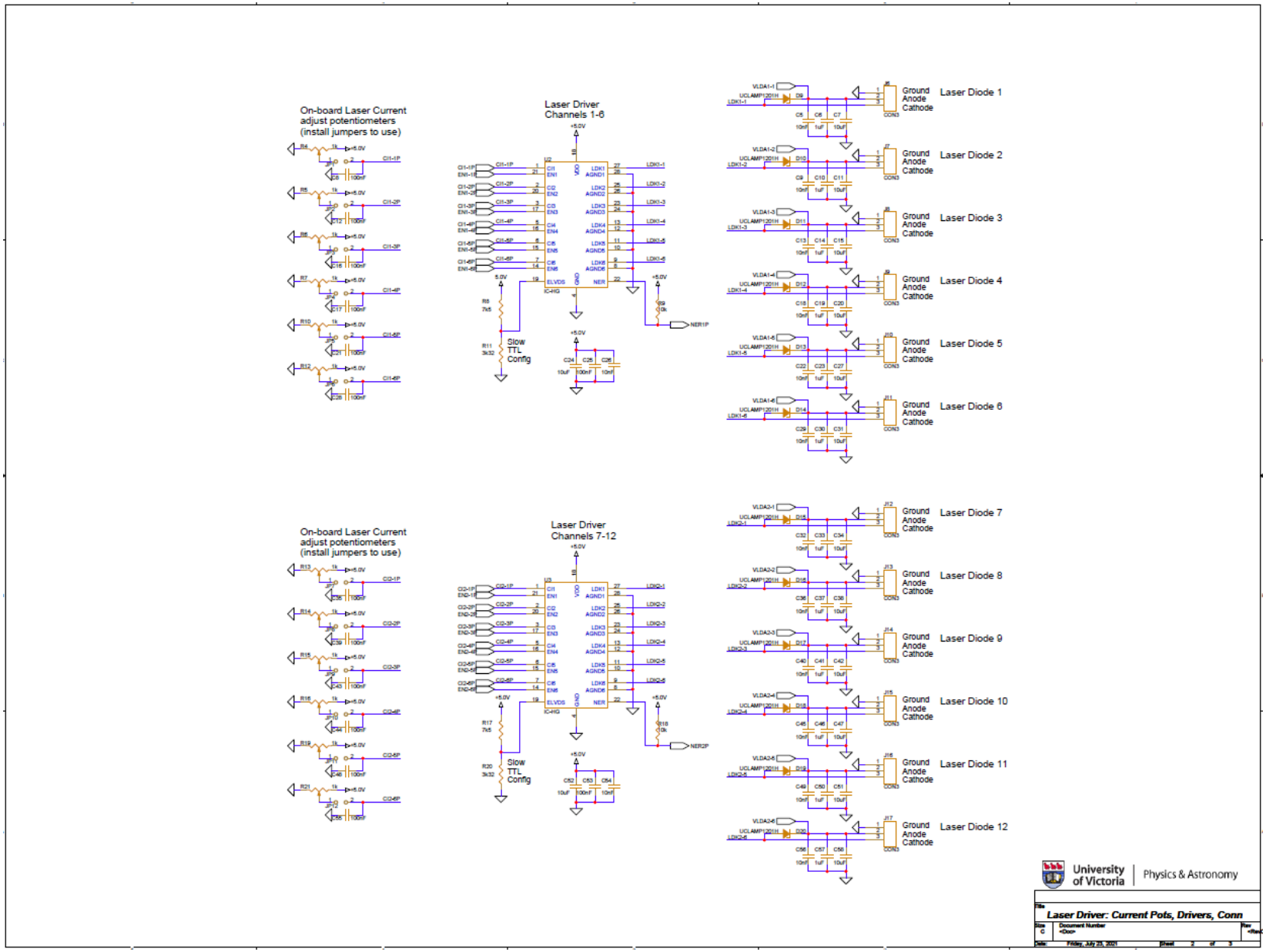
On-board Laser Current adjust potentiometers (install jumpers to use)
Laser Driver Channels 1-6
Slow TTL Config
Ground
Anode
Cathode
Laser Diode 1
Laser Diode 2
Laser Diode 3
Laser Diode 4
Laser Diode 5
Laser Diode 6
On-board Laser Current adjust potentiometers (install jumpers to use)
Laser Driver Channels 7-12
Slow TTL Config
Laser Diode 7
Laser Diode 8
Laser Diode 9
Laser Diode 10
Laser Diode 11
Laser Diode 12
University of Victoria
Physics & Astronomy
Laser Driver: Current Pots, Drivers, Conn

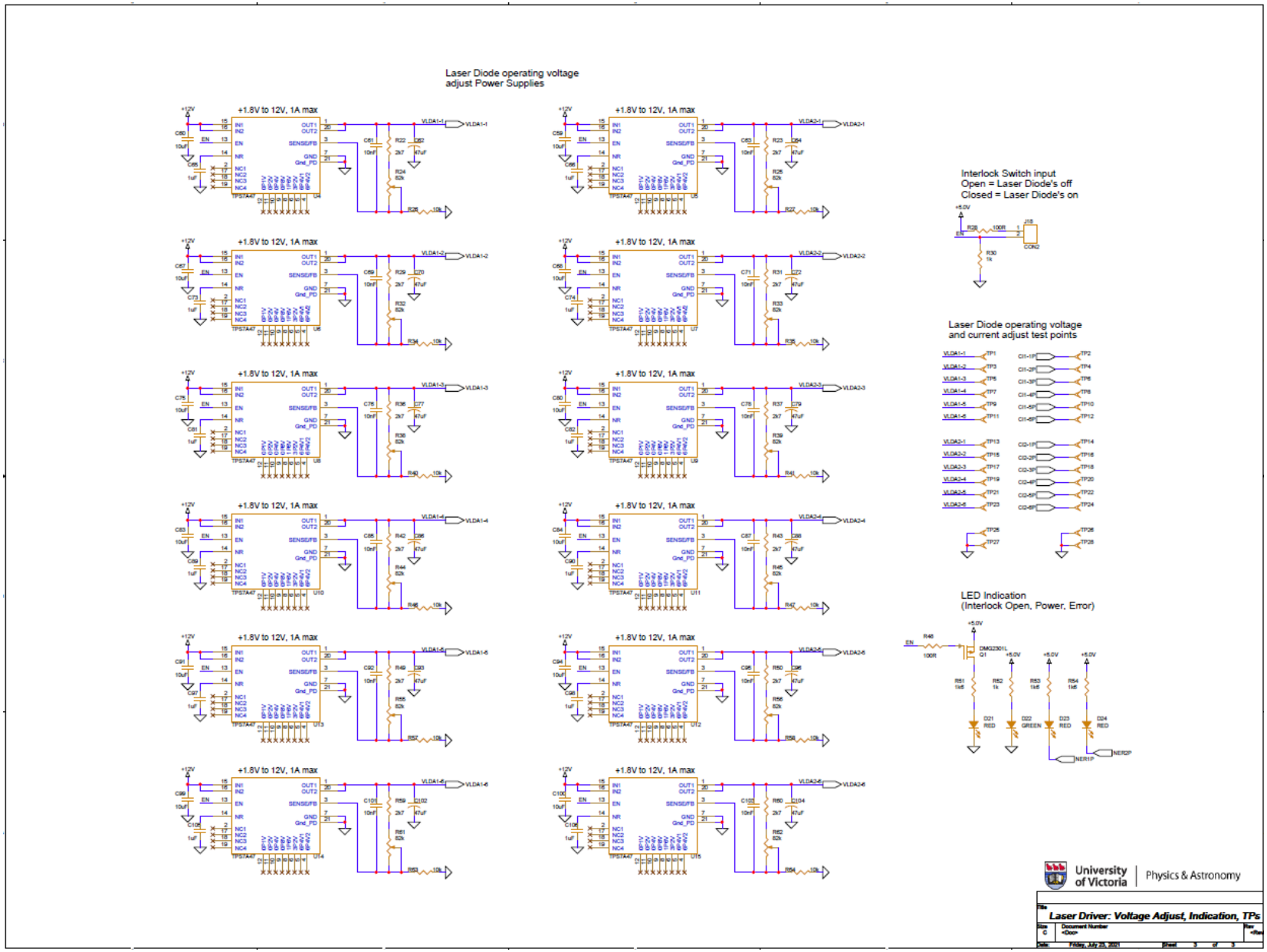
Laser Diode operating voltage
adjust Power Supplies
+1.8V to 12V, 1A max
Interlock Switch input
Open = Laser Diode's off
Closed = Laser Diode's on
Laser Diode operating voltage
and current adjust test points
LED Indication
(Interlock Open, Power, Error)
University of Victoria | Physics & Astronomy
Laser Driver: Voltage Adjust, Indication, TPs

A.15 Setting Voltage and Current on Laser Driver Board

To set the supply current to each laser diode (LD), the supply voltage (V_{set}) should first be determined. This can be done by attaching a multimeter to test points TP2–TP24 (even points) (Appendix A.14) in parallel to act as a voltmeter. The voltage should be adjusted using the potentiometer on the board to be approximately 1 V above the typical operating voltage given in the product information sheets of the respective LD. This allows for the full operating voltage to be accessed by the LD. The operating voltage (V_{op}) can then be set using a multimeter the same way as V_{set} but across odd test points (TP1-TP23) (Appendix A.14). Testing and setting the operating voltage is shown in the diagram below, which shows which test points are used for each of V_{set} (to control the current reaching the laser diode, measured as shown after) and V_{op} (to set the operating voltage for each laser driver channel). In each case, the red test cable (clip) is attached to the appropriate test point, and the black test cable is attached to any one of the four ground test points (TP25, TP26, TP27, TP28).

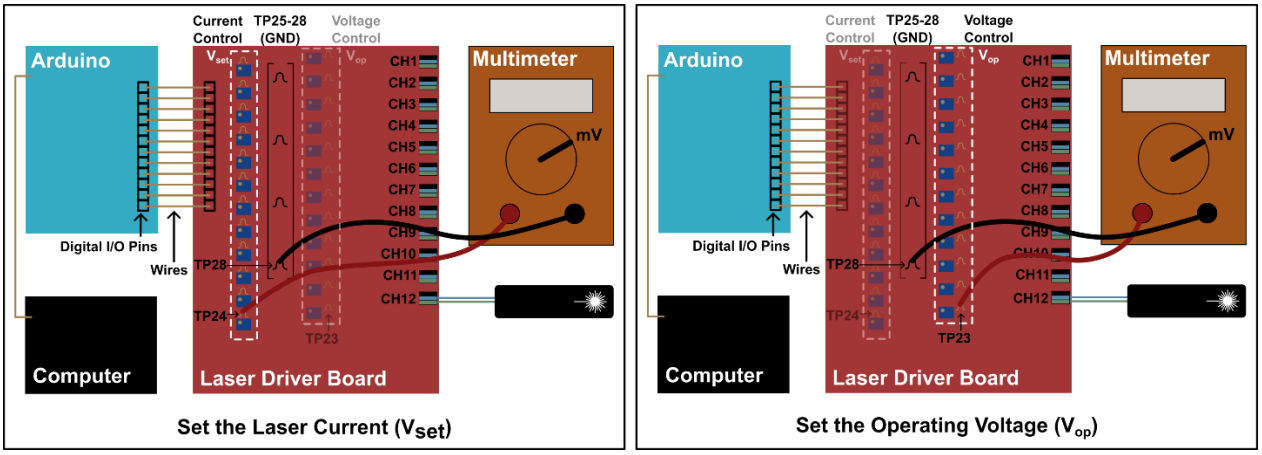

The current output to the LD is monitored using a custom-made cable—created for this purpose by Nick Braam in the UVic Physics and Astronomy Electronics Shop—connected between the laser cable and the board socket, attached to a multimeter in series acting as an ammeter.

The setup for testing the power output of the LDs is shown in the image below. The setup tests the power output for different current and voltage supply settings on the laser driver board. Laser power was detected by reading out the voltage of photodetector, using a voltmeter and 50 Ω terminating resistor.

A.16 Testing Current Reaching Laser Diode and Power Output

Current supply is measured using a multimeter through the red test cable which connects the laser diode cable to the laser driver board, and to the multimeter through banana plugs. The cable was custom-made by Nick Braam at the UVic Physics & Astronomy Electronics Shop, and measures the current being supplied to the laser diode by the laser driver board to be tested (in series) as shown in the setup below.

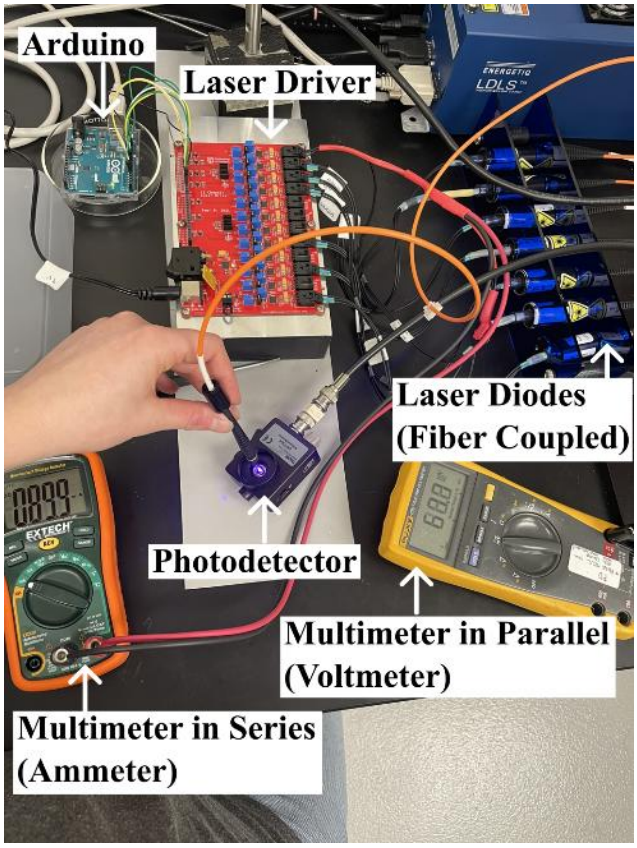

The cable is covered with red heat-shrink tube and has two banana plugs—one red and one black, and two black connector heads—one plug and one socket. The black plug attaches to the driver board in the channel for that laser diode, and the socket accepts the black plug connector from the usual laser diode cable (black) (Figure 3.17). The red banana plug should be connected to the red socket in a multimeter (while off), and the black banana plug to the black socket in the multimeter. The multimeter should then be turned to current-reading mode (milliamps preferred if the option exists). All connections should be done while the driver board is powered off. After the power switch on the board is turned on, the laser channel being tested should be turned on using the computer control via the Arduino, as described in Appendix A.2.

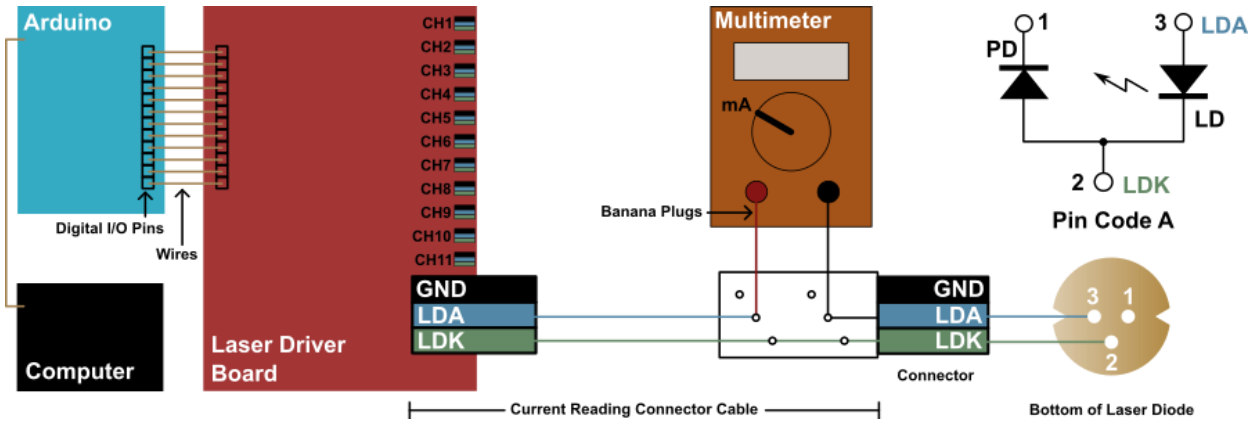

The testing cable allows for easy connection to the laser diodes which already have individual cables corresponding to their pin codes to connect to the laser driver board, however this can also be done without the test cable and laser diode cables, for example a new laser diode which hasn't yet been tested or one with a pin configuration that hasn't been made previously. On a laser diode without a connector cable, the same electronic path can be followed using alligator clips and banana plugs to connect to the laser diode pins, multimeter, and a cable plugged into the board but with free wires on the other end, for connecting to via alligator clips. When the cables are used that were made for each laser diode in the original setup, no extra steps need to be taken to determine which pins to use, as those have already been connected correctly. When the pre-made cables are not used (bare laser diode, for example), care must be taken to ensure that the pins are going to the correct ones in the driver board, and it would be wise to start with the voltage (current) control set to zero before turning on, in case incorrectly attached, to prevent permanently damaging the laser diode.

Manual current control via the on-board potentiometers can be disabled if remote current control is instead required for an application. The board is equipped with easy connection to a Mikroe DAC5 Click (x2) mounted on an Arduino UNO Click Shield, at J3 and J4 (Appendix A.14).

The power output of each laser was read using a photodetector, set up as described in Section 3.3.4. Operating voltage V_{op} should be set so that the laser is above the lasing threshold but less than around 80% of the maximum current allowable to prolong the lifetime of the LD.

A.17 Responsivity Curve for DET36A

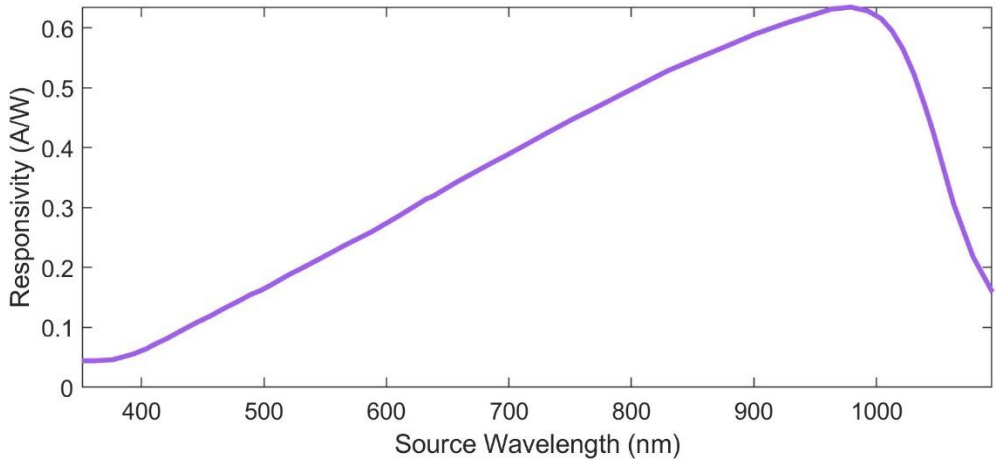

From the specifications sheet of DET36A (Thorlabs).

A.18 Microscope Pixel Size Calibrations

The following images are those which were used to determine the pixel size for the MSC and HSC through the Olympus CK2 microscope with a 10x objective lens. This is discussed in Section 7.3.1. The pixels were manually counted for each spacing (*e.g.,* 1.0 to 1.1), then those values were averaged to find the number of pixels per 0.1 mm, then 1 pixel was defined as 0.1 mm divided by the number of pixels.

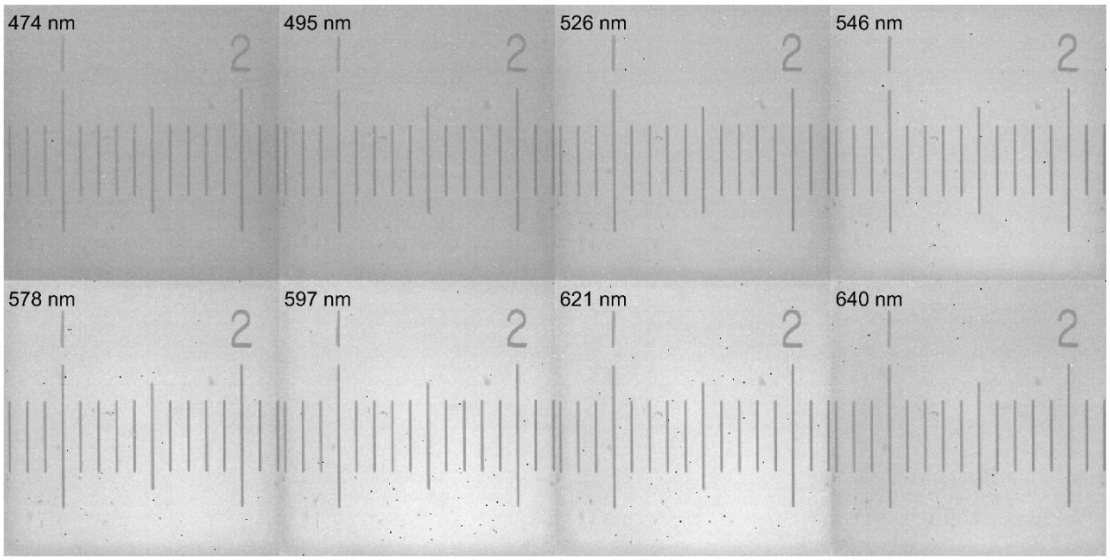

Figure A.18a. Calibration disk on an Olympus CK2 microscope with a 10x objective lens, imaged through a multispectral camera (Spectral Devices). Each colour channel of the camera is plotted separately, and the band centers of those channels are shown in text on each

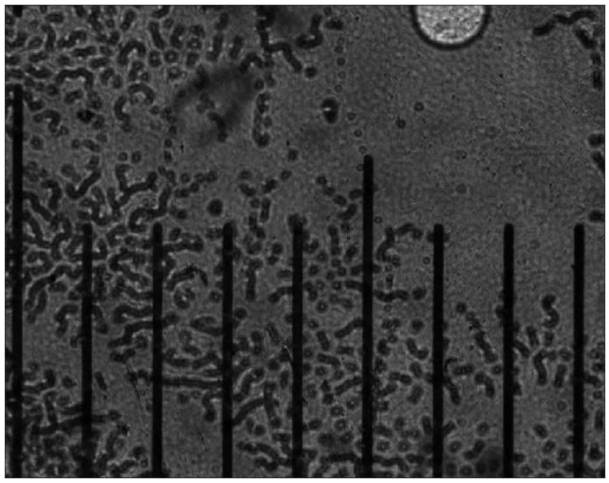

Figure A.18b. Calibration disk on an Olympus CK2 microscope with a 10x objective lens, imaged through a hyperspectral camera (GoldenEye, BaySpec). The mean of all 141 bands is shown in the image. The long tick on the left of the image is the "1" value on the calibration disk, each further increment is 0.1. Note that less of the calibration disk is captured in this HSC image compared with the MSC image because the sensor size of the HSC is smaller than that of the MSC.

A.19 Monitoring Fluorescence Changes due to Diffusion

In this appendix, a brief demonstration shows that using loading fits made using F-EEMs using an Avantes spectrometer and DMA-PLS can be used to monitor the relative composition of dye diffusion through a hydrogel through time. The three images in the figure below show the beginning, middle, and end of a time series of the gel described below.

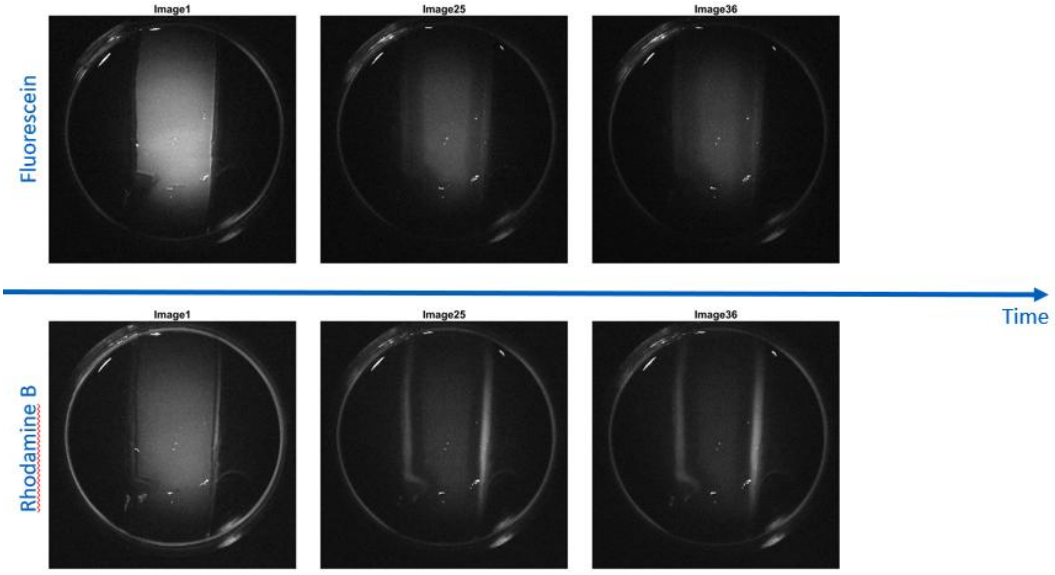

Agarose was prepared using 1 gram agarose stirred into 50 mL boiling deionized water, then 50 mL of a solution containing 100 μM fluorescein in aqueous sodium hydroxide and 100 μM rhodamine B, in deionized water which had been cooled in an ice bath. The agarose-dye solution was poured into petri dishes and left to set to a gel. A section of this gel was sliced using a razor blade and added to a petri dish containing an acid solution composed of 50% glacial acetic acid and 50% deionized water by volume. The fluorescence of the gel was monitored over time through the MSC equipped with a 50 mm lens (V5024-MPZ, Computar) with a +7 diopter, and a fiber-coupled Avantes spectrometer, with excitation illumination from the DMA-PLS.

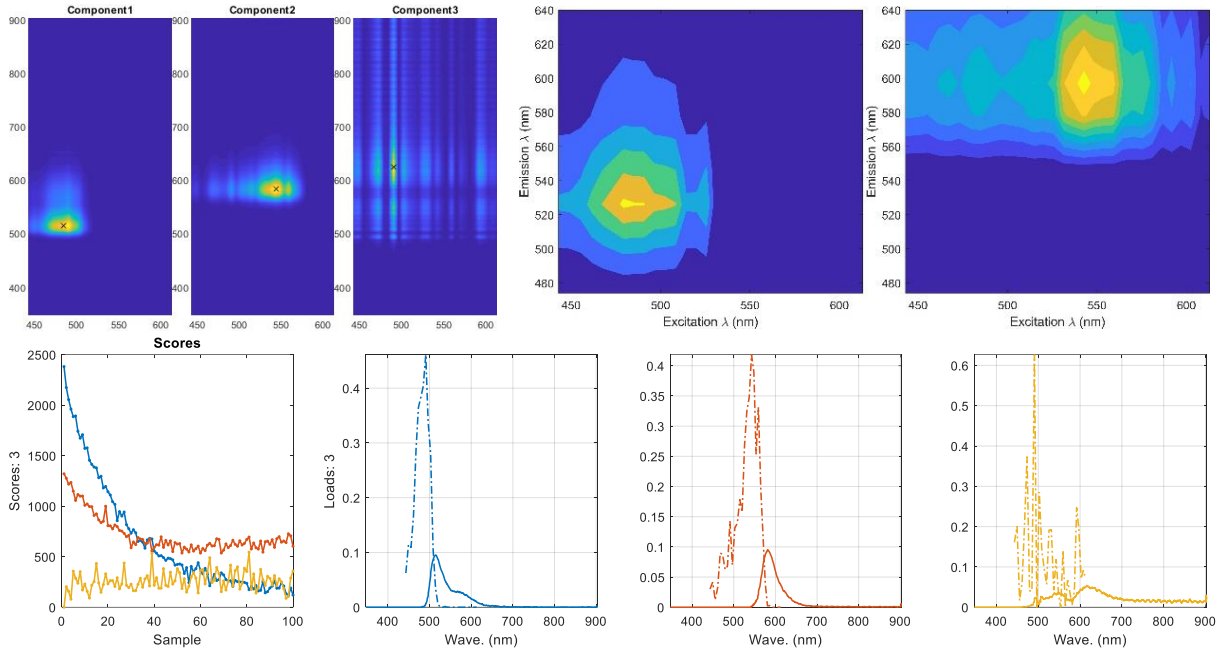

Figure A.19. Components in dyed agarose in an acidic solution over time. Component EEMs acquired by the Avantes spectrometer are shown on the top left, through a 3-component PARAFAC fit, and components from the initial loading fit using every nth pixel described in text are shown on the top right. In the bottom row, the component scores are shown over time, and the excitation and emission scores are shown beside. Components fluorescein, rhodamine B, and noise, are represented by blue, orange, and yellow lines, respectively.

The data were analyzed using PARAFAC and results of that fit are shown in Figure A.19. The fit used an initial fit of a sub-section of pixels, chosen using every n^{th} pixel. This loading fit was then applied to the full dataset through time (sample number, in Figure A.19). The three components can be seen in the bottom row, with the scores over time shown in the bottom left. Through time, as the dye-agarose gel absorbs more acid, the fluorescein component decreases as expected for fluorescein in acid instead of a basic solution (component 1, blue). Rhodamine B, which is not so sensitive to acidic or basic environments, remains relatively even throughout the experiment (component 2, red/orange). The noise component (component 3, yellow) remains consistently fluctuating through time, as expected for a noise component.

This experiment demonstrates both the ability of the MSC to monitor dyes through time, as well as the validity of choosing every n^{th} pixel to use as a loading fit, as shown in Figure 5.5, as a method of data reduction for fit speed and accuracy.